A microscopically and vibrationally resolved study of Rydberg macrodimers

Simon Hollerith

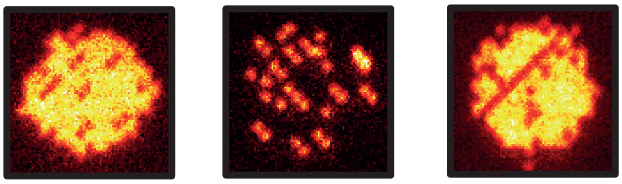

München, März 2022

A microscopically and vibrationally resolved study of Rydberg macrodimers

Simon Hollerith

Dissertation der Fakultät für Physik
der Ludwig-Maximilians-Universität München

vorgelegt von

Simon Hollerith

aus Moosburg a. d. Isar

München, 18. März 2022

Erstgutachter: Prof. Dr. Immanuel Bloch
Zweitgutachter: Prof. Dr. Johannes Deiglmayr

Tag der mündlichen Prüfung: 29. April 2022

Zusammenfassung

Aufgrund ihrer starken dipolaren Wechselwirkungen zählen Rydberg Atome zu den vielversprechendsten Plattformen für Quanten-Simulationen und Quanten-Computing. Die selben Wechselwirkungen liefern auch molekulare Bindungspotentiale, deren extreme Bindungslängen bis in den Mikrometer-Bereich hinein reichen. Diese Arbeit präsentiert die ersten vibrationsaufgelösten Spektroskopien dieser Rydberg Makrodimere. Die beobachteten Vibrationsspektren stimmen mit ab initio Berechnungen überein. Die scharfen spektroskopischen Signaturen der Wechselwirkungen im nicht-perturbativen Abstandsbereich stellen den präzisesten experimentellen Zugang zu Rydberg Wechselwirkungen dar.

Die Makrodimere werden aus einem vollbesetzten zweidimensionalen optischen Gitter aus Atomen im Grundzustand heraus angeregt und verlassen anschließend das System. Die Bindungslänge stimmt in den meisten Fällen mit dem Diagonalabstand im Gitter überein. Durch optisches Abbildung der verbleibenden Atome können Molekülanregungen über den korrelierten Paarverlust von Atomen nachgewiesen werden. Diese Konfiguration erlaubt die Untersuchung von Photoassoziation in einem Bereich, in dem der Anfangszustand und die Orientierung des externen Magnetfeldes und der Lichtpolarisation relativ zur Molekülachse vollständig kontrolliert sind. Die beobachteten Abhängigkeiten liefern einen Fingerabdruck der elektronischen Struktur der Moleküle und legen ihre Quantenzahlen offen. Die orientierungsabhängige Zeeman Aufspaltung der Moleküllinien zeigt einen deutlichen Beitrag der Hyperfeinwechselwirkung der beitragenden Rydbergatome. Abschließend werden nicht-adiabatische Kopplungen zwischen Paarpotentialen durch die Kernbewergung in einem Bereich in dem die der Born-Oppenheimer Näherung zusammenbricht spektroskopisch beobachtet und über externe Magnetfelder verstärkt.

Nach dieser präzisen Charakterisierung wurden Makrodimer Zustände in einem nicht-resonanten Kopplungsschema verwendet um abstandsselektive Wechselwirkungen im Grundzustand zu erzeugen. Das im Experiment realisierte System lässt sich durch einen Ising Hamiltonian beschreiben. Die erzeugten Wechselwirkungen wurden durch korrelierte Phasenentwicklung mittels Ramsey Interferometrie nachgewiesen. Hierbei wurden für wachsende Wechselwirkungszeiten Zwei-Spin Korrelationen und Drei-Spin Korrelationen beobachtet. Nach dem Berücksichtigen einer Energieverschiebung der Molekülresonanz aufgrund von Photodissoziation in ungebundene Bewegungszustände ist die beobachtete Spin Dynamik in Übereinstimmung mit der theoretischen Erwartung.

Mit der vorgestellten Arbeit erreicht die experimentelle Kontrolle über Rydberg Wechselwirkungen eine neue Ebene. Die Resultate liefern darüber hinaus experimentellen Zugang zu generischen Eigenschaften von Molekülen die normalerweise nicht zugänglich sind. Das realisierte Spin System zeigt zudem eine erste Anwendung von Makrodimeren für mögliche Quanten-Simulationen.

Abstract

Because of their strong dipolar interactions, Rydberg atoms are now among the most promising platforms for quantum simulation and computation. The same interactions also give rise to molecular binding potentials with extreme bond lengths reaching into the micrometer regime. This dissertation presents the first vibrationally resolved spectroscopies of these so-called Rydberg macrodimers. The observed vibrational spectra agree with ab initio calculations. The sharp spectroscopic signatures of the interactions in the non-perturbative distance regime represent the most stringent tests of the interactions between Rydberg atoms.

In the experiments, macrodimers are excited from a unity-filled two-dimensional atomic array in the electronic ground state and then removed from the system. In most cases, the bond lengths match the diagonal distance in the array. Imaging the remaining atoms in the array therefore enables to observe the excited molecules via correlated atom loss. The well-defined alignment of the initial ground state atom pairs as well as the excited molecules provides unique access to the molecular frame of reference. This enables photoassociation studies where the initial ground state, the orientation of an applied magnetic field and the light polarization relative to the molecular axis is fully controlled. The observed dependencies provide direct fingerprints of the electronic structure of the molecules and expose their quantum numbers. The orientation-dependent Zeeman splittings furthermore reveals a significant contribution of the hyperfine interaction of the macrodimer states. Finally, non-adiabatic motional couplings between pair potentials, where the Born-Oppenheimer approximation breaks down, have been spectroscopically observed and enhanced using an external magnetic field.

After this precise characterization, macrodimer states are used to engineer Rydberg-dressed interactions between ground state atoms in an off-resonant coupling scheme. The system realized in the experiment can be mapped to an Ising Hamiltonian with strongly distance-selective interactions. The interactions realized in the experiments were probed through correlated phase evolution using many-body interferometry. For increasing integration time, the admixed interactions induce two-spin correlations as well as three-spin correlations. After accounting for an additional energy shift originating from photodissociation into motional states in the chosen coupling scheme, the observed dynamics again agrees with the calculations.

The present study raises the experimental control over Rydberg interactions to a new level and provides novel experimental access to generic properties of molecular quantum states that are usually not accessible. The realized Ising Hamiltonian furthermore shows a first application how macrodimers can be used for quantum simulations.

Contents

Chapter 1

Introduction

The field of atomic, molecular and optical physics has a history of more than hundred years. Probing the structure of atoms and molecules [1–5] with light led to important contributions to our current understanding of quantum mechanics [6–10], quantum field theory [11–13] and possible theories beyond the standard model [14–16]. The possibility to create coherent electromagnetic light in the visible spectrum with lasers [17] revolutionized the efficiency in studying and manipulating electronic quantum states of atoms and molecules [18]. The invention of laser cooling enabled the creation of atomic samples in the mikrokelvin regime [19]. Performing evaporative cooling allowed researchers to reach the even lower ultracold temperature regime where quantum degenerate phenomena such as Bose-Einstein condensation [20–22] or degenerate Fermi gases [23] have been observed.

The versatile control over many-body Hamiltonians in the ultracold temperature regime contributed heavily to the field of quantum simulation [24, 25]. Here, the idea is to experimentally realize specific quantum systems, prepare their eigenstates, and study the corresponding unitary time dynamics. In the optimal case, the quantum simulator performs better than a classical calculation of the same problem, allowing to probe novel regimes of physics. Most prominent Hamiltonian parameters are the interaction between particles, the different electronic states of the atoms, their quantum statistics, or the external potential [26]. In many cases, the atomic ensembles are confined in focussed laser beams whose frequency is chosen such that the light field creates an attractive potential.

Similarly, standing waves created by interfering laser beams realize periodic potential landscapes that allow for the realization of Hamiltonians which are of relevance in the fields of solid state and condensed matter physics [27–29]. Among them is the so-called Hubbard model [30, 31] where the atoms confined in the optical lattice are described only by the coherent tunneling rate between neighboring sites and the on-site interaction of two atoms occupying the same lattice site. Dependent on the relative srength of both parameters, the many-body ground state for bosonic particles can be either an insulating state, a so-called Mott insulator, or a Bose-Einstein condensate. Dynamically tuning the parameter of the Hamiltonian enables the study of quantum phase transitions [32]. In contrast to thermodynamic phase transitions where thermal fluctuations play a crucial role, these are driven by quantum fluctuations and only depend on the parameters of the Hamiltonian [33]. In the Mott insulating phase in the vicinity of the phase transition, Hubbard models can be mapped to spin models. Operating in this regime allows one to simulate quantum magnetism [34, 35] and maybe probe whether Hubbard models can be used as effective models to describe high-temperature superconducting phases observed in real solid state systems [36–38].

There exist several pathways to probe the prepared quantum states. By releasing the atoms from the system and detecting their position after an expansion time in a time-of-flight experiment, the occupied momentum states and the band structure can be probed [26]. In contrast to real solids, the ten thousand times larger distances in optical lattices also allows to directly probe their position with optical methods [39]. Here, the possibility to image and manipulate individual atoms in optical lattices [40–42] with laser light using quantum gas microscopy enabled the characterization the prepared many-body states directly by their correlation functions [43, 44].

Interactions in ultracold atomic systems are usually restricted to short-ranged contact interactions [45] where the motional wave packets have to overlap. A way to further extend the toolbox of quantum simulations is to engineer interactions at larger distances. Here, the most prominent examples are atoms that interact through their magnetic moments [46], polar molecules [47], or highly-excited Rydberg atoms [48, 49]. The latter two interact via electrostatic dipole-dipole interactions. The interactions between Rydberg atoms are the strongest and also highly tunably by the choice of the Rydberg state [50]. During the last decade, Rydberg atoms enabled a large variety of experiments in the fields of quantum simulation [51–53] as well as quantum computation [54]. The interaction energies easily exceed the lifetime of the Rydberg states [55] and therefore enable a coherent manipulation of the system without significant loss. Rydberg interactions also demonstrated that tweezer arrays [56, 57], where atoms are trapped in individually focused laser beams, are an attractive platform for quantum simulations. Here, their strong and long-ranged interactions enable experiments at temperatures and interatomic distances that are both larger compared to typical values realized for ultracold atoms in optical lattices.

Systems of ultracold atoms also enabled studies of molecules at an unprecedented level of control [58]. At room temperature, chemical reactions are described by the laws of thermodynamics. In contrast, molecules at ultracold temperatures can be coherently associated and transfered between different internal quantum states using magnetic fields and lasers [59]. Using these techniques, the molecules can be coherently prepared in the rovibrational ground states [60, 61]. Addressing different rotational states can induce a permanent dipole moment and the previously listed interactions [62, 63]. Furthermore, reactions can be studied on a level of individual molecules [64].

Also Rydberg atoms contributed to ultracold molecular physics in the context of ultralong range Rydberg molecules. The large separation of the Rydberg electron from the nucleus and the large interactions between Rydberg atom pairs give rise to new exotic types of molecules [65, 66]. These molecules are special because of their large bond lengths, their small binding energies, and their comparatively easy theoretical description. Among them are Rydberg macrodimers [67], whose micrometer-sized interatomic separations make them the largest existing diatomic molecules. They are bound by the same Rydberg interactions used for quantum simulations and the main topic of this dissertation. Because their bond length exceeds optical wavelenghts, the atoms in the molecule can be individually adressed using laser light. Furthermore, because their long rotational timescales are beyond their lifetime and cannot be spectroscopically resolved, atom pairs excited into macrodimer states keep their spatial alignment. Both features combined enable unique access to the molecular frame of reference and, as a consequence, to the electronic structure of the molecular state. Previous studies on macrodimers were performed in bulk systems with randomly oriented atom pairs [68–70]. The quantized vibrational states and the orientation of the excited macrodimers remained unresolved.

The measurements presented in this dissertation used quantum gas microscopy to resolve rubidium atoms in an optical lattice [71]. As an initial state, the experiments started with a two-dimensional unity-filled lattice in the electronic ground state, provided by the Mott insulating state. The excitation into Rydberg states has been implemented using a single-photon transition in the ultraviolet [72]. Using the same ultraviolet laser, Rydberg macrodimers were excited using a two-photon transition. Here, ground state atom pairs were excited into the binding potentials that are energetically located several hundreds of megahertz off-resonant to the Rydberg resonance. After the experiment, the ground state atoms were imaged with a high-resolution objective placed below the atoms. Rydberg atoms and macrodimers were ejected from the array and can be detected via atom loss. The quantized vibrational structure of the binding potentials has been resolved by high-resolution atom-loss spectroscopy. The observed vibrational spectra agreed with the expected vibrational energies after accounting for sufficiently many multi-pole terms in the expansion of the Rydberg interaction Hamiltonian. By the choice of the principal quantum number of the Rydberg state, the macrodimer bond lengths were tuned to match the lattice diagonal distance. Macrodimer excitation therefore led to correlated loss of ground state atoms at that distance, which can be probed by the microscope. Because of the orientation of the optical lattice, the observed correlation signal quantifies the excitation of macrodimers that were aligned in the laboratory frame. This enabled a photoassociation study where the orientation of the magnetic field and the polarization relative to the alignment of the molecules is well-defined. Studying the dependency of the photoassociation rate on these variables enabled a characterization of the electronic structure of macrodimer states. After a precise characterization of macrodimers, possible applications for quantum simulations have been tested. Using optimized coupling conditions and a phase-modulated excitation laser, off-resonant coupling into macrodimer states realized distance-selective long-range interactions in the ground state. The engineered interactions were observed in a Ramsey experiment. In future experiments with improved coherence times, his provides a path towards the realization of highly-entangled cluster states in a single massive entanglement operation, also in two dimensions.

Outline

This section presents the organization of the dissertation. Chapter 2 discusses the properties of Rydberg atoms and their applications in quantum science. The chapter closes with a short introduction of Rydberg macrodimers and compares their properties with other diatomic molecules. Chapter 3 starts with a discussion of quantum gas microscopy and then presents the experimental apparatus used in this dissertation. This part focuses on the UV system used for Rydberg excitation. Chapter 4 provides a more thorough overview of macrodimer states and discusses their optical excitation and the role of the motional wave packets. The chapter furthermore presents first vibrationally resolved spectroscopies. In chapter 5, the calculations of Rabi frequencies between ground state atom pairs and Rydberg macrodimer states and their dependency on the molcular quantum numbers is discussed. Subsequently, the validity of the description is verified for several different macrodimer binding potentials. For all potentials, additional spectroscopies of the vibrational structure is presented. Also the response of the macrodimer states to applied magnetic fields, the hyperfine interaction of macrodimer states, and the dependence of the electronic structure of the macrodimer states on the interatomic distance is discussed. Chapter 6 demonstrates the contributions of non-adiabic motional coupling elements between nearby pair potentials and demonstrates how it externally induced by a magnetic field. Chapter 7 presents a coupling configuration where maximum macrodimer Rabi frequencies can be achieved. In this two-color excitation scheme where the intermediate detuning in the excitation can be strongly reduced, the contribution of photodissociation into unbound motional states is discussed. In chaper 8, this two-color excitation scheme is used in an off-resonant configuration to realize distance-selective Ising Hamiltonian in the electronic ground state. Using Ramsey interferometry, the presence of the dressed interactions is observed via two-spin and three-spin correlations.

Complete list of publications

A) Peer-Reviewed publications

1. **Hollerith S.**, Srakaew, K., Wei, D., Rubio-Abadal, A., Adler, D., Weckesser, P., Kruckenhauser, A., Walther, V., van Bijnen, R., Rui, J., Gross, C., Bloch, I., Zeiher, J., (2022): **Realizing distance-selective interactions in a Rydberg-dressed atom array.** Published in: *Physical Review Letters*, 128, 113602.

2. Barbier, M., **Hollerith, S.**, Hofstetter, W., (2021): Extended Bose-Hubbard models with Rydberg macrodimer dressing. Published in: *Physical Review A*, 104, 053304

3. **Hollerith S.**, Rui, J., Rubio-Abadal, A., Srakaew, K., Wei, D., Zeiher, J., Gross, C. & Bloch, I., (2021): **Electronic structure tomography of Rydberg macrodimers.** Published in: *Physical Review Research*, 3, 013252.

4. Rui, J., Wei, D., Rubio-Abadal, A., **Hollerith S.**, Zeiher, J., Stamper-Kurn, D. M., Gross, C. & Bloch, I., (2020): A subradiant optical mirror formed by a single structured atomic layer. Published in: *Nature* 583, 369–374.

5. Rubio-Abadal, A., Ippoliti, M., **Hollerith S.**, Wei, D., Rui, J., Sondhi, S. L., Khemani, V., Gross, C. & Bloch, I., (2020): Floquet Prethermalization in a Bose-Hubbard System. Published in: *Physical Review X*, 10, 021044.

6. **Hollerith, S.**, Zeiher, J., Rui, J., Rubio-Abadal, A., Walther, V., Pohl, T., Stamper-Kurn, D. M., Bloch, I. & Gross, C., (2019): **Quantum gas microscopy of Rydberg macrodimers.** Published in: *Science*, 364, 664–667.

7. Rubio-Abadal, A., Choi, J.-Y. , Zeiher, J., **Hollerith S.**, Rui, J., Bloch, I.& Gross, C., (2019): Many-Body Delocalization in the Presence of a Quantum Bath. Published in: *Physical Review X*, 9, 041014.

B) Preprints sent out for Peer-Review

1. Wei, D., Rubio-Abadal, A., Ye, B., Machado, F., Kemp, J., Srakaew, K., **Hollerith, S.**, Rui, J., Gopalakrishnan, S., Yao, N. Y., Bloch, I., & Zeiher, J., (2021): Quantum gas microscopy of Kardar-Parisi-Zhang superdiffusion. (Accepted in Science)

Chapter 2

Interacting Rydberg atoms

The goal of this chapter is to provide an overview over the physics of Rydberg atoms. Whenever necessary, a discussion of the state-of-the-art in the field allows the reader to put the results presented later into context. Over the last two decades, Rydberg atoms attracted significant attention because of their strong dipolar interactions [50, 73]. Even at distances of several micrometers, these can easily be the dominating energy scale of a typical experimental system. They provide a toolset to engineer different long-range interacting many-body Hamiltonians for quantum simulations [52, 74, 75]. Because they are capable of realizing entanglement gates between atoms, they are furthermore regarded as a promising platform for quantum computation [49, 76–78]. Finally, Rydberg atoms give rise to highly-excited molecules [65] that are unique because of their large bond lengths and their exotic binding mechanisms.

2.1 Long-range interactions & experimental platforms

This section discusses long-range interactions in cold atomic systems from a general point of view. While Rydberg atoms provide the strongest long-range interactions among neutral particles, they are not the only option. Furthermore, different types of long-range interactions are more suitable for different experimental platforms. These can currently be divided into two main categories.

Ultracold atomic gases cooled down to quantum degeneracy provide a versatile platform to study many-body physics. Experimental cycling times are typically longer than ten seconds due to the time required for evaporative cooling and temperatures are on the order of nanokelvin [26]. Realizing interactions at distances where the motional wave functions do not overlap, such as between atoms located at different sites in an optical lattice, requires some quantum engineering. One possibility is to use atoms with large magnetic moments in the ground state which interact via magnetic dipole interactions [79, 80]. These interactions give rise to self-bound quantum droplets [46] and dipolar supersolids [81–83]. As a third option, the electric dipole interactions between polar molecules can be used. Preparing the molecules [47, 84] in superpositions of rotational states using static electric or radiofrequency fields induces the required dipole moments. In contrast to atoms, molecules have additional rotational and vibrational degrees of freedom [85, 86]. Furthermore, they suffer from additional loss channels [87, 88]. Despite these additional difficulties, there has been remarkable progress [84, 89] during the last years.

On the other hand, recent experiments succeeded in initializing defect-free atomic arrays made of individually focused laser beams [56, 57, 90], so-called optical tweezers. The tweezers are directly loaded from a magneto-optical trap and rearranged after imaging the initially randomly populated tweezers. Mainly because evaporative cooling is not required, cycling times are only on the order of a second. In order to avoid interference between neighboring tweezers, their distance is usually larger than a micrometer and therefore larger than the spacings in optical lattices. The larger distances make it hard to observe the interactions of magnetic atoms and also realizing interactions between individual molecules trapped in optical tweezers is a current challenge [91]. This is different for Rydberg interactions which are strong enough to bridge the distance between the tweezers [92–94].

In addition to the two presented experimental platforms, hybrid systems where the fast cycling times of optical tweezers are combined with the short distances and low temperatures achieved with conventional ultracold atom experiments are currently developed [95, 96].

Other new directions involve interactions mediated by near-resonant light [97, 98]. For interatomic distances below the optical wavelength, this led to the observation of superradiant [99, 100] and subradiant states [101]. Using cavities, these interactions can be further enhanced and scaled to a long-distance range [102–106]. Recently, this platform also achieved to engineer spin Hamiltonians with tunable non-local interactions [107]. Finally, ions traditionally confined in Paul traps [108] are interacting with long-ranged Coulomb interactions. Extending these systems to optically trapped ions that are arranged in certain spatial patterns might also lead to interesting results [109, 110].

2.2 Properties of Rydberg atoms

Rydberg atoms are highly-excited atoms where one electron populates a high principal quantum number n [48]. The excited Rydberg electron which is mostly located at large distances from the nucleus has only a small overlap with the rest of the atom. In this limit, the description can be simplified by combining the nucleus and the remaining ground state electrons to an effectively singly-charged nucleus. As a consequence, properties of Rydberg atoms and their scalings with principal quantum number are very similar to hydrogen and can be calculated with high accuracy. Typical principal quantum numbers are within the range $n \in [15, 100]$. Rydberg states have also been studied for higher $n > 100$ [111] but the difficulty in spectroscopically resolving and coherently exciting the states and the high electric-field sensitivity make them hard to control.

2.2.1 Binding energies

Historically, studying Rydberg states led to important contributions to the development of atomic theory [1, 112, 113], in particular because of the characteristic scaling of the binding energy with the principal quantum number n. For hydrogen, it is given by $E_n = -\frac{R_\infty}{n^2}$ if the mass of the electron, relativistic effects, and contributions arising from the nuclear structure and quantum field theory are neglected [114]. Here, $R_\infty = \frac{m_e e^4}{8\epsilon_0^2 h^3 c} = h \times 3289.8419602508\,\mathrm{THz}$ is the Rydberg constant, obtained from the NIST database [115]. For atoms with more electrons, deviations from hydrogen can be quantified using quantum defect theory. For alkali atoms such as ^{87}Rb, the binding energies are given by the Rydberg-Ritz formula [116, 117]

$$E_{n,L,J} = -\frac{R^\star}{(n - \delta_{n,L,J})^2} = -\frac{R^\star}{(n^\star)^2}, \tag{2.1}$$

nL_J	$nS_{1/2}$	$nP_{1/2}$	$nP_{3/2}$	$nD_{3/2}$	$nD_{5/2}$
δ_0	3.131 [122]	2.6545 [122]	2.6415 [122]	1.348 [118]	1.346 [118]
δ_2	0.179 [122]	0.290 [122]	0.295 [122]	-0.605 [118]	-0.594 [118]

Table 2.1: **Most relevant quantum defects for ^{87}Rb.** Calculating $\delta(n, L, J)$ from δ_0 and δ_2 allows to predict quantities of Rydberg atoms by their scaling with $n^\star$. The quantum defects decrease for higher L where the system becomes more hydrogen-like. In section 5.2.3, the dependence of the spatial overlap between the Rydberg electron and the nucleus on $n^\star$ enabled the prediction of the hyperfine structure of Rydberg macrodimers.

with $R^\star = m_{\text{Rb}}/(m_{\text{Rb}} + m_e) \times R_\infty$ [48, 118], m_{Rb} the mass of the ionic core, m_e the mass of the electron, and $n^\star = n - \delta_{n,L,J}$ the so-called effective principal quantum number. Here,

$$\delta_{n,L,J} = \delta_0 + \left(\frac{\delta_2}{n-\delta_0}\right)^2 + \left(\frac{\delta_4}{n-\delta_0}\right)^2 + ... \tag{2.2}$$

are the quantum defects. They mainly depend on the orbital angular momentum L and weakly on n and the total angular momentum J. Here, the spin-orbit coupling combines L and the electron spin $s = \frac{1}{2}$ to J. Quantitative numbers for δ_0 and δ_2 are provided in table 2.1. Many properties of Rydberg states can be derived from their characteristic scaling with $n^\star$. The effective reduction of the principal quantum number by the quantum defect can be intuitively understood from the overlap of the Rydberg electron with the remaining electron cloud. Because this part of the wave function will experience a higher nuclear charge, the electron is more deeply bound compared to hydrogen [119]. This results in a deviation from the Coulomb potential of one-electron systems, in particular at small distances from the nucleus, see Fig. 2.1 (**a,b**). Equivalently, this interaction with the ionic core also affects the remaining electron orbitals through the core polarizability, which slightly modifies the total polarizability of the atom [120, 121]. As expected from this discussion, quantum defects decrease for higher L where the centrifugal barrier decreases the probability density of the Rydberg electron at the ionic core.

2.2.2 Rydberg wave function

To predict experimental outcomes involving Rydberg atoms, calculating the Rydberg wave functions is usually the first step. Assuming a spherically symmetric potential for the Rydberg electron, the angular wave function has a well-defined angular momentum and can be separated from the radial wave function via

$$|nLJm_J\rangle = |R_{nLJ}\rangle \otimes |LJm_J\rangle. \tag{2.3}$$

Strictly speaking, the spherical symmetry of the Rydberg wave function will be violated by the interaction of the highly excited electron with the remaining electrons. Note that the angular momentum of all electrons combined will always be conserved. Because of the large separation from the ionic core, this can typically be neglected. This framework even provides reliable results for Rydberg states of more complex atoms with submerged shells such as erbium where the angular momentum states in the ground state are mixed [123]. The Rydberg states are expressed in the eigenbasis of the total electron

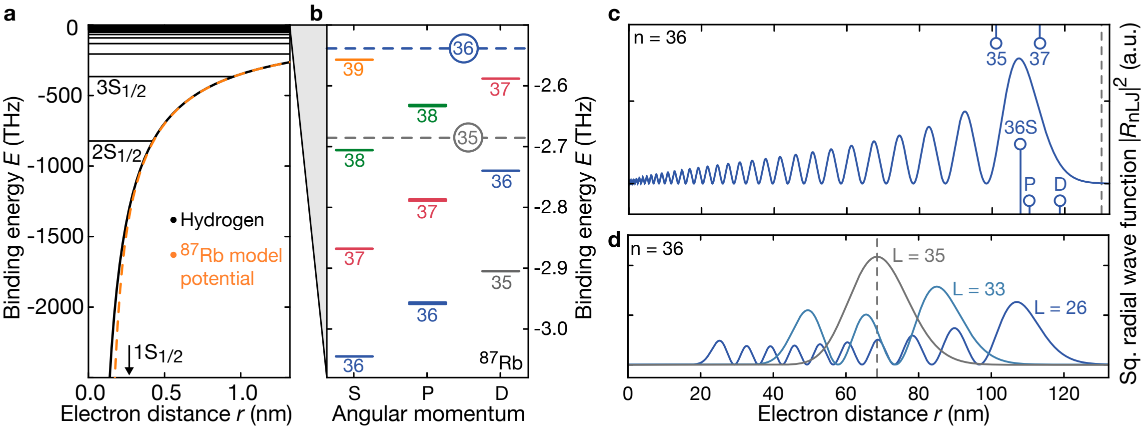

Figure 2.1: **Basic properties of Rydberg states of ^{87}Rb.** (**a**) The interaction potential of the Rydberg electron can be approximated using $L-$dependent model potentials (orange) which resemble the Coulomb potential of the hydrogen atom (black) at large distances. At short distances or lower angular momenta where the Rydberg electron penetrates the orbitals of the remaining electrons, the binding energy shifts below the hydrogen reference. Here, the energy levels of ^{87}Rb also significantly deviate from the energies for hydrogen (horizontal black lines) where different $L-$states are basically degenerate. (**b**) Exemplary Rydberg energy levels for $L = \{0, 1, 2\}$. The higher L, the closer the energy levels shift towards the values for hydrogen (dashed lines). (**c**) Rydberg wave function for $36S_{1/2}$ (solid blue line). Changing n or L, the position of the outer lobe slightly shifts (upper and lower markers). For different J, the effect is too small to be visible. The dashed gray line to the right indicates the position for hydrogen in $36S_{1/2}$. (**d**) For even higher L, the outer lobe again moves towards smaller r and the value at the ionic core vanishes (blue to gray). For circular Rydberg states with maximum $L = n - 1$ and $m_L = L$, the wave function matches the semiclassical Bohr orbit $r_n = n^2 \times 0.0529\,\mathrm{nm}$ for hydrogen (dashed gray line).

angular momentum operator $\hat{\boldsymbol{J}} = \hat{\boldsymbol{S}} + \hat{\boldsymbol{L}}$ due to the presence of spin-orbit coupling. Here, $\hat{\boldsymbol{L}}$ and $\hat{\boldsymbol{S}}$ are the operators of the orbital and the spin angular momentum of the valence electron. The hyperfine coupling to the nuclear spin is typically neglected due to the large spatial separation. The states $|LJm_J\rangle$ can be decomposed into the basis of uncoupled angular momenta via $|LJm_J\rangle = \sum_{m_L m_s} \mathcal{C}^{L\ \ J\ \ 1/2}_{m_L\, m_J\, m_S} |Lm_L\rangle|\frac{1}{2}m_S\rangle$. The expansion coefficients $\mathcal{C}^{1/2\ J\ \ L}_{m_S\, m_J\, m_L} = \langle\frac{1}{2}m_S Lm_L|Jm_J\rangle$ are called Clebsch-Gordan coefficients. The decomposition allows one to compute the spatial probability amplitudes via

$$\langle \boldsymbol{r}|nLJm_J\rangle = R_{nLJ}(r) \sum_{m_S, m_L} \mathcal{C}^{1/2\ J\ \ L}_{m_S\, m_J\, m_L} Y_L^{m_L}(\theta, \phi)|\frac{1}{2}m_S\rangle, \tag{2.4}$$

where the spherical harmonics $Y_L^{m_L}(\theta, \varphi)$ are the real space representations of the angular momentum states $|Lm_L\rangle$. The radial wave function $R_{nLJ}(r)$ is independent of angular momentum projections but still depends on J because of spin-orbit coupling. It can be calculated by solving the Schrödinger equation of the Rydberg electron in a species-dependent model potential $V_L(r) + V_{\mathrm{so}}(r)$ using a Numerov algorithm [124–126], see Fig. 2.1 (**a**). Here, $V_{\mathrm{so}}(r) = \alpha_F \frac{\hat{\mathbf{L}} \cdot \hat{\mathbf{S}}}{2r^3}$ accounts for the spin-orbit coupling [117] and α_F is the fine-structure constant. The most frequently used formalism parametrizes the potential of the ^{87}Rb Rydberg electron in atomic units using a spherically symmetric potential

$$V_L(r) = -\frac{Z_L}{r} - \frac{\alpha_c}{2r^4}\left[1 - e^{-(r/r_c)^6}\right]. \tag{2.5}$$

This model potential is used in most available software [50, 55] and was introduced in [126]. The quantity $\alpha_c = 9.0760$ is the static polarizability of the ion core, the cut-off radius r_c, $L-$dependent parameters $\{a_1, a_2, a_3, a_4\}$, and the effective nuclear charge

$$Z_L = 1 + (Z-1)\,e^{-a_1 r} - r\,(a_3 + a_4 r)\,e^{-a_2 r}, \tag{2.6}$$

with $Z = 37$ the nuclear charge. Generally, the description becomes closer to hydrogen at higher L where the overlap with the remaining electrons decreases. Hence, the model potential modifies the simple Coulomb potential $V_h(r) = 1/r$ of a hydrogen atom in order to estimate the effect of the remaining electrons. It provides particularly accurate predictions at large distances from the ionic core. As a consequence, the polarizability and the interaction potentials of Rydberg atoms can be calculated with high accuracy. Here, because these quantities depend only on the overlap between different Rydberg states, the short-distance behavior is negligible. For other quantities such as transition dipole matrix elements between the ground state and different Rydberg states or the hyperfine interaction of a Rydberg state, the properties of the Rydberg wave function at short distances are important. A more accurate prediction of these quantities requires to extend the current theoretical framework.

The root-mean-square distance $\langle \hat{r}^2 \rangle = \int_0^\infty r^{2+2} |R_{nLJ}(r)|^2 dr$ has a characteristic scaling $\langle \hat{r}^2 \rangle \propto (n^\star)^2$. For low angular momentum quantum numbers L, $R_{nLJ}(r) = \langle r | R_{nLJ} \rangle$ is rapidly oscillating in r and has up to $n-1$ zero crossings, see Fig. 2.1 (**c**). The radial density $\rho(r) = r^2 |R_{nLJ}(r)|^2$ peaks at the outer lobe of the Rydberg wave function and is exponentially damped afterwards. For typical principal quantum numbers $n = 36$ used in this dissertation, the outer lobe is located at a distance $r \approx 110\,\mathrm{nm}$. Because this quantity is much smaller than the typical interatomic seperation of our experimental apparatus, different Rydberg electrons are not overlapping. Another important quantity is the value of the Rydberg wave function at the origin, which decreases with principal quantum number as $\propto (n^\star)^{-\frac{3}{2}}$. This scaling directly transfers to the dipole matrix element between the ground state and a Rydberg state as well as the small hyperfine coupling strength A_hfs of Rydberg states.

2.2.3 Dipole matrix elements & Rabi frequencies

Many properties of Rydberg atoms can be directly linked to transition dipole matrix elements. This includes their optical coupling rates from the ground state, their radiative lifetime, their response to static and radiofrequency fields and also the interaction between Rydberg atoms. The dipole operator is defined as $\hat{\boldsymbol{d}} = e\hat{\boldsymbol{r}}$, with $\hat{\boldsymbol{r}} = (\hat{x}, \hat{y}, \hat{z})$ the position operator of the electron and e the elementary charge. The dipole matrix elements between initial and final states $|i\rangle$ and $|f\rangle$ are given by $\boldsymbol{d}_{fi} = \langle f | \hat{\boldsymbol{d}} | i \rangle$. Because $\hat{\boldsymbol{d}}$ only couples the orbital angular momentum $\hat{\boldsymbol{L}}$ while spin degrees of freedom remain unaffected, calculating $\boldsymbol{d}_{fi}$ requires to again tranform into the uncoupled basis $|nLJm_J\rangle = \sum_{m_L m_S} \mathcal{C}^{1/2\ J\ L}_{m_S\, m_J\, m_L} |nLm_L\rangle |\frac{1}{2} m_S\rangle$. Generally, the dipole operator can couple states with a difference $\Delta L = \pm 1$ in their orbital angular momenta $\hat{\boldsymbol{L}}$, which translates into $\Delta J = \pm 1, 0$ in the coupled basis if the contributing orbital angular momenta are not zero [5, 19].

For initial and final states $|i\rangle = |nLJm_J\rangle$ and $|f\rangle = |n'L'J'm_{J'}\rangle$, the matrix elements $\boldsymbol{d}_{fi} = e\langle f|\hat{\boldsymbol{r}}|i\rangle$ are calculated in the spherical basis $\hat{\boldsymbol{r}} = (\hat{r}_{-1}, \hat{r}_0, \hat{r}_{+1})$ with $\hat{r}_0 = \hat{z}$ and $\hat{r}_{\pm 1} = \mp\frac{1}{\sqrt{2}}(\hat{x} \pm i\hat{y})$ because of existing selection rules. Here, one finds that $\hat{r}_0$ can couple states with $\Delta m_J = 0$ and $\hat{r}_{\pm 1}$ couples states with $\Delta m_J = \pm 1$. Motivated by the separation introduced in Eq. 2.3, the matrix elements can be divided into a part accounting for the angular overlap and a part which only depends on a radial integral. This is often also discussed in the context of the Wigner-Eckhardt theorem [127]. Applying the conventions introduced in [55], the components $r_q = \langle f|\hat{r}_q|i\rangle$ of $\langle f|\hat{\boldsymbol{r}}|i\rangle$ can be written as

$$r_q = (-1)^{\phi} \begin{pmatrix} J' & 1 & J \\ -m_{J'} & -q & m_J \end{pmatrix} \begin{Bmatrix} J' & 1 & J \\ L & 1/2 & L' \end{Bmatrix} \sqrt{(2J'+1)(2J+1)} \langle n'L'J'||\hat{r}||nLJ\rangle, \quad (2.7)$$

with a phase factor $\phi = J' - m_{J'} + L' + J + \frac{3}{2}$. The quantities expressed in the round (curly) brackets are called Wigner-3j (Wigner-6j) symbols and account for the expansion into the uncoupled angular momentum basis and the angular momentum overlap in the coupling. They provide the selection rules discussed in the previous paragraph and can also be expressed using Clebsch-Gordan coefficients. The term

$$\langle n'L'J'||\hat{r}||nLJ\rangle \propto \int_0^{\infty} R^{\star}_{J'L'm_{J'}} r^{2+1} R_{JLm_J} dr \quad (2.8)$$

is the so-called reduced matrix element. It is proportional to the radial integral including the initial and final radial wave functions and is independent of the spatial orientation specified by the index $q \in \{0, \pm 1\}$. In the literature there exist different definitions where some prefactors are either absorbed by or pulled out of the reduced matrix element. In order to verify the consistency between different definitions, it helps to express everything in quantities which are well-defined, such as the radial integrals or Rabi frequencies which are well-defined up to a phase.

Single-photon excitation from the ground state

Due to their small spatial overlap, dipole matrix elements between the ground state and a Rydberg state are suppressed by several orders of magnitude compared to stronger transitions at lower n such as the D-line in alkali atoms. This results in small Rabi frequencies and long radiative lifetimes. For the electronic ground state of ^{87}Rb, the coupling between the nuclear spin $\hat{\boldsymbol{I}}$ and the total electronic angular momentum $\hat{\boldsymbol{J}}$ results in a strong hyperfine splitting of $6.835\,\mathrm{GHz}$ between both hyperfine states $F \in \{1, 2\}$ which typically dominates over other energy scales. As a consequence, the $5S_{1/2}$ hyperfine ground state $|F, m_F\rangle$ is expressed using the coupled angular momentum basis $\hat{\boldsymbol{F}} = \hat{\boldsymbol{I}} + \hat{\boldsymbol{J}}$. Expanding into the basis where the electronic spin is uncoupled from the nuclear spin leads to $|F, m_F\rangle = \sum_{m_J, m_J} \mathcal{C}^{1/2\ F\ 3/2}_{m_J\, m_F\, m_I} |m_J m_I\rangle$. Here, $\mathcal{C}^{1/2\ F\ 3/2}_{m_J\, m_F\, m_I} = \langle m_J m_I|F, m_F\rangle$ are Clebsch-Gordan coefficients, $J = \frac{1}{2}$ is the angular momentum of the electron in the ground state and $I = \frac{3}{2}$ is the nuclear spin of ^{87}Rb. Because J and I are fixed in the electronic ground state, the explicit labeling is omitted.

Due to the small hyperfine interaction, Rydberg states $|n'L'J'm_{J'}; m_{I'}\rangle$ can be well described in the fine structure basis. For completeness, the labeling of the nuclear spin $|m_{I'}\rangle = |m_I\rangle$ which remains unchanged in the transition was included here. Driving a transition from the ground state to the Rydberg state using a light field with amplitude

$\boldsymbol{E} = \boldsymbol{\varepsilon} E_0$ induces a Rabi frequency

$$\widetilde{\Omega} = \frac{eE_0}{\hbar} \langle n'L'J'm_{J'}; m_{I'} | \boldsymbol{\varepsilon} \cdot \hat{\mathbf{r}} | F, m_F \rangle = \frac{eE_0}{\hbar} \sum_{m_J, q} \mathcal{C}^{1/2\ F\ 3/2}_{m_J\ m_F\ m_{I'}} c_q r_q, \tag{2.9}$$

with $m_{I'} = m_F - m_J$. By convention, the $z-$axis is parallel to the quantization axis of the atom, typically given by the magnetic field. Similarly as the position operator, the normalized polarization vector is expanded in the spherical basis $\boldsymbol{\varepsilon} = \sum_{q \in \{0 \pm 1\}} c_q \boldsymbol{e}_q$, with unit vectors $\boldsymbol{e}_0 = \boldsymbol{e}_z$ and $\boldsymbol{e}_{\pm 1} = \mp \frac{1}{\sqrt{2}} (\boldsymbol{e}_x \pm i \boldsymbol{e}_y)$ in order to account for the selection rules. Here, $c_0 = 1$ defines π polarization and $c_{\pm 1} = 1$ defines $\sigma^{\pm}$ polarization.

Combining Eq. 2.7 and Eq. 2.9 one finds that coupling rates for different polarizations q and different initial and final angular momentum projections m_F and $m_{J'}$ only differ by their Clebsch-Gordan coefficients. The reduced matrix element scales as

$$\langle nJL || \hat{r} || 5S_{1/2} \rangle \propto (n^{\star})^{-\frac{3}{2}}. \tag{2.10}$$

Because the contributing spatial integral essentially probes the spatial overlap of the ground state with the Rydberg state, it has the same scaling as $|R_{nLJ}(0)|$. Due to the interaction with the inner electrons, the uncertainty of the calculated Rydberg wave functions is largest at the origin. From our experience, the calculation of Rabi frequencies from Eq. 2.9 with the *ARC* package [55] overestimates the Rabi frequencies observed for alkali atoms by a factor 2-3.

Transitions between Rydberg states

Unlike the weak coupling to the electronic ground state, the dipole matrix elements between different Rydberg states can be extraordinarily large. For two different Rydberg states $|nJL\rangle$ and $|n'J'L'\rangle$ coupled by a microwave field $\boldsymbol{E}$, the hyperfine interaction is too small to play a role. Because of their large separation from the nucleus, transition dipole matrix elements

$$\langle n'L'J' || \hat{r} || nLJ \rangle \propto (n^{\star})^2 \tag{2.11}$$

between neighboring Rydberg states with equal or similar principal quantum numbers $n' \approx n$ and $L' = L \pm 1$ are much larger compared to the corresponding matrix elements at lower principal quantum numbers. This induces strong coupling rates even at low field amplitudes, which might enable them to be used as sensitive microwave field sensors [128]. Furthermore, transitions to nearby Rydberg states can be triggered by blackbody photons at room temperature [129, 130]. Additionally, the large matrix elements contribute to a high sensitivity to static fields and to the strong interactions between Rydberg atoms. Following the conventions of the last paragraphs, Rabi frequencies are now given by

$$\widetilde{\Omega} = \frac{eE_0}{\hbar} \langle n'L'J'm_{J'} | \boldsymbol{\varepsilon} \cdot \hat{\mathbf{r}} | nLJm_J \rangle = \frac{eE_0}{\hbar} \sum_{q \in \{0, \pm 1\}} c_q r_q. \tag{2.12}$$

2.2.4 Polarizability

Because of their large dipole moment, Rydberg states experience large energy shifts in the presence of static external electric fields $\boldsymbol{E}_{\mathrm{dc}}$. Choosing the z-axis to be parallel with the electric field, the Hamiltonian for the Rydberg electron writes

$$\hat{H} = \hat{H}_0 + \hat{z} E_{\mathrm{dc}}, \tag{2.13}$$

with $\hat{H}_0$ the Hamiltonian of the isolated atom and E_{dc} the field amplitude [48].

For small fields where the energy shift ΔE_{dc} is lower than the energy splitting between neighboring Rydberg levels, second order perturbation theory directly provides the DC Stark shift

$$\Delta_{\mathrm{dc}} \approx \alpha E_{\mathrm{dc}}^2. \tag{2.14}$$

Here, the polarizability

$$\alpha = \sum_i \frac{|\langle nLJm_J|\hat{z}|r_i\rangle|^2}{\Delta E_{r_i}} \propto (n^\star)^7 \tag{2.15}$$

covers the sum over nearby Rydberg states $|r_i\rangle = |n_i L_i J_i m_{J_i}\rangle$ at energy spacings $\Delta E_{r_i} = E_{nLJ} - E_{r_i}$. The separation of radial and angular coordinates in the Rydberg states motivates to calculate the matrix elements via $r_0 = \langle nLJm_J|\hat{r}\cos\hat{\theta}|r_i\rangle$ with $\hat{z} = \hat{r}\cos\hat{\theta}$. Neglecting the angular dependent integrals which are independent of n, the matrix elements again depend on reduced matrix elements, which scale as $\langle nJL||\hat{r}||r_i\rangle \propto (n^\star)^2$. Combined with the energy separation $\Delta E_{r_i} \propto (n^\star)^{-3}$ between nearby Rydberg states, one obtains the strong dependency of the polarizability on the principal quantum number $\alpha \propto (n^\star)^7$. Besides the enhanced polarizability, the presented formalism is identical for the Stark effect in the electronic ground state. If the electric field is large enough such that Δ_{dc} is on the order of the energy splitting ΔE_{r_i} between nearby Rydberg states, the perturbative method breaks down and the Stark maps are dominated by crossing energy levels. This regime shifts towards lower fields for either higher n or higher L. Generally, the observed shifted Rydberg levels can be well predicted by theory [131–133].

Many Rydberg experiments benefit from electric field control. This enables to control the resonance frequency using the induced Stark shift or to compensate slowly-varying electric fields in the environment, in particular if the atoms are close to surfaces which can have fluctuating surface charges [134–136]. Experiments have shown that these charges can also be removed by illuminating the surfaces with UV light, for example using light emitting diodes (LED's) [137–139]. The large polarizability and the energy close to the ionization threshold can also be used for detection. Here, Rydberg atoms are ionized either by static electric fields [140, 141] or via pulsed field ionization (PFI) [140]. Subsequently, the ions are accelerated to a microchannel plate (MCP) which can detect charged particles by the emission of secondary electrons [142–145]. The field sensitivity has also been used to control the motion of the Rydberg atom by Stark acceleration [146] and observe interference fringes in the wave packet dynamics [147]. Finally, Rydberg atoms are possible candidates for electric field sensors [148, 149].

2.2.5 Lifetimes of Rydberg states

Neglecting state-changing collisions occuring at small distances where the electron orbitals overlap [150], Rydberg atoms are typically decaying via two channels [48]. First, they can radiatively decay to the electronic ground state with a rate Γ_{dec} [151]. Second, thermally populated microwave modes can trigger transitions to nearby Rydberg states at rates Γ_{bb} [152, 153]. For the Rydberg states studied in this thesis, the lifetime associated with both decay rates is typically a few tens of microseconds. As derived in the following paragraphs, increasing n generally increases the lifetime. Because $\Gamma_{\mathrm{bb}}/\Gamma_{\mathrm{dec}} \propto n^\star$ for high principal quantum numbers, black-body transitions contribute stronger to the total decay rate $\Gamma_{|r\rangle} = \Gamma_{\mathrm{dec}} + \Gamma_{\mathrm{bb}}$ at higher n. For ^{87}Rb, one finds that $\Gamma_{\mathrm{bb}} \approx \Gamma_{\mathrm{dec}}$ for $n \approx 30$ and $L \in \{0, 1, 2\}$ [72].

For many experiments, black-body transitions are a serious limitation because they create contaminant atoms in the system [154, 155]. A recently demonstrated way to increase the lifetime is to cool the experimental apparatus to cryogenic temperatures [156–158]. Also engineering the local density of states of photons, e.g. by using microwave cavities [159, 160], enables control over certain black-body channels [161]. Furthermore, the radiative decay to the ground state $\mathit{\Gamma}_{\text{dec}}$ can be essentially switched off by exciting circular Rydberg states with vanishing transition dipole matrix element with the electronic ground state [162, 163].

Direct decay to the electronic ground state

Within Wigner-Weisskopf theory, excited atoms decay because the electromagnetic field of the vacuum depopulates the exciting state by stimulated emission into the available vacuum modes [164]. A Rydberg state $|nLJm_J\rangle$ decays into a hyperfine ground state $|Fm_F\rangle$ with a rate

$$\mathit{\Gamma}_{\text{dec}}^{F,m_F} = \frac{|\langle nLJm_J|\hat{\boldsymbol{d}}|Fm_F\rangle|^2\omega_r^3}{3\pi\epsilon_0\hbar c^3} \propto (n^\star)^{-3}. \tag{2.16}$$

Here, ϵ_0 is the vacuum permittivity and $\hbar\omega_{\text{r}}$ is the energy separation between the Rydberg state and the ground state. Rydberg states are energetically close and $\hbar\omega_{\text{r}}$ can be approximated by the $n-$independent ionization energy. Because $\langle nLJm_J|\boldsymbol{d}|Fm_F\rangle \propto \langle nJL||\hat{r}||5S_{1/2}\rangle$, the total decay rate scales as $\mathit{\Gamma}_{\text{dec}} \propto (n^\star)^{-3}$. As long as the vacuum modes are isotropic, the total decay rate $\mathit{\Gamma}_{\text{dec}} = \sum_{F,m_F} \mathit{\Gamma}_{\text{dec}}^{F,m_F}$ of a state $|nJLm_J\rangle$ does not depend on the quantization axis of the atom and therefore is independent of m_J. However, it can slightly depend on J due to different reduced matrix elements. For alkali atoms $\mathit{\Gamma}_{\text{dec}}$ is about 30% higher for S-states and D-states compared to P-states because selection rules lead to different sets of available states at lower n [55]. Generally, observations are in good agreement with the calculated decay rates [157, 165–167]. For lower principal quantum numbers $\mathit{\Gamma}_{\text{dec}}$ is by far the dominating decay channel. For Rydberg atoms however, transition rates are smaller because of the reduced matrix elements.

Black-body radiation induced transitions

The black-body transition rate $\mathit{\Gamma}_{\text{bb}}$ between two Rydberg states depend linearly on the density of black-body photons and quadratically on the transition dipole moments [168]. According to Planck's law, the spectral radiance of the black-body spectrum is given by

$$B(\nu_L, T) = \frac{2h\nu_L^3}{c^2}\frac{1}{e^{\frac{h\nu_L}{k_B T}} - 1}. \tag{2.17}$$

Here, ν_L is the frequency of the emitted electromagnetic waves and k_B is the Boltzmann constant. The rates $\mathit{\Gamma}_{\text{bb}}$ typically experience a maximum at relatively low $n \approx 20$ where the total rate $\mathit{\Gamma}_{|r\rangle}$ is still dominated by the decay into the ground state and then decrease with n [169]. At room temperature $T \approx 300\,\text{KT}$, $B(\nu_L, T)$ peaks around a frequency $\nu_L \approx 30\,\text{THz}$, the corresponding distribution for the wavelength $-B(\nu_L, T)\frac{d\nu_L}{d\lambda_L}$ with $c = \nu_L\lambda_L$ peaks at $\lambda_L \approx 10\,\mu\text{m}$. This frequency is well above the typical transition frequency $\nu_{r_i} \propto (n^\star)^{-3}$ between neighboring Rydberg states at high principal quantum numbers. In this regime where $e^{\frac{h\nu_L}{k_B T}} \approx 1 + \frac{h\nu_L}{k_B T}$, the spectral radiance scales as $B(\nu_L, T) \propto \nu_L^2$, yielding $B(\nu_{r_i}, T) \propto (n^\star)^{-6}$. Furthermore, the transition dipole matrix elements increase as

$\langle nJL||\hat{r}||r_i\rangle \propto (n^\star)^2$. As verified by experiments, this provides black-body transition rates $\Gamma_{\mathrm{bb}} \propto (n^\star)^{-2}$ [55] at high n. Compared to P-state and D-state Rydberg atoms, S-state Rydberg atoms have less available states for black-body transitions due to dipole selection rules. Observed black-body rates do agree with the calculated values but also suggest that the local environment close to the atomic sample can influence the black-body spectrum [170], also in the absence of special microwave cavities.

2.3 Rydberg interactions

Interactions between Rydberg atoms have been first observed as broadening mechanisms of the Rydberg transitions [171–174]. These exceptionally strong interactions are the main reason behind the recent interest in Rydberg atoms because they are a versatile and useful tool for quantum science [49, 52]. The dipole moment of an isolated Rydberg state in a well-defined orbital angular momentum is zero because of dipole selection rules related with the parity conservation of electromagnetism. However, due to the large dipole matrix elements between neighboring Rydberg atoms, significant dipole moments can be created already by slightly admixing nearby Rydberg states. Furthermore, the large polarizability allows to create such a dipole moment already for small perturbations, such as by the presence of a second Rydberg atom at a typical distance of a few micrometers.

Rydberg interactions are usually discussed at interatomic distances where the electron clouds do not overlap. Only at that distance where autoionization does not limit experiments [73], their interactions can be applied for applications in quantum science. For two atoms in Rydberg states $|r_1\rangle$ and $|r_2\rangle$, this boundary is typically quantified using the Le Roy radius[50, 175]

$$R_{\mathrm{LR}} = 2\left(\sqrt{\langle \hat{r}_1^2\rangle} + \sqrt{\langle \hat{r}_2^2\rangle}\right), \tag{2.18}$$

with $\sqrt{\langle \hat{r}_i^2\rangle} = \int_0^\infty |R_{n_i,L_i,J_i}(r)|^2 r^{2+2} dr$ the root-mean-square size of the two Rydberg wave functions $i \in \{1,2\}$. All disucssions in this dissertations assume an interatomic distance $R \gg R_{\mathrm{LR}}$.

2.3.1 Electrostatic interaction Hamiltonian

At infinite distances, the Hamiltonian $\hat{H}_0$ of two isolated Rydberg atoms provides eigenstates $|r_i r_j\rangle \equiv |r_i\rangle \otimes |r_j\rangle$ with $|r_{i/j}\rangle = |n_{i/j} L_{i/j} J_{i/j} m_{J_{i/j}}\rangle$ and energies $E_{n_i,L_i,J_i,m_{J_i}} + E_{n_j,L_j,J_j,m_{J_j}}$. At finite distances, the electrostatic interaction adds a term [50, 176]

$$\hat{H}_{\mathrm{int}}(\boldsymbol{R}) = \frac{e^2}{4\pi\epsilon_0}\left(\frac{1}{|\boldsymbol{R} + \hat{\boldsymbol{r}}_2 - \hat{\boldsymbol{r}}_1|} + \frac{1}{|\boldsymbol{R}|} - \frac{1}{|\boldsymbol{R} - \hat{\boldsymbol{r}}_1|} - \frac{1}{|\boldsymbol{R} + \hat{\boldsymbol{r}}_2|}\right) \tag{2.19}$$

to the total electronic Hamiltonian $\hat{H}_e$, with $\hat{\boldsymbol{r}}_{1/2}$ the position of both Rydberg electrons and $\boldsymbol{R}$ the distance vector between both nuclei. The first two terms represent the repulsion of both nuclei and both Rydberg electrons. The second two terms represent the attraction of the Rydberg electrons by the nucleus of the other atom. The interaction Hamiltonian can be expressed as [50, 73, 177, 178]

$$\hat{H}_{\mathrm{int}}(\boldsymbol{R}) = \sum_{\kappa_1,\kappa_2=1}^{\infty} \frac{\hat{H}_{\kappa_1\kappa_2}}{4\pi\epsilon_0 R^{\kappa_1+\kappa_2+1}} \tag{2.20}$$

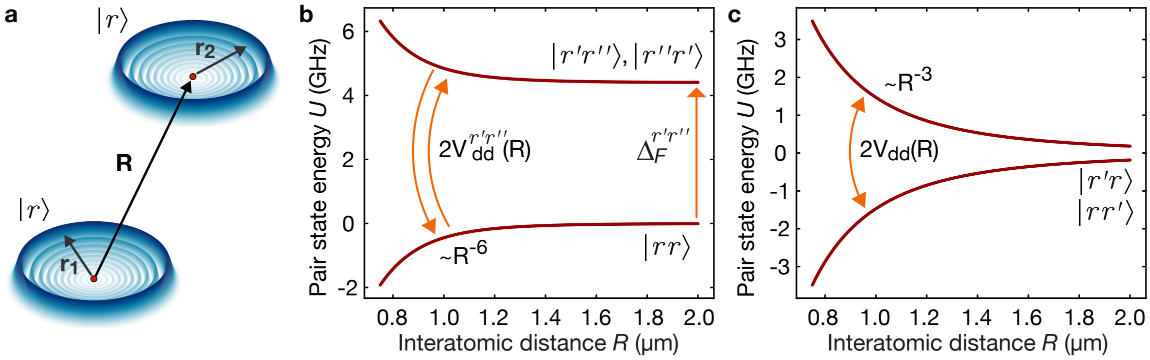

Figure 2.2: **Interactions between Rydberg atoms.** (**a**) The interactions between Rydberg atoms in states $|r\rangle$ are calculated at distances where orbits do not overlap. Rydberg orbits are represented in blue via cross sections through the radial wave function. (**b**) Exemplary van der Waals interactions between $|rr\rangle = |36P_{1/2}36P_{1/2}\rangle$, accounting only for the coupling to the pair state $|r'r''\rangle = |36S_{1/2}37S_{1/2}\rangle$ strongly contributing in Eq. 2.26 for typical interaction matrix elements. (**c**) Non-perturbative exchange interaction as described by Eq. 2.27. This can occur either for trivially degenerate states $|rr'\rangle = |36P_{1/2}36S_{1/2}\rangle$ and $|r'r\rangle = |36S_{1/2}36P_{1/2}\rangle$ or because of a Förster resonance. Realistic multi-channel calculations accounting also for the angular momentum projections are presented in Fig. 2.3 and Appendix A.

using spherical multipole operators

$$\hat{H}_{\kappa_1\kappa_2} = \frac{e^2(-1)^{\kappa_2}4\pi}{\sqrt{(2\kappa_1+1)(2\kappa_2+1)}} \sum_{m=-\kappa_<}^{\kappa_<} \sqrt{\binom{\kappa_1+\kappa_2}{\kappa_1+m}\binom{\kappa_1+\kappa_2}{\kappa_2+m}} \tag{2.21}$$

$$\times\ \hat{r}_1^{\kappa_1}\hat{r}_2^{\kappa_2} Y_{\kappa_1}^{m}(\hat{\theta}_1,\hat{\varphi}_1) Y_{\kappa_2}^{-m}(\hat{\theta}_2,\hat{\varphi}_2), \tag{2.22}$$

with spherical harmonics $Y_\kappa^m(\hat{\theta},\hat{\varphi})$ and $\kappa_< = \min(\kappa_1,\kappa_2)$. Now, calculating the matrix elements of $\hat{H}_{\text{int}}(\boldsymbol{R})$ reduces to the evaluation of single-atom multipole moments

$$\langle R_{n_jL_jJ_j}|\hat{r}^\kappa|R_{n_iL_iJ_i}\rangle = \int_0^\infty R^\star_{n_j,L_j,J_j} r^{2+\kappa} R_{n_i,L_i,J_i} dr \tag{2.23}$$

of order κ and angular integrals

$$\langle L_j m_{L_j}|Y_\kappa^m(\hat{\theta},\hat{\varphi})|L_i m_{L_i}\rangle = \int\int \left(Y_{L_j}^{m_{L_j}}\right)^\star(\theta,\varphi) Y_{\kappa_1}^m(\theta,\varphi) Y_{L_i}^{m_{L_i}}(\theta,\varphi)\sin\theta d\theta d\varphi \tag{2.24}$$

after expanding $|L_{i,j}J_{i,j}m_{J_{i,j}}\rangle$ into the uncoupled basis. Because higher orders decrease more rapidly with the distance R, the number of multipole terms required for accurate calculations depends on the distance between both atoms. The interactions are typically calculated within a subspace $\{|r_ir_j\rangle\}$. Due to the decreasing multipole matrix elements for different principal quantum numbers and due to selection rules in the angular momentum quantum numbers, nearby Rydberg pair states contribute most.

2.3.2 Dipole-dipole interactions

Most experiments operate in a regime where only the lowest order in the multipole expansion is important. In this limit, the interaction Hamiltonian simplifies to the dipole-dipole interaction Hamiltonian [179]

$$\hat{H}_{\text{int}}(\boldsymbol{R}) \approx \hat{H}_{\text{dd}}(\boldsymbol{R}) = \frac{\hat{\boldsymbol{d}}_1\hat{\boldsymbol{d}}_2 - 3(\hat{\boldsymbol{d}}_1 \cdot \boldsymbol{e_R})(\hat{\boldsymbol{d}}_2 \cdot \boldsymbol{e_R})}{4\pi\epsilon_0 R^3}, \tag{2.25}$$

with $\hat{\boldsymbol{d}}_{1,2}$ the dipole operators of both individual atoms and $\boldsymbol{e_R}$ the unit vector along the interatomic distance. As for most properties of Rydberg atoms discussed so far, the matrix elements of $\hat{H}_{\text{dd}}$ mainly depend on single-atom dipole matrix elements. Furthermore, for many experiments, only the asymptotic behavior of the interactions at large distances is important. Here, they can be classified by three limiting cases, which are pedagogially relevant and will be presented in the next paragraphs. At shorter distances and larger interactions, Eq. 2.19 and Eq. 2.25 typically lead to large energy shifts and a strong mixing of pair states. This regime will be covered in the next chapters.

Van der Waals interactions

If a pair state $|rr\rangle$ corresponding to two Rydberg atoms in the state $|r\rangle$ is energetically isolated, it is detuned from other pair states $\{|r_i r_j\rangle\}$ by the so-called Förster defects $\varDelta_F^{ij} = 2E_r - E_{r_i} - E_{r_j}$. Then, the other states can be only virtually populated in a second order process. This induces a dispersive energy shift [176, 180, 181]

$$V_{\text{vdW}}(\boldsymbol{R}) = \sum_{ij} \frac{|\langle rr|\hat{H}_{\text{dd}}(\boldsymbol{R})|r_i r_j\rangle|^2}{\varDelta_F^{ij}} = \frac{C_6(\theta)}{R^6} \propto (n^\star)^{11}, \tag{2.26}$$

which shows the typical $1/R^6-$dependency of van der Waals interactions. The $C_6(\theta)$ coefficients which cover the sum over the intermediate states feature a strong dependency on the principal quantum number. This can be understood because the Förster defects $\varDelta_F^{ij} \propto (n^\star)^{-3}$ in most cases have the same scaling with principal quantum number as the the energy separation between neighboring Rydberg states. Additionally, the interaction matrix elements $V_{dd}^{ij}(R) = \langle rr|\hat{H}_{\text{dd}}(\boldsymbol{R})|r_i r_j\rangle \propto (n^\star)^4$ are proportional to products of transition dipole matrix elements between nearby Rydberg states, which individually increase quadratically with $n^\star$. The angular dependency enters because the interaction matrix elements depend on the angle θ between the interatomic axis and the quantization axis of the atoms where the projections m_J, m_{J_i} and m_{J_j} are defined. Experimentally, the presense of such a quantization axis requires to energetically split different angular momentum projections by an amount larger than the interatomic interaction. Measured van der Waals interaction coefficients agree with the calculated values [182, 183]. In the literature, the angular dependency is often separated from the van der Waals coefficient via $C_6(\theta) = \widetilde{C}_6 D(\theta)$ by using reduced matrix elements and Clebsch-Gordan coefficients [184].

In many cases, there is a small set of pair states $\{|r'r''\rangle, |r''r'\rangle\}$ which dominate the sum in Eq. 2.26 because of the small Förster defect $\varDelta_F^{r'r''}$. The sign of the interaction then depends on the sign of the contributing $\varDelta_F^{r'r''}$. For ^{87}Rb Rydberg S-states with $|rr\rangle = |nS\,\tfrac{1}{2}\,m_J; nS\,\tfrac{1}{2}\,m_J\rangle$, these dominating channels are given by the states $|r'r''\rangle$ with $|r'\rangle = |nPJ'm_{J'}\rangle$, $|r''\rangle = |(n-1)PJ''m_{J''}\rangle$, $J', J'' \in \{\tfrac{1}{2}, \tfrac{3}{2}\}$ and the possible spin projections. Because $\varDelta_F^{r'r''} = 2E_{nS} - E_{nPJ'} - E_{(n-1)PJ''} > 0$, interactions are generally repulsive. Furthermore, the Förster defect is typically larger than the splitting between $J = \{\tfrac{1}{2}, \tfrac{3}{2}\}$. Neglecting the fine structure splitting, evaluating the sum over J', J'', $m_{J'}$ and $m_{J''}$ in Eq. 2.26 leads to isotropic interactions $C_6(\theta) \approx C_6$ [129, 184].

For ^{87}Rb Rydberg P-states $|r\rangle = |nPJm_J\rangle$, the dominant states are $|r'\rangle = |nS\,\frac{1}{2}\,m_{J'}\rangle$ and $|r''\rangle = |(n+1)S\,\frac{1}{2}\,m_{J''}\rangle$, see Fig. 2.2 (**b**). In contrast to S-states, the sign of the smallest Förster defects now depend on the principal quantum number n. The interactions between Rydberg states for $L > 1$ can also have significant angular dependencies [72, 185, 186]. In the absence of an external quantization axis, the interactions furthermore split into several interaction branches [50] because of the larger set of possible angular momentum projections. Interaction curves for both S-states and P-states in this regime are discussed in Appendix A. As discussed in the next paragraph, the van der Waals coefficient is larger for $J = \frac{3}{2}$ compared to $J = \frac{1}{2}$ for the principal quantum numbers relevant for this dissertation.

Förster resonances

The perturbative method for calculating the van der Waals interaction only holds if the interaction matrix elements are smaller than the Förster defects. At close distances where the matrix elements increase, this condition breaks down and one can observe a transition from the $1/R^6-$scaling to a regime of on-resonant dipole-dipole interactions where interactions scale as $1/R^3$ [49]. For some Rydberg states $|rr\rangle$, there exist pair states $\{|r'r''\rangle, |r''r'\rangle\}$ with vanishingly small Förster defects. Here, the transition to the non-perturbative regime occurs already at large distances and interactions generally scale as $1/R^3$. Such a configuration where interactions are strong and decrease slower in distance is called a *Förster resonance*.

Förster resonances naturally occur at principal quantum numbers n where the C_6 coefficient switches sign. For ^{87}Rb, the Förster defect between the pair states $|37P_{3/2}37P_{3/2}\rangle$ and $|36S_{1/2}37S_{1/2}\rangle$ is almost vanishing [55]. As a result, the interactions of Rydberg P-states relevant in this dissertation are stronger and longer in range for the $J = 3/2$ state compared to the $J = 1/2$ where the Förster defect is larger. Similar conditions can also be found at higher principal quantum numbers [187].

Förster resonances can also be realized by energetically shifting the Rydberg levels using electric fields [188, 189]. By tuning a prepared pair state $|rr\rangle$ into a Förster resonance by abruptly changing the eletric field allows one to observe coherent oscillations between $|rr\rangle$ and the Förster-resonant state $|r'r''\rangle$ [190, 191]. This is an example of dipolar exchange and the formalism of the next paragraph can be applied. The concept of Förster resonances is not restricted to two-atom systems and also three-body [192–194] and four-body [195] Förster resonances have been found. However, observing coherent oscillations was so far not possible for these multi-atom Förster resonances.

Dipolar exchange

Another interesting situation is the realization of two atoms $|rr'\rangle$ in different Rydberg states $|r\rangle = |nLJm_J\rangle$ and $|r'\rangle = |n'L'J'm_{J'}\rangle$ with non-vanishing single-atom dipole matrix elements $d_{rr'} = |\langle r|\boldsymbol{d}|r'\rangle|$. Experimentally, this can be realized by using one P-state Rydberg atom and another Rydberg atom in either a S-state or a D-state, see Fig. 2.2 (**c**). If other Rydberg pair states are energetically far away, the description simplifies to a two-level system where either the first (second) or the second (first) atom is in the state $|r\rangle$ ($|r'\rangle$). After expanding into the basis $\{|rr'\rangle, |r'r\rangle\}$, the Hamiltonian becomes

$$\hat{H}_{\text{dd}}(R,\theta) = \begin{pmatrix} 0 & V_{\text{dd}}(R,\theta) \\ V_{\text{dd}}(R,\theta) & 0 \end{pmatrix}, \tag{2.27}$$

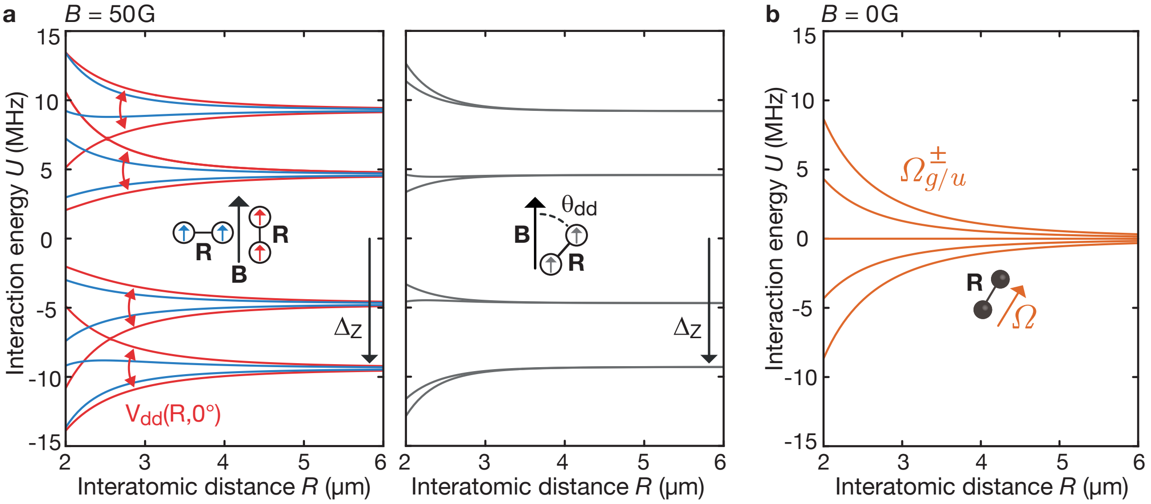

Figure 2.3: **Exact diagonalization of $\hat{\mathbf{H}}_{\mathrm{dd}}(\mathbf{R})$ for various magnetic fields B.** (**a**) For $B = 50\,\mathrm{G}$, different angular momentum projections of the S-state and the P-state split up. At large distances R, one can find isolated pairs $|rr'\rangle = |36P_{1/2}36S_{1/2}\rangle$ and $|r'r\rangle = |36S_{1/2}36P_{1/2}\rangle$ whose dipole moments are oriented by the magnetic field $\boldsymbol{B}$ which serves as a quantization axis for the two individual atoms. The interactions in the two-dimensional subspace are given by Eq. 2.27. As expected from Eq. 2.28, the interaction $V_{\mathrm{dd}}(R, 0°)$ (red) is larger than $V_{\mathrm{dd}}(R, 90°)$ (blue) and vanishes for $\theta_{\mathrm{dd}} \approx 54.7°$ (gray). At short distances where the interactions dominate over the the Zeeman splitting Δ_Z, more angular momentum projections contribute. Now, the picture breaks down and $\boldsymbol{R}$ serves as a quantization axis for the interacting state. (**b**) At zero field, R serves as quantization axis for all distances. In this regime, the symmetries of the interaction Hamiltonian allow one to label the pair potentials by molecular quantum numbers $\Omega^{\pm}_{g/u}$, see section 4.1.

with off-diagonal coupling elements

$$V_{\mathrm{dd}}(R, \theta) \approx \frac{d^2_{rr'}\left(1 - 3\cos^2\theta\right)}{4\pi\epsilon_0 R^3} \propto (n^\star)^4. \tag{2.28}$$

The scaling with $n^\star$ follows immediately from the discussion of the van der Waals interaction. One implication of Eq. 2.27 is that the initially prepared state coherently oscillates between $|rr'\rangle$ and $|r'r\rangle$ at a frequency $\frac{2}{\hbar}V_{\mathrm{dd}}(R, \theta)$ [196]. Here, $V_{\mathrm{dd}}(R, \theta)$ shows the typical dependency of dipolar interactions on R and θ [92]. To experimentally initialize the state $|rr'\rangle$ instead of adiabatically creating an eigenstate of Eq. 2.27 requires to switch the interactions faster than the exchange time . This can be realized by using AC Stark shifts [197] of additional laser beams or electric fields [190]. Furthermore, isolating a single pair requires to energetically split different spin projections. This can again be achieved by enforcing an external quantization axis that is stronger than the interatomic interaction, for examply by applying an external magnetic field as shown in Fig. 2.3.

The same formalism as the one presented can be applied to the Förster resonant exchange process discussed in the previous paragraph after replacing $|rr'\rangle$ and $|r'r\rangle$ with two Förster resonant pair states $|rr\rangle$ and $|r'r''\rangle$.

Property	**Symbol**	**Scaling**	**Ref.**	**$36\mathbf{P}_{1/2}$**	**$36\mathbf{P}_{3/2}$**
Binding energy	E_{nJL}	$(n^\star)^{-2}$	[48, 55]	$-2.958\,\text{THz}$	$-2.956\,\text{THz}$
Fine-structure	$\varDelta_{\text{fs}}$	$(n^\star)^{-3}$	[55, 122]	$2.342\,\text{GHz}$	
Orbital size	$\sqrt{\langle \hat{r}^2 \rangle}$	$(n^\star)^{2}$	[48, 55]	$105\,\text{nm}$	$105\,\text{nm}$
Red. m. el. $\lvert r\rangle \leftrightarrow \lvert r'\rangle$	$\langle r \vert\vert \hat{r} \vert\vert r' \rangle$	$(n^\star)^{2}$	[55]	$-1245\,ea_0$	$-1264\,ea_0$
Radiative dec. rate	$\varGamma_{\text{dec}}$	$(n^\star)^{-3}$	[55, 129]	9.0ms^{-1}	$9.9\,\text{ms}^{-1}$
Red. m. el. $\lvert g\rangle \leftrightarrow \lvert r\rangle$	$\langle r \vert\vert \hat{r} \vert\vert 5S_{1/2} \rangle$	$(n^\star)^{-\frac{3}{2}}$	[55]	$-0.0043\,ea_0$	$-0.0057\,ea_0$
Black-body dec. rate	$\varGamma_{\text{bb}}$	$(n^\star)^{-2}$	[55, 129]	$14.3\,\text{ms}^{-1}$	$14.4\,\text{ms}^{-1}$
Van der Waals coeff.	C_6	$(n^\star)^{11}$	[50, 55]	$-0.2\,\text{GHz}\,\mu\text{m}^6$	$6.5\,\text{GHz}\,\mu\text{m}^6$
Rydberg blockade	R_b	$(n^\star)^{\frac{11}{6}}$	[55]	$1.9\,\mu\text{m}$	$3.4\,\mu\text{m}$

Table 2.2: **Summary of the most relevant properties of Rydberg atoms**. Exemplary values are provided for the two fine-structure states $36P_{1/2}$ and $36P_{3/2}$. All single-atom properties were obtained from the *ARC* software [55], the interaction parameters were obtained using the software *pair interaction* [50]. The reduced matrix elements do not cover the Clebsch-Gordan coefficients which enter in the Rabi couplings. Despite the fact that black-body transitions starting from $36P_{1/2}$ can only populate states $nS_{1/2}$ and $nD_{3/2}$ while the state $36P_{3/2}$ can additionally couple to $nD_{5/2}$, the total black-body decay rates are similar. Here, the larger transition rates into states $nD_{3/2}$ for $36P_{1/2}$ compensate for the additional channel for $36P_{3/2}$. Because there are more than one van der Waals potential, only the largest C_6 coefficient is presented here, see appendix A. Furthermore, because there exists an almost Förster resonant state for $36P_{3/2}$, interactions also have a contribution which scales as $1/R^3$. The blockade radius R_b was calculated for a typical Rabi frequency $\varOmega/(2\pi) = 4.0\,\text{MHz}$ assuming only van der Waals interactions $\propto 1/R^6$.

2.3.3 Multipole interactions

Because of the different distance dependence in Eq. 2.20, higher-order multipole interactions become more important at shorter distance. For experimentally relevant densities, the dipole-dipole Hamiltonian $\hat{H}_{\text{dd}}(R)$ is always the dominating term in the interaction Hamiltonian $\hat{H}_{\text{int}}(R)$ and describes the coarse structure of the pair potentials. However, calculations showed that also higher-order terms can have an influence on the expected pair potentials [198, 199]. Also spectroscopic signatures of pair potentials clearly indicate a coupling between potential curves where dipole-dipole interactions vanish but a dipole-quadrupole couplings are finite [200]. Furthermore, in the formation of so-called Rydberg aggregates [201–203], dipole-quadrupole interactions were identified to play a role [204]. So far, experimental access beyond dipole-quadrupole interactions was not possible. The spectroscopic data which will be presented later shows clear experimental signatures of dipole-quadrupole interactions, see chapter 6. Furthermore, in order to get quantitative agreement with the observed spectroscopic lines, even further multipole terms had to be included, see section 4.2.1.

2.4 A summary of the properties of Rydberg states

In the previous paragraphs, the most important signatures of Rydberg states were calculated based on their transition dipole matrix elements and their energy splittings. The wave functions required for the contributing radial integrals can be calculated from model potentials. The energy levels of Rydberg states and effective principle quantum numbers can be calculated from the quantum defect. Both quantities were obtained empirically as ab-initio calculations require to solve the many-body problem including the electrons occupying the filled lower orbitals [48]. Properties such as the polarizability or the interaction potentials which rely on the spatial overlap between different Rydberg states have typically very high accuracy. Properties such as Rabi couplings from the ground state or hyperfine couplings which depend on the overlap of the Rydberg wave function with the ionic core have higher uncertainty. All relevant scalings are again summarized in table 2.2. Because of relevance regarding the following chapters, also the fine-structure splitting was also included while the polarizability is not included. Nowadays, there exist freely available scripts to calculate all those quantities to high precision. Throughout this dissertation, the *ARC* package [55] was used to calculate Rydberg resonances and estimate Rabi frequencies and lifetimes of Rydberg states. The pair-interaction [50] package was used for the calculation of Rydberg interaction potentials.

2.5 Applications for quantum science

About twenty years ago, scientists realized that Rydberg interactions can be useful for quantum simulation and computation [205, 206]. After a rapid progress over the last years, Rydberg atoms are now among the most promising platforms in these fields [49, 52, 54]. The most important developments in the field will be summarized in the following.

2.5.1 Blockade physics

Imagine a ground-state atom $|g\rangle$ coupled to a Rydberg state $|r\rangle$ with a Rabi frequency $\widetilde{\Omega}$ and a single-photon detuning Δ. Here, $\widetilde{\Omega}$ can be either an effective two-photon Rabi frequency by using two different lasers, typically at one red and one blue wavelength for rubidium, or a single-photon Rabi frequency in the ultraviolet (UV). For an isolated atom, the coupling is described by the two-level Hamiltonian [5]

$$\hat{H}_L = \hbar \begin{pmatrix} 0 & \widetilde{\Omega}/2 \\ \widetilde{\Omega}^\star/2 & -\Delta \end{pmatrix} \tag{2.29}$$

after transforming into a frame rotating with the laser frequency and neglecting fast oscillating terms within the framework of the rotating wave approximation (RWA) [5]. For $\Delta = 0$, an atom initially prepared in $|g\rangle$ gets projected into the new eigenbasis and experiences Rabi oscillations between $|g\rangle$ and $|e\rangle$ after switching on the coupling. For $|\Delta| \gg |\widetilde{\Omega}|$, the initial state $|g\rangle$ will be adiabatically transfered into the new dressed ground state. Here, second order perturbation theory provides the AC Stark shift

$$\Delta_{\mathrm{AC}} = \frac{\hbar\widetilde{\Omega}^2}{4\Delta}. \tag{2.30}$$

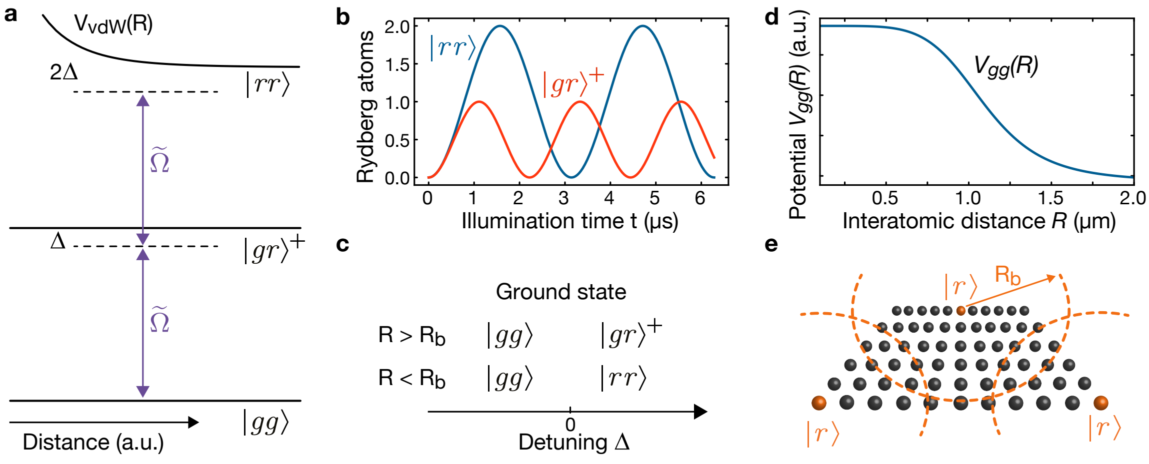

Figure 2.4: **Rydberg blockade.** (**a**) The pair-state description of two ground-state atoms $|g\rangle$ coupled to interacting Rydberg states $|r\rangle$ with a Rabi frequency $\widetilde{\Omega}$ and a detuning Δ is fundamental for many Rydberg experiments. (**b**) Coherently exciting ground-state atoms for $\Delta = 0$, one observes a transition from two individually evolving atoms (blue) for $R > R_b$ to collectively enhanced Rabi oscillations into the state $|gr\rangle^+$ for $R < R_b$. (**c**) The ground state of Eq. 2.31 is $|gg\rangle$ for $\Delta < 0$ and $|gr\rangle^+$ ($|rr\rangle$) for $R < R_b$ ($R > R_b$) and $\Delta > 0$. By adiabatically ramping Δ one can dynamically switch between them. (**d**) Working at detunings $\Delta > \widetilde{\Omega}$, Rydberg interactions can be admixed to the ground state in the context of Rydberg dressing. (**e**) All mechanisms discussed here can be extended to larger systems where R_b covers large numbers of ground-state atoms.

Because the energy shift originates from the coupling with the light field, $\Delta_{\rm AC}$ is also called light shift. For two Rydberg atoms, a doubly excited state $|rr\rangle$ experiences an additional interaction energy $V_{\rm vdW}(R) = C_6/R^6$. Even at distances $R \approx 1\,\mu$m, the interactions $V_{\rm vdW}(R)$ can easily exceed $\widetilde{\Omega}$. Expressing the Hamiltonian in the pair-state basis $\{|gg\rangle, |gr\rangle, |rg\rangle, |rr\rangle\}$ provides the two-atom Hamiltonian

$$\hat{H} = \begin{pmatrix} 0 & \hbar\widetilde{\Omega}/2 & \hbar\widetilde{\Omega}/2 & 0 \\ \hbar\widetilde{\Omega}^\star/2 & -\Delta\hbar & 0 & \hbar\widetilde{\Omega}/2 \\ \hbar\widetilde{\Omega}^\star/2 & 0 & -\Delta\hbar & \hbar\widetilde{\Omega}/2 \\ 0 & \hbar\widetilde{\Omega}^\star/2 & \hbar\widetilde{\Omega}^\star/2 & -2\Delta\hbar + V_{\rm vdW}(R) \end{pmatrix}, \tag{2.31}$$

see also Fig. 2.4 (**a**). Here, the atom-light interaction Hamiltonian $\hat{H}_L = \hat{H}_L^{(1)} \otimes \mathbb{1}^{(2)} + \mathbb{1}^{(1)} \otimes \hat{H}_L^{(2)}$ couples the ground state $|gg\rangle$ to the intermediate state and the intermediate state to the doubly excited state by the corresponding single-atom Hamiltonians $\hat{H}_L^{(1/2)}$ of both atoms, given by Eq. 2.29. If deviations from the van der Waals are significant, $V_{\rm vdW}(R)$ can be replaced by any other interaction curve.

For $\Delta = 0$, the dynamics now strongly depends on the interatomic distance R. For large R where $V_{\rm vdW}(R) \approx 0$, the two atoms will undergoe independent Rabi oscillations. Here, a description in the pair state basis is not required and Eq. 2.29 captures the dynamics. For small R where $|V_{\rm vdW}(R)| \gg |\widetilde{\Omega}|, |\Delta|$, the state $|rr\rangle$ is energetically unaccessible and only the states $\{|gg\rangle, |ge\rangle, |eg\rangle\}$ are relevant. By expanding the Hamiltonian in the basis $\{|gg\rangle, |gr\rangle^+, |rg\rangle^-\}$ with $|gr\rangle^\pm = \frac{1}{\sqrt{2}}(|gr\rangle \pm |rg\rangle)$ one furthermore finds that $|gg\rangle$ only couples to $|gr\rangle^{+}$ with a Rabi frequency $\sqrt{2}\widetilde{\Omega}$ while the coupling to the dark state $|ge\rangle^{-}$ vanishes. Expressing the Hamiltonian in the basis $\{|gg\rangle, |gr\rangle^{+}\}$ yields

$$\hat{H} = \hbar \begin{pmatrix} 0 & \widetilde{\Omega}/\sqrt{2} \\ \widetilde{\Omega}^{\star}/\sqrt{2} & -\Delta \end{pmatrix}. \tag{2.32}$$

Now, one observes oscillations between $|gg\rangle$ and $|gr\rangle^{+}$ at an enhanced frequency $\sqrt{2}\widetilde{\Omega}$ [207], see Fig. 2.4 (**b**). This mechanism where nearby Rydberg excitations are off-resonant for the excitation laser because of the large interaction shift is called *Rydberg blockade* and was verified in many experiments [208, 209]. It can be generalized to N atoms where one finds an enhancement by $\sqrt{N}$ [210, 211]. In general, Rydberg interactions circumvent the excitation if the interaction shift exceeds the bandwidth of the coupling, given by the respective Rabi rate $\widetilde{\Omega}$. In oder to define a cut-off criterion, one typically estimates the blockade radius R_b via $V_{\mathrm{vdW}}(R_b) \approx \widetilde{\Omega}$, providing [209]

$$R_b \approx \left(\frac{C_6}{\widetilde{\Omega}}\right)^{1/6}. \tag{2.33}$$

Implications of Eq. 2.31 for $\Delta \gg \widetilde{\Omega}$ are are discussed in section 2.5.2.

A Hamiltonian similar as Eq. 2.31 where the doubly excited state $|rr\rangle$ is replaced by a Rydberg macrodimer state will be presented later in section 5.1. For 0_g^{+} potentials, it will be discussed that also $|gr\rangle^{-}$ can be the relevant intermediate state in the excitation. Because the interactions mix certain atomic pair states, the molecular state for certain molecular quantum numbers can have antisymmetric contributions from different pair states $|rr'\rangle$ and $|r'r\rangle$, see section 4.1.3 and section 4.1.4. This will be treated by directly decomposing the ground state $|gg\rangle$ into the relevant symmetry eigenstates. It will found that the ground state can have antisymmetric components in the fine-structure basis because of the hyperfine interaction in the ground state.

Transverse-field Ising Hamiltonian

Extending the Hamiltonian Eq. 2.31 to more than two particles and defining operators $\hat{\sigma}^{x} = |g\rangle\langle r| + |r\rangle\langle g|$ and $\hat{n} = |r\rangle\langle r|$ leads to

$$\frac{\hat{H}}{h} = \frac{\widetilde{\Omega}}{2}\sum_i \hat{\sigma}_x^i - \Delta \sum_i \hat{n}_i + \sum_{i<j} V_{\mathrm{vdW}}(R_{ij})\hat{n}_i\hat{n}_j, \tag{2.34}$$

where the sum captures all atoms in the system. Motivated by the repulsive van der Waals interactions of Rydberg S-states for ^{87}Rb, the coefficient $C_6 > 0$ is assumed to be positive. For the terms acting on atoms i and j, the operators acting on the remaining atoms are implicitly assumed to be identities. The Hamiltonian Eq. 2.34 has been intensively studied in recent experiments [93, 212–214]. For $\Delta < 0$, the many-body ground state is trivially given by all atoms in the ground state. For $\Delta > 0$, one experiences a competition between the detuning and the interatomic interaction, providing spatially ordered many-body ground states, see Fig. 2.4 (**c,e**). The phase transition can be studied by adiabatically ramping the detuning from $\Delta < 0$ to $\Delta > 0$. This has been benchmarked in one [93, 212] and two dimensions [215], also for frustrated geometries [216]. By rapidly switching $\Delta \approx 0$ after preparing a specific eigenstate enables studying non-equilibrium dynamics of the many-body states [93, 217].

2.5.2 Rydberg dressing

The two-particle Hamiltonian Eq. 2.31 also shows interesting signatures for large detunings. In order to avoid resonances when the detuning compensates for the interaction, the detuning $|\varDelta| \gg \widetilde{\varOmega}$ is assumed to be negative $\varDelta < 0$ and interactions $C_6 > 0$ are again assumed to be positive. At infinite distance, the ground-state atom pair experiences twice the light shift $\varDelta_{AC}$ of an individual atom. When approaching each other, this pair state energy gets shifted from that asymptotic energy by the Rydberg dressing potential $V_{\mathrm{dr}}(R) \approx \beta^4 V_{\mathrm{vdW}}(R)$, with $\beta = \widetilde{\varOmega}/(2\varDelta)$ the Rydberg admixture in the dressed ground state $|\widetilde{g}\rangle \approx |g\rangle + \beta|r\rangle$ [218, 219]. The interaction shift can be calculated using fourth order perturbation theory. It can be intuitively understood because it represents the probability of both atoms being in the Rydberg state multiplied with the interaction of the Rydberg atom pair [72]. At short distances, the coupling to $|rr\rangle$ vanishes again due to the large interaction shift. Now, the contribution of the doubly-excited state to the light shift is absent and the pair state energy saturates to a value $V_{\mathrm{dr}}(0) = \widetilde{\varOmega}^4/(8\varDelta^3)$ that is independent of the van der Waals coefficient. Hence, by off-resonantly coupling to long-range interacting Rydberg atoms, one can engineer soft-core interaction potentials for ground-state atoms, see also Fig. 2.4 (**d**).

For two atoms trapped in individually focussed beams, the soft-core potential has been experimentally benchmarked [220]. Rydberg dressing has also been used to engineer long-range interacting spin Hamiltonians where both spin states $|{\downarrow}\rangle$ and $|{\uparrow}\rangle$ are encoded in the electronic ground state because Rydberg states are only virtually populated. By only coupling the spins $|{\uparrow}\rangle$ to the Rydberg state, the admixed interactions $V_{\mathrm{dr}}(R)\,|{\uparrow\uparrow}\rangle\,\langle{\uparrow\uparrow}|$ between two spins in the state $|{\uparrow}\rangle$ can be mapped into $S^z S^z$ interactions after replacing $|{\uparrow}\rangle\,\langle{\uparrow}| = \hat{S}^z + \frac{1}{2}\mathbb{1}$ for both atoms. For a two-dimensional many-body system of spins trapped in an optical lattice, the long-range interactions have been shown to induce correlated spin-flips in a Ramsey sequence [155]. In a one-dimensional system, the coherence time was pushed into a regime where coherent revivals have been observed [221]. In a different experimental system, the competition between dressed interactions and coherent tunneling has been demonstrated to prevent the spreading of initially prepared atomic arrangements in an optical lattice [222]. This is interesting because Rydberg experiments are usually performed in the *frozen gas regime* [223, 224] where the motion of the particles is frozen on the short timescales of the Rydberg lifetime. However, in the dressed regime, the lifetime as well as the interaction time are increased and therefore quantum simulation on motional timescales is in principle possible.

Further improving the coherence time in such a system might enable to study the phase diagram of itinerant models such as extended Hubbard models [225–231], which are theoretically expected to host phases such as supersolids and charge density waves [232–234]. In a regime with larger Rydberg fraction, Rydberg dressing might also allow to observe multi-atom interactions [235, 236]. Theoretical studies also showed that spin models realized with Rydberg dressing are not limited to $\hat{S}^z\hat{S}^z$ spin interactions. By coupling both ground states $|{\downarrow}\rangle$ and $|{\uparrow}\rangle$ to Rydbeg states $|r\rangle$ and $|r'\rangle$ whose pair states are mixed by their Rydberg interactions at shorter distances, also interaction terms $\hat{S}^-\hat{S}^-$, $\hat{S}^\pm\hat{S}^\mp$ and $\hat{S}^+\hat{S}^+$ can be realized [237, 238]. As recently proposed [239] and demonstrated in chapter 8, optically coupling to minima and maxima of the pair potentials enables the engineering of interactions that are non-negligible only at a specific distance. Because Rydberg-dressed interactions can be easily switched on and off, also proposals to realize time-periodic Hamiltonians exist [240]. Further proposals suggest to use Rydberg dressing for spin squeezing [241], quantum annealing [242, 243], to study the interaction between Rydberg-dressed ground-state atoms with other Rydberg atoms [244] or to engineer Rydberg interactions by dressing Rydberg states with other Rydberg state by using microwaves [245, 246].

Currently, the coherence time of Rydberg dressing is limited by the admixed scattering rates, which have been found to be larger than the expected rates $\beta^2 \Gamma_{|r\rangle}$ and furthermore have collective character [154, 155, 247]. For many proposed schemes, also the single-atom light shift induced by the off-resonant coupling to the Rydberg state is problematic [222, 248]. Furthermore, operating at small detunings, Rydberg dressing critically depends on laser phase noise [130].

2.5.3 Quantum simulation in the Rydberg manifold

An alternative approach is to operate entirely in the Rydberg manifold. One approach is to encode the spins $|\downarrow\rangle = |r\rangle$ and $|\uparrow\rangle = |r'\rangle$ in two Rydberg states that are coupled by a resonant dipolar exchange interaction introducted in section 2.3.2, a spin ensemble naturally realizes a $XY-$Hamiltonian [74, 196, 249, 250]. If both spins are additionally coupled by a microwave Rabi frequency $\widetilde{\Omega}_{\mathrm{mw}}$ at a detuning Δ_{mw}, the Hamiltonian writes

$$\hat{H} = \sum_{i \neq j} V_{\mathrm{dd}}(\boldsymbol{R}_{ij}) \left(\hat{\sigma}_i^- \hat{\sigma}_j^+ + \hat{\sigma}_i^+ \hat{\sigma}_j^- \right) + \hbar \frac{\widetilde{\Omega}_{\mathrm{mw}}}{2} \sum_i \hat{\sigma}_i^x + \hbar \frac{\Delta_{\mathrm{mw}}}{2} \sum_i \hat{\sigma}_i^z, \tag{2.35}$$

with the Pauli matrices $\hat{\sigma}_i^z = |\uparrow\rangle\langle\uparrow| - |\downarrow\rangle\langle\downarrow|$ and $\hat{\sigma}_i^x = |\downarrow\rangle\langle\uparrow| + |\uparrow\rangle\langle\downarrow|$, $\hat{\sigma}^+ = |\uparrow\rangle\langle\downarrow|$ and $|\sigma\rangle^- = |\downarrow\rangle\langle\uparrow|$. By utilizing the angular dependency of the dipolar exchange interaction, this Hamiltonian has been used to realize the SSH model and study the topological character of its ground state [92] and to realize density-dependent Peierls phases [251]. A second approach is to use to two Rydberg states without first order resonant dipole-dipole exchange. Here, second order perturbation theory enables off-diagonal exchange terms via intermediate pair states. Together with the diagonal van der Waals interactions which are of the same order and represent $\hat{S}^z\hat{S}^z$ interactions, this realizes a XXZ Hamiltonians [94, 252–255].

2.5.4 Quantum computing

Another rapidly emerging research direction is to use Rydberg atoms as a platform for quantum computation [49, 205, 206]. Single-qubit operations can be performed using laser fields, also with single-qubit resolution. Entanglement gates can be realized in different ways [94]. Encoding the qubit in the ground state $|g_1\rangle \equiv |0\rangle$ and the Rydberg state $|r\rangle \equiv |1\rangle$, entanglement can be created at high fidelities $\geq 99.1(4)\%$ [78] by performing a $\pi-$rotation in the blockaded regime because the state $|gr\rangle^+$ introduced in section 2.5.1 represents an entangled Bell state. By using the same qubit for systems of more than two atoms as described by Eq. 2.34, the blockade has also been used to create Dicke or $|W\rangle$ states [210, 211] and Greenberger–Horne–Zeilinger (GHZ) states [256].

For computational tasks it is typically more practical to encode the qubit in two ground states [257] $|g_1\rangle \equiv |0\rangle$ and $|g_2\rangle \equiv |1\rangle$ because Rydberg atoms decay fast and are typically antitrapped in optical potentials. There exist several available entanglement schemes where the coupling to the Rydberg state is only switched on for a short time during the gate operation. One way is to sequentally perform three qubit-resolved coherent excitation pulses on the two qubits. This method demonstrated fidelities $\leq$ 90% [258] and has also been extended to entangle different isotopes [259]. Another way is to perform detuned Rabi oscillations in the blockaded regime, where the phase evolution of the doubly-excited state differs from the singly-excited terms because of the enhanced Rabi frequency. After initializing isolated atom pairs at distances lower than the blockade radius, this entanglement scheme which does not require individual adressing achieves fidelities $\lesssim 97.4(3)\%$ [76, 260]. Finally, also Rydberg dressing can be used for entanglement [220]. By additionally adiabatically ramping the dressing laser close to resonance, a recent experiment realized fidelities around $92.8(2.0)\%$ [96]. Another recent experiment also demonstrated the ability to move the atoms between performing individual entanglement operations while preserving the coherence of the quantum register [54]. Finally, an Rydberg-based entanglement scheme of ions trapped in a Paul trap has been demonstrated [261]. Because this is currently a very active field of research, much progress can be expected in the near future.

2.5.5 Rydberg quantum optics

Rydberg atoms contributed to quantum optics in several ways. The large transition dipole matrix elements between neighboring Rydberg states introduced in Eq. 2.11 enables to use Rydberg atoms as readout-tools for the quantum state of the *microwave field* in superconducting microwave cavities [262, 263]. Here, measuring the quantum state of a circular Rydberg atom after moving through the cavity allows one to determine the photon number in the cavity in a non-demolition measurement [264, 265] and observe quantum jumps in the population [266]. This allows one to reconstruct the photon distribution of coherent states by collapsing them into photonic Fock states according to their Poissonian distribtion [267, 268]. Furthermore, the Wigner function — a quasiprobability distribution which can be used to describe a quantum state in phase space — of Fock states and Schrödinger cat states of photons in the cavity have been reconstructed [160, 269]. Note that, in contrast to most recent applications of Rydberg atoms, this technique does not rely on Rydberg interactions.

Alternatively, Rydberg states also allow to control the quantum states of *optical fields*. Here, the strong interactions of Rydberg atoms are mapped on the light field using electromagnetically induced transparency (EIT) [270–272]. Because the absorption of a single photon creates a Rydberg excitation in the atomic ensemble that shifts the Rydberg transition and therefore the EIT window of the remaining atoms, one can realize exceptionally high optical nonlinearities [273–275]. This mechanism leads to a different definition of the Rydberg blockade – the so-called EIT blockade – in this subfield. Typically, the EIT scheme relies on a pump field and a weak probe field [276]. By strongly decreasing the probe field, it can be converted into strongly interacting Rydberg polaritons [277–279]. These systems can be used to realize all-optical transistors where a gate light pulse switches the transmission of a target pulse [187, 280], phase gates between photons [281], single-photon sources [282, 283], and super- and subradiance [284]. The manipulated light fields can be characterized using photon-photon correlations [285]. Rydberg EIT can also be used to image Rydberg excitations [286–289]. Furthermore, the $\sqrt{N}$ enhancement of the collective Rabi frequency in these system discussed in section 2.5.1 provides coherent Rabi oscillations for light pulses carrying only a few photons without using cavities. This allows one to measure Rabi oscillations directly in the photon domain [290]. Here, instead of observing oscillations of the atomic population, one can directly observe the a oscillation in the photon distribtion of the pulse which is correlated with the state of the atom.

2.5.6 Further directions

Alternatively to alkali atoms, many new laboratories use *alkaline-earth atoms* (AEAs) and *alkaline-earth-like* atoms such as strontium [291] or ytterbium [292, 293] which have a Helium-like two-electron structure consisting of singlet and triplet states. While the preparation and the control of these divalent atoms is technically more challenging, they have other useful features and the qubits and spins can be encoded in internal states fundamentally different from alkali atoms. Narrow transitions between the singlet ground state and the weakly coupled triplet states provide long-lived metastable states, which enables to independently measure the population in the ground state and the metastable state [294]. Atoms occupying the metastable states have larger spatial overlap with the Rydberg states, which significantly increases the Rabi frequencies achievable in experiments [78]. Because of the two-electron structure, off-resonant laser light now affects the energies of the Rydberg electron and the remaining electron in the singly-occupied orbital in the ground state. While alkali Rydberg atoms experience repulsion from laser fields [295], this enables optical trapping of Rydberg states [296]. Furthermore, exciting the remaining ground state electron of a AEA atom excited to a Rydberg state triggers a fast ionization process which allows to efficiently remove Rydberg atoms from an atomic ensemble [78].

Currently, experimentalists also try to realize a quantum simulator based on *circular Rydberg atoms* [297, 298]. Spins can be encoded in different circular Rydberg states which can again interact via Rydberg interactions. Black-body transitions to other circular Rydberg states — the only dipole-allowed transition — can be reduced by cooling the apparatus down to cryogenic temperatures [156, 299]. The lifetime can be additionally enhanced by engineering the density of states with microwave cavities. Other directions include quantum simulations at ultrashort timescales by combining Rydberg interactions with the toolset of attosecond physics [300–302]. Interestingly, there exist also electron-hole pairs in solids which with similar properties than Rydberg atoms [303]. These so-called Rydberg excitons also give rise to a Rydberg blockade [304] and hold promises for quantum optics [305]. Finally, also the coupling to so-called ultra-long range Rydberg molecules which are introduced in the next section can be used to control interatomic interactions [239, 248, 306, 307].

2.6 Ultracold Rydberg molecules

Another active research direction is the study of weakly bound Rydberg molecules by associating initially laser cooled atoms. Molecules can be defined as *"an electrically neutral entity consisting of more than one atom (n>1). Rigorously, a molecule, in which n>1 must correspond to a depression on the potential energy surface that is deep enough to confine at least one vibrational state."* [308]. In the electronic ground state, even in the diatomic case, ab-initio calculations of the molecular structure solely based on the properties of the atoms forming the molecules are usually extremely difficult because of the interaction of the large number of contributing electrons and the correlations in the many-electron wave function. Furthermore, their small size and their large binding energies limit the experimental access. Weakly bound molecules with binding mechanisms that rely on highly excited atomic Rydberg states inherit the simplicity of Rydberg atoms. Now, calculations of the

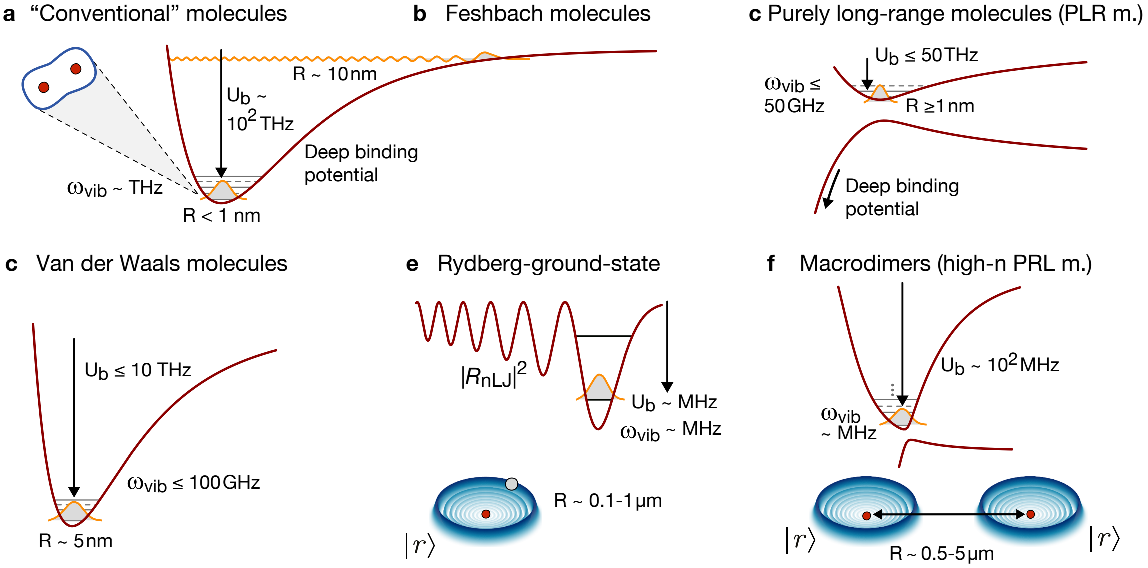

Figure 2.5: **A map of energy scales and bond lengths for different diatomic molecules.** (**a**) For deeply bound *conventional molecules* with high binding energies U_b and vibrational energies frequencies ω_{vib}, the atoms form chemical bonds where electrons in partially filled orbitals occupy hybrid orbitals that are delocalized over both nuclei [4], indicated by the solid blue line. The molecular bond length is tyipcally less than a nanometer. (**b**) *Feshbach molecules* [45] are occupying the highest vibrational states of deep binding potentials (**c**) *Purely long-range molecules* (PLR) can occur at avoided crossings of pair potential curves in the large-distance region where electron orbitals do not overlap and hybrid orbitals do not form [58, 318]. (**d**) For noble gases where chemical bonding does not occur because all electron orbitals are occupied, remaining *van der Waals bonds* can provide weaker binding potentials [319–321]. (**e**) *Rydberg–ground-state molecules* are ultra-long-range Rydberg (ULR) molecules where ground-state atoms are bound to a Rydberg atom by their interaction with the Rydberg electron [65]. (**f**) *Rydberg Macrodimers* are PLR-molecules where both atoms populate highly-excited Rydberg states [67].

molecular structure based on the known properties of the individual atoms are possible. Furthermore, their large size and small energy scales provides an experimental level of control not present for other molecules.

There exist several different ways to combine molecules and Rydberg excitations and the word Rydberg molecule is not sufficient to specify the type of molecule. First, there are *Rydberg excited molecules* where a conventional deeply bound molecule is excited to Rydberg states [309–312]. Second, there exist *ultra-long range Rydberg molecules* [65]. These include *Rydberg–ground-state molecules* where ground-state atoms are bound to a Rydberg atom and *Rydberg macrodimers* where Rydberg atom pairs are bound by their Rydberg interaction potentials. In this dissertation, the initial proposals [67, 313], and recent publications [314, 315] *Rydberg–ground-state molecules* as well as *Rydberg macrodimers* are classified as *ultra-long range Rydberg molecules*. Because the field is relatively new, the terminology sometimes depends on the literature. Recently, also bound states where a Rydberg atom is electrostatically bound to an ion has been discovered [314–317].

2.6.1 Rydberg–ground-state molecules

Here, ground-state atoms are bound to a Rydberg atom by the interaction between the Rydberg electron and the ground-state atoms [66, 322], see Fig. 2.5 (**e**). The potential energy depends on the probability density of the Rydberg wave function and the energy-dependent scattering length between both particles. This interaction, which was first observed in 1934 via pressure-dependent shifts of Rydberg resonances in vapor cells [323] and first explained by Fermi [324], can be predicted from ab-initio calculations using relativistic quantum mechanics [325–327]. Long-range Rydberg molecules provide a experimental way to further characterize the scattering length [327]. Because the ground-state atom is trapped in the outer lobes of the Rydberg wave function, the bond length is given by the separation of the Rydberg electron from the nucleus. The binding potential typically only hosts a small amount of vibrational states. First experimental studies focused on molecules where the Rydberg electron is in a S-state [66], with binding energies of several megahertz. Dependent on the impact of the ground-state atom on the state of the Rydberg electron, the non-interacting Rydberg states might not be a good basis to describe the molecule [328, 329]. For so-called trilobite and butterfly Rydberg molecules where the interactions with the ground state atom mixes many orbital momentum states due to the presence of a shape resonance, the resulting Rydberg wave function can be strongly distorted. Here, also the binding potentials can be significantly deeper. Even in the case of homonuclear diatomic molecules, this can provide large permanent dipole moments [330, 331]. The binding mechanism can be extended to multiple ground-state atoms bound to the Rydberg atom [332, 333] and also the many-body limit where a Rydberg impurity interacts with a bath of ground-state atoms in a polaronic picture [334] has been studied. They have been used to extract the quantum statistics of the ground-state atoms bound to the Rydberg atom [335].

2.6.2 Rydberg macrodimers

Rydberg macrodimers — the main topic of this dissertation — are Rydberg atom pairs bound together by their electrostatic interaction [67]. Because Rydberg interactions are large at distances above the extension of the Rydberg orbit, Rydberg macrodimers are about one order of magnitude larger than Rydberg–ground-state molecules at the same principal quantum number [65]. The resulting bond lengths which can easily be beyond a micrometer make Rydberg macrodimers the largest existing diatomic molecules.

While first experimental indications of macrodimers were discovered almost 20 years ago [68, 336], only two previous experiments reported on their observation. The first experiment studied the kinetic energy released from ion-repulsion after ionizing all Rydberg atoms in the sample [69, 337]. At certain spectroscopic signatures, the kinetic energy released after ionization did not depend on the waiting time between the Rydberg excitation and the ionization pulse, which implied that the distance between the excited Rydberg atoms did not change. From this it has been concluded that a bound object has been observed. The second experiment performed a seeded excitation scheme using Rydberg s-states and Rydberg p-state excitation to excite Rydberg atom pairs detuned from the Rydberg resonance [70, 338, 339]. Macrodimers were then identified from the background by their spontaneous ionization rate. Before this dissertation, a vibrationally and microscopically resolved study of Rydberg macrodimers has not been achieved.

Macrodimers and other molecules

Besides their large size and their small energy scales, Rydberg macrodimers are conceptually not so different from conventional molecules, see Fig. 2.5. They have the same symmetry properties as any homonuclear diatomic molecule, their quantum state can be labelled using molecular quantum numbers, and they have quantized vibrational motion. Macrodimers are mainly different because of the absence of overlapping electron clouds where the exchange interaction between the electrons can be neglected. As a result, the formation of hybrid orbitals between both atoms which are then occupied by electrons that are delocalized over the whole molecule does not occur and the fermionic nature of the electrons does not play a role.

The purely electrostatic binding classifies Rydberg macrodimers as *purely long-range molecules* [58]. These molecules, where the overlap of electron clouds vanishes over the full spatial extension of the vibrational wave function, also exist at lower principal quantum numbers. In the 1970's, they were theoretically predicted to exist in the avoided crossings between asymptotic potential curves [318, 340]. This happens, for example, when two pair potentials asymptotically connected to different atomic fine-structure pair states cross before the electrons start to overlap, see Fig. 3.5 (**c**). They were experimentally observed in photoassociation studies of laser cooled alkali atoms [341–344] and predicted to also exist for alkaline-earth atoms [345].

For most other molecules, the electron orbitals of the contributing atoms do overlap. For molecules consisting of multi-electron atoms, this leads to repulsive barriers at short distances because the Pauli principle pushes the electrons on higher orbits. For Feshbach molecules at high vibrational quantum numbers close to the dissociation energy, such an overlap occurs at the inner turning point of the vibrational motion [45]. Also for weakly bound van der Waals molecules such as bound noble gases [346–349], potentially the largest diatomic molecule in the electronic and vibrational ground state, the electron exchange interaction describes the repulsive barrier at short distances [319, 350].

Chapter 3

Experimental platform

This chapter introduces the most relevant features of the experimental apparatus used in this dissertation [71, 124, 351–353]. For documentation, a new laser system for Rydberg excitation which was built together with Kritsana Srakaew and Simon Evered is presented and characterized. Most experiments performed in this dissertation used a first generation laser system which was identical in its capabilities but provided less power [72]. Finally, the atomic physics describing the excitation of single-atom Rydberg states is discussed.

3.1 Quantum gas microscopy

The experiments in this dissertation have been performed using *quantum gas microscopy* [39]. Here, atoms are typically trapped in a single layer of a three-dimensional periodic optical potential. This so-called optical lattice is realized by interfering laser beams [26]. The standing wave of the laser field creates a periodically modulated potential landscape for the atoms whose internal energies are sligthly shifted due to the dispersive interaction with the oscillating field [29]. Ultracold atoms confined in optical lattices have been proven to be a fruitful platform to realize many-body Hamiltonians relevant for condensed matter physics [28, 354]. The idea of quantum gas microscopy was to spatially resolve the lattice occupation using fluorescence imaging. To this end, a high-resolution objective which is able to resolve the point spread function of atoms populating neighboring lattice sites is placed at some distance of the atomic layer [39]. The imaging process requires to scatter sufficiently many photons at each individual atom to distinguish whether a given lattice site is populated with an atom or not. In this process, the atoms leave the ultracold temperature regime and heat up. In order to still pin the motionally excited atoms at their position and to avoid hopping during the imaging process, the laser intensity of the lattice beams has to be high enough during this stage of the experiment. Furthermore, laser cooling techniques have to be applied to avoid heating up to a critical threshold where pinning does not work anymore [355].

Bose-Hubbard Hamiltonian

The first laboratories using quantum gas microscopy — such as the one presented here — used bosonic ^{87}Rb atoms [40, 41]. Because ultracold atoms confined in a two-dimensional layer of a lattice naturally realize the two-dimensional Bose-Hubbard Hamiltonian

$$\hat{H} = -J \sum_{\langle \boldsymbol{i}, \boldsymbol{j} \rangle} \hat{a}_{\boldsymbol{i}}^{\dagger} \hat{a}_{\boldsymbol{j}} + \frac{U}{2} \sum_{\boldsymbol{i}} \hat{n}_{\boldsymbol{i}} \left(\hat{n}_{\boldsymbol{i}} - 1 \right) - \sum_{\boldsymbol{i}} \mu_{\boldsymbol{i}} \hat{n}_{\boldsymbol{i}}, \tag{3.1}$$

the first studies focused on phenomena related to this Hamiltonian. Here, $\hat{a}_{\boldsymbol{i}}$ ($\hat{a}_{\boldsymbol{i}}^{\dagger}$) annihilate (create) a particle at site $\boldsymbol{i}$, $\hat{n}_{\boldsymbol{i}} = \hat{a}_{\boldsymbol{i}}^{\dagger} \hat{a}_{\boldsymbol{i}}$ counts the atom number and $\langle \boldsymbol{i}, \boldsymbol{j} \rangle$ denotes summing over pairs of lattice sites that are coupled by nearest neighbor tunneling. Furthermore, μ_i is the chemical potential which determines the total atom number in the ground state. It depends on the lattice site in order to account for the external trapping potential, typically determined by the size of the laser beam forming the lattice potential. The two main parameters of the Hamiltonian are the coherent tunneling rate J between neighboring lattice sites and the on-site interaction U [30, 32]. Along the third direction, the lattice is deep enough to freeze the corresponding dynamics. Interactions between atoms located at different sites and tunneling rates between distances larger than one lattice spacing can be efficiently suppressed. The tunneling parameter J between neighboring lattice sites can be tuned by the depth of the lattice potential [26]. The interaction parameter U is determined by contact interactions which can in principle also be varied. In most cases, this is realized by tuning the magnetic field close to a Feshbach resonance [45]. Mainly because of the high field of $B = 1007\,\mathrm{G}$ required for $^{87}\,\mathrm{Rb}$, this tunability is not used here. [356–358]. Depending on the relative strength of U and J, the many-body ground state has very different signatures [351]. If the tunneling parameter dominates, the kinetic energy dominates the properties of the many-body ground state and the atoms are delocalized over the system, see Fig. 3.1 (**a**). The corresponding many-body state is called a *Bose-Einstein condensate* (BEC) [359, 360]. It can be described by a single macroscopic wave function centered around the potential minimum of the external trap, whose coherence can be experimentally verified in time-of-flight experiments [361, 362]. If the repulsive interaction parameter dominates, tunneling to a site that is already occupied by an atom is energetically unfavorable. In this case, the atoms will arrange themself into a configuration with fixed atom number per lattice site. The many-body state is called a *Mott insulator* [32]. If the overall confining potential created by the lattice beams varies on the scale of U, the Mott insulating ground state can also contain regions with different fixed atom numbers. Assuming a Gaussian laser beam, this leads to a shell-like structure with areas containing different numbers of fixed atom numbers per site [30, 41]. Quantum gas microscopy resolved the signatures of both phases and the correlations close to the phase transition [43].

Hubbard Hamiltonians and quantum magnetism

Extending the toolset by fermionic atoms such as $^6\mathrm{Li}$ allows to also realize the Fermi-Hubbard Hamiltonian where the different quantum statistics gives rise to new states such as *band insulators* [363]. In the Mott insulating phase where first order tunneling is suppressed due to interactions, second-order tunneling processes can still occur and affect the Hamiltonian for systems with more than one internal quantum state. Mapping the internal states to different spin orientations, this enables the study of quantum magnetism [364]. The system can be described by a Heisenberg model and the corresponding spin correlations can be observed with the microscope. Depending on the quantum statistics of the atoms, ferromagnetic (bosons) [365–367] as well as antiferromagnetic (fermions) [44, 368] spin interactions can be observed. Here, particularly the doped Fermi-Hubbard model with less or more than excactly one atom per site is an interesting field of research [35, 369–372] because the interactions between the holes or doubly-occupied sites and the antiferromagnetic environment might give rise to novel many-body phases [37, 373, 374]. Experimentally realizing this regime at sufficiently low temperatures might give insights into the physics underlying high-temperature superconductivity which is currently not understood [36, 375, 376]. Future experiments will also cover the microscopic study of tunable anisotropic spin interactions which can be realized for spin-dependent on-site interaction parameter [34, 377]. In addition to pure Hubbard models and the quantum magnetism observable close to the Mott transition, quantum gas microscopes studied effects of site-dependent disorder potentials [378–381], time-periodic potentials [382], or complex tunneling rates [383] where topologically nontrivial Bloch bands can be realized [384–387].

Unity-filled atom arrays

For many experiments, a unity-filled array is the desired starting point. Here, the Mott insulating phase or also the band insulating phase for fermions provides a pathway to initialize such a system for short distances where rearrangement using optical tweezers is challenging. The details of the underlying Hubbard model are not important. One example is the experimental study of cooperative superradiant or subradiant states hosted by atomic arrays at subwavelength spacing [98, 100, 101, 388]. Here, the geometric arrangement of the array leads to interference effects in the radiated fields of the atoms trapped in the array. This allows for an increase of the lifetime of an excitation stored in the array compared to the corresponding lifetime of an isolated atom. As a consequence, the linewidth of the cooperative atomic transition narrows. The same holds true for most Rydberg experiments. Because Rydberg interactions are typically much stronger than the tunneling parameter contributing to the Hubbard Hamiltonian, the motional degree of freedom remains frozen over the experimental timescale. Here, the Mott insulating state is a suitable initial state because of the deterministic lattice occupation. Starting with an atomic Mott insulator enabled the first *in situ* snapshots of the Rydberg blockade [209], the study of the transverse Ising Hamiltonian [212, 213] introduced in Eq. 2.34 and the realization of a long-range interacting Ising Hamiltonian using Rydberg dressing [155, 221]. Comparing Mott insulators with atoms loaded in optical tweezer arrays shows that both platforms are able to create unity-filled arrays [56, 57]. Because of the smaller spacing of Mott insulators, Rydberg experiments are typically performed at lower principal quantum numbers $n \approx 30$ compared to optical tweezers where $n \approx 60 - 70$ in order to realize the same interaction strength at the relevant distance. While this allows one to achieve higher Rabi frequencies between the ground state and the Rydberg state in lattice systems, optical tweezer systems benefit from higher initial fillings and shorter experimental cycling times.

3.1.1 Technical challenges

Performing experiments with cold atomic gases is challenging because it requires to control a large amount of parameters. Assuming a stable vacuum system and stable laser sources, this includes many different laser frequencies and intensities at different stages of the experiment as well as different magnetic field values. While this has not been used in the experiments presented here, many Rydberg laboratories also have to control their electric fields. Typically, the laser frequencies are electronically stabilized to references such as atomic spectroscopy lines or optical resonators. Here, laser fields oscillating at hundreds of terahertz have to be stabilized to a linewidth lower than the atomic transition addressed in the experiments, typically a few megahertz. For Rydberg experiments where narrow linewidths in the kilohertz regime are necessary, frequency references are typically given by optical resonators built from ultra-low expansion glass (ULE cavities). Parameters that require dynamical tunability are controlled from a control software that communicates with a field programmable gate array (FPGA) that sends analog and digital signals to different modules of the experimental setup. The digital signals are typically

TTL (transistor-transistor logic) signals. Among other applications, they switch control circuits for magnetic field stabilization, arbitrary waveform generators, mechanical shutters to block or unblock laser beams, or accousto-optical modulators (AOM's) which can be used to stabilize laser intensities and – to some degree – their frequency. The analog signals are set values for control circuits that control laser intensities or current stabilizations for magnetic field control. Additional communication between the control software and different devices is necessary to control values such as microwave frequencies or the orientation of micromirrors on digital mirror devices (DMD). Furthermore, because the size of typical atomic ensembles as well as the waists of the laser beams used to trap and manipulate them have only a length scale of a few tens of micrometers, experiments are very sensitive to thermal drifts.

3.2 Preparation of cold atomic ensembles

The longer cycling times in quantum gas microscopes originate from the preparation of the ultracold atomic gas and the extremely low temperatures needed to realize the many-body ground state. Generally, performing quantum simulations with cold atoms requires many preparation steps. In order to isolate the quantum systems from the environment and avoid interactions with the background gas at room temperature, the atomic ensembles have to be prepared in vacuum chambers. Here, the atoms are guided from an initial source into a so-called magneto-optical trap by using combinations of magnetic fields and lasers. In the magneto-optical trap, atoms are trapped by a combination of optical and magnetic fields and at the same time laser cooled to temperatures close to zero Kelvin. For optimized parameters, the final temperature in the magneto-optical trap depends on the linewidth of the cooling transition and is typically on the order of tens to hundreds of microkelvin [19]. For very narrow transitions also lower temperatures have been achieved [389]. Now, the atoms are cold enough to be trapped in optical tweezers where they can be used for experiments. Additional cooling techniques such as Sisyphus cooling [390, 391] or Raman sideband cooling [392, 393] allow one to further reduce the temperature.

3.2.1 Preparing two-dimensional atomic Mott insulators

In order to reach ultracold temperatures where quantum degenerate phenomena can be observed, even further cooling is required. The additionally implemented preparation stages are typical for laboratories such as the one presented here. They are shortly summarized in the following paragraph and discussed in more detail in our previous dissertations [71, 72, 124, 351–353]. First the atoms are loaded from the magneto-optical trap into a magnetic trap. Subsequently, the atomic cloud trapped in the magnetic trap undergoes an evaporative cooling stage where hot atoms are successively removed from the system. This step is time consuming because the atoms in the sample have to continuously reach thermal equilibrium by interatomic scattering. After evaporation, the temperature can be low enough to reach quantum degeneracy and perform experiments at ultracold temperatures [20, 21].

In order to guarantee enough optical access at the different stages of the experimental sequence, the atoms are transported from the MOT chamber to a different vacuum chamber first. Therefore, the atoms are loaded from the magnetic trap into a focused far-off-

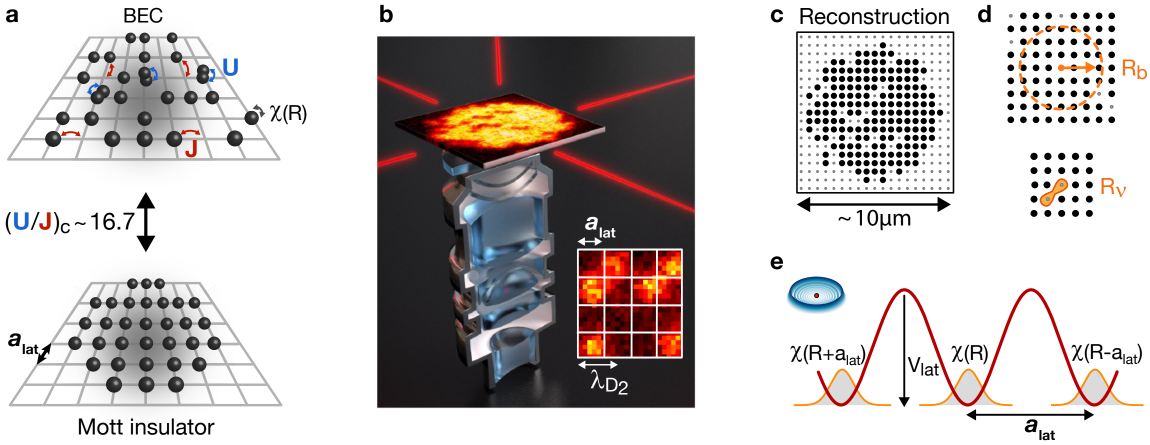

Figure 3.1: **Quantum gas microscopy and relevant length scales.** (**a**) The two-dimensional system is described by the on-site interaction U and the tunneling rate J. Lowering J below a critical value, the system arranges itself into a unity filled Mott insulating state located at the trap center [351]. The motional wave functions $\chi(R)$ of the ground state atoms (illustrated as black balls) are a few hundred times larger than their electron orbitals. (**b**) The lattices are created by three retroreflected laser beams (red). The vertical lattice is directly reflected at the lower vacuum window. Below the atomic plane, a high-resolution objective collects fluorescence photons for imaging. The lattice constant $a_{\text{lat}} = 532\,\text{nm}$ is slightly smaller than the width of the point spread function of $700\,\text{nm}$ [71] of the atoms which are imaged at a wavelength of $\lambda_{D_2} = 780\,\text{nm}$. The image was provided by Christoph Hohmann (MCQST). (**c**) By collecting enough photons, occupied (filled black circles) and empty (gray dots) sites can be distinguished. (**d**) A typical Rydberg blockade R_b [72, 124] or a macrodimer bond length R_ν at a principal quantum number $n \approx 36$ is larger than a_{lat}. (**e**) The spatial width of $\chi(R)$, here shown for $V_{\text{lat}} = 40\,E_r$, is comparable to the $36S_{1/2}$ Rydberg orbit (blue).

resonant laser beam whose focus is then moved. After the movement, the atoms are loaded from the transport trap into a dipole trap formed by the two in-plane lattice beams where an additional stage of evaporative cooling keeps the temperature low. At this stage, the retroreflected beam of the lattices is blocked in order to allow the atoms to redistribute.

Subsequently, the atoms are loaded into the vertical lattice and all atoms but the ones populating a single plane of the vertical lattice are removed. This slicing process represents another critical step required for quantum gas microscopes. For the apparatus used here, this is realized using a strong magnetic field gradient of $24\,\text{G/cm}$ perpendicular to the atomic plane. As a consequence, the microwave resonance between the hyperfine states $|2,-2\rangle$ to $|1,-1\rangle$ experiences a spatial gradient $5\,\text{kHz}/\mu\text{m}$[71]. This can be used to prepare the atoms in a single selected plane in a different hyperfine ground state compared to the rest of the system. Then, by pushing out all remaining atoms from the system with a resonant laser pulse, only a single occupied layer remains. After transport as well as after slicing, further evaporation stages are implemented to keep the temperature low enough.

Finally, when the intensity of the in-plane lattices is adiabatically ramped up, the ultracold atomic cloud arranges itself in the selected atomic plane according to the coherent tunneling J and the on-site interaction U which contribute to the underlying Bose-Hubbard Hamiltonian. Both quantities can be derived from the single-atom motional states in the lattice. Generally, the eigenstates of non-interacting particles confined in periodic potentials are delocalized Bloch waves. The localized Wannier wave functions $\chi(\mathbf{R})$ can be obtained from the Bloch waves by applying a Fourier transform. For deep lattices, they transfer into the motional ground state obtained from solving the on-site Schrödinger equation after performing a harmonic approximation at the potential minima, yielding [26]

$$\chi(\mathbf{R}) = \frac{1}{\left(2\pi\sigma_{\text{lat}}^2\right)^{3/4}} e^{-\left(\frac{\mathbf{R}}{2\sigma_{\text{lat}}}\right)^2}. \tag{3.2}$$

The width of the Wannier states is given by

$$\sigma_{\text{lat}} = \left(\langle\hat{\mathbf{R}}^2\rangle - \langle\hat{\mathbf{R}}\rangle^2\right)^{1/2} = \sqrt{\frac{\hbar^2}{4mE_r}}\left(\frac{V_0}{E_{\text{r}}}\right)^{-1/4} = \sqrt{\frac{\hbar}{2\pi\omega_{\text{lat}}}}. \tag{3.3}$$

The coherent tunneling depends on the spatial overlap of neighboring Wannier states [351]

$$J = -\int \chi^\star(R \pm a_{\text{lat}}) \left(-\frac{\hbar^2}{2m_{\text{Rb}}}\frac{\partial^2}{\partial R^2} + V_{\text{lat}}(R)\right)\chi(R)dR. \tag{3.4}$$

At deep lattices, it can be effectively frozen on experimental timescales due to the suppression of the tunneling rate $J = \frac{4}{\sqrt{\pi}}E_r\left(\frac{V_0}{E_r}\right)^{3/4}\exp\left(-2\sqrt{\frac{V_{\text{lat}}}{E_r}}\right)$ with the lattice depth V_{lat} [26]. The on-site interaction depends on the overlap integral of both atoms occupying the same single particle Wannier state. Assuming contact interactions at a s-wave scattering length a_s, the on-site interaction energy can be computed via

$$U = \frac{4\pi\hbar a_s}{m_{\text{Rb}}}\int dR|\chi(R)|^4. \tag{3.5}$$

For a two-dimensional bosonic system, the phase transition between the BEC and the Mott insulator occurs at a lattice depth of $V_{\text{lat}} \approx 10\,E_r$, in agreement with the theoretical expectation $U/J \approx 16.7$ [351, 394]. Here, $E_r = h^2/(8m_{\text{Rb}}a_{\text{lat}}^2) = h \times 2.0\,\text{kHz}$ is the recoil energy of the lattice. In the experimental apparatus used here, the interaction $U \approx h \times 500\,\text{Hz}$ only weakly depends on the lattice depth. The temperature required to observe the Mott insulating state can be estimated using $T \lesssim \frac{U}{k_B} = 24\,\text{nK}$, underlining the extreme temperature regime of the experiments.

3.3 The ^{87}Rb quantum gas microscope

In the experimental setup used here, all three lattices are created by retroreflected laser beams at a wavelength of $\lambda_{\text{lat}} = 1064\,\text{nm}$, providing lattice constants $a_{\text{lat}} = 532\,\text{nm}$, see Fig. 3.1 (**b**). Cross-interference between lattice beams corresponding to different axes is avoided by choosing perpendicular polarizations and preparing them at slightly different frequencies using an AOM. The beating frequency of a few hundred megahertz is too fast to influence the atomic ensemble. Interestingly, the associated sidebands can be observed in our Rydberg spectroscopies, see the discussion in Fig. 4.2. After performing the experiments at ultracold temperatures, the lattices are ramped to deep values around $\approx 2000\,E_r$ in order to avoid hopping within the plane or atom loss during the imaging process. The same laser operating at the D_2 transition between $5S_{1/2}, F = 2$ and $5P_{3/2}, F' = 3$ of ^{87}Rb at $\lambda_{D_2} \approx 780\,\mathrm{nm}$ providing the fluorescence photons keeps the atoms cold by performing laser cooling in an optical molasses configuration. To avoid population transfer into the hyperfine ground state $F = 1$ which is dark during the imaging process, an additional repumper laser brings them back into the imaging and cooling cycle. In order to cool all dimensions accordingly, we illuminate the atoms with 5 molasses beams. Within the plane, each direction is cooled along both directions by an incoming and a retroreflected beam. Along the vertical direction, we only have a single beam which is sent through the objective to avoid direct illumination of the electron-multiplying camera charge-coupled device (EMCCD) camera used for imaging. During the imaging process, around 7000 fluorescence photons [71] are detected per atom for an illumination time of $850\,\mathrm{ms}$, followed by a reference image where the atoms are removed from the system. After subtracting the reference image, a reconstruction algorithm calculates the lattice occupation. If the focal plane of the objective is aligned with the atomic plane and atom loss during the imaging process is small, the histograms of the photon counts for occupied and empty sites are well separated and the reconstruction works with a fidelity better than 99.5% [71]. In order to keep this alignment, the objective position has to be optimized using a high-precision piezo on a timescale that dependends on the thermal stability of the experiment. This is realized using an autofocusing sequence that typically runs every ten to twenty minutes and images the same cloud for different objective positions. During imaging, the summed rate of atom loss and hopping within the plane is around $\approx 1\%$ and strongly depends on the alignment of the lattice beams and the molasses beams as well as the magnetic field. One feature of quantum gas microscopes and also optical tweezer setups is that the imaging only accesses the parity of the atom population. This is called parity projection and originates from the fact that the imaging light couples to asymptotic molecular potentials. The created bound pairs leave the system and do not contribute to the imaging signal. As a consequence, doubly occupied sites appear as empty sites and sites occupied by three atoms appear as a singly-occupied sites.

The single-site resolution provided by the microscope can not only be used to image the atoms but also to address individual atoms with lasers [42, 378, 395]. This is implemented for a laser at a wavelength of $787\,\mathrm{nm}$ that illuminates an array of electronically controllable mirrors. By switching the mirrors of this digital mirror device (DMD) on and off, certain lattice sites can be illuminated or not. This allows to tune the differential light shift of the hyperfine ground states. As a consequence, the microwave transition between two hyperfine ground states $|1, m_F\rangle$ and $|2, m_F\rangle$ can be tuned to be on or off resonant only for the addressed or not-addressed lattice sites. By removing the atoms in the state $|2, m_F\rangle$ from the system by applying a push-out beam certain initial atomic configurations can be created from an initial Mott insulator.

In order to efficiently transfer the atoms between different hyperfine ground states, we typically perform microwave Landau-Zener transitions where the frequency is adiabatically swept over the resonance. During single-site addressing and also during slicing, the microwave Rabi rate is decreased to low values to avoid that power broadening covers the energy splitting between addressed and not-addressed sites or between neighboring atomic planes. At high powers of the microwave field, different hyperfine ground states can be driven by Rabi rates up to $20\,\mathrm{kHz}$. If even faster Rabi couplings are required, one can use Raman processes using laser beams instead of microwave fields [396].

3.4 The ULE-locked infrared laser source

In order to excite Rydberg P-states using a single-photon transition from the ground state, laser light at an ultraviolent (UV) wavelength $\lambda_{\mathrm{uv}} = 298\,\mathrm{nm}$ is required. In the experiment, this is realized by frequency quadrupling a laser operating at $1192\,\mathrm{nm}$. The infrared laser is a commercial diode laser from Toptica. The main laser path is coupled into a fiber which seeds a commercial Raman fiber amplifier (RFA) that amplifies the infrared light to a power of roughly $5-6\,\mathrm{W}$. To guarantee frequency stability and tunability, a few tens of microwatt of the laser beam is split from the main path before the RFA and coupled into a broadband fiber electro-optical modulator. Here, the laser light is modulated by the two frequencies ν_{ULE} and ν_{PDH}. Afterwards, the light is sent to a cavity made of ultra-low expansion glass which represents the absolute frequency reference for the Rydberg experiments. The lower frequency at $\nu_{\mathrm{PDH}} = 15\,\mathrm{MHz}$ is used to create the error signal according to traditional Pound-Drever Hall frequency locking [397]. Modulating at a second tunable frequency ν_{ULE} between tens of megahertz up to a gigahertz creates two additional error signals at the blue and red sidebands detuned by $\pm\nu_{\mathrm{ULE}}$ from the ULE resonances. Locking the laser to these sideband error signals stabilizes the frequency separation between between the ULE cavity resonance and the carrier field of the laser. The free-spectral range (fsr) of the ULE cavity is $\mathit{\Delta}_{\mathrm{ULE}} = 1496.66\,\mathrm{MHz}$, corresponding to a cavity length of $L = c/(2\mathit{\Delta}_{\mathrm{ULE}}) = 10\,\mathrm{cm}$. Within the bandwidth of the frequency doubling cavities described below, the frequency of the excitation light can now be varied during the experiments by tuning ν_{ULE}. The tuning range can be extended on longer timescales where the locks of the doubling cavity locks can follow, either between different sequences or for long experimental timescales. Performing spectroscopy, it is important to verify whether the offset-locked infrared laser is blue-detuned or red-detuned from the ULE reference resonance, for examply by using a wavemeter. In the blue-detuned (red-detuned) case, increasing ν_{ULE} will increase (decrease) the frequency of the UV light. Because of the two doubling stages, it is essential to account for the factor of four entering in the two doubling stages. As a consequence, changing the modulation frequency will lead to a four times larger shift in the UV. More details of the laser system up to this stage can be found in Ref. [72].

3.5 Cavity-enhanced frequency doubling

In order to enhance the available output power in the UV, the experimental system was extended by two new bow-tie cavities where laser light is resonantly doubled using non-linear crystals. Both bow-tie cavities consist of four mirrors. Two of them are curved in order to focus the laser beam into the crystal where high intensities are required and provide a stable cavity mode. Once per roundtrip, the fundamental beam is propagating through a non-linear crystal where the response of the material to the laser field creates components oscillating at twice the frequency of the fundamental. If the *phase matching* condition is fulfilled, the frequency doubled waves created at different positions in the crystal are interfering constructively. Because this strongly increases the power of the total frequency doubled wave after the crystal, it is a necessary requirement. If frequency conversion is the dominating loss process in the cavity, this can lead to high conversion efficiencies. To increase the stability of the systems and because the crystal used for the second doubling stage is very sensitive to humidity and cracks at atmospheric conditions [398, 399], both

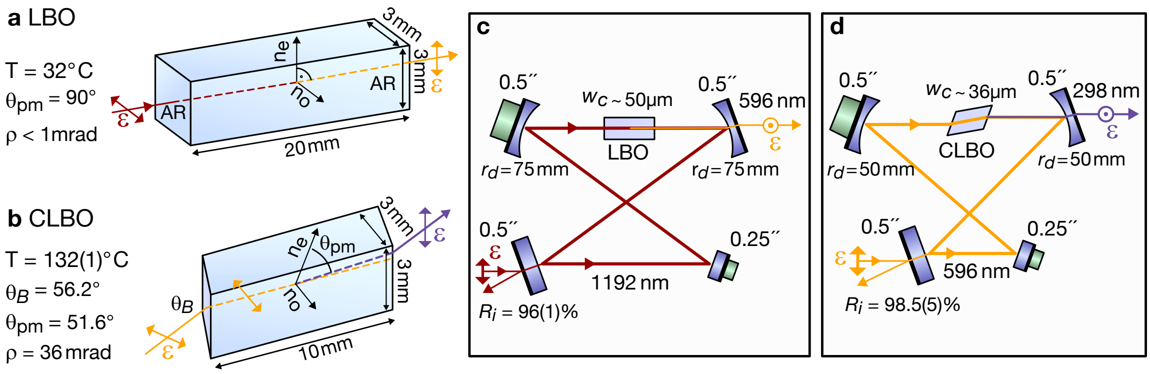

Figure 3.2: **Technical specifications of both frequency doubling systems.** (**a**) The LBO crystal used for the first doubling stage allows one to realize non-critical phase matching where $\theta_{\mathrm{pm}} = 90°$ with vanishing walk-off angle ρ. The phase matching condition requires temperature stabilization to $T = 32°$. Reflection losses are suppressed using antireflection coatings. (**b**) The CLBO crystal used for the second stage requires critical phase matching at an angle $\theta_{\mathrm{pm}} = 51.6°$ where the second harmonic slightly displaces from the fundamental due to the contributing walk-off angle ρ. Now, reflections are supressed using the Brewster angle θ_B. For both crystals, the light is polarized along the ordinary axis of the crystal which coincides with the plane of the optical layout. The crystal has to be stabilized to $T \approx 132°\mathrm{C}$. (**c**,**d**) The main difference between both doubling cavities is a different incoupling reflectivity R_i required for impedance matching as well as different radial curvatures r_d for the curved mirrors that focus the beam into the crystal. This results in different arm lengths and minimum beam waists w_c within the crystal. Both cavities have two piezos (green) to stabilize the cavity length to the incoming light field.

cavities are evacuated. By either reducing the pressure to around one millibar or flooding the cavities with argon, high stability has been achieved.

3.5.1 Phase matching

Phase matching requires to fix the phase relation between the fundamental and the frequency doubled wave at frequencies ω_f and $2\omega_f$ over the full length of the doubling crystal. This requires their refractive indices to fulfill $n_{\omega_f} = n_{2\omega_f}$. While this is difficult for normal dispersion relations, it can be realized using ordinary and extraordinary refractive indices of birefringent materials. This requires the polarization of the frequency doubled wave to be perpendicular relative to the fundamental wave. Generally, one distinguishes between *type-1* and *type-2* phase matching. Both frequency doubling systems belong to the first category where both photons combined in the doubling process have the same polarization. In both cases, the fundamental wave is polarized along the ordinary crystal axis which matches the horizontal plane parallel to the optical table.

The optimum way to obtain phase matching is so-called *non-critical phase matching* where the ordinary and the extraordinary crystal axes are perpendicular to the propagation direction in the crystal. Here, the phase matching angle between the optical axis and the extraordinary axis in the crystal is $\theta_{\mathrm{pm}} = 90°$. The wave vector of the fundamental wave and the second harmonic wave are parallel and the so-called *walk-off* vanishes. As a consequence, secondary waves created at different locations in the crystal correspond to the same spatial mode, which leads to a good beam profile after the cavity. This method is implemented for the frequency doubling of the high-power infrared laser at $1192\,\mathrm{nm}$ to yellow light at $596\,\mathrm{nm}$ using a lithium triborate (LBO) crystal. In order to avoid losses, the crystal surface is additionally anti-reflection (AR) coated for both wavelengths. The technical specifications of the system are summarized in Fig. 3.2 (**a**).

Often, non-critical phase matching cannot be achieved for the typically used nonlinear crystals. In these cases, varying the angle θ_pm from 90° provides additional tunability. For the second doubling stage from $595\,\mathrm{nm}$ to $298\,\mathrm{nm}$, this has been implemented to achieve phase matching with a cesium lithium borate (CLBO) crystal for $\theta_\mathrm{pm} = 51.6^\circ$. This time, because of the lower wavelengths where antireflection coatings might get damaged due to the high circulating power, the reflections at the crystal surfaces were supressed by coupling into the crystal at the Brewster angle. The technical specifications are summarized in Fig. 3.2 (**b**). In contrast to other possible crystals such as BBO [72] which is less sensitive to humidity, CLBO provides higher damage thresholds and a smaller walk-off angle which results in a better beam quality after doubling [400].

3.5.2 Impedance matching

An additional critical quantity is the reflection of the incoupling mirror, which determines the coupling efficiency into the cavity. On resonance, the light field $\boldsymbol{E}_\mathrm{ref}$ directly reflected at the incoupling mirror is out of phase with the field $\boldsymbol{E}_\mathrm{cav}$ which leaves cavity after propagating in it. As a consequence, both fields interfere destructively and the cavity transmission reaches a maximum. Maximum conversion efficiencies requires perfect destructive interference, which requires both field amplitudes to be equal. This condition is called *impedance matching*. The field $\boldsymbol{E}_\mathrm{cav}$ coupled out of the cavity depends on the loss per roundtrip, which is dominated by the frequency conversion. The conversion efficiency per roundtrip depends on the laser intensity. As a consequence, by adjusting the reflectivity of the incoming mirror according to the laser power, maximum conversion efficiencies can be obtained. A last parameter entering in the optimization is the beam waist ω_C of the fundamental beam within the crystal because it affects the laser intensity within the crystal. This determines the curvature of the two curved mirrors of the cavities and the length of the cavity arms. Optimizing all parameters in order to obtain maximum laser power is typically realized following the protocol by Boyd and Kleinman [401]. To increase the lifetime of the crystals and reduce thermal lensing, the beam waist in the crystal was chosen to be twice as large as the result obtained from Boyd Kleinman optimization [400].

3.5.3 Summary over both bow-tie cavities

In summary, all cavity mirrors besides the incoupling mirror are highly reflective for the fundamental beam, see Fig. 3.2 (**c,d**). While the reflectivity of the incoming mirror has to be optimized to guarantee impedance matching, the reflectivity of the remaining mirrors has to be as high as possible – or at least high enough such that frequency conversion is the dominant loss process in the cavity. Additionally, the outcoupling mirror is highly transmissive for the second harmonic to efficiently collect the frequency doubled light. Both cavities are locked to the frequency of the incoming light field using piezos. Here, two mirrors are mounted on two different piezo stacks which operate at different frequency bands to provide the feedback for the slow and the fast frequency components of the control circuit. The fast feedback is realized with the quarter inch mirror mounted on a small

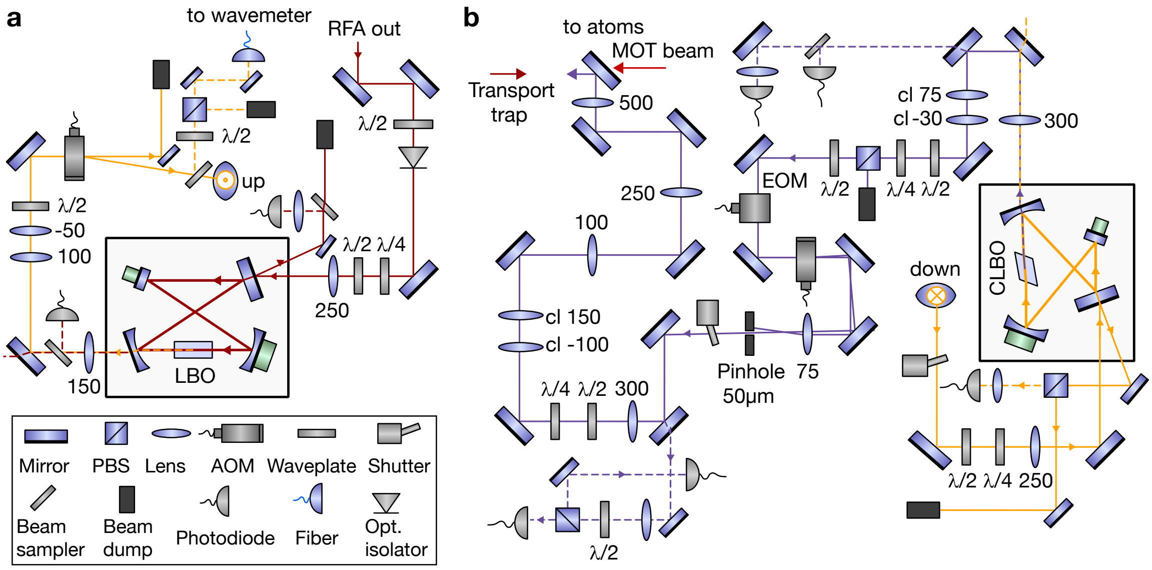

Figure 3.3: **Schematic of the UV laser system.** The two bow-tie cavities are placed on two vertically displaced breadboards. (**a**) On the lower breadboard, the output of the Raman fiber amplifier (RFA) is sent through an optical isolator and focused into the first doubling cavity after optimizing the polarization. The frequency doubled light is collimated, passes an AOM and is then sent upwards to the higher lying breadboard. A small amount of the light is coupled into a fiber and sent to a wavemeter. (**b**) The yellow laser beam is coupled into the second bow-tie cavity and frequency doubled to the ultraviolet. After collimation, the light passes an EOM which can be used for phase modulation and an AOM used for fast switching and intensity stabilization. Then, the beam profile is cleaned using a pinhole and then expanded using two telescopes. To maximize the light intensity in the plane of the atoms, one telescope is made of cylindrical lenses. Finally, the beam passes the last focusing lens, is combined with the beam path of the magneto-optical trap (MOT), and focused into the vacuum chamber. For both cavities, the reflection signal provides the error signal for Pound-Drever-Hall (PDH) locking and the transmission beam is used for monitoring. Further photodiodes for monitoring and stabilization are placed after the pinhole. The focal lenghts integrated in the main beam path are given in units of milimeters, cylindrical lenses (cl) are explicitly labelled. Low power fractions sampled from the main beams are denoted as dashed lines.

piezo stack which has a resonance frequency above 500 kilohertz. In combination with a special conical-shaped copper mounting system that is optimized for damping the vibrational motion, this enables feedback up to 50 kilohertz [400, 402]. The sideband of both Pound-Drever Hall locks is created by modulating the current of the diode laser at a single modulation frequency. Even if the modulation frequency is larger than the $\approx 5\,\mathrm{MHz}$ linewidth of the doubling cavities, the sideband amplitude after the first cavity is still large enough to efficiently lock the second cavity. The system implemented here is very similar to a similar system for potassium built in a neighboring laboratory described in [400]. All differences originate from the UV wavelength required for Rydberg excitation which is $286\,\mathrm{nm}$ potassium and $298\,\mathrm{nm}$ for rubidium. This changes the optical coatings, the phase matching angle and the Brewster angle θ_B relevant for the CLBO crystal.

3.6 The UV laser system

This paragraph discusses the laser system containing both doubling stages as presented in Fig. 3.3. After collimating the amplified laser light from the RFA, it is sent through an optical isolator to avoid back reflections into the amplifier. Subsequently, the polarization is optimized for the nonlinear crystal and focused into the cavity using a lens which provides sufficient spatial mode overlap with the cavity mode. The reflected light which is high if the cavity is not locked it sent to a beam dump. A small amount of the reflected light is sent to a photodiode and used to create the error signal for the PDH lock. At full power, the high conversion efficiency of 65% of the locked cavity provides $4\,\mathrm{W}$ of yellow laser light at a high-quality Gaussian beam shape. The cavity is typically continuously locked during our experiments. After the first doubling stage, the yellow beam is collimated, sent through an AOM and reflected upwards to another breadboard where the second cavity is placed. The incoupling procedure into the second cavity is identical to the first. Now, an additional shutter protects the cavity from continuous high-power operation to increase the lifetime of the CLBO crystal. Once the shutter opens, the control circuit recognizes the error signal when scanning over the cavity resonance and starts locking.

The locked second cavity provides output powers up to $1\,\mathrm{W}$, corresponding to an efficiency of 40%. The beam is again collimated after passing the outcoupling mirror. The output power and also the stability of the UV light strongly depends on the alignment of the cavity. Sometimes, the UV beam pointing was instable and drifted during the first few milliseconds after locking the cavity. By realigning the cavity, stable configurations have been found. Other experiments using high-power UV light at even lower wavelengths such as $286\,\mathrm{nm}$ [400] observed a degradation of their optical components, possibly due to the reaction with hydrocarbons. Over time, their transmission decreased due to the appearance of an opaque layer on the surface which can be removed by cleaning. In the presented UV system operating at $298\,\mathrm{nm}$, this has not been observed.

The finite walk-off angle for critical phase matching and also astigmatism originating from the Brewster configuration [400] requires beam shaping and mode cleaning of the UV beam after the second cavity. A first telescope made of cylindrical lenses provides a non-elliptic beam shape without astigmatism. After cleaning and optimizing the polarization, the beam is sent through an electro-optical modulator (EOM). The EOM enables to modulate sidebands on the UV light which will be used in chapter 7 to increase the coupling rates into Rydberg macrodimer states. Afterwards, the beam passes an AOM, which allows to switch the light on and off on a faster timescale (100 nanoseconds) compared to the shutter (milliseconds). The deflected light now passes a pinhole where about 20% of the AOM mode is damped in order to enhance the beam quality. In addition to mode cleaning, the pinhole simplifies the alignment of the UV beam with the atoms because the optical elements after the pinhole image the beam at the pinhole position to the position of the atoms. This implies that after changing the optical path before the pinhole (e.g. realigning the UV cavity or the UV AOM), a realignment of the pinhole will also coarse align the UV beam with the atoms. After collimating the beam diverging from the pinhole, two telescopes enlarge the beam size significantly to provide small beam waists at the location of the atomic cloud. One of both telescopes is implemented using cylindrical lenses to make the beam slightly elliptical. Because the atoms are confined in a two-dimensional plane, a smaller waist perpendicular to the atomic plane increases the UV intensity at the position of the atoms without introducing additional intensity gradients over the atomic cloud. Including all losses, the final UV beam focused into the vacuum chamber has a power of up to $350\,\mathrm{mW}$.

3.7 Calibration of the Rydberg system

Performing Rydberg experiments requires several preparation steps. First, the UV beam has to be properly aligned with the atomic cloud. In addition to maximum Rabi couplings, this provides stable intensities less susceptible to beam pointing fluctuations. Furthermore, the direction of the applied magnetic field, the polarization of the UV laser, the Rydberg resonance, and the Rabi frequency have to be calibrated.

3.7.1 Alignment of the UV laser

After propagating through a two inch lens with focal length $f = 500\,\mathrm{mm}$, the UV beam is combined with one of the MOT beams at a dicroic mirror and sent into the vacuum chamber. Here, in addition with one of the MOT beams, the UV shares its path with the dipole trap used for transporting the atoms from the MOT chamber into the experimental chamber where the atomic Mott insulators are created. Despite the long focusing path, the short wavelength enables a small Gaussian beam waist $w_0 \approx 20\,\mu\mathrm{m}$ at the focus position due to the long Rayleigh length $z_R = \frac{\pi w_0^2}{\lambda_{uv}}$ [403]. Such small beam waists require efficient alignment protocols.

Coarse alignment

The first step is to align the UV beam with the dipole trap beam at both sides of the vacuum chamber. An efficient way to further coarse align the UV beam is to excite atoms trapped in the dipole potential of one of the two lattice beams using *absorption imaging*. Because the dipole trap used for transport is aligned with the UV beam, it is beneficial to load the atoms into one of the lattice beams. By blocking the retroreflecing mirror, the atoms can furthermore redistribute within the elongated dipole trap after transport, which enlarges the spatial range of the alignment technique. Assuming a UV beam near-resonant with a Rydberg P-state transition, the excitation of antitrapped Rydberg excitations will lead to local loss signatures which can be used for beam alignment. In order to avoid redistribution of the atoms within the dipole trap after UV illumination, it is important to image directly after the Rydberg excitation pulse. The sligthly larger matrix elements for $nP_{3/2}$ Rydberg states makes them more suitable to find the resonance compared to states $nP_{1/2}$. The large length of the elongated dipole trap makes it easy to find the UV beam along the direction of the lattice beam. This effectively reduces the optimization to the direction perpendicular to the elongated dipole trap. Coarse alignment of the UV beam along this direction can be done manually. The method also works for coarse alignment of the focus position using a lens mounted on a z-translator. A typical absorption images of the UV beam is presented in Fig. 3.4 (**a**).

Fine alignment

Fine alignment can be performed using the piezo mirror and the fluorescence images from the microscope. Again, the atoms are used to image the UV beam. In order to have a image area, the atoms are prepared in a large dilute cloud within a two dimensional plane instead of a small Mott insulator. This can be done by reducing the evaporation time or actively shaking the lattice by modulating its intensity using an AOM. Detuning the UV laser from the Rydberg transition induces an AC Stark shift

$$\Delta_{\mathrm{AC}}(x) = \left(\sum_i \frac{\widetilde{\Omega}_i^2}{4\Delta_i} \right) e^{-\frac{2y^2}{w_0^2}}, \tag{3.6}$$

where $\widetilde{\Omega}_i$ is the Rabi coupling from the prepared ground state to the coupled Rydberg states and Δ_i their detuning. Furthermore, w_0 is the Gaussian beam waist and y is the distance from the waist position. Because $\widetilde{\Omega}_i^2(y) \propto I_0(y)$ is proportional to the light intensity, knowing the AC Stark shift can be used for beam alignment. A straight-forward way to probe the AC Stark shift is to perform narrow microwave Landau-Zeener ramps between the two hyperfine ground states $|2, m_F\rangle$ and $|1, m_F\rangle$ at low microwave powers. Here, because only one hyperfine ground state is coupled to the Rydberg state, the AC Stark shift induces a differential energy shift. The detunings should be chosen large enough such that losses are small over the timescale of the ramp but small enough such that the AC-Stark shift is still significant. Far away from the beam center, the microwave resonance frequency will not be affected. Approaching the center of the UV beam, the shift can be observed. In order to see the spatially dependent transfer, atoms in $F = 2$ are removed from the system using a push-out beam after the ramp. A typical image is prestented in Fig. 3.4 (**b**). Perpendicular to the UV propagation direction at both sides of the beam center one can find one position where the microwave field is resonant and transfer takes place. In the absence of a magnetic gradient, the large Rayleigh length guarantees linear and parallel resonance lines along the propagation direction, justifying the independence of Eq. 3.6 on x. The thickness of the lines can be tuned by the bandwidth of the ramp and the microwave power. If the UV beam is aligned in within the atomic plane, the position of the atomic cloud is centered relative to the resonance lines. Alignment perpendicular to the plane can be done by tuning the vertical degree of freedom of the piezo mirror. Moving the UV beam through the atomic plane at a fixed microwave frequency, the spatial distance between the resonance lines will increase and then decrease again. If the maximum of the UV beam lays in the atomic plane, their separation reaches a maximum. Due to the small size of the UV beam, the thermal stability of the laboratory during Rydberg experiments is essential.

3.7.2 Rabi frequency and beam waist

Spatially resolving the differential light shifts Eq. 3.6 is not only helpful for beam alignment. It can also be used to calibrate the Rydberg Rabi frequency and the beam waist. Here, the detunings Δ_i as well as the microwave transition frequency without UV light have to be carefully measured before. Averaging over all atoms along x and subtracting the total mean atom number of a dilute cloud provides the local atom number deviation $\Delta N_{\mathrm{av}}(y)$ at a specific microwave frequency. The two local microwave resonances corresponding to identical local UV intensities can then be obtained by fitting two resonance profiles to $\Delta N_{\mathrm{av}}(y)$, see the upper plot of Fig. 3.4 (**c**). Repeating the procedure for various microwave frequencies provides the Rabi frequency as well as the beam waist. To keep the formalism simple, it makes sense to use a configuration where only a single Resonance contributes, such as the coupling from $|2, -2\rangle$ to states $nP_{1/2}$ with $m_J = +1/2$ using purely σ^+ polarized light. This configuration also leads to a large signal because of the

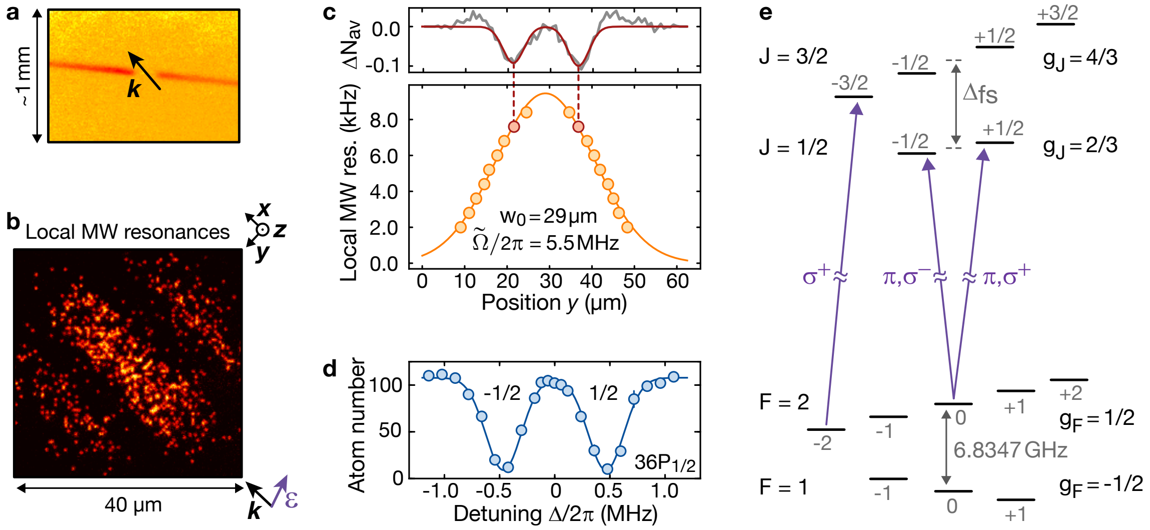

Figure 3.4: **Excitation of P-state Rydberg atoms and system calibration.** (**a**) Coarse alignment of the UV beam by Rydberg-exciting atoms in the elongated dipole potentials of the lattice beams. (**b**) Fine alignment by driving narrow microwave (MW) transitions between hyperfine ground states. Removing the transfered atoms from the system enables to spatially resolve their differential AC Stark shift induced by off-resonant coupling to a Rydberg resonance and therefore the UV beam. (**c**) The spatially resolved microwave spectroscopy also enables to measure the UV beam waist and the experimental Rabi frequencies. The upper plot shows the mean density of the images after averaging over x and subtracting the density of a dilute cloud without transfer (gray). Fitting two resonance profiles (red) provides the two local MW resonances at both sides of the beam, indicated as red data points in the lower plot. Combining the results for several MW frequencies allows to extract the beam parameters from fitting. (**d**) Spectroscopy of both Zeeman states of $36P_{1/2}$, starting from $|F = 2, m_F = 0\rangle$ and for $B = 1.0\,\mathrm{G}$. The detuning is measured relative to the center of the Zeeman split lines. (**e**) The relative coupling strengths between ground states $|F, m_F\rangle$ and Rydberg states nP_J with $J \in \{\frac{1}{2}, \frac{3}{2}\}$ and angular momentum projections m_J for different light polarizations can be calculated from Eq. 2.9. In a magnetic field, the spin projections split according to their Landé factor g_F and g_J.

large Clebsch-Gordan coefficients contributing to the coupling. An alternative method to calibrate the Rabi frequency which provides results consistent with the method presented here is to measure the differential Stark shift using Ramsey spectroscopy [72, 155, 222]. While this takes significantly more time, it can be applied also to lower Rabi couplings and is more precise because of the enhanced sensitivity of Ramsey spectroscopy. In agreement with the increase of the UV power sent into the vacuum chamber while keeping the beam parameters comparable to the old UV system, we find a factor of two larger Rabi frequencies compared to previous results.

3.7.3 Magnetic field amplitude and UV polarization

Rydberg experiments are usually performed with spin-polarized ground state atoms at finite magnetic fields $\boldsymbol{B}$ where the total angular momentum F and its projection m_F on the quantization axis is identical for all atoms. The different quantized angular momentum projections for the ground states $|F, m_F\rangle$ as well as the Rydberg states $|J, m_J\rangle$ are energetically separated by the Zeeman effect [5]. As long as experiments are performed in the perturbative regime where splittings are much smaller than the hyperfine splittings of the ground state or the fine-structure splitting of the Rydberg state, first-order Zeeman splittings can be computed via

$$\varDelta E_Z^{|g\rangle} = g_F m_F \mu_B B \quad \text{and} \quad \varDelta E_Z^{|r\rangle} = g_J m_J \mu_B B. \tag{3.7}$$

Here, g_F and g_J are the Landé factors of the ground state $|g\rangle$ and the Rydberg state $|r\rangle$, see also Fig. 3.4 (**e**). Furthermore, $\mu_B = h \times 1.3996 \frac{\mathrm{MHz}}{\mathrm{G}}$ is the Bohr magneton [5]. The Zeeman splitting can be used to measure the magnetic field at the position of the atoms. The splittings can be measured either in the ground state using microwave transitions or directly from the Rydberg spectroscopies.

For many experiments, also the direction of the magnetic field is essential. Because of the Clebsch-Gordan coefficients entering in the angular momentum coupling, the coupling strength between a ground state atom $|F, m_F\rangle = \sum_{F, m_F} \mathcal{C}^{1/2\ F\ 3/2}_{m_J\, m_F\, m_I} |m_J m_I\rangle$ and a Rydberg state $|nPJm_{J'}\rangle$ depends on the orientation of the light polarization relative to the projection of F, see also Eq. 2.9. Atomic transitions with $\varDelta m_J = m_{J'} - m_J = \pm 1$ can only be coupled with $\sigma^{\pm}$ polarized light while transitions with $\varDelta m_J = 0$ are only possible for π polarization. Exemplary transitions are presented in Fig. 3.4 (**e**) for initial states $|2, -2\rangle = |-\frac{1}{2}\rangle_J |-\frac{3}{2}\rangle_I$ and $|2, 0\rangle = \frac{1}{\sqrt{2}}(|-\frac{1}{2}\rangle_J |\frac{1}{2}\rangle_I + |\frac{1}{2}\rangle_J |-\frac{1}{2}\rangle_I)$. Expanding the light polarization into the spherical basis with the $z-$axis parallel to $\boldsymbol{B}$ and using that light is a transversal wave, one finds that pure σ^+ polarization or pure σ^- polarization is only possible for $\boldsymbol{B} \parallel \boldsymbol{k}$. Furthermore, π polarization requires $\boldsymbol{B} \perp \boldsymbol{k}$ [5].

In order to compensate for ambient fields, the experimental apparatus has offset coils to adjust the magnetic field in the atomic plane as well as perpendicular to the atomic plane. The offset coils are mounted such that independent tuning of the magnetic field up to $\approx 1\,(1.5)\,\mathrm{G}$ parallel (perpendicular) to $\boldsymbol{k}$ is possible for the implemented current supplies. The system compensating for the *transverse* field perpendicular to $\boldsymbol{k}$ consists of two coils, providing a homogeneous field at the location of the atoms. The *longitudinal* field parallel to $\boldsymbol{k}$ is compensated using a single coil where the offset field also adds a gradient. The magnetic field perpendicular to the atomic plane can be tuned up to 25 G using the vertical compensation coil. Using additionally the gradient coil which realizes the magnetic field gradient required for slicing enables fields up to 60 G perpendicular to the atomic plane. Starting from zero magnetic field as for example during fluorescence imaging and changing the current of a specific offset coil realizes a magnetic field which points in one of the three specified directions. After a careful calibration of the coils, arbitrary magnetic field configurations can be realized by superposition. In agreement with the discussion in the previous paragraph, the available Rydberg transitions depend on the relative orientation of $\boldsymbol{k}$ and $\boldsymbol{B}$. The polarization of the excitation light can be further optimized by supressing certain transitions in the Rydberg spectroscopies.

3.7.4 Rydberg spectroscopy

In the experimental setup, Rydberg excitation spectra are aquired by measuring atom loss for various laser frequencies. Because Rydberg atoms are antitrapped in the optical lattice and furthermore Rydberg atoms are motionally excited due to the momentum of the UV photon, the probability of retrapping is low. Furthermore, a significant fraction of excited

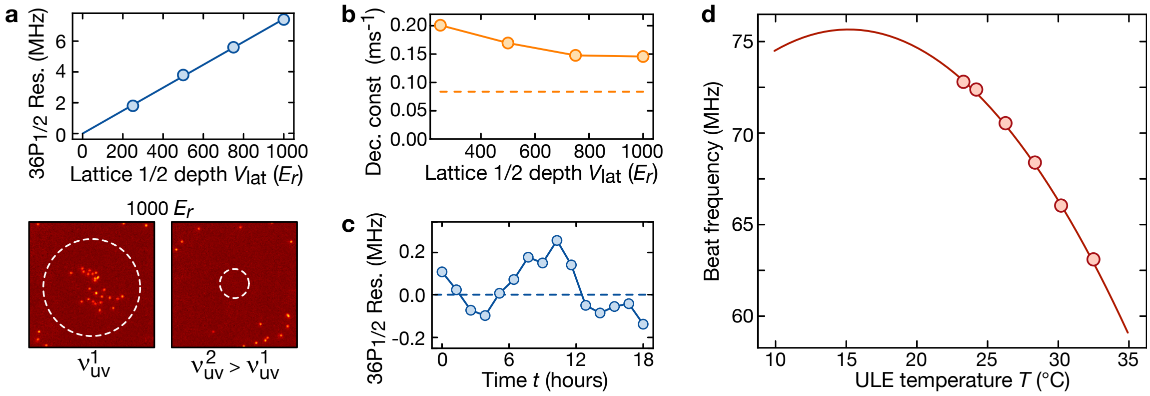

Figure 3.5: **Further characterization of the Rydberg system** (**a**) For deeper lattice depth, decreasing (increasing) the energy of the trapped ground state (antitrapped Rydberg state) shifts the Rydberg resonance towards higher frequencies. A Rydberg spectroscopy at deep lattices in a dilute cloud also reveals that the Rydberg resonance (white dashed circles) moves to higher UV frequencies ν_uv towards the trap center. On the ring where the UV laser can on-resonantly excite the atoms, the observed atom number vanishes. (**b**) The measured Rydberg-dressed lifetime for $\widetilde{\Omega} < \Delta$ of atoms in a dilute cloud does not increase with lattice depth, indicating that photoionization does not occur. The blue dashed line represents the calculated Rydberg-dressed lifetime of a single atom. (**c**) Exemplary time trace of the Rydberg resonance over several hours. The observed drifts of up to several hundreds of kilohertz were possibly connected to surface charges at the vacuum window, temperature fluctuations of the ULE cavity, or drifts of the lattice beams. (**d**) Beating a laser locked to the ULE cavity with a second narrow-lindwidth reference and changing the temperature of the ULE cavity suggests a vanishing thermal expansion for a temperature of $T = 15^\circ\mathrm{C}$.

Rydberg atoms will decay to other Rydberg states because of black-body transitions before decaying back to the ground state. In order to find the Rydberg resonance, the *ARC* package [55] provides a good reference. First, a broad spectroscopy is performed starting from a dense cloud for long illumination times of a few hundreds of milliseconds at full power. The dense cloud additionally broadens the transition due to density-dependent losses. Under these configurations, the Rydberg transition is usually several hundreds of megahertz broad, see also the central loss resonance in Fig. 4.4 (**a**).

At very lower powers where density-dependent loss signatures and power broadening are reduced, the linewidth of the Rydberg spectroscopy can reach values of about one hundred kilohertz [72]. An exemplary spectroscopic dataset is presented in Fig. 3.4 (**d**). In addition to a decreased UV power, such narrow linewidths require to optimize the locking parameters of the infrared ULE cavity lock. The measured linewidth is still limited by the laser [72] and larger than the natural linewidth which is on the order of only a few kilohertz. As long as the Rabi frequency $\widetilde{\Omega}$ is larger than the measured linewidth, one will still observe Rabi oscillations.

3.7.5 Rydberg resonance drifts

For most measurements, it is required to continuously track the Rydberg resonance to verify the laser detunings over the timescale of the experiment. An exemplary measurement of a P-state Rydberg resonance over several hours which shows typical resonance drifts is shown in Fig. 3.4 (**c**). We observe drifts on the order of up to a few hundreds of kilohertz. The uncertainty of the Rydberg resonance was contributing the largest in the calibration of the detunings at which the vibrational resonances of macrodimer binding potentials presented later in this dissertation were observed.

One possible reason are fluctuating charges on the view port which is only five millimeter below the atomic plane [71]. Because the experimental system does not have options to control the electric field, future experiments might benefit from illuminating the vacuum window with an UV LED to remove the charges in the beginning of the experimental sequence [137–139]. Also drifts of the ULE reference might contribute, in particular because the ULE cavity cannot be used at the temperature where the thermal expansion coefficient vanishes.

Drifts of the ULE reference and temperature dependence

Cavities made of ULE glass are attractive frequency references for high-precision spectroscopies because of their low temperature expansion coefficient. The expansion coefficient typically has a quadratic dependence on temperature and vanishes at the zero expansion point where the highest stability can be achieved. Because of fluctuations in the manufacturing process, the zero expansion temperature has to be measured for each cavity individually. Here, the zero expansion point was obtained by beating a laser operating at $770\,\mathrm{nm}$ locked to the same ULE cavity with a second narrow-linewidth laser provided by a nearby laboratory [400]. The temperature stabilization set point of the ULE cavity system was changed once per day and the observed shift of the beat frequency was recorded, see Fig. 3.5 (**d**). By fitting a quadratic function, the zero expansion point was found to be $T \approx 15°\mathrm{C}$. Because our current stabilization system does only allow to heat the cavity, temperature stabilization below room temperature is currently not possible. At the chosen temperature around $T \approx 30°\mathrm{C}$, the cavity resonances shift as $\varDelta\nu \approx -2\frac{\mathrm{MHz}}{°C}\varDelta T$. In the UV where another factor of four enters from frequency quadrupling, a temperature drift of $0.012°\mathrm{C}$ already induces a frequency shift of $100\,$kilohertz. This demonstrates the significance of keeping the power sent to the ULE cavity stable and low. The high finesse $\mathcal{F} = 10800$ [72] of the cavity leads to several Watts of circulating power within the cavity for only tens of microwatt coupled into the cavity. In addition to short term drifts, long-term drifts of the ULE cavity occur due to the degradation of the material [124]. As a consequence, the detuning between a given ULE resonance line and a specific Rydberg resonance experiences a deterministic drift which is on the order of a megahertz per year.

Lattice-depth dependent Rydberg resonances

The Rydberg transition frequency also depends on the intensity of the lattice light. The electronic ground state is trapped by the lattice potential in the light field red detuned to the atomic transitions. In contrast, in the Rydberg state, the Rydberg electron experiences a repulsive ponderomotive force [124, 404]. Here, the assumption of a quasi-free electron interacting with the oscillating light field leads to a good agreement with experimental results [405, 406] .

This was studied by measuring the shift of the Rydberg resonance for various depths of both in-plane lattices 1 and 2 while the vertical lattice 3 depth was kept identical. Here, the ground state energy lowers by $2 \times 2.0\,\mathrm{kHz}\frac{V_{\mathrm{lat}}}{E_r}$ while the energy of the Rydberg state is expected to increase. Changing the intensity of both lattice beams reveals an experimental shift of the $36P_{1/2}$ resonance of $\varDelta\nu = 7.4\,\mathrm{kHz}\frac{V_\mathrm{lat}}{E_r}$, see Fig. 3.5 (**a**). This confirms the repulsive potential because the observed differential light shift is larger than the shift of the ground state atom. In an optical lattice, a comparison with the theoretical expectation would require to spatially average the Rydberg wave function over the periodic potential [407, 408]. This introduces the relative length scale between the Rydberg wave function and the lattice constant as a parameter into the trapping potentials and results in different lattice potentials for different Rydberg states [409].

For deep lattices, the corresponding differential light shift also leads to spatially dependent Rydberg resonances, see Fig. 3.5 (**a**). Performing Rydberg spectroscopy in fluorescence starting from a large dilute cloud, one can observe how that resonance moves from the edge towards the center of the lattice beam for increased UV frequencies. This is similar as for the spatially resolved microwave spectroscopy used for alignment. Again, a differential light shift is used to resolve the intensity profile of a laser. However, in this case it is the UV beam showing the intensity profile of the lattice beam.

3.7.6 Lattice-induced losses and photoionization

Some Rydberg experiments performed in this dissertation benefit from deep lattice potentials where the initial motional wave function introduced in Eq. 3.2 has a small spatial extension. In this context, it is important to show the insignificance of lattice-intensity dependent loss mechanisms such as photoionization [406, 410] which has been observed in optical tweezer systems where intensities are high [296]. In order to estimate the contribution in our system, the ground state was coupled to the Rydberg state in a dressed configuration with $\widetilde{\varOmega}/(2\pi) = 2.8(1)\,\mathrm{MHz}$ and a detuning $\varDelta/(2\pi) = 24\,\mathrm{MHz}$. In order to suppress density-dependent losses, the initial state was again a dilute cloud at low density. Because atom loss coefficients are significantly higher at high densities, this configuration was essential for the experiment, see also appendix C.1. The observed atom loss coefficient at different lattice depths obtained from independent exponential fits are presented in Fig. 3.5 (**b**). At each lattice depth, the UV laser was adjusted according to the drift of the Rydberg resonance. The observations do not show an increase of the atom-loss rate with the lattice depth. Assuming that the atom loss is dominated by black-body transitions and ground state decay, the theoretical atom loss rate can be estimated via $\frac{\widetilde{\varOmega}^2}{4\varDelta^2}\varGamma_{|r\rangle}$. Here, $\frac{\widetilde{\varOmega}^2}{4\varDelta^2}$ is the Rydberg fraction of the dressed ground state and $\varGamma_{|r\rangle} = \varGamma_\mathrm{bb} + \varGamma_\mathrm{dec}$ is the decay rate of the Rydberg atom, see also section 2.2.5. The observed atom loss was slightly larger than the theoretical expectation. This might be due to the presence of nearby atoms in the initial dilute cloud, which leave the system together due to collective loss signatures [155].

Chapter 4

Rydberg macrodimers

The previous chapters focused on the properties of Rydberg atoms, their relevance in current research, and the experimental apparatus. After providing this background, the discussion now shifts towards Rydberg macrodimers, which are the main topic of the thesis. The first part of the chapter discusses the symmetries of the electronic macrodimer states and the vibrational and rotational structure. Following the publication [411], the two-photon excitation scheme and the experimentally observed vibrational spectrum is presented. The interpretation of the observed spectra was worked out in close discussion with Jun Rui and Johannes Zeiher. In the end of the chapter, the contribution of the nuclear motion to the excitation process and the loss of the excited molecules is discussed.

4.1 Properties of macrodimers

Rydberg macrodimers are Rydberg atom pairs electrostatically bound by their long-ranged interaction potentials [67]. Following the increase of the Rydberg interaction coefficients C_3 and C_6 [249], their size increases with principal quantum number [412]. Their macroscopic bond length easily reaches the micrometer regime, which makes them the largest existing diatomic molecules. As their size becomes larger than typical optical wavelengths on the order a few hundred nanometers, one can spatially resolve the individual atoms bound within the molecule by optical methods. This allows studying their quantum state at an unprecedented level of control not present for other molecules [413]. They feature quantized vibrational states which can be spectroscopically resolved and theoretically calculated based on ab-initio calculations [411]. The depth of their binding potentials as well as their vibrational energies are six orders of magnitude lower than for ”conventional” ground-state diatomic molecules. The total amount of quantized vibrational levels hosted by their binding potential is similar in both cases, see also Fig. 2.5. Related to their large size, their small rotational constant is well below a kilohertz and the rotational splitting cannot be resolved on a timescale of a macrodimer lifetime. Because of the symmetry of the interatomic interaction, their electronic states are specified using molecular quantum numbers. The following sections contain a more thorough discussion of these properties.

4.1.1 Macrodimers & molecular symmetries

Molecular quantum states are different from bare atomic states for several reasons. The additional motional degrees of freedom — vibration and rotation — increase the complexity. Due to the interatomic interaction introduced in Eq. 2.19, the non-interacting atomic pair states are not eigenstates anymore and the electronic molecular states consist of a superposition of non-interacting atomic pair states. Adding the interaction Hamiltonian $\hat{H}_{\text{int}}(R)$ to a system of two isolated atoms furthermore restricts the symmetry of the total system [50, 177]. Now, the total Hamiltonian is not rotationally invariant and the total

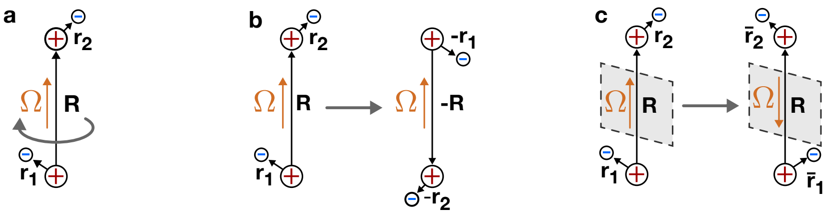

Figure 4.1: **Macrodimers & molecular symmetries.** (**a**) Because the electrostatic interaction Hamiltonian Eq. 2.19 is symmetric with respect to rotations around the interatomic axis, the total electronic angular momentum projection Ω is conserved. (**b**) Inversion symmetry allows one to label the interaction potentials as gerade (g) and ungerade (u). The projection Ω remains unaffected under inversion. (**c**) The interaction is symmetric with respect to reflections through any plane containing the interatomic axis. Here, Ω undergoes a sign flip. There are two additional symmetries which are not shown because they are not relevant to label the molecular quantum states $\Omega^{\pm}_{g/u}$.

electronic angular momentum is not conserved. However, there are other symmetries that provide conserved quantities. For homonuclear diatomic molecules such as the macrodimers described here, the system is linear and has an inversion center. The set of relevant symmetry operations which commute with the total Hamiltonian of the system can be summarized by the *point group* $D_{\infty h}$ [4, 414, 415]. The terminology comes from the fact that all symmetry operations leave the position of the center of symmetry unchanged. In addition to the identity operation, the point group contains *1)* rotations around the molecular axis which acts as an internal quantization axis. As a result, the projection $\Omega = m_{J_1} + m_{J_2}$ of the angular momentum on the molecular axis is conserved. Then, $D_{\infty h}$ contains *2)* inversion and *3)* reflection symmetry with respect to any plane which contains the molecular axis. Both are further discussed in the sections 4.1.3 and 4.1.4. These three symmetries provide the quantum numbers to label macrodimer states, they are illustrated in Fig. 4.1. Finally, $D_{\infty h}$ also contains *4)* rotations at an angle of 180° about any axis perpendicular to the interatomic axis which contains the symmetry center and *5)* so-called improper rotations or rotation-reflections which are a combination of a rotation and a reflection. A complete description of the point group $D_{\infty h}$ requires to list all symmetry operations *1)-5)* since none of them can be represented by using combinations of the others.

For heteronuclear diatomic molecules or molecules containing more than two atoms, one finds other point groups and as a consequence different sets of conserved quantities. In particular for molecules that are more complex than macrodimers where the Schrödinger equation cannot be solved, group theory provides powerful tools to the molecular states by their symmetry properties.

Hund's coupling case (c)

Angular momentum coupling for molecules is complex because all angular momenta of the individual atoms as well as the rotational angular momenta contribute. Dependent on the strength of their couplings and the strength of the molecular binding, different angular momentum projections can be assumed to be conserved. This leads to different idealized cases, known as *Hund's cases* [4]. Macrodimers are characterized using Hund's case (c), where the binding potentials are labeled as $\Omega^{\pm}_{g/u}$ and Ω is conserved. The subindex labels gerade (g) and ungerade (u) inversion states, the superindex labels the reflection symmetry. These are weakly bound molecules where the binding energy is lower than the $LS-$coupling and the coupling of the rotational angular momentum can be neglected. For deeply bound molecules, also other projections like $\Lambda = m_{L_1} + m_{L_2}$ and $\Sigma = m_{S_1} + m_{S_2}$ can be assumed to be conserved and other Hund's cases apply.

4.1.2 Macrodimer binding potentials

At large interatomic distances, where Rydberg interactions are much smaller than the energetic spacing between neighboring Rydberg states, the interaction potentials are described by their perturbative van der Waals interactions, see section 2.3.2. Rydberg states are energetically closely packed in the energy region below the ionization continuum and furthermore interact via large van der Waals coefficients. As a consequence, crossings between pair potentials can occur at experimentally relevant distances. In this regime where a perturbative treatment of the interactions fails, the pair potentials can be calculated by diagonalizing the total electronic Hamiltonian $\hat{H}_e$ via

$$\hat{H}_e|\psi_{\mathrm{Mol}}(R)\rangle = V(R)|\psi_{\mathrm{Mol}}(R)\rangle. \tag{4.1}$$

The Hamiltonian $\hat{H}_e = \hat{H}_0 + \hat{H}_{\mathrm{int}}$ consists of the Hamiltonian $\hat{H}_0$ of both isolated atoms as well as the ineraction Hamiltonian $\hat{H}_{\mathrm{int}}$, see Eq. 2.19. The distance-dependent eigenvalues $V(R)$ represent the Born-Oppenheimer potentials for the internuclear motion. The potentials $V(R)$ are binding potentials for macrodimer states if they have a spatial minimum that can host vibrational eigenstates.

The electronic eigenstates

$$|\psi_{\mathrm{Mol}}\rangle = \sum_{ij} c_{ij}(R)|r_i r_j\rangle \tag{4.2}$$

consist of a superposition of non-interacting atomic pair states $|r_i r_j\rangle$ mixed by $\hat{H}_{\mathrm{int}}$. For macrodimers, $|r_i\rangle$ and $|r_j\rangle$ are the single-atom Rydberg states populated by the first and the second atom. Because of the small hyperfine coupling of Rydberg states, both are expressed in their fine-structure basis. Later in section 5.2.3, the effects of an observed hyperfine interaction can still be described as a perturbation using the states obtained from Eq 4.1. They can be further specified by $|r_i\rangle = |n_i L_i J_i m_{J_i}\rangle$, with n_i the principal quantum number, L_i the orbital angular momentum, J_i the total angular momentum, and m_{J_i} its projection on the molecular axis. The expansion coefficients $c_{ij}(R)$ depend on the interatomic distance R because the interaction Hamiltonian $\hat{H}_{\mathrm{int}}(R)$ mixing the atomic quantum states depends on R as well, see Eq. 2.19.

At even shorter distances, the potentials enters the so-called *Spaghetti* regime which is dominated by a large number of steep crossing pair potentials [55, 220] where many asymptotic pair states are mixed.

A paradigmatic example

A typical landscape of Rydberg interaction potentials is illustrated in Fig. 4.2 for states close to the asymptotic energy of two isolated Rydberg atoms $|35P_{1/2}35P_{1/2}\rangle$. Because of the symmetry of the interaction Hamiltonian, one finds sets of decoupled potential curves which belong to certain molecular numbers $|\Omega|^{\pm}_{g/u}$. One can identify the pair potential

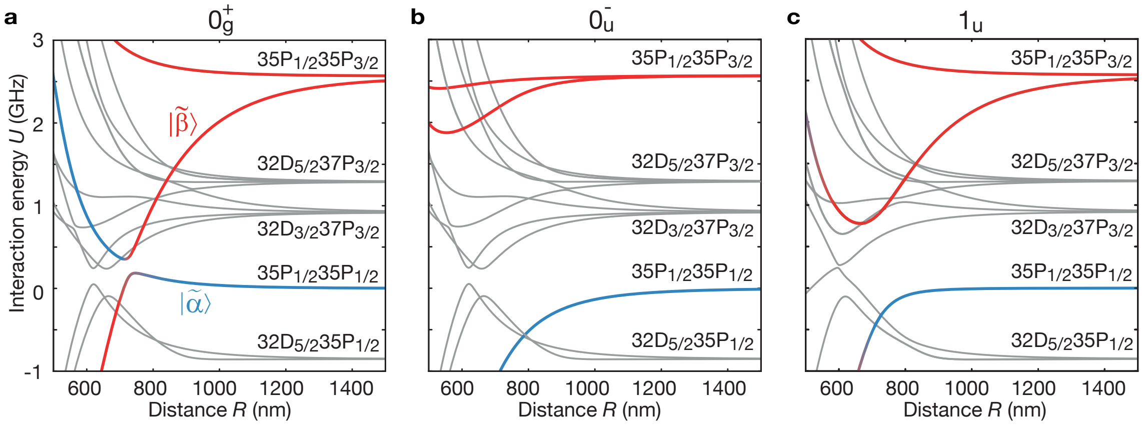

Figure 4.2: **Macrodimer binding potentials in the vicinity of the $35P_{1/2}$ resonance.** Due to the symmetry of the interaction Hamiltonian, the pair potentials decouple into potentials 0_g^+ (**a**), 0_u^- (**b**) and 1_u (**c**). At asymptotically large interatomic distances, all pair state energies equal the added energies of the non-interacting atomic states. Decreasing the distance, the pair potentials shift from their asymptotic energy due to van der Waals interactions. At closer distances, one can find several molecular binding potentials which can host vibrational states. The blue (red) color illustrates the overlap with the fine-structure pair states $|35P_{1/2}35P_{1/2}\rangle$ ($|35P_{1/2}35P_{3/2}\rangle$) which can be optically excited with the laser used in this dissertation. The gray pair potentials cannot be optically excited because of dipole selection rules. Figure adapted from Ref. [411].

$|\widetilde{\alpha}\rangle = \sum_{ij} c_{ij}(R)|r_i r_j\rangle$ within the 0_g^+ pair potential manifold which is asymptotically connected to $|35P_{1/2}35P_{1/2}\rangle$. Decreasing the distance R, it bends towards larger energies due to the van der Waals repulsion from another energetically lower-lying pair potential. With increasing energy shift, additional pair states $|r_i r_j\rangle$ contribute to $|\widetilde{\alpha}\rangle$ with $R-$dependent amplitudes $c_{ij}(R)$. Similarly, the state $|\widetilde{\beta}\rangle$ asymptotically connected to the energetically higher-lying state $|35P_{1/2}35P_{1/2}\rangle$ bends downward. At a specific distance of $R \approx 720\,\mathrm{nm}$ where both potentials cross, the finite coupling between the potentials forms an avoided crossing. If the coupling term between the crossing potential curves exceeds the vibrational energy in the upper well of the forming avoided crossing, the formed binding potential can host vibrational macrodimer states [411]. This is typically the case if the coupling between the crossing potentials is mediated by the strong dipole-dipole interaction term Eq 2.25 dominating in the multipole expansion of Eq. 2.19. It holds true for the exemplary potential formed by the crossing potentials $|\widetilde{\alpha}\rangle$ and $|\widetilde{\beta}\rangle$. Here, even if the asymptotic states are not coupled by the dipole-dipole interaction term, states admixed by the van der Waals interactions mediate a significant dipole-dipole coupling at the relevant distance. This gives rise to a gap large enough to support an adiabatic vibrational motion in the upper binding potential while diabatic transition rates to the lower pair potential curve contributing to the avoided crossing are low.

Scaling with principal quantum number

Neglecting the influence of Förster resonances, properties of macrodimer potentials at different principal quantum numbers can be estimated using known scaling laws. Increasing $n^\star$, Rydberg interactions increase and the energy spacing between asymptotic pair states decreases. As a result, crossings occur at larger distances where the pair potentials are less steep and binding potentials more shallow [248, 412]. As a result, the bond length increases as $R_\nu \propto (n^\star)^{8/3}$. The vibrational energy decreases as $\omega_{\text{vib}} \propto (n^\star)^{-3}$, see also section 4.1.5. Consistent with the scaling of the energy spacing between neighboring single-atom Rydberg states, the interaction shifts U^ν of the vibrational states ν relative to the asymptotic pair state energies (or, equivalently, the depth of the macrodimer potential wells) decrease as $(n^\star)^{-3}$.

4.1.3 Inversion symmetry

All homonuclear diatomic molecules are symmetric with respect to inversion, see Fig. 4.1 (**b**). Here, all electronic coordinates $\{\boldsymbol{r}_i\}$ and nuclear coordinates $\{\boldsymbol{R}_i\}$ are inverted at the inversion center and eigenstates can be labeled as gerade (ungerade) with $p = +1\,(-1)$ [50, 412]. For macrodimers, the inversion symmetry ($\boldsymbol{r}_i \to -\boldsymbol{r}_i, \boldsymbol{R} \to -\boldsymbol{R}$), with $\boldsymbol{R} = \boldsymbol{R}_1 - \boldsymbol{R}_2$ the distance vector between both nuclei, fixes the relation between the coefficients c_{ij} and c_{ji} in the expansion Eq. 4.2. Using the symmetry properties of spherical harmonics, a symmetrized pair state for $p = \pm 1$ writes

$$|r_i r_j; \Omega^{\pm}_{g/u}\rangle = |r_i r_j\rangle - p(-1)^{L_1+L_2}|r_j r_i\rangle. \tag{4.3}$$

Now, one can further specify the states admixed into the previously introduced 0_g^+ pair potential $|\widetilde{\alpha}\rangle$. Using the conventions $|e\rangle = |35P_{1/2}\rangle$ and $\uparrow (\downarrow) = +1/2\,(-1/2)$ for m_J, the symmetrized pair state $|e\uparrow e\downarrow; 0_g^+\rangle$ which contributes most is

$$|e\uparrow e\downarrow; 0_g^+\rangle = \frac{1}{\sqrt{2}}\left(|e\uparrow e\downarrow\rangle - |e\downarrow e\uparrow\rangle\right). \tag{4.4}$$

Inversion symmetry should not be confused with permutation [50]. Only approximating the interaction Hamiltonian by the dipole-dipole interaction term where the spatial separation of the Rydberg electrons from their nuclei is neglected, the system is symmetric with respect to a permutation of the dipoles ($\boldsymbol{R} \to -\boldsymbol{R}$).

4.1.4 Reflection symmetry

Another symmetry of homonuclear as well as heteronuclear diatomic molecules is the reflection through planes containing the interatomic axis [50, 412], see Fig. 4.1 (**c**). Acting with the reflection operator on a molecular state introduces a multiplication factor $d = \pm 1$. The corresponding symmetrized asymptotic pair states are given by

$$|r_i r_j; \Omega^{\pm}_{g/u}\rangle = |r_i r_j\rangle + d(-1)^{L_1+L_2+m_{J_1}+m_{J_2}-J_1-J_2}|\bar{r}_i \bar{r}_j\rangle. \tag{4.5}$$

The reflection operator switches sign of the angular momentum projections $m_{J_i} \to -m_{J_i}$ and $m_{J_j} \to -m_{J_j}$ but leaves all other quantum numbers invariant. Hence, states $|\bar{r}_i\rangle = |n_i L_i J_i {-} m_{J_i}\rangle$ and $|\bar{r}_j\rangle = |n_j L_j J_j {-} m_{J_j}\rangle$ differ from $|r_i\rangle$ and $|r_j\rangle$ in their angular momentum projection on the molecular axis. Usually, the reflection symmetry is only specified for states $|\Omega| = 0$ because for higher Ω, there is always a degenerate doublet of states with the same absolute value of Omega, but opposite signs. In this case, the reflection operator couples the two degenerate pair potentials $\Omega = \pm|\Omega|$.

The pair potential $|\widetilde{\beta}\rangle$ is asymptotically connected to the pair state $|35P_{1/2}35P_{3/2}\rangle$. Defining $|e'\rangle = |35P_{3/2}\rangle$, the most dominant state symmetrized with respect to inversion and reflection is

$$|e\uparrow e'\downarrow; 0_g^+\rangle = \frac{1}{2}\left(|e\uparrow e'\downarrow\rangle - |e'\downarrow e\uparrow\rangle + |e\downarrow e'\uparrow\rangle - |e'\uparrow e\downarrow\rangle\right). \tag{4.6}$$

Here, the interatomic axis was chosen as the quantization axis because Ω is conserved. These decompositions into electronic states become more important in the following chapter.

4.1.5 Vibrational states

The vibrational states $\Phi_\nu(R)$ are obtained from solving the time-independent Schrödinger equation in the relative coordinate R using the calculated binding potentials $V(R)$, see Fig. 4.3. This assumes the Born-Oppenheimer approximation where the electronic pair state decomposition adiabatically adapts to the nuclear motion. Because the bond lengths R_ν are typically much larger than the width σ_ν of the vibrational wave function, a one-dimensional approach provides an accurate description. The resulting differential equation

$$\left(\frac{-\hbar^2}{2\mu_{\mathrm{Rb}}}\frac{\partial^2}{\partial R^2} + V(R)\right)\Phi_\nu(R) = E_\nu \Phi_\nu(R) \tag{4.7}$$

was solved using a Numerov algorithm [416, 417]. For all studied macrodimer potentials, the vibrational states were almost equidistant in energy and very well approximated by a harmonic oscillator. Deviations mainly arise due to non-adiabatic vibrational motion where the Born-Oppenheimer treatment is not valid, see chapter 6. For the studied macrodimer potentials within principal quantum numbers $n \in [31, 42]$, we found typical vibrational spacings $\omega_{\mathrm{vib}} \in 2\pi \times [2.0, 6.0]\,\mathrm{MHz}$, corresponding to a temperature of a few hundred µK. Vibrational frequencies at higher principal quantum numbers can be estimated using $\omega_{\mathrm{vib}} \propto (n^\star)^{-3}$, see section 4.1.2.

4.1.6 Rotational states

The rotational energy is given by the angular momentum in the interatomic motion. The rotational states $|\ell\rangle$ are obtained from the rigid rotor Hamiltonian, the energies are $E_\ell = hB_r\ell(\ell+1)$ [418]. For macrodimers, the rotational constant $B_r = \hbar^2/(2\mu R_\nu)$ is typically well below a kilohertz. This is less than the expected radiative decay rate on the order of a few tens of kilohertz. Therefore, at least for the rotational quantum numbers involved, rotation cannot be resolved and only broadens the linewidth of the measured vibrational resonances.

This has implications for photoassociation experiments because the electronic and vibrational quantum states can be studied in a regime where the interatomic orientation follows the classical intuition. Before photoassociation, atom pairs have a certain orientation in the sample. Using rotational states, this initial spatial arrangement requires to superimpose rotational states according to their overlap coefficients f_ℓ. The rotational states are given by spherical harmonics [418]. The relevant rotational states are effectively degenerate. As a consequence, a molecular Rabi frequency $\widetilde{\Omega}_\nu$ exciting macrodimers will split into coupling rates $\widetilde{\Omega}_\nu^\ell = f_\ell \widetilde{\Omega}_\nu$. Hence, all rotational states will be populated according to their initial expansion coefficient f_ℓ and the orientation of the angular wave function

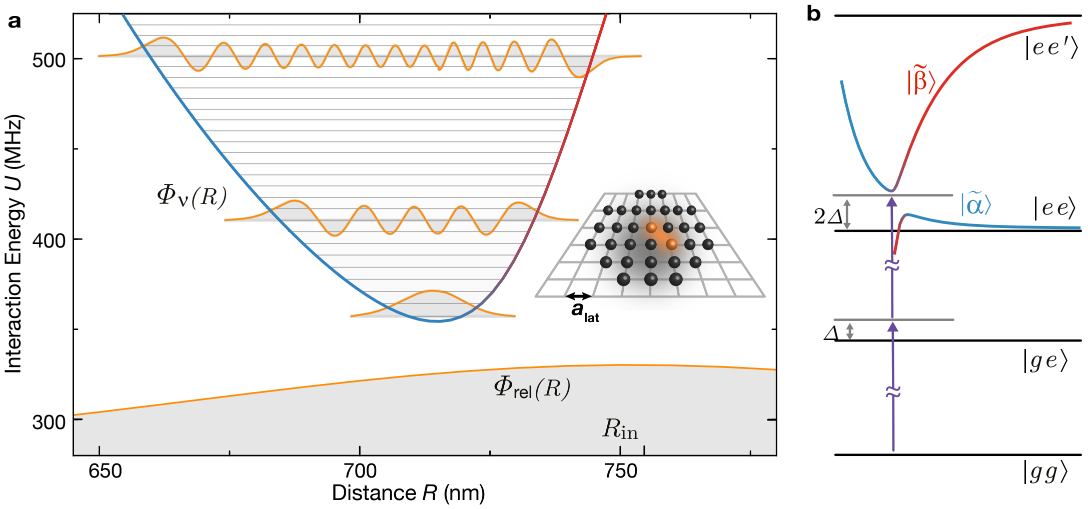

Figure 4.3: **Two-photon macrodimer excitation.** (**a**) The potential well hosts bound states with an energy spacing of around 6 MHz (gray horizontal lines). Before photoassociation, the atoms are arranged in a two-dimensional array with lattice spacing $a_\mathrm{lat} = 532\,\mathrm{nm}$. The vibrational wave functions are much narrower in the internuclear distance R than the root mean square width $\sqrt{2}\sigma_\mathrm{lat}$ of the initial relative wave function $\Phi_\mathrm{rel}(R)$ in the lattice, see also section 4.3.1. Here, $\Phi_\mathrm{rel}(R)$ is shown for the relevant distance $\sqrt{2}a_\mathrm{lat}$ and for the lattice depth chosen in the spectroscopy in arbitrary units. (**b**) The two-photon and two-atom excitation from the ground state $|gg\rangle$ occurs off-resonantly with detuning Δ via intermediate states where one atom is excited to the Rydberg state $|e\rangle \equiv |35P_{1/2}\rangle$. The molecular states can be laser-excited if 2Δ matches the interaction shift from the asymptotic pair state $|ee\rangle$. Figure adapted from Ref. [411].

stays conserved in the excitation process, see also section 7.4. This gives unique access to the molecular frame of reference by aligning unbound ground state atoms using optical traps before associating them into molecular states.

4.1.7 Macrodimer decay

In the theoretical literature, Rydberg macrodimers are expected to be limited by the decay rates of the individual Rydberg states admixed to the molecule [67, 337]. Using Eq. 4.2, the decay rate can be calculated by

$$\gamma_\mathrm{Mol} = \sum_{ij} |c_{ij}|^2 (\gamma_i + \gamma_j), \tag{4.8}$$

where the single-atom decay rates $\gamma_{i/j}$ include transitions to the ground state as well as room temperature black-body rates to neighboring Rydberg pair states. For the studied macrodimers this value is close to twice the decay time of the Rydberg states at the given principal quantum number n. For $n = 35$, one finds lifetimes $\tau_\mathrm{Mol} = \gamma_\mathrm{Mol}^{-1} \approx 20\,\mu\mathrm{s}$. Dependent on the particular binding potential, non-adiabatic couplings in the vibrational motion between coupled pair potentials can decrease the lifetime, see chapter 6.

Penning ionization

Rydberg atoms at close distances are known to autoionize [419–423]. In the underlying Penning ionization process [424], the deexcitation of one Rydberg electron provides the energy to ionize a second one [425]. At their equilibrium distance, the electron clouds are too distant and ionization rates are much lower than the radiative decay [67, 337]. However, in the presence of diabatic coupling rates to attractive potentials where both Rydberg atoms reach a closer distance, autoionization can occur. This is expected to happen in particular at finite fields where the broken molecular symmetries increase the number of gaps between crossing potential curves, or in the presence of other contaminant Rydberg atoms. Possibly due to such non-adiabatic motional couplings between different pair potentials (see also section 6), macrodimers were identified in previous experimental studies by exactly their spontaneous ionization rate [70] . Finally, ionization can also be possible after a black-body transition to a attractive interaction curve.

4.2 Two-photon macrodimer spectroscopy

In this thesis, Rydberg macrodimers are created by exciting ground state atoms by using laser light. Because macrodimers consist of two Rydberg atoms, this requires to excite two atoms into the Rydberg manifold. This can be done either sequentially [70] or using a two-photon transition [69]. In this work, macrodimers are excited using a two-photon transition in the ultraviolet (UV) starting from the electronic ground state. Here, a pair ground state $|gg\rangle$ gets excited into a state $|\Psi_{\mathrm{Mol}}\rangle$ by absorbing two UV photons. As shown in Fig. 4.2 and Fig. 4.3 (**a**) and discussed in Section 4.1.2, the interaction shift U^ν of the vibrational series from the bare Rydberg resonance is typically several hundreds of megahertz. For a single-photon detuning Δ of the UV laser relative to the transition $|g\rangle$ to $|e\rangle$, the two-photon detuning from an initial pair state $|gg\rangle$ to a non-interacting doubly-excited Rydberg state $|ee\rangle$ is 2Δ, see Fig. 4.3 (**b**). Hence, one expects the macrodimer states to be resonant at intermediate state detunings $\Delta/(2\pi) = U^\nu/2$. The only difference of the excitation scheme to the Rydberg blockade scheme introduced in 2.4 (a) is that the laser couples to molecular binding potentials instead of asymptotic van der Waals potentials. This is similar to so-called *Rydberg antiblockade* [426] configurations where a large laser detuning compensates for a Rydberg interaction shift such that the pair potentials can be resonantly excited.

Experimentally, macrodimers can be detected via atom loss spectroscopy. As discussed in section 4.3, excited Rydberg atoms and macrodimers leave the optical lattice with high probability and are not detected in the images taken after the excitation pulse. The initial state of the spectroscopy was a two-dimensional Mott insulator at a lattice depth of $V = (40, 40, 80)\, E_r$ in the electronic ground state $|g\rangle = |F = 2, m_F = 0\rangle$. The UV laser was directing along the lattice diagonal direction and was linearly polarized in the atomic plane. We furthermore applied a magnetic field of 28.6 Gauss perpendicular to the atomic plane. The Rabi frequency from $|g\rangle$ to both Zeeman states $|e\downarrow\rangle$ and $|e\uparrow\rangle$ was $\widetilde{\Omega}/(2\pi) = 1.2(1)$ MHz. The detuning Δ was calculated relative to the center of both transitions, which are split by ± 13.3 MHz. To ensure full coverage of the spectral region between neighboring data points, the excitation laser was swept by 480 kHz during the total illumination time of $t_{\mathrm{uv}} = 100\,\mathrm{ms}$. The recorded atom loss spectrum covering hundreds of megahertz on both sides of the Rydberg resonances shown in Fig. 4.4 (**a**).

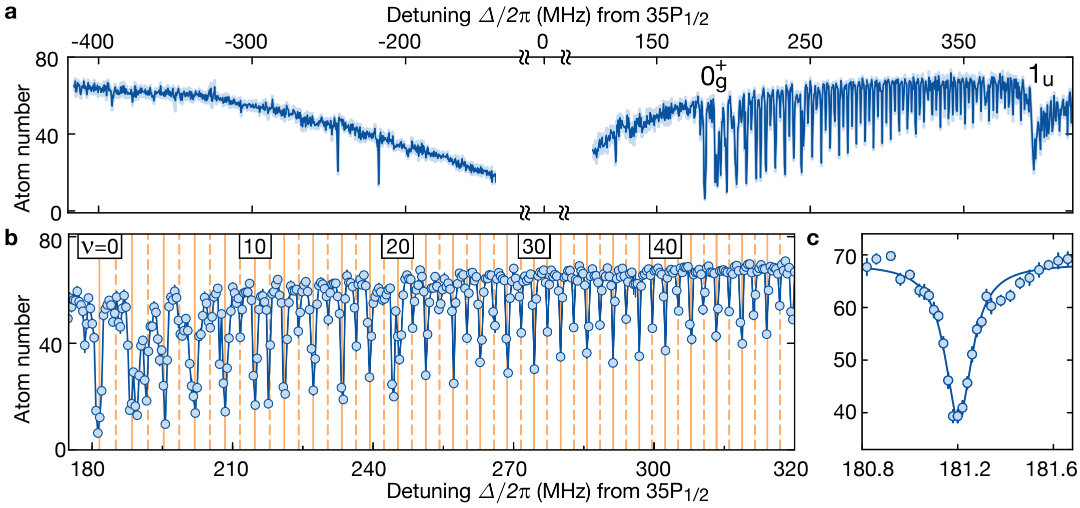

Figure 4.4: **High-resolution two-photon spectroscopy detuned from the $35P_{1/2}$ Rydberg resonance.** (**a**) Starting from a two-dimensional atomic Mott insulator, atom loss signatures are recorded for single-photon detunings $\Delta/2\pi \in [-400, 400]\mathrm{MHz}$ of the UV laser. On the blue-detuned side of the resonance, one observes atom loss resonances with regular spacing and alternating line strength due to the coupling to macrodimers. For very large detuning a second series of molecular bound states belonging to a 1_u potential becomes resonant. We find no signatures of bound states on the interaction-broadened red-detuned side of the Rydberg resonance. (**b**) Zooming into the frequency region between 180 and 320 MHz reveals a spacing of the vibrational resonances of around 3 MHz, which is half the energy spacing between the vibrational energies and slightly decreases for higher vibrational states. We find very good agreement between the measured resonance positions and the theoretical predictions (orange lines). (**c**) High-resolution spectroscopy of the lowest vibrational level. Each datapoint represents an average of about ten experimental shots. All error bars on the data points denote one standard error of the mean (s.e.m.). Figure adapted from Ref. [411].

At a detuning $\Delta/(2\pi) \approx 180\,\mathrm{MHz}$, the 0_g^+ binding potential starting at an interaction shift of $U = 2\Delta/(2\pi) \approx 360\,\mathrm{MHz}$ becomes two-photon resonant. In Fig. 4.4 (**b**) one can see more than 50 spectroscopically resolved vibrational resonances, which agree well with the calculated vibrational energies using Eq. 4.7. Mainly due to the dominating motional overlap integral, the lowest vibrational state features the strongest coupling, see also sections 4.3.1 and 5.3. For higher vibrational states, we find a decrease of the coupling rates into even vibrational states. The coupling into odd vibrational modes which is very small at low ν increases with the vibrational quantum number. Similar observations will be presented later for other macrodimer potentials. At detunings higher than $\Delta/(2\pi) = 390\,\mathrm{MHz}$, another 1_u macrodimer potential becomes resonant. In principle, single-atom states $|e\rangle$ as well as $|e'\rangle$ can act as intermediate states in the excitation process. However, because of the larger fine structure splitting of $2.556\,\mathrm{GHz}$ and because the chosen potential which is much closer to the state $|e\rangle$, the contribution from $|e'\rangle$ is small for this specific potential.

Because single-atom Rydberg states are excited by the absorption of a single UV photon, the transitions $|g\rangle \rightarrow |e\downarrow\rangle$ and $|g\rangle \rightarrow |e\uparrow\rangle$ appear much stronger than the molecular resonances. As a consequence, the saturated region at small detunings is excluded from the spectrum. Both Rydberg transitions are asymmetrically broadened towards negative detunings due to attractive 0_u^- and 1_u van der Waals interaction potentials shown in Fig. 4.2 (**b**,**c**). The two narrow resonances at negative detunings are lattice-induced Raman resonances and also appear at the corresponding positive detunings, where they are overlapped with the macrodimer spectrum. They are centered around the 230 MHz detuning between both lattice lasers. Their splitting matches the Zeeman splitting of the two states $|e\downarrow\rangle$ and $|e\uparrow\rangle$.

4.2.1 Precision test of calculated pair potentials

For deeply bound molecules closer to the electronic ground state, ab initio calculations of the molecular binding potentials based only on the properties of the individual atoms contributing to the molecule is usually not possible. For macrodimers where electron orbitals do not overlap, the vibrational resonances can be predicted at a remarkable accuracy of a few hundred kilohertz. From the quantum defects introduced in chapter 2, the energy spacing between Rydberg levels, their wave functions, and the multipole matrix elements can be calculated. The vibrational macrodimer states provide narrow spectroscopic signatures in the short-distance regime where the interactions are non-perturbative and Eq. 4.2 consists of many different asymptotic Rydberg states. Therefore, resolving the vibrational resonances experimentally represents currently the most precise test of the calculated Rydberg interaction potentials.

The calculation of the binding potentials relies on a diagonalization of the interaction Hamiltonian Eq. 2.19 after performing the multipole expansion Eq. 2.20. All calculations used the open-source program *pair interaction* [50]. One crucial parameter is the order of the multipole expansion. In order to calculate asymptotic van der Waals potentials or resonant dipole-dipole interactions, the dipole-dipole interaction term Eq. 2.25 $\propto R^{-3}$ is sufficient. In the non-perturbative distance regime at shorter distances, also higher-order multipole terms have to be taken into account [73, 200, 204, 339]. A prediction of the observed vibrational resonance positions required to include even higher multipole terms up to $R^{-6} - R^{-7}$, see also appendix B. This precision highlights the importance of macrodimer spectroscopy to benchmark the ab-initio calculations of the interaction potentials.

Accurate calculations also rely the selection of basis states used for the diagonalization. In order to reduce the dimension of the Hamiltonian, the diagonalization was restricted to the molecular symmetry of the potential of interest. To get accurate potentials, available states within an energy band $\Delta E \approx 550\,\mathrm{GHz}$ were included for the single-atom basis as well as the two-atom basis. Within these states, only single-atom states whose quantum numbers differ from the starting state by $\Delta n = 7$ and $\Delta L = 4$ were selected. For J and m_J, no further selection was necessary in most cases. The coupling between states with large Δn can be neglected because the spatial overlap integral decreases. For larger ΔL, the coupling reduces because higher multipole interaction terms are required due to selection rules. In total, the dimension of the interaction Hamiltonian was $d \approx 10\,000 - 15\,000$. At higher (lower) principal quantum number n, the energy band ΔE has to be decreased (increased) because nearby Rydberg states become energetically closer at higher n.

For magnetic fields $\boldsymbol{B} \nparallel \boldsymbol{R}$, the symmetry of the interaction Hamiltonian is broken and different potentials $|\Omega|_{g/u}^{\pm}$ mix. Because this strongly increases the dimension of the Hamiltonian, a calculation of the binding potentials as accurate as the observed vibrational spectra was not possible. Whenever finite fields were essential for the experiments, we calculated molecular states at zero field and then treated the magnetic field as a perturbation.

4.2.2 Vibrational linewidth & lifetime

Measuring the linewidth of the vibrational resonances provides a lower limit for the experimental macrodimer lifetime using the Fourier uncertainty principle between energy and time [427]. From Eq. 4.8, one theoretically expects a macrodimer lifetime of $\tau_{\text{th}} \approx 20\,\mu\text{s}$, which is half of the bare Rydberg lifetime at the same n. Fitting a Lorentz profile to the spectroscopically resolved lowest vibrational resonance yields a FWHM of 139(5) kHz. Note that the width shown in Fig. 4.4 (**c**) appears only half as broad as it actually is in the two-photon spectroscopy because changing the frequency of a single UV photon shifts the summed frequency of two UV photons by the double amount. Accounting for the factor of two, we obtain $\tau_{\text{lim}} \approx 0.6\,\mu\text{s}$ for the experimental limit of the macrodimer lifetime.

Because of the linewidth of the laser, it is challenging to be conclusive about the range between τ_{lim} and τ_{th}. The natural linewidth of the bare Rydberg states cannot be resolved in the experimental apparatus [72]. At deep lattices, also lattice inhomogeneities lead to broadening, see Fig. 3.5. Additionally, the accessible motional states of the antitrapped Rydberg atoms which are spread over a certain energy band are expected to broaden the resonance even at constant lattice depth. For macrodimers, this partly contributes via the contributing rotational states. This effect is illustrated in Fig. 4.5 (**d**) and is larger than the natural lifetime. This results in larger experimental linewidths, independent of the radiative lifetime or the laser.

4.3 Motional overlap & loss dynamics

In addition to the mixing of electronic Rydberg pair states, macrodimer states are different from the asymptotic Rydberg pair states because their interatomic motion is constrained by the vibrational wave functions. At principal quantum numbers relevant here, the vibrational energy is roughly ten times larger than the kinetic energy of a ground state atom in the motional ground state in the optical lattice. This has two consequences which will be discussed in the following section. On the one hand, the motional overlap integral is far from unity, which will decrease the optical coupling rates into macrodimer states. On the other hand, a decaying macrodimer will release enough kinetic energy to efficiently remove the corresponding pair.

4.3.1 Franck-Condon factor

The coupling rate into molecular states by the light field is mediated via the electronic state. During photoassociation, the nuclear motion will be projected into the vibrational wave function of the macrodimer state. Here, a Franck-Condon overlap integral between the initial motional wave function and the vibrational wave functions enters as a prefactor into the optical coupling. Initially, the ground-state atoms populate the lowest motional state in the optical lattice, see Eq. 3.2. The root mean square (RMS) width of a single-particle wave function and its relation to the on-site trapping frequency was introduced in Eq. 3.3. For the 0_g^+ macrodimer potential presented in Fig. 4.3 and Fig. 4.4 where the binding potential minimum appears at a interatomic distance larger than 700nm, the motional overlap at a distance of a lattice diagonal is expected to dominate. Fixing the origin of the coordinate system to be between both atoms and the interatomic axis as the $z-$axis and assuming isotropic optical trapping, the normalized initial motional wave function $\chi_{\mathrm{m}}(\boldsymbol{R}_1, \boldsymbol{R}_2)$ of two atom pairs at the distance $R = \sqrt{2}a_{\text{lat}}$ in the lattice reads

$$\chi_{\mathrm{m}}(\boldsymbol{R_1}, \boldsymbol{R_2}) = \frac{1}{\left(2\pi\sigma_{\text{lat}}^2\right)^{6/4}} e^{-\frac{1}{4\sigma_{\text{lat}}^2}\left[\left(\boldsymbol{R_1}-\frac{a_{\text{lat}}}{\sqrt{2}}\boldsymbol{e}_z\right)^2+\left(\boldsymbol{R_2}+\frac{a_{\text{lat}}}{\sqrt{2}}\boldsymbol{e}_z\right)^2\right]}, \tag{4.9}$$

with $\boldsymbol{e}_z$ the unit vector along the $z-$axis. After separating the center-of-mass motion and transforming the relative coordinates $\boldsymbol{R} = \boldsymbol{R}_1 - \boldsymbol{R}_2$ into spherical coordinates, this becomes

$$\chi_{\text{rel}}(R, \theta) = \frac{1}{\left(4\pi\sigma_{\text{lat}}^2\right)^{3/4}} e^{-\frac{1}{8\sigma_{\text{lat}}^2}\left[\left(R-\sqrt{2}a_{\text{lat}}\right)^2+2\sqrt{2}a_{\text{lat}}R(1-\cos\theta)\right]}. \tag{4.10}$$

Because of the choice of the z-axis and the cylindrical symmetry of the relative motion of two atoms pinned in the laboratory frame, $\chi_{\text{rel}}(R, \theta)$ shows no $\varphi-$dependence. The mean separation $\langle R\rangle = \sqrt{2}a_{\text{lat}}$ of the motional wave function in the ground state greatly exceeds the width σ_{rel}. It is therefore well justified to separate the radial and angular parts and write $\chi_{\text{rel}}(R, \theta) \approx \Phi_{\text{rel}}(R)\Psi_{\text{rel}}(\theta)$, with

$$\Phi_{\text{rel}}(R) = \frac{1}{\left(16\pi\sigma_{\text{lat}}^2 a_{\text{lat}}^4\right)^{1/4}} e^{-\frac{1}{8\sigma_{\text{lat}}^2}\left(R-\sqrt{2}a_{\text{lat}}\right)^2}, \tag{4.11}$$

$$\Psi_{\text{rel}}(\theta) = \sqrt{\frac{a_{\text{lat}}^2}{2\pi\sigma_{\text{lat}}^2}} e^{-\left(\frac{a_{\text{lat}}}{\sigma_{\text{lat}}}\sin(\frac{\theta}{2})\right)^2}, \tag{4.12}$$

and normalization conditions $\int R^2|\Phi_{\text{rel}}(R)|^2 dR = 1$ and $2\pi\int|\Psi_{\text{rel}}(\theta)|^2\sin\theta d\theta = 1$.

Also for the macrodimer state, the radial part which is given by the vibrational wave function $\Phi_\nu\left(R\right)$ is assumed to be decoupled from the angular wavefunction. The angular states are rotational states $Y_\ell^m\left(\theta, \varphi\right)$. For the isotropic trapping conditions, contributions can only be found for $\varphi-$independent states $Y_\ell^0\left(\theta\right)$.

The Franck-Condon integral

$$\begin{aligned} f_{\nu\ell} &= 2\pi \int\int \chi_{\text{rel}}^\star(R, \theta) Y_\ell^0\left(\theta\right) \Phi_\nu\left(R\right) R^2 \sin\theta dR d\theta \\ &\approx 2\pi \int \Psi_{\text{rel}}^\star(\theta) Y_\ell^0\left(\theta\right) \sin\theta d\theta \int \Phi_{\text{rel}}^\star(R) \Phi_\nu\left(R\right) R^2 dR = f_\ell f_\nu \end{aligned} \tag{4.13}$$

quantifies the overlap of the nuclear motion. The second line uses that $\sigma_{\text{rel}} \ll \langle R\rangle$. This provides two independent Franck-Condon integrals f_ℓ for the rotational contribution and f_ν for the vibrational contribution. Justified by the same limits, f_ν can be also further simplified by a one dimensional integral. The different overlap coefficients are related via

$$\sqrt{\sum_\ell |f_{\nu\ell}|^2} \approx f_\nu, \quad \sum_\ell |f_\ell|^2 = 1. \tag{4.14}$$

Since the rotational basis represents a complete basis, the original angular distribution can always be reproduced by a sufficiently large amount of contributing rotational states, if they are energetically accessible.

Tunability of the motional overlap

Since the coupling rates will be proportional to the motional overlap integrals f_ν, coupling rates can be optimized by engineering a ground state relative wave function which equals the vibrational wave function of the molecule. On the one hand, this requires to choose binding potentials where the bond length matches the relevant distance in the lattice. On the other hand, the size of the initial relative wave function σ_{lat} has to be comparable to the vibrational wave function σ_ν. For the macrodimers studied in this work, σ_ν was significantly lower than σ_{lat}. As a consequence, one observes a stronger coupling starting from a Mott insulating state at deeper lattice depths V_0. Starting from a Bose-Einstein condensate where Wannier wave functions are broad and particles are delocalized, the vibrational resonances were almost within the background atom loss. Here, in addition to lower molecular excitation rates, the background atom loss increased due to collective loss signatures, see also appendix C.1.

For the lowest vibrational modes, the maximum achievable spatial overlap integral was found to be $f_\nu \approx 0.6$ for the available laser power. This limit arises because of the weak scaling of $\sigma_{\text{lat}} \propto V_0^{1/4}$ [26]. Note that deeper lattices also induce motional side effects, as discussed in section 4.2.2 and 4.3.2. As an alternative, one can use more shallow macrodimer potentials. Using the scalings discussed in section 4.1.2, one finds that at principal quantum numbers $n \approx 60$, unity Franck-Condon factors are possible. It might be interesting to perform further studies on macrodimers in this regime using optical tweezers.

4.3.2 Macrodimer loss dynamics

After photoassociation of macrodimers, their ejection from the trap is unavoidable due to several motional effects. First, associated molecules gain a recoil velocity $v_{\text{rec}} = 15.4\frac{\text{nm}}{\mu\text{s}}$ from the absorption of two UV-photons. Second, Rydberg states are antitrapped in the optical lattice. As a result, the kinetic energy initially stored in the confined Wannier wave function gets released into the center-of-mass coordinate of the excited macrodimer. Additional acceleration occurs due to the repulsive lattice potential, which depends on the depth V_0 of the optical lattice. These mechanisms occur also for single-atom Rydberg states and are of similar order. As a consequence, the excitation of single-atom Rydberg states is usually also experienced as atom loss. Additional motional effects which make retrapping for macrodimers even more unlikely are discussed in the following paragraphs.

Rotational dephasing

Due to the kinetic energy stored in the Wannier states, the associated molecules which, in contrast to the ground state atoms, not trapped by the lattice potential, experience a dephasing of their relative orientation while the interatomic distance stays locked to the minimum of the binding potential. The rotational states $Y_\ell^m(\theta, \varphi)$ superimposed for the initial interatomic orientation are assumed to be energetically split by the rigid rotator Hamiltonian $\hat{H} = B_r \hat{L}^2$. The eigenenergies are $E_\ell = B_r \ell(\ell+1)$. The rotational constant $B_r = \frac{\hbar^2}{2\mu_{\text{Rb}}(R_\nu)^2}$ depends on the reduced mass $\mu_{\text{Rb}} = m_{\text{Rb}}/2$ and the molecular bond length R_ν. For molecules excited at $R_b = \sqrt{2}a_{\text{lat}}$, the rotational constant is $B_r \approx 200\,\text{Hz}$, which is significantly smaller than the vibrational splitting. Assuming that all rotational states needed to reproduce the initial wave functions are occupied accordingly, the initialized

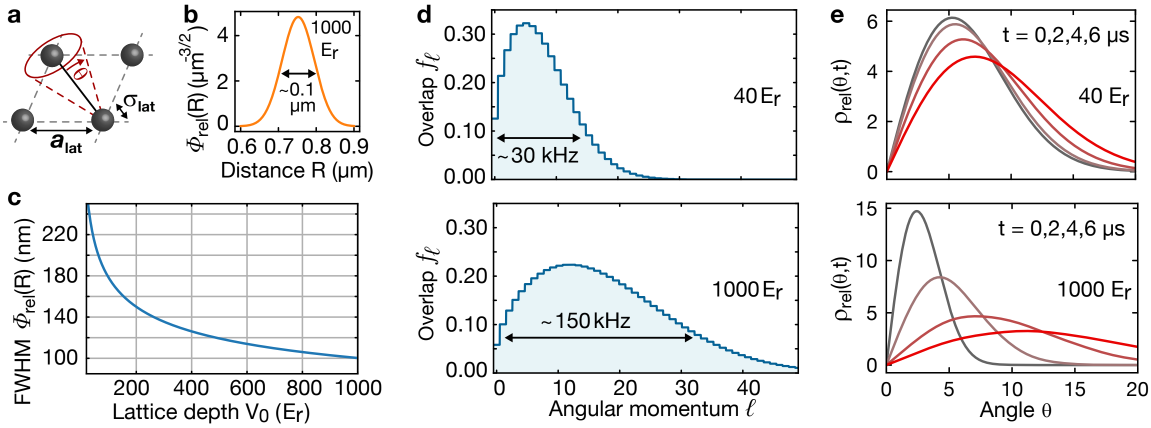

Figure 4.5: **Motional overlap and angular dephasing.** (**a**) The motional relative wave function in the ground state is decomposed into a radial contribution $\Phi_{\text{rel}}(R)$ and an angular contribution $\Psi_{\text{rel}}(\theta)$. (**b**) The radial relative wave function $\Phi_{\text{rel}}(R)$, here for a lattice depth of $V_0 = 1000\,E_r$. (**c**) Full width at half maximum (FWHM) of $\Phi_{\text{rel}}(\theta)$, shown for different lattice depths. Because of the weak scaling $\sigma_{\text{lat}} \propto V_0^{-1/4}$, the tunability of the ground state wave function is limited. (**d**) Decomposition of the inital angular wave function $\Psi_{\text{rel}}(\theta)$ for different lattice depths into angular momentum states $Y_\ell^0(\theta,\varphi)$ for two different lattice depths. (**e**) After photoassociation, the interatomic distance R is strongly confined by $\Phi_\nu(R)$. Because of the kinetic energy stored in the Wannier wave functions, the orientation of the macrodimers after photoassociation will get lost at a faster timescale than the expected radiative decay rate. The narrower the initial distribution $\Phi_{\text{rel}}(\theta)$, the faster the dephasing.

state evolves as

$$\Psi_{\text{rel}}(\theta,t) = \sum_\ell f_\ell Y_\ell^0(\theta) e^{-\frac{i}{\hbar}E_\ell t}. \tag{4.15}$$

The time-dependent angular probability density $\rho_{\text{rel}}(\theta,t) = 2\pi|\Psi_{\text{rel}}(\theta,t)|^2\sin(\theta)$ which is normalized according to $\int \rho_{\text{rel}}(\theta,t)d\theta = 1$ is shown in Fig. 4.5 (**e**) for two initial relative wave function. In particular at deep lattices one finds that the initial orientation is lost at times lower than the radiative lifetime of the macrodimer. This result can also be understood as a time-of-flight expansion in the angular degree of freedom.

Kinetic energy in macrodimer decay

The decay of macrodimers is different from the decay of Rydberg atom pairs at distances larger than a blockade radius R_b because of the released kinetic energy. If one of both Rydberg atoms decays back to the electronic ground state, the final electronic pair state is effectively non-interacting. However, the kinetic energy stored in the vibrational wave function gets released and both nuclei expand in their relative distance coordinate. Since the confinement of the macrodimer binding potentials studied here exceeds the optical lattice potential, the related velocity

$$\delta v_\nu = \left(\frac{(\nu+1/2)\hbar\omega_{\text{vib}}}{\mu_{\text{Rb}}}\right)^{1/2} \approx (\nu+1/2)^{1/2} \times 150\frac{\text{nm}}{\mu\text{s}} \tag{4.16}$$

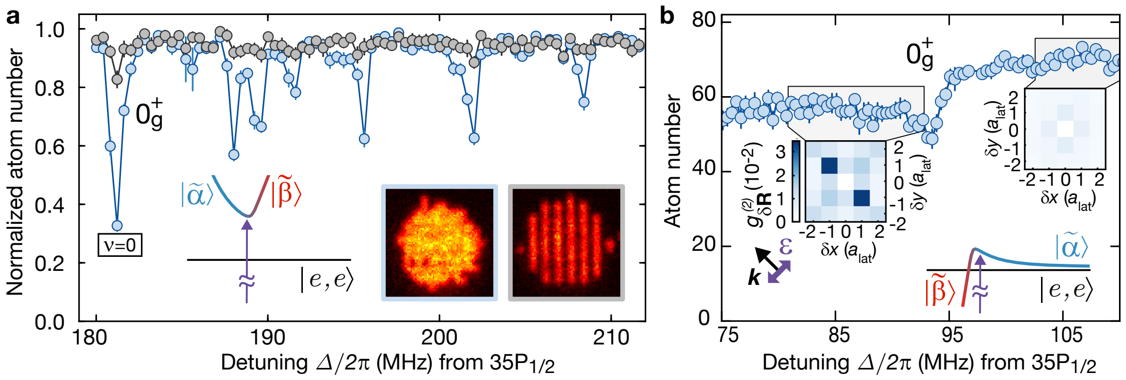

Figure 4.6: **Distance-dependent loss signatures.** (**a**) Changing the initial density distribution from a Mott insulator with unity filling (gray datapoints and left inset) to a configuration without atom pairs at distances of $\sqrt{2}a_{\mathrm{lat}}$ (right inset) leads to a strong suppression of the macrodimer resonances (gray data points). For both spatial configurations, the atom number was normalized to the initial atom number without UV light and the illumination time was $t_{\mathrm{UV}} = 20\,\mathrm{ms}$. (**b**) Spectroscopic signature at the lower branch of the studied avoided crossing. The pair states can be excited within a broad energy region below the potential maximum. At the maximum where the continuum states have low kinetic energy, the coupling reaches a maximum because of large motional overlap. Afterwards, due to the energy gap between the potential maximum and the binding potential, the pair potential becomes off-resonant and pair excitation turns off. As expected, the hole-hole correlation signal can only be observed at detunings below the potential maximum and vanishes within the gap. The UV light was polarized linearly in the atomic plane. For the calculation of the correlation signals, all data points within the gray boxes were combined. All error bars denote one s.e.m. Figure adapted from Ref. [411].

for the vibrational states ν [9] is significantly larger than the expansion velocity of a released Wannier wave function.

If a macrodimer decays via a black-body process instead, dipole-dipole selection rules favor final states where both Rydberg atoms interact via strong resonant dipole-dipole interactions. Because of the short distance, a fast acceleration process releases up to hundreds of megahertz within less than a microsecond, resulting in atom pairs moving at relative velocities of several micrometers per microsecond. If the final pair potential is attractive, this can induce ionization [420]. If it is repulsive, both Rydberg atoms separate at high relative kinetic energies. After such a decay, the rotational dephasing typically already strongly affected their orientation and it cannot be assumed that both repelling Rydberg atoms separate along their original orientation during photoassociation, see Fig. 4.5 (**e**).

4.3.3 Spatially resolved atom pair losss

The discussion of the Franck-Condon overlap in section 4.3.1 concluded that the atom loss occurs pairwise and at a distance of $\sqrt{2}a_{\mathrm{lat}}$. Using the site-resolved imaging system of the experimental platform, one should therefore be able to detect the macrodimer excitation microscopically. In a first experimental test, one can compare the atom loss spectrum for different initial spatial arrangements in the lattice. In addition to a unity-filled Mott insulator, the spectrum was measured in a system where the rows in the lattice are alternatively occupied and empty [395, 411]. As expected, the result shown in Fig. 4.6 (**a**) suggests that macrodimer excitation in the density-modulated initial state is much lower due to the absence of initial atom pairs at a distance of $\sqrt{2}a_{\text{lat}}$. In total, the suppression was found to be roughly a factor of ten. The remaining macrodimer excitation rate in the density-modulated state comes from imperfect initial state preparation and a small remaining Franck-Condon factor at nearest-neighbor distance.

Another direct method is to observe the correlated pair loss by evaluating ensemble-averaged hole-hole correlation functions

$$g^{(2)}_{\delta \boldsymbol{R}} = \left(\langle \hat{h}_{k+\delta x, l+\delta y} \hat{h}_{k,l} \rangle - \langle \hat{h}_{k+\delta x, l+\delta y} \rangle \langle \hat{h}_{k,l} \rangle \right)_{k,l} \tag{4.17}$$

at distances $\delta \boldsymbol{R} = (\delta x, \delta y)$. Here, $(.)_{k,l}$ denotes averaging over the relevant pairs in the ensemble. Furthermore, $\hat{h}_{k,l} = 1 - \hat{n}_{k,l}$ is the hole operator at site (k, l) which is one for an empty site and zero for an occupied site and $\hat{n}_{k,l}$ is the number operator. For our system size, evaluating $g^{(2)}_{\delta \boldsymbol{R}}$ requires a dataset of about 200 experimental shots at a similar scattering rate. In the spectroscopy of the vibrational resonances where each data point represents the average of about 10 realizations, this was not possible. However, the spectroscopy in the vicinity of the lower branch of the avoided crossing of the potentials $|\widetilde{\alpha}\rangle$ and $|\widetilde{\beta}\rangle$ shows a broad loss signature which stops at the potential maximum, see Fig. 4.6 (**b**). Here, the coupling to the motional continuum does not lead to such sharp resonances as observed for the vibrationally bound states and the distance still agrees with $\sqrt{2}a_{\text{lat}}$. By combining a sufficiently large amount of data points close to the maximum of the potential, the correlation signal $g^{(2)}_{\delta \boldsymbol{R}}$ converges. In agreement with the expectation, the correlation signal peaks at the corresponding distance vector $\delta \boldsymbol{R} = (1, -1)\, a_{\text{lat}}$. Interestingly, the small signal for the perpendicular orientation $\delta \boldsymbol{R} = (1, 1)\, a_{\text{lat}}$ suggests that the excitation rate is strongly directional. The excitation rate was observed to be much stronger perpendicular to the polarization of the UV light, which was linearly polarized along the direction with the weak signal. The solution to that puzzle lies in the electronic structure of the pair potential at the crossing point and will be presented in the end of the next chapter.

Chapter 5

Electronic structure tomography

The previous chapter focused on the spectroscopically resolved vibrational resonances of macrodimer potentials. In section 4.1.6 it was furthermore argued that the orientation of the atom pairs stays conserved in the photoassociation process. This unique access to the molecular frame of reference motivates to further characterize the molecular states by their orientation-dependent photoassociation rates, see Fig. 5.1. After calculating the associated molecular Rabi frequencies, the microscopic signal recorded for different molecular states blue-detuned from the $36P_{1/2}$ is discussed. Then, the response of macrodimer states on applied magnetic fields and the influence of a spatially varying electronic structure on the photoassociation (PA) process are discussed. This chapter discusses results from the publications [411] and [413]. The presented description of the optical coupling process was developed in close discussion with Jun Rui.

5.1 Molecular Rabi frequencies

Rabi frequencies between internal states of atoms depends on the initial state, the final state and the light polarization. The excitation process is described in the atomic frame of reference, which can be externally controlled by applying a magnetic field $\boldsymbol{B}$. For molecules, controlling the quantization axis requires to control the orientation of the molecular state. Here, the interatomic axis $\boldsymbol{R}$ defines an internal quantization axis and the angular momentum projection Ω is only well-defined on $\boldsymbol{R}$. In the optical excitation process of molecules, this introduces the angle β between the quantization axis of the initially unbound atoms and the molecular orientation as an additional parameter to the coupling. Similar to the selection rules appearing in the optical coupling between atomic states, one finds dependencies that are characteristic for different molecular quantum numbers $\Omega^{\pm}_{g/u}$ and allow for their identification, see Fig. 5.1 (**d**,**e**). Furthermore, the mixing of atomic states leads to a larger number of contributing single-atom Rabi couplings to the molecular coupling rates [428].

5.1.1 Competing reference frames

Before photoassociation, the atoms are initialized in the ^{87}Rb [429] ground state $|g\rangle_{\boldsymbol{B}} = |F, m_F\rangle \equiv |g\rangle$, here expressed in the frame of the applied magnetic field $\boldsymbol{B}$. The reference frame of the molecule is given by the interatomic axis $\boldsymbol{R}$ and has a relative angle β relative to $\boldsymbol{B}$. A consistent microscopic description of the photoassociation process thus requires to rotate either the initial state into the molecular frame or vice versa. Rotating $|g\rangle_{\boldsymbol{B}}$ expressed in the magnetic frame into the molecular frame using the rotation operator $\hat{U}(\beta)$ yields

$$|g\rangle_{\boldsymbol{B}} \to \hat{U}(\beta)|g\rangle_{\boldsymbol{B}} = \sum_{m_F} c^F_{m_F} |F, m_F\rangle \equiv |g\rangle_{\boldsymbol{R}}, \tag{5.1}$$

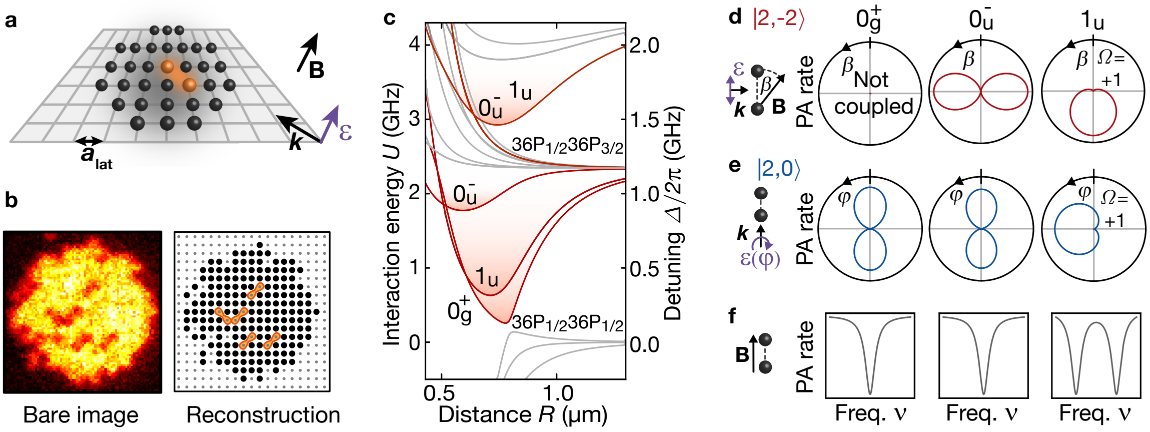

Figure 5.1: **Electronic structure tomography of Rydberg macrodimers.** (**a**) The orientation of the atom array is fixed in the laboratory frame by the optical lattice. The direction of the magnetic field ***B*** is tunable and the wave vector ***k*** of the ultraviolet (UV) laser is pointing along the lattice diagonal direction. As indicated in the individual figures, the polarization $\boldsymbol{\varepsilon}$ of the UV laser is either linear in the atomic plane, linear orthogonal to the atomic plane, or circular. (**b**) Excited macrodimers were observed as correlated atom loss. (**c**) Blue-detuned from the $36P_{1/2}$ Rydberg resonance, one finds macrodimer binding potentials with different molecular symmetries $0_g^+, 0_u^-$ and 1_u potentials. (**d,e**) The unique spatial configuration allows one to study the dependence of photoassociation on the angle β between the orientation of the atom pairs relative to a magnetic field (**d**) and on the circularity φ of the light polarization $\varepsilon(\varphi)$ (**e**). (**f**) Additionally, the response of the molecular state to magnetic fields can be studied. These signatures provide an experimental fingerprint of the electronic structure of the molecule and will be studied in the following paragraphs. Figure adapted from Ref. [413].

where $c^F_{m_F}$ are the coefficients of the populated hyperfine states after the rotation. Alternatively, the molecular state

$$|\Psi_{\mathrm{Mol}};\Omega^{\pm}_{g/u}\rangle_{\boldsymbol{R}} \rightarrow \hat{U}(-\beta)|\Psi_{\mathrm{Mol}};\Omega^{\pm}_{g/u}\rangle_{\boldsymbol{R}} \equiv |\Psi_{\mathrm{Mol}};\Omega^{\pm}_{g/u}\rangle_{\boldsymbol{B}} \tag{5.2}$$

can be rotated into the atomic frame [411, 412, 430]. Because the molecular states $|\Psi_{\mathrm{Mol}};\Omega^{\pm}_{g/u}\rangle$ consist of a large number of atomic pair states which have to be rotated individually, it is more convenient to rotate the initial state using Eq. 5.1.

5.1.2 Decomposition of the initial state

The strong hyperfine coupling in the electronic ground state mixes the electronic angular momentum with the nuclear angular momentum. Because the Rydberg states contributing to $|\Psi_{\mathrm{Mol}};\Omega^{\pm}_{g/u}\rangle$ are expressed in the fine-structure basis, it is convenient to do the same for the ground state. Decomposing the previously rotated initial pair state $|gg\rangle_{\boldsymbol{R}}$ yields

$$|gg\rangle_{\boldsymbol{R}} = \sum_{\substack{m_{J_1}m_{J_2}\\ \in\{\uparrow,\downarrow\}}} |m_{J_1}m_{J_2}\rangle \sum_{\substack{m_{I_1},m_{I_2}\in\\ [-3/2,3/2]}} \mathcal{C}^{1/2\;\;F\;\;\,3/2}_{m_{J_1}\,m_{F_1}\,m_{I_1}}\,\mathcal{C}^{1/2\;\;F\;\;\,3/2}_{m_{J_2}\,m_{F_2}\,m_{I_2}}\,c^F_{m_{F_1}}c^F_{m_{F_2}}|m_{I_1}m_{I_2}\rangle \tag{5.3}$$

after reordering the electron and nuclear angular momenta. Furthermore, the spin projections m_{J_1} and m_{J_2} of both atoms are denoted as $\uparrow\,(\downarrow) = +1/2\,(-1/2)$ and $\mathcal{C}^{1/2\,F\,3/2}_{m_J\,m_F\,m_I} =$

$\langle 1/2, m_J, 3/2, m_I | F, m_F\rangle$ are Clebsch-Gordan coefficients. For ^{87}Rb with a nuclear spin $I = 3/2$, the four spin projections are $m_{I_{1(2)}} \in \{-3/2, -1/2, 1/2, 3/2\}$. The index $1\,(2)$ refers to the first (second) atom contributing to the pair state. The sum over the different spin projections $m_{F_{1(2)}}$ contributing after applying the rotation operator $\hat{U}(\beta)$ in Eq. 5.1 on the initial state is omitted because only contributions $m_{F_{1(2)}} = m_{J_{1(2)}} + m_{I_{1(2)}}$ have non-vanishing Clebsch-Gordan coefficients. After introducing coefficients

$$c^2_{m_{J_1}, m_{J_2}} = \sum_{\substack{m_{I_1} \\ m_{I_2}}} \left(\mathcal{C}^{1/2\ \ F\ \ 3/2}_{m_{J_1}\, m_{F_1}\, m_{I_1}} \mathcal{C}^{1/2\ \ F\ \ 3/2}_{m_{J_2}\, m_{F_2}\, m_{I_2}} c^F_{m_{F_1}} c^F_{m_{F_2}} \right)^2 \tag{5.4}$$

and normalizing the nuclear spin states $|\Psi^{m_{J_1} m_{J_2}}\rangle_I$ corresponding to the electronic states $|m_{J_1} m_{J_2}\rangle$, this can be simplified to

$$\begin{aligned} |gg\rangle_{\boldsymbol{R}} = {} & c_{\downarrow\downarrow} \, |{\downarrow\downarrow}\rangle_J \otimes |\Psi^{\downarrow\downarrow}\rangle_I + c_{\uparrow\uparrow} \, |{\uparrow\uparrow}\rangle_J \otimes |\Psi^{\uparrow\uparrow}\rangle_I \\ & + c_{\downarrow\uparrow} \left(|{\downarrow\uparrow}\rangle_J \otimes |\Psi^{\downarrow\uparrow}\rangle_I + |{\uparrow\downarrow}\rangle_J \otimes |\Psi^{\uparrow\downarrow}\rangle_I \right). \end{aligned} \tag{5.5}$$

Throughout this thesis, both atoms are initialized in the same single-atom ground state $|g\rangle$. Because this configuration leads to $c_{\uparrow\downarrow} = c_{\downarrow\uparrow}$, the coefficient is placed outside of the brackets in the second line. Since dipole-allowed single-photon transitions enforce an inversion symmetry flip, our two-photon photoassociation (PA) conserves the inversion symmetry of the initial state. It is therefore convenient to further decompose $|gg\rangle_{\boldsymbol{R}}$ into gerade (g) and ungerade (u) inversion eigenstates $|M_{J\,g/u}\rangle$, with $M_J = m_{J_1} + m_{J_2}$ the summed angular momentum projection on $\boldsymbol{R}$. For ground state ^{87}Rb with orbital angular momentum $L = 0$, applying Eq. 4.3 leads to pair states $|0_g\rangle_J = 1/\sqrt{2}\,(|{\uparrow\downarrow}\rangle_J - |{\downarrow\uparrow}\rangle_J)$, $|-1_u\rangle_J = |{\downarrow\downarrow}\rangle_J$, $|0_u\rangle_J = 1/\sqrt{2}(|{\uparrow\downarrow}\rangle_J + |{\downarrow\uparrow}\rangle_J)$ and $|+1_u\rangle_J = |{\uparrow\uparrow}\rangle_J$, which are formally equivalent to the singlet and triplet basis states of two coupled spin-1/2 systems. Introducing new normalized nuclear spin states $|\Psi_u^{-1}\rangle_I = |\Psi^{\downarrow\downarrow}\rangle_I$, $|\Psi_u^0\rangle_I = \frac{1}{\sqrt{2}}\left(|\Psi^{\downarrow\uparrow}\rangle_I + |\Psi^{\uparrow\downarrow}\rangle_I\right)$, $|\Psi_u^{+1}\rangle_I = |\Psi^{\uparrow\uparrow}\rangle_I$ and $|\Psi_g^0\rangle_I = \frac{1}{\sqrt{2}}\left(|\Psi^{\downarrow\uparrow}\rangle_I - |\Psi^{\uparrow\downarrow}\rangle_I\right)$ yields

$$\begin{aligned} |gg\rangle_{\boldsymbol{R}} = {} & c_u^{-1} \, |{-1_u}\rangle_J \otimes |\Psi_u^{-1}\rangle_I + c_u^0 \, |0_u\rangle_J \otimes |\Psi_u^0\rangle_I \\ & + c_u^{+1} \, |{+1_u}\rangle_J \otimes |\Psi_u^{+1}\rangle_I + c_g^0 \, |0_g\rangle_J \otimes |\Psi_g^0\rangle_I. \end{aligned} \tag{5.6}$$

The β-dependent coefficients for the three studied ground states $|F = 2, m_F = -2\rangle$, $|2, -1\rangle$ and $|2, 0\rangle$ are shown in Fig. 5.2. Note that no normalized spin state $|\Psi_g^0\rangle_I$ can be constructed for $|\Psi^{\downarrow\uparrow}\rangle_I = |\Psi^{\uparrow\downarrow}\rangle_I$. This is the formal reason why the initial state $|2, -2\rangle$ has no contribution from $|\Psi_g^0\rangle_I$, see also section 5.2.2. In many cases only one of the four initial states is coupled to a specific molecular state. As discussed in the following paragraphs, measuring the photoassocation rates for various angles β then directly reproduces these plots. For ungerade states and certain light polarizations, more than one state can contribute to the coupling. Since both final macrodimer states are distinguishable by their different nuclear spin state, this will lead to different molecular Rabi frequencies which cannot interfere. In these cases, the corresponding excitation rates add up.

5.1.3 Light polarization

For atoms, the anomalous Zeeman effect provides a useful example to visualize the interplay between the quantization axis and the angular momentum conservation during

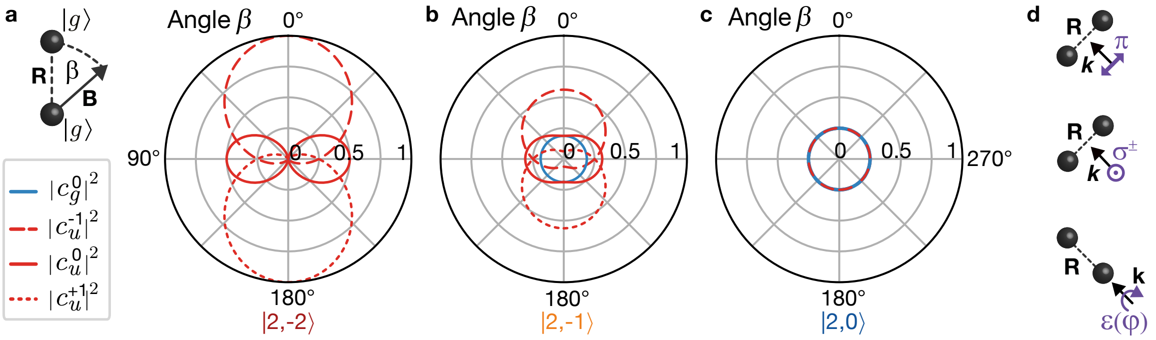

Figure 5.2: **Initial pair state decomposition and light polarization.** (**a**) For $|g\rangle = |2, -2\rangle$ and $\beta = 0°\,(180°)$, only $|-1_u\rangle_J$ ($|+1_u\rangle_J$) contributes. For $\beta = 90°$, the initial pair state is a superposition of all three ungerade states. There is no contribution from $|0_g\rangle_J$. (**b**) For $|g\rangle = |2, -1\rangle$, the tendency is similar but the dependence is weaker. Additionally, c_g^0 is now finite but independent of β. (**c**) For $|g\rangle = |2, 0\rangle$, all states contribute with the same amplitude for all angles. (**d**) For $\boldsymbol{R} \perp \boldsymbol{k}$, the polarization can be decomposed into a $\pi-$component and a component representing an equally weighted superposition of σ^+ and σ^-. For $\boldsymbol{R} \parallel \boldsymbol{k}$, π polarization is not possible. Now, the polarization can be varied from σ^- to σ^+ by tuning the ellipticity φ. Figure adapted from Ref. [413].

optical tranistions. Here, the presence of a magnetic field $\boldsymbol{B}$ guarantees a well-defined angular momentum projection of the atomic states along the magnetic field. As a consequence, some transitions can only be observed only parallel or perpendicular to the field. Because light is a transversal wave, π polarized light where the field oscillates parallel to the quantization axis requires a propagation direction $\boldsymbol{k} \perp \boldsymbol{B}$ perpendicular to it. On the other hand, pure σ^+ or pure σ^- polarization can only be realized parallel to $\boldsymbol{k} \parallel \boldsymbol{B}$. An equally weighted superposition $\sigma^\pm$ can be achieved in both cases.

For molecules, such a study is more difficult because the angular momentum projection of molecules is only well-defined along the molecular axis $\boldsymbol{R}$. As a consequence, a useful quantization axis is $\boldsymbol{R}$ instead of $\boldsymbol{B}$ and a experimental study similar as the one for atoms requires to orient the molecular state in the laboratory frame. For the macrodimer excitation scheme used in this thesis, this requirement is fulfilled. Replacing $\boldsymbol{B}$ by $\boldsymbol{R}$, the intuition gained from the anomalous Zeeman effect can now directly be translated to the excitation of molecules.

Here, the polarization $\boldsymbol{\varepsilon}$ of the excitation light field $\boldsymbol{E} = E_0\boldsymbol{\varepsilon}$ with amplitude E_0 is expanded into the spherical basis $\boldsymbol{\varepsilon} = \sum_{q\in\{0,\pm1\}} c_q \boldsymbol{e}_q$ in the molecular frame where $\boldsymbol{e}_z \parallel \boldsymbol{R}$. Again, π polarized light is oscillating parallel to the interatomic axis $\boldsymbol{e}_0 = \boldsymbol{e}_z$ and $\sigma^\pm$ polarized light $\boldsymbol{e}_{\pm1} = \mp\frac{1}{\sqrt{2}}\left(\boldsymbol{e}_x \pm i\boldsymbol{e}_y\right)$ oscillates in a plane perpendicular to $\boldsymbol{R}$. In the experiment, the PA laser propagates along one lattice diagonal and the bond length for most molecules studied here is close to the lattice diagonal distance. This leads to PA either parallel or perpendicular to $\boldsymbol{k}$. For $\boldsymbol{R} \perp \boldsymbol{k}$ and a UV polarization parallel (perpendicular) to the atomic plane, the polarization vector is $\boldsymbol{e}_z$ ($\boldsymbol{e}_x$), see Fig. 5.2 (**d**). For $\boldsymbol{R} \parallel \boldsymbol{k}$, the π-component is always zero and all linear polarizations are equivalent. Now, the phase delay φ between $\boldsymbol{e}_x$ and $\boldsymbol{e}_y$ parametrizes a general polarization vector $\boldsymbol{\varepsilon}(\varphi) = \frac{1}{\sqrt{2}}\left(\boldsymbol{e}_x + e^{i\varphi}\boldsymbol{e}_y\right)$. An experimental study of the related selection rules is dicussed in section 5.2.4.

5.1.4 Calculation of Rabi frequencies

In a three-level system, the effective two-photon Rabi frequency $\widetilde{\Omega}_{\mathrm{ef}}$ coupling an initial state to a final state via an intermediate state amounts to $\widetilde{\Omega}_{\mathrm{ef}} = \frac{\widetilde{\Omega}_1\widetilde{\Omega}_2}{2\Delta}$. Here, $\widetilde{\Omega}_{1(2)}$ are the Rabi couplings from the final state to the intermediate state and from the intermediate state to the initial state and $\Delta \gg \widetilde{\Omega}_{1\,(2)}$ is the intermediate state detuning. The same formalism describes our PA, however, with more than one intermediate state and also several coupled asymptotic pair states within the macrodimer state. The coupling Hamiltonian reads

$$\hat{H}_L(\boldsymbol{E}) = -(\hat{\boldsymbol{d}}^{(1)} \otimes \mathbb{1}^{(2)} + \mathbb{1}^{(1)} \otimes \hat{\boldsymbol{d}}^{(2)}) \cdot \boldsymbol{E}, \tag{5.7}$$

with $\hat{\boldsymbol{d}}^{(1(2))}$ the dipole operators of both individual atoms forming the molecule. The molecular states $|\Psi_{\mathrm{Mol}}; \Omega^{\pm}_{g/u}\rangle = \sum_{i,j} c_{ij}(R)|r_i r_j\rangle$ consist of several asymptotic Rydberg pair states $|r_i r_j\rangle = |n_i L_i J_i m_{Ji}; n_j L_j J_j m_{Jj}\rangle$, mixed by the interatomic interaction. Since the UV laser can only excite Rydberg P-states, only pair states where $L_i = L_j = 1$ contribute. Acting with Eq. 5.7 on the initial ground state $|gg\rangle$ can only couple singly-excited states. As a consequence, the macrodimer states are coupled from $|gg\rangle$ by two-photon transitions via the two intermediate states where only one atom is excited, see also Fig 4.3 (b). This provides molecular Rabi frequencies

$$\widetilde{\Omega}_\nu = \langle gg|\hat{H}_L(\boldsymbol{E}) \left(\sum_k \frac{|r_k g\rangle\langle r_k g| + |g r_k\rangle\langle g r_k|}{2\Delta_k} \right) \hat{H}_L(\boldsymbol{E}) \sum_{ij} f^\nu_{ij}(R)|r_i r_j\rangle. \tag{5.8}$$

The Franck-Condon overlap first introduced in Eq. 4.13 now enters via state-dependent integrals

$$f^\nu_{ij} = \int \Phi^*_\nu(R) c^*_{ij}(R) \Phi_{\mathrm{rel}}(R) R^2 \mathrm{d}R \tag{5.9}$$

where the motional overlap is evaluated for each of the contributing pair states $|r_i r_j\rangle$ individually. Again, $\Phi_\nu(R)$ is the vibrational wave function of the molecular state and $\Phi_{\mathrm{rel}}(R)$ is the relative wave function before PA, in our case given by the Wannier state in the optical lattice. In principle, the presented coupling scheme is similar to the Rydberg blockade Hamiltonian introduced in Eq. 2.31. The main difference is the presence of a macrodimer state instead of an asympototic pair state, an additional interaction shift of the doubly-excited state, and the possibility to have several intermediate states.

For $|r_i r_j\rangle$ one finds that only the intermediate states $|g r_j\rangle$ for $k = j$ and $|r_i g\rangle$ for $k = i$ contribute with a coupling strength

$$\widetilde{\Omega}_{ij} = \frac{\widetilde{\Omega}_i \widetilde{\Omega}_j}{2} \left(\frac{1}{\Delta_i} + \frac{1}{\Delta_j} \right) = \widetilde{\Omega}_{ji}. \tag{5.10}$$

Here, $\Delta_{i/j}$ are detunings to either $36P_{1/2}$ or $36P_{3/2}$, dependent on the electron angular momentum $J_{i/j}$ of the states $|r_i\rangle$ and $|r_j\rangle$. The product of single-atom Rabi couplings $\widetilde{\Omega}_{i/j} = \frac{1}{\hbar}\langle r_{i/j}|\hat{\boldsymbol{d}} \cdot \boldsymbol{E}|g\rangle$ is the same for both possible paths.

In a typical experiment, the single-photon Rabi frequency between the ground state and one particular Rydberg state is calibrated at high precision. Different Rabi couplings vary due to different Clebsch-Gordan coefficients and reduced matrix elements, see section 3.7.3. Because their relations are well-known, all other coupling terms can be referenced to the experimentally calibrated one and Eq. 5.10 provides accurate predictions for

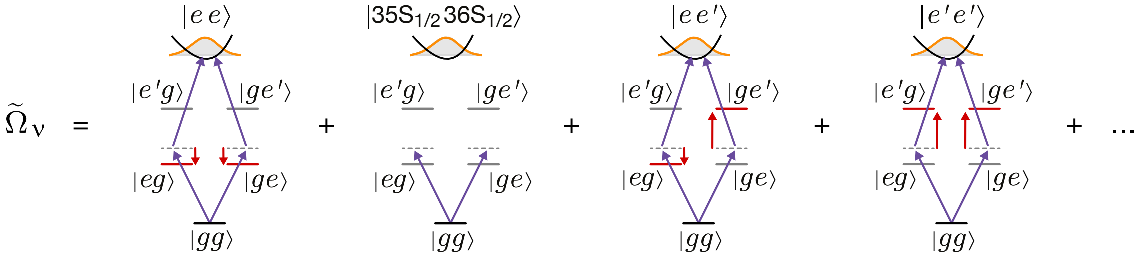

Figure 5.3: **Visualization of the coupling.** Throughout this thesis, macrodimer states are excited from the ground state $|gg\rangle$ via intermediate states where one atom populates excited states $|e\rangle$ or $|e'\rangle$. Following the convention introduced in section 4.1, states $|e, m_J\rangle$ and $|e', m_J\rangle$ represent Rydberg P-states nP_J with $J = 1/2$ and $J = 3/2$ and angular momentum projection m_J. The total coupling rate decouples into a sum of the contributions of the individual pair states $|r_i r_j\rangle$, which contribute via a product of single-atom Rabi frequencies. As indicated by the red color, one generally finds two intermediate states for each contributing pair state. The red arrows illustrate the two corresponding detunings. Due to selection rules, only Rydberg pair states with $L_i = L_j = 1$ can be coupled. In addition to the shown parameters, the coupling terms also depend on the single-atom angular momentum projections of the ground state and the Rydberg states and the light polarization.

the experimental coupling rates. Summing over all contributing states, the total coupling rate $\widetilde{\Omega}_\nu$ to the molecular state is

$$\widetilde{\Omega}_\nu = \sum_{ij} f_{ij}^{\nu} \widetilde{\Omega}_{ij} \approx f_\nu \sum_{ij} c_{ij} \widetilde{\Omega}_{ij}. \tag{5.11}$$

A visualization of the coupling process showing the intermediate states and the contributing pair states is shwon in Fig. 5.3. If the electronic state decomposition of the molecule remains roughly constant over the extension of the vibrational wave function, only a single Franck-Condon integral remains and f_ν can be calculated based on Eq. 4.13 . In this case, the motional overlap f_ν decouples from the electronic contribution to the Rabi coupling and contributes as an overall scaling factor. This is a good approximation for the results presented in section 5.2. Here, the excitation rates were studied for the narrow lowest vibrational state and the discussion focuses on the electronic structure. Later, studying higher vibrational modes in section 5.3, the approximation breaks down and the spatially-dependent optical couplings become important.

5.1.5 Interpretation

One implication of Eq. 5.10 and Eq. 5.11 is the conservation of inversion symmetry in the optical excitation process. As discussed in section 4.1.3 and 4.1.4, the molecular symmetries fix the relation between the coefficients c_{ij} and c_{ji} in the decomposition $|\Psi_{\mathrm{Mol}}; \Omega^{\pm}_{g/u}\rangle = \sum_{i,j} c_{ij} |r_i r_j\rangle$ introduced in Eq. 4.2. Since dipole matrix elements vanish for $\Delta L \neq \pm 1$, both ground state atoms $|gg\rangle$ with $L = 0$ can only couple to pair states $|r_i r_j\rangle$ with $L_{i/j} = 1$, yielding $c_{ij} = \pm c_{ji}$ for coupled ungerade (gerade) pair states. Using Eq. (5.6), one finds that only for an initial state which has the same inversion symmetry as the molecular state, both added coupling terms $\widetilde{\Omega}_{ij}$ and $\widetilde{\Omega}_{ji}$ in Eq. (5.11) interfere constructively, while they cancel each other otherwise.

Another implication of Eq. 5.10 is that asymptotic pair states $|36P_{1/2}36P_{3/2}\rangle = |ee'\rangle$ and $|e'e\rangle$ energetically located between $|ee\rangle$ and $|e'e'\rangle$ cannot be optically excited. From the two-photon coupling scheme introduced in Fig. 4.3 (**b**) one expects a two-photon resonance for intermediate state detunings equal to half the fine-structure splitting between $|36P_{1/2}\rangle$ and $|36P_{3/2}\rangle$ which both act as intermediate states in the coupling. However, because both intermediate state detunings have the opposite detuning, the contribution vanishes. For the state $|ee'\rangle$ these are $|eg\rangle$ and $|ge'\rangle$. It has also been experimentally confirmed that there are no striking spectroscopic signatures at these frequencies.

5.1.6 Excitation rates and correlation signal

For all experiments presented in this chapter, the coupling rates $\widetilde{\Omega}_\nu$ were below the calculated scattering rate based on Eq. 4.8. Hence, the photoassociation rate can be estimated using the steady-state solutions of the optical Bloch equations in the incoherent coupling regime [5]. On resonance, this yields a calculated photoassociation rate

$$\gamma_{\mathrm{th}} \approx \frac{\widetilde{\Omega}_\nu^2}{\gamma_{\mathrm{Mol}}}. \tag{5.12}$$

Throughout this chapter, macrodimers were observed by the correlation signal introduced in section 4.17. Because the molecular bond length of all studied molecular potentials at a principal quantum number of $n = 36$ is close to a lattice diagonal distance, the relevant correlation signals are $g^{(2)}_{1,\pm1}$ for both possible orthogonal orientations. In the experiments, Mott insulators at initial fillings of $94(2)\%$ were illuminated by a UV pulse for an illumination time t_{uv}. Here, the laser was tuned on resonance to different macrodimer resonances and the excitation was studied in a non-saturated regime where only a few molecules were excited. In that regime, experimental photoassociation rates can be estimated by

$$\gamma_{\mathrm{exp}} \approx g^{(2)}_{1,\pm1}/t_{\mathrm{uv}}. \tag{5.13}$$

In order to get statisticially significant values for $g^{(2)}_{1,\pm1}$, the experimental datasets covered about 200 images at identical conditions. A comparison of the experimental and theoretical scattering rates based on these equations can be found in Ref. [413].

5.2 Identifying molecular quantum numbers

In the following paragraphs, the previously presented theoretical framework will be experimentally tested using the quantum gas microscope. This reveals the state-specific optical excitation rates in the molecular frame. Furthermore, the response of the macrodimer state to an applied magnetic field will be tested. The results provide knowledge about the electronic structure of the molecular state and expose the molecular quantum numbers.

5.2.1 0_{u}^- molecules: The frame matters

In a first experiment, 0_u^- molecules are characterized using a potential energetically located at an interaction shift $U = 1.84\,\mathrm{GHz}$ above the $|36P_{1/2}36P_{1/2}\rangle$ reference asymptote, see Fig. 5.1 (**b**). The separaration from the higher-lying pair state $|36P_{3/2}36P_{3/2}\rangle$ is only $-2\Delta_{\mathrm{fs}} + U = -3.02\,\mathrm{MHz}$. At these large detunings, single-atom states $|e\rangle$ as well as $|e'\rangle$ contribute to the intermediate states in the optical coupling. Performing two-photon spectroscopy as described in section 4.2, one observes the vibrational resonances starting from initial states $|F = 2, m_F = -2\rangle$ as well as $|2, 0\rangle$. The observed vibrational series presented in Fig. 5.4 agrees well with the calculation. As expected from the Franck-Condon principle, one again finds that PA rates are maximal for the lowest vibrational quantum number ν and are higher for even compared to odd ν.

While the spectroscopic signal only provides excitation rates averaged over all possible orientations, hole-hole correlations $g^{(2)}_{\delta\boldsymbol{R}}$ provide information about the excitation rates for a specific molecular orientation, see Eq. 4.17. In order to access $g^{(2)}_{\delta\boldsymbol{R}}$, the laser was tuned on resonance to the lowest vibrational level. The UV laser was directing along one lattice diagonal direction and the polarization $\boldsymbol{\varepsilon}$ was linear in the atomic plane. As a consequence, the two possible molecular orientations are $\boldsymbol{R} \parallel \boldsymbol{\varepsilon}$ and $\boldsymbol{R} \perp \boldsymbol{\varepsilon}$. In order to have a well-defined initial quantization axis, a magnetic field $B = 1.0\,\mathrm{G}$ was applied. The prepared Mott insulators were illuminated with the UV until about three molecules were excited in the system. The atoms were first initialized in the ground state $|2, -2\rangle$ and the magnetic field was parallel to the light polarization $\boldsymbol{B} \parallel \boldsymbol{\varepsilon}$. The result is shown in the upper part of Fig. 5.4 (b). The observed correlation signal suggests that photoassociation is only possible for $\boldsymbol{R} \perp \boldsymbol{B}$. Interestingly, by rotating the magnetic field by 90°, also the correlation signal flips and molecules can again only be excited perpendicular to $\boldsymbol{B}$. All other parameters were kept identical. This dependence on the relative orientation between the molecule and an external field is a striking signature of the molecular states which have their own internal frame of reference.

These observations can be explained using the formalism presented above. Characterizing the excitation in the molecular frame, the UV light is π polarized for $\boldsymbol{\varepsilon} \parallel \boldsymbol{R}$ (i.e. $g^{(2)}_{1,1}$) and a superposition of $\sigma^{\pm}$-components for $\boldsymbol{\varepsilon} \perp \boldsymbol{R}$ (i.e. $g^{(2)}_{1,-1}$). For $\boldsymbol{R} \parallel \boldsymbol{B}$, the initial state in the molecule frame writes $|gg\rangle = |2, -2\rangle \otimes |2, -2\rangle = |-1_u\rangle_J \otimes |M_I = -3\rangle$ using the decomposition $|2, -2\rangle = |m_J = -1/2\rangle \otimes |m_I = -3/2\rangle$. For π polarization as well as $\sigma^{\pm}$ polarization, dipole selection rules do not allow a transition from $|-1_u\rangle_J$ with $M_J = -1$ to $\Omega = 0$ by the absorption of two photons. However, if the initial state would have a contribution from $|0_u\rangle_J$, excitation would be possible. From Fig. 5.2 (**a**), one can see that the state $|0_u\rangle_J$ has a large contribution in a frame rotated by $\beta = 90°$. Here, because the initial state $|2, -2\rangle$ appears different in the rotated frame of reference, molecules can be excited.

A systematic study

In a more detailed study, the relative angle β between the atom pairs and the magnetic field $B = 1.0\,\mathrm{G}$ was varied in five steps from 0° to 90°. We then quantified the PA signal by the observed hole-hole correlations along both diagonals $\boldsymbol{\varepsilon} \parallel \boldsymbol{R}$ and $\boldsymbol{\varepsilon} \perp \boldsymbol{R}$. The result for different initial states $|2, -2\rangle$, $|2, -1\rangle$ and $|2, 0\rangle$ is shown in Fig. 5.4 (**c**). In agreement with the previous findings, PA rates starting from $|2, -2\rangle$ vanish for $\beta = 0$ and are maximal for $\beta = 90°$ for both linear polarization configurations. Starting from $|2, -1\rangle$, one finds a strikingly different β-dependence, again consistent with the calculation. For $|2, 0\rangle$, the photoassociation does not depend on β any longer. The observed angular distributions are characteristic for 0_u^- potentials and can be attributed to the angular dependent electronic decomposition of the ground state in the molecular frame. Because for both

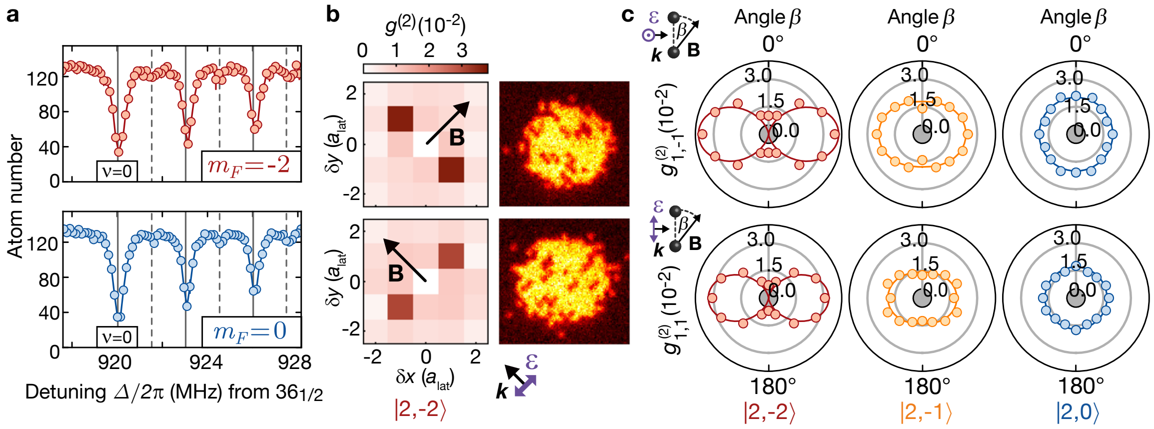

Figure 5.4: **Microscopic excitation signatures for 0_u^- molecules.** (**a**) The spectroscopic photoassociation signal can be observed starting from $|2,-2\rangle$ (red) and $|2,0\rangle$ (blue) and matches the calculated energies for even (odd) vibrational quantum numbers ν, indicated by solid (dashed) gray lines. **b** Comparing the hole-hole correlations $g^{(2)}_{\delta x,\delta y}$ starting from $|2,-2\rangle$ (red) for two orthogonal magnetic field orientations, one observes that excitation only occurs for atom pairs oriented perpendicular to the magnetic field. For both cases, a exemplary image from the quantum gas microscope from which the correlation strengths are calculated is included. (**c**) Rotating the orientation of the magnetic field for three different initial states, one finds excitation curves characteristic for 0_u^-, which depend on the initial state and the polarization $\boldsymbol{\varepsilon}$. As indicated in (**b**), $\boldsymbol{\varepsilon}$ was parallel (perpendicular) to $\boldsymbol{R}$ for $g^{(2)}_{1,\pm 1}$. Solid lines are theoretically expected angular dependencies, where the overall amplitude was left as a fitting parameter. All error bars on the data points denote one standard error of the mean and gray filled circles indicate the expected background correlation signal. Figure adapted from Ref. [413].

light polarizations only the initial state $|0_u\rangle_J$ can be excited to the $\Omega = 0$ macrodimer state, the observed dependencies match the contributions $|c_u^0|^2$ in Fig. 5.2 (**a**).

Furthermore, it has been observed that the PA rates in Fig. 5.4 (c) for $\boldsymbol{\varepsilon} \parallel \boldsymbol{R}$ reach only 83% of the value for $\boldsymbol{\varepsilon} \perp \boldsymbol{R}$. This is close to the theoretical value of 87% obtained from evaluating the sum Eq. 5.11 for the electronic decomposition of this specific 0_u^- potential.

5.2.2 0_g^+ molecules: Entangling nuclei

In a second experiment, 0_g^+ molecules are studied using a molecular potential shifted by $U = 0.34\,\text{GHz}$ relative to the reference asymptote, see Fig. 5.1 (**b**). In contrast to the previous discussion of 0_u^- molecules where molecular excitation was possible for both initial states $|2,-2\rangle$ and $|2,0\rangle$, one finds that the vibrational series can now only be observed starting from $|2,0\rangle$, see Fig. 5.5 (**a**). Because of the conservation of inversion symmetry, only the state $|0_g\rangle_J = 1/\sqrt{2}\,(|\uparrow\downarrow\rangle_J - |\downarrow\uparrow\rangle_J)$ can contribute to the excitation. For $\beta = 0$, the initial state $|2,-2\rangle \otimes |2,-2\rangle = |-1_u\rangle_J \otimes |M_I = -3\rangle$ with $|-1_u\rangle_J = |\downarrow\downarrow\rangle_J$ has no contribution of $|0_g\rangle_J$. Starting from $|-1_u\rangle_J$, all terms in Eq. 5.11 cancel each other because of the shape of the contributing symmetrized asymptotic pair states, see also Eq. 4.4 and Eq. 4.6. Because the state $|0_g\rangle_J$ is formally equivalent to a rotationally invariant spin singlet, the contribution c_g^0 is independent of β, see also Fig. 5.1 (**b**,**c**). As a consequence, excitation

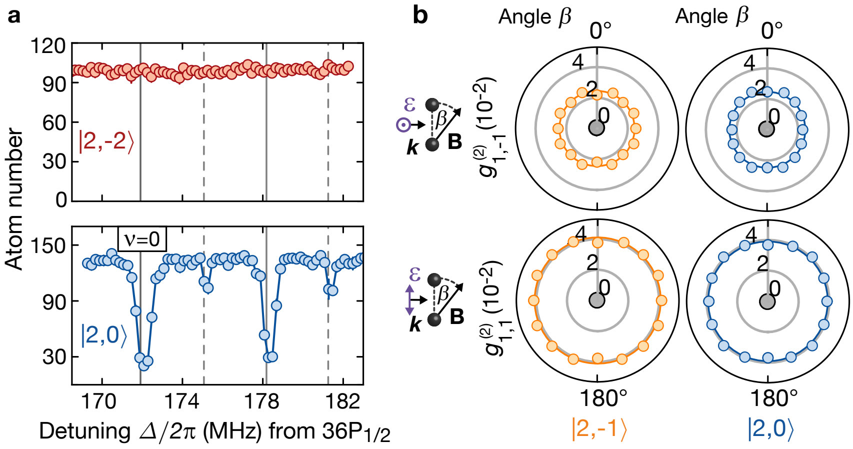

Figure 5.5: **Excitation signatures for 0_g^+ molecules.** (**a**) Because the electronic and nuclear angular momenta in the ground state $|F = 2, m_F = -2\rangle = |\frac{1}{2}, -\frac{1}{2}\rangle_J \otimes |\frac{3}{2}, -\frac{3}{2}\rangle_I$ separate, the coupling vanishes. The vertical gray lines denote the calculated vibrational energies for even (solid) and odd (dashed) vibrational quantum numbers ν. (**b**) Only the fraction of the ground state in the inversion eigenstate $|0_g\rangle_J$ can take part in the excitation. For the ^{87}Rb ground state used here, $|0_g\rangle_J$ is rotationally invariant. In contrast to 0_u^- molecules, this leads to excitation rates that are independent of β. However, the excitation rates still depend on the molecular orientation relative to the polarization. In agreement with the calculations, excitation rates are larger for $\boldsymbol{\varepsilon} \parallel \boldsymbol{R}$ compared to $\boldsymbol{\varepsilon} \parallel \boldsymbol{R}$. All error bars on the data points denote one standard error of the mean and gray filled circles indicate the expected background correlation signal. Figure adapted from Ref. [413].

starting from $|2, -2\rangle$ is generally not possible.

The situation changes starting from $|2, 0\rangle$ and $|2, -1\rangle$. Now, because of the hyperfine interaction in the ground state, one finds a finite contribution of $|0_g\rangle_J$. A systematic study verifies the expected independence of the angle β, see Fig. 5.5 (**b**).

In addition to these signatures that are characteristic for all 0_g^+ macrodimers, Fig. 5.5 (**b**) also suggests that the excitation rates is larger for $\boldsymbol{\varepsilon} \parallel \boldsymbol{B}$ compared to $\boldsymbol{\varepsilon} \perp \boldsymbol{B}$. This is again specific for the chosen 0_g^+ potential and agrees with a calculation of the molecular Rabi frequencies using Eq. 5.11. From the decomposition in Eq. 5.6 one can furthermore infer that exciting a 0_g^+ macrodimer projects the nuclear spin state into $|\Psi_g^0\rangle_I$. For $|2, 0\rangle$ and $\beta = 0$, one finds the non-separable state $|\Psi_g^0\rangle_I = 1/\sqrt{2}\left(|\frac{3}{2}, \frac{1}{2}\rangle_I \otimes |\frac{3}{2}, -\frac{1}{2}\rangle_I - |\frac{3}{2}, -\frac{1}{2}\rangle_I \otimes |\frac{3}{2}, \frac{1}{2}\rangle_I\right)$. Here, $|\frac{3}{2}, m_I\rangle$ are the single-atom nuclear spin states of both atoms. As a consequence, exciting macrodimers also provides an interesting possibility to entangle nuclear spins at micrometer distance. Similar entangled nuclear spin pairs can be found for other binding potentials $|\Omega_{g/u}^{\pm}|$. Unfortunately, there was no possibility to experimentally verify this entanglement in this dissertation.

5.2.3 1_u molecules: Magnetic field response & hyperfine coupling

In a third experiment, 1_u molecules are characterized based on the molecular potential shifted by $U = 0.73\,\mathrm{GHz}$ relative to $|36P_{1/2}36P_{1/2}\rangle$, see Fig. 5.1 (**b**). Performing atom loss spectroscopy at zero field again shows the agreement between the observed vibrational resonances with the calculated vibrational energies, see Fig. 5.6 (**a**). The previous discussion suggests to measure again the characteristic $\beta-$dependent excitation rates, see Fig. 5.1 (**d**). Because this is now well understood, the response to applied magnetic fields indicated in Fig. 5.1 (**f**) is presented instead. A finite magnetic field does not induce energy shifts for $|\Omega| = 0$ potentials to first order. Also second order couplings are typically weak because other pair potentials are detuned by hundreds of megahertz. This changes for $|\Omega| \neq 0$, where the two degenerate states with angular momentum projections $\pm|\Omega|$ are expected to shift in opposite directions if the magnetic field has components parallel to the molecular axis.

Orientation-dependent Zeeman shift

In order to show this effect, a magnetic field of $B = 2.0\,\mathrm{G}$ was applied perpendicular to the propagation direction of the UV-light. Because the UV laser propagates along the diagonal direction, the molecular alignment will be either parallel or perpendicular to $\boldsymbol{B}$. The resulting spectroscopic signal of the lowest vibrational level is shown in Fig. 5.6 (**b**) for linear polarization either pointing out of the atomic plane or laying in the atomic plane. Furthermore, the signal was recorded for all three initial states $|2,-2\rangle$, $|2,-1\rangle$ and $|2,0\rangle$. While the strength of the different resonance profiles depends on the initial state and the polarization, one can generally identify three available spectroscopic signatures. The observed splitting of two degenerate pair potentials into three lines is possible because the orientation of the molecule adds as an additional parameter and is discussed in the following paragraphs.

At the current status, a diagonalization of the interaction Hamiltonian at finite fields is not feasible at the required precision. This problem appears because the magnetic field breaks the molecular symmetry of the interaction Hamiltonian, leading to a mixing of different molecular quantum numbers and an increase of the Hilbert space dimension. However, for the energetically isolated 1_u potential where only the two states $|\Psi_{\mathrm{Mol}}; \pm 1_u\rangle = \sum_{i,j} c_{ij}^{\pm 1} |r_i r_j\rangle$ with $\Omega = \pm 1$ are relevant, perturbation theory is expected to provide solid results. Combining the coupling term for both contributing atoms, the perturbation $\hat{H}_1$ can be written as

$$\hat{H}_1 = \hat{H}_B^{(1)} \otimes \mathbb{1}^{(2)} + \mathbb{1}^{(1)} \otimes \hat{H}_B^{(2)}, \tag{5.14}$$

with single particle operators

$$\hat{H}_B = \mu_B \left(g_S \hat{\boldsymbol{S}} + g_L \hat{\boldsymbol{L}} \right) \cdot \boldsymbol{B}. \tag{5.15}$$

Here, $\hat{\boldsymbol{L}}$ and $\hat{\boldsymbol{S}}$ are orbital angular momentum and electronic spin operators, g_S and g_L the corresponding Landé factors. Furthermore, the total angular momentum of the electron is given by $\hat{\boldsymbol{J}} = \hat{\boldsymbol{L}} + \hat{\boldsymbol{S}}$. The angular momentum operators perpendicular to $\boldsymbol{R}$ can be expressed as $\hat{L}^{\pm} = \hat{L}^x \pm i\hat{L}^y$ and $\hat{S}^{\pm} = \hat{S}^x \pm i\hat{S}^y$. In this representation, one can see that $\hat{H}_B$ can only couple states with $\Delta\Omega = 0, \pm 1$. As a consequence, both degenerate states $\Omega = \pm 1$ of the 1_u potential remain uncoupled. However, the $z-$component of the magnetic field which is parallel to $\boldsymbol{R}$ can induce a first order Zeeman shift

$$\Delta E_Z = g_{\mathrm{eff}} \mu_B \Omega B_z. \tag{5.16}$$

Using $g_S \hat{S}_z + g_L \hat{L}_z = g_L \hat{J}_z + (g_S - g_L)\hat{S}_z$ with $g_L = 1$ and $g_S \approx 2$, the effective molecular

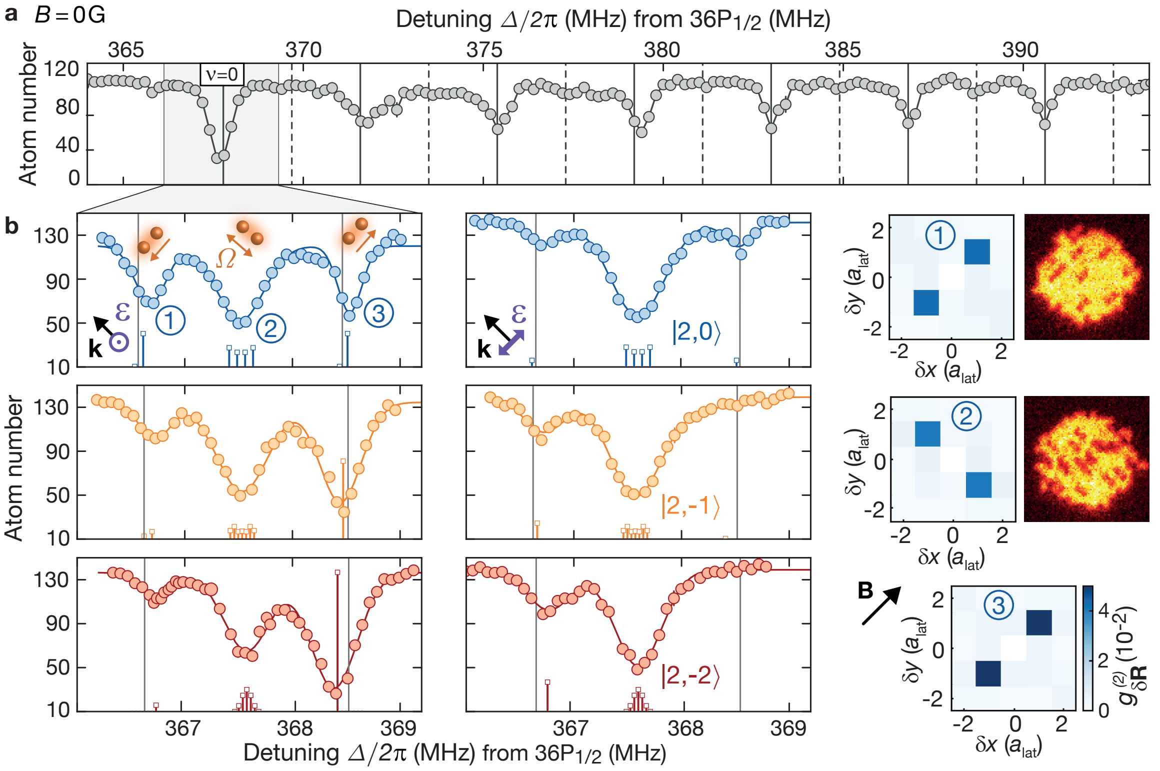

Figure 5.6: **Molecular Zeeman shift & hyperfine coupling of macrodimers for $n = 36$.** (**a**) At zero field, the vibrational spectrum for a 1_u potential features narrow resonances as observed for molecular potentials with $\Omega = 0$. As predicted, the vibrational modes ν are observed at detunings half the calculated vibrational energies U_ν (vertical gray lines). Solid (dashed) lines indicate even (odd) ν. (**b**) Measurements at finite magnetic field reveal a splitting of the lines. The two outer resonances can be associated with a molecular alignment $\boldsymbol{R} \parallel \boldsymbol{B}$, molecules excited at the central resonance have an alignment $\boldsymbol{R} \perp \boldsymbol{B}$, as shown in the recorded correlation signals. The signal was recorded for a linearly polarized UV laser either oscillating perpendicular (left) or parallel (right) to the atomic plane. The difference between the data and a calculation accounting only for the electronic state decomposition (gray solid line) can be explained by the hyperfine interaction of the admixed Rydberg pair states (colored bars). The calculated relative coupling strengths are indicated by the heights of the bars (arbitrary units) and agrees with the observation. Figure adapted from Ref. [413].

g-factor can be written as

$$\begin{aligned} g_{\text{eff}} = \Big| \pm 1 &+ \langle \Psi_{\text{Mol}}; \pm 1_u | \hat{S}_z^{(1)} \otimes \mathbb{1}^{(2)} | \Psi_{\text{Mol}}; \pm 1_u \rangle \\ &+ \langle \Psi_{\text{Mol}}; \pm 1_u | \mathbb{1}^{(1)} \otimes \hat{S}_z^{(2)} | \Psi_{\text{Mol}}; \pm 1_u \rangle \Big|, \end{aligned} \tag{B17}$$

yielding $g_{\text{eff}} \approx 0.66$ after expanding the contributing asymptotic states $|r_i r_j\rangle$ into uncoupled spin and orbital angular momenta.

From this analysis, the experimental observation can be understood. For $\boldsymbol{R} \parallel \boldsymbol{B}$, both degenerate states split up by an energy shift $\pm\Delta E_Z$. For $\boldsymbol{R} \perp \boldsymbol{B}$, the energy shift vanishes and both 1_u molecular states remain degenerate. The correlation signals $g^{(2)}_{\delta\boldsymbol{R}}$ plotted below the spectroscopic signal in Fig. 5.6 (**b**) confirm this interpretation. The calculated line

nL_J	$nS_{1/2}$	$nP_{1/2}$	$nP_{3/2}$	$nD_{3/2}$	$nD_{5/2}$
$A_{\mathrm{hfs}}^{\mathrm{ref}}$ (MHz)	2.14 ($28S_{1/2}$)	59.9 ($7P_{1/2}$)	4.05 ($9P_{3/2}$)	4.53 ($7D_{3/2}$)	2.2 ($7D_{5/2}$)

Table 5.1: **Hyperfine constants for Rydberg states.** The hyperfine constants $A_{\mathrm{hfs}}^{r_i} \propto (n^\star)^{-3}$ are calculated by extrapolating from reference values $A_{\mathrm{hfs}}^{\mathrm{ref}}$ obtained from the literature [122, 431] using $n^* = n - \delta(n, L, J)$, $\delta(n, L, J) \approx \delta_0 + (\delta_0)^2 / (n - \delta_2)^2$, and $A_{\mathrm{hfs}}^{r_i} = (n_{\mathrm{ref}}^\star)^3 / (n_i^\star)^3 \, A_{\mathrm{hfs}}^{\mathrm{ref}}$ [432]. Contributions from D-states were included but affected the effective hyperfine coupling A_{eff} of the macrodimer state by less than 1%, states with $L > 2$ were neglected.

splitting for the oriented molecules $\boldsymbol{R} \parallel \boldsymbol{B}$ from the non-shifted reference using Eq. 5.20 is indicidated as vertical gray lines in the spectroscopies. Here, the factor of two entering from the two-photon spectroscopy has been taken into account. In the spectroscopy, changing the single-photon detuning Δ affects the two-photon detuning by the double amount. Overall, the observations agree with the calculation. However, a closer look reveals a systematic deviation which will be explained in the next paragraph.

Hyperfine structure of macrodimers

Comparing the deviations between the observed resonance shift and the calculated Zeeman shifts ΔE_Z for $|2, 0\rangle$ in Fig. 5.6 (**b**), one finds a significant asymmetry between $\Omega = \pm 1$. Starting from $|2, -2\rangle$, the splitting is symmetric but significantly below the expectation. Additionally, the line splitting depends sligthly on the light polarization. These observations motivate to extend the calculations by the hyperfine coupling terms for the macrodimer state. This adds a term

$$\hat{H}_2 = \hat{H}_{\mathrm{hfs}}^{(1)} \otimes \mathbb{1}^{(2)} + \mathbb{1}^{(1)} \otimes \hat{H}_{\mathrm{hfs}}^{(2)} \tag{5.18}$$

to the Hamiltonian of the system. The single-particle hyperfine Hamiltonians were included via

$$\hat{H}_{\mathrm{hfs}} = \sum_i A_{\mathrm{hfs}}^{r_i} |r_i\rangle\langle r_i| \hat{\boldsymbol{I}} \cdot \hat{\boldsymbol{J}}. \tag{5.19}$$

Here, $\hat{\boldsymbol{I}}$ is the nuclear spin operator and operators $|r_i\rangle\langle r_i|$ project the corresponding terms in the molecular wave function to the associated hyperfine coupling term $A_{\mathrm{hfs}}^{r_i}$. The Zeeman interactions of both isolated nuclei with the magnetic field were neglected because of the small g-factor $g_I = 9.95 \times 10^{-4}$ [431]. In particular for Rydberg P-states and D-states, there exists only limited experimental data for hyperfine couplings at higher principal quantum numbers. However, the hyperfine constants $A_{\mathrm{hfs}}^{r_i}$ can be calculated based on measurements at lower principal quantum numbers and known quantum defects, see Table 5.1. For $n = 36$, one expects $A_{\mathrm{hfs}}^{36S_{1/2}} \approx 487\,\mathrm{kHz}$, $A_{\mathrm{hfs}}^{36P_{1/2}} \approx 132\,\mathrm{kHz}$ and $A_{\mathrm{hfs}}^{36P_{3/2}} \approx 28\,\mathrm{kHz}$.

Extending the wave function by the nuclear spin, the relevant Hilbert space is given by $\{|\Psi_{\mathrm{Mol}}; \pm 1_u\rangle \otimes |m_{I_1}, m_{I_2}\rangle\}$. Here, $m_{I_{1(2)}}$ are the nuclear spin orientations of both atoms. Accounting for both molecular states $\Omega = \pm 1$ and the four nuclear spin projections of

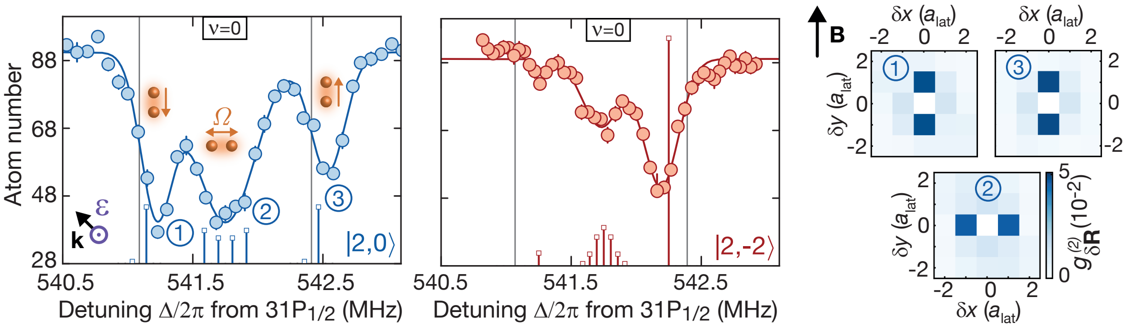

Figure 5.7: **Molecular Zeeman shift & hyperfine coupling of macrodimers for $n = 31$.** At the lowest vibrational mode of the corresponding 1_u potential blue-detuned from $31P_{1/2}$, one again finds a splitting of the molecular resonances in the presence of a magnetic field of $B = 1.5\,\mathrm{G}$. Here, $\boldsymbol{\varepsilon}$ was directing out of the atomic plane and the magnetic field was applied along the lattice direction. Because of the lower principal quantum number, the vibrational series starts at higher detunings and the bond length is reduced to a value close to the lattice constant a_{lat}. The correlation signal at the three resonances, recorded with $|2,0\rangle$ as an initial state, shows correlated loss rates at nearest neighbor distance. While two outer resonances correspond to molecular alignment $\boldsymbol{R} \parallel \boldsymbol{B}$, the molecular alignment at the central line is perpendicular to $\boldsymbol{B}$. Furthermore, the hyperfine coupling strength almost doubled while the Zeeman interaction remained essentially the same. As a consequence, the asymmetric splitting starting from $|2,0\rangle$ and the underestimated splitting starting from $|2,-2\rangle$ are even more prominent. Again, the gray lines indicates the calculated line positions accounting only for the electronic structure while the position of the colored bars also accounts for the hyperfine splitting. The height of the bars represents the calculated relative line strength. Figure adapted from Ref. [413].

both atoms, one finds 32 states. It is convenient to express the hyperfine interaction as $\hat{\boldsymbol{I}}\cdot\hat{\boldsymbol{J}} = \frac{1}{2}(\hat{I}^-\hat{J}^+ + \hat{I}^+\hat{J}^-) + \hat{I}^z\hat{J}^z$, with $\hat{J}^\pm = \hat{J}^x \pm i\hat{J}^y$ and $\hat{I}^\pm = \hat{I}^x \pm i\hat{I}^y$. As for the magnetic field, one finds that none of the contributing states can be coupled by $\hat{H}_1$ and $\hat{H}_2$ and all shifts are diagonal.

As a result, all angular momentum operators can be replaced by their $z-$components. The hyperfine energy shifts are then obtained by

$$\Delta E_{\mathrm{hfs}} = A_{\mathrm{eff}}(m_{I_1} + m_{I_2})\frac{\Omega}{2}, \tag{B20}$$

with the effective hyperfine interaction strength

$$A_{\mathrm{eff}} = \sum_{i,j} |c_{ij}^{\pm 1}|^2 (A_{\mathrm{hfs}}^{r_i} m_{Ji} + A_{\mathrm{hfs}}^{r_j} m_{Jj}). \tag{5.21}$$

The hyperfine interaction of the macrodimer state increases from the contributing S-states and decreases from contributions from higher angular momenta. Using the electronic structure of the studied 1_u potential, the equation provides $A_{\mathrm{eff}} \approx 127\,\mathrm{kHz}$. Because the molecular bond lengths and the lattice spacing are larger than the contributing Rydberg orbits ($\approx 130\,\mathrm{nm}$), the calculations only consider the coupling of the Rydberg electrons to the nucleus they are bound to.

Using the initial nuclear spin wave function before photoassociation and the dipole selection rules for different light polarizations, one can now calculate the expected hyperfine interaction shifts. The calculated line positions are shown as colored bars in Fig. 5.6 (**b**). The height of the bars indicates the calculated photoassociation rates, referenced to the strongest transition from $|2,-2\rangle$ to $\Omega = +1$ for $\boldsymbol{R} \parallel \boldsymbol{B}$ and orthogonal polarization. Now, the deviations from the previously calculated line position can be explained and the observations agree with the calculations. Comparing the three resonances, one also finds that the central line has typically a larger linewidth. This is in agreement with the expectation and originates from the perpendicular orientation between $\boldsymbol{R}$ and $\boldsymbol{B}$. Here, rotating the initial states into the molecular frame leads to a larger number of contributing nuclear spin orientations, which differ in their hyperfine interaction and therefore broaden the resonance.

To further verify the presence of the hyperfine coupling, also the magnetic field splitting for the corresponding 1_u potential at the blue-detuned side of the lower-lying Rydberg state $31P_{1/2}$ has been measured, see Fig. 5.7 (**c**). The reduced bond length close to the lattice constant now leads to a correlation signal peaking at a distance of a_{lat}. This requires a magnetic field applied along the lattice direction in order to keep the conditions identical to Fig. 5.6 (**b**). While $g_{\text{eff}} \approx 0.63$ remains almost the same, the hyperfine interaction $A_{\text{eff}} \approx 216\,\text{kHz}$ is significantly larger. This leads to an even more striking deviation from the calculation neglecting the hyperfine interaction. Because the linear UV polarization was pointing out of the atomic plane, the dataset can be compared to the scans at the left side in Fig. 5.6 (**b**). For $n = 31$ and an initial state $m_F = 0$, it has been reproducibly observed that the $\Omega = -1$ resonance appears stronger than the $\Omega = +1$ resonance. Furthermore, the calculations now seem to slightly underestimate the effect of the hyperfine interaction.

5.2.4 Identification via polarization

Here, the role of the light polarization on the photoassociation process is discussed in more detail. The discussion follows the conventions introduced in section 5.1.3. The oriented molecular states, the conservation of angular momentum during photoassociation enables to measure the molecular quantum number Ω.

Linear polarization

The relative height of the two outer resonances $\Omega = \pm 1$ for $\boldsymbol{R} \parallel \boldsymbol{B} \perp \boldsymbol{k}$ in Fig. 5.6 (**b**) allows one to study how photoassociation differs between π polarization and $\sigma^{\pm}$ polarization. Starting from $|2,0\rangle$, all four states in Eq. 5.6 are equally populated, see also Fig. 5.2. For out-of-plane polarization, the states $\Omega = \pm 1$ are excited from $|\mp 1_u\rangle_J$ using two $\sigma-$ polarized photons. For in-plane polarization, the states $\Omega = \pm 1$ are excited from $|\pm 1_u\rangle_J$ using two π polarized photons. Evaluating Eq. 5.11, the larger Clebsch-Gordan coefficients contributing for out-of-plane polarization lead to a larger signal. Additionally, because the nuclear spin states are different for $|\mp 1_u\rangle_J$, the hyperfine couplings excite macrodimer states that are sligthy shifted in energy.

Starting from $|2,-2\rangle$, the initial state for $\boldsymbol{B} \parallel \boldsymbol{R}$ is $|-1_u\rangle_J$. For out-of-plane polarization, the $\Omega = +1$ state is strongly coupled by the absorption of two σ^+ photons. The excitation rate of the $\Omega = -1$ molecular state which requires one σ^+ and one σ^- photon is supressed. Here, the number of pair states $|r_i r_j\rangle$ contributing to the optical coupling is limited because

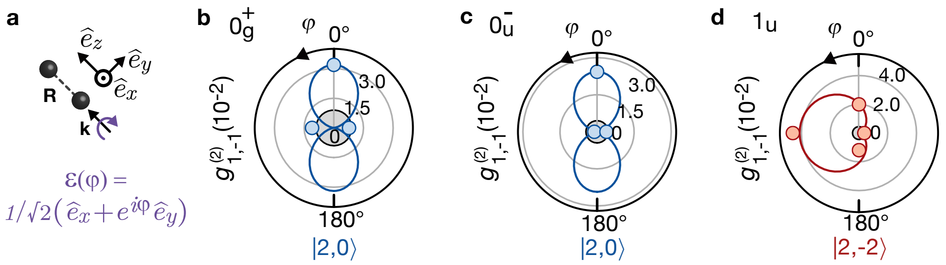

Figure 5.8: **Identifying Ω from polarization dependent excitation rates.** (**a**) The spatial arrangement $\boldsymbol{R} \parallel \boldsymbol{k}$ allows one to study photoassociation using σ^- and σ^+ polarziation. For the two potentials 0_g^+ (**b**) and 0_u^- (**c**) with $\Omega = 0$ one finds that photoassociation reaches a maximum for linear polarization $\boldsymbol{\varepsilon} \perp \boldsymbol{R}$. (**d**) Exciting 1_u macrodimer states with $\Omega = +1$ from $|2,-2\rangle$, one finds a strong maximum for σ^+ polarization. In all three plots, the correlation signal $g^{(2)}_{1,-1}$ quantifies the excitation rate, see Eq. 5.13. Gray filled circles represent the observed background correlation signal. Figure adapted from Ref. [413].

it requires a single-atom Rydberg states with $J = \frac{3}{2}$ and $m_J = -\frac{3}{2}$, see also Fig. 5.3. For in-plane polarization, the $\Omega = +1$ resonance vanishes because π polarization does not allow excitation from $|-1_u\rangle_J$.

Circular polarization

Realizing σ^+ or σ^- polarized light requires the interatomic axis to be aligned with $\boldsymbol{R} \parallel \boldsymbol{k}$. Here, the light polarization can be parametrized as $\varepsilon(\varphi) = \frac{1}{\sqrt{2}}(\boldsymbol{e}_x + e^{i\varphi}\boldsymbol{e}_y)$, see Fig. 5.8 (**a**). For $\varphi = 0$, the light is linearly polarized and therefore a superposition of $\sigma^\pm$. For $\varphi = -90°$, the light is σ^+ polarized. The dependence of the photoassociation on φ was studied by measuring the correlation signal $g^{(2)}_{1,-1}$ for $\boldsymbol{R} \parallel \boldsymbol{k}$ at the lowest vibrational resonance for the three previously studied molecular states 0_g^+, 0_u^- with $\Omega = 0$ and 1_u with $\Omega = +1$ blue-detuned from $|36P_{1/2}\rangle$, see Fig. 5.8 (**b,c,d**). Before performing the experiments, the light polarization was calibrated comparing the coupling strength to magnetic sublevels of single-photon Rydberg transitions, see section 3.7.3.

First, the two potentials 0_g^+ and 0_u^- with $\Omega = 0$ were studied. The initial state was $|2,0\rangle$. Here, the magnetic field orientation β is irrelevant, see also Fig. 5.2 (**c**). Because π polarization cannot be realized for $\boldsymbol{R} \parallel \boldsymbol{k}$, the two-photon excitation requires one σ^- and one σ^+ photon. For σ^+ or σ^- polarization, the excitation rate vanishes. For the 1_u potential, a magnetic field $\boldsymbol{B} \parallel \mathbf{k}$ with $B \approx 0.5$ G was applied to energetically separate the two resonances $\Omega = \pm 1$ for molecular orientations parallel to $\boldsymbol{k}$. In contrast to Fig. 5.4 (**b**) where the magnetic field direction $\boldsymbol{B} \perp \boldsymbol{k}$ induced a separation for the perpendicular orientation, this now requires to apply the field parallel to $\boldsymbol{k}$. The measurements show that photoassociation vanishes for σ^- polarization and reaches a strong maximum for σ^+ polarization. This particular configuration of initial and final states, light polization, and spatial arrangement where $|2,-2\rangle$ atoms are excited into $\Omega = +1$ molecules by absorbing two σ^+ photons is special because all contributing Clebsch-Gordan coefficients reach a maximum. It will be used to maximize macrodimer excitation rates in chapter 7 and 8.

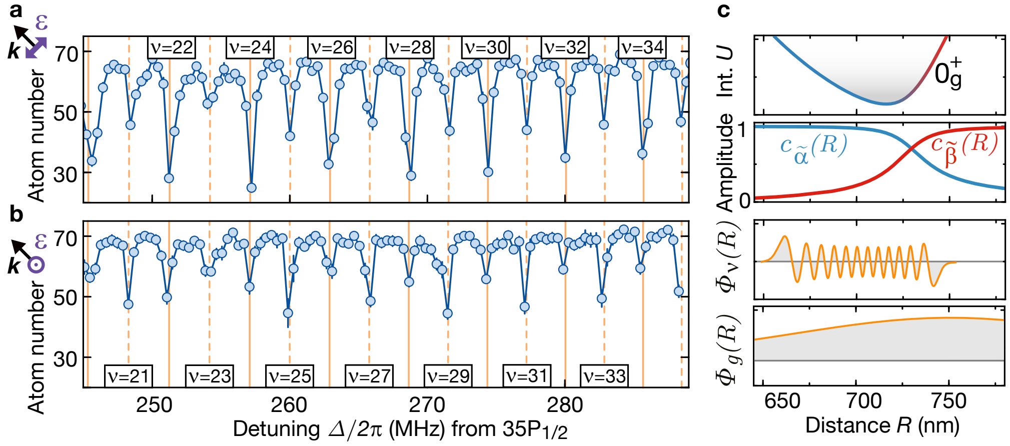

Figure 5.9: **Spatially dependent electronic state amplitudes.** (**a**) A zoom into the spectroscopic signal presented in Fig. 4.4 for the 0_g^+ potential blue-detuned from $35P_{1/2}$ for a UV laser linearly polarized in the atomic plane. As observed for most other binding potentials, one finds a stronger signal for even vibrational quantum numbers. (**b**) For a linear polarization pointing out of the atomic plane, odd vibrational modes are coupled more strongly. For both spectroscopies, the distance between neighboring data points is larger than the widths of the vibrational resonances. In order to be able to compare the different datasets, a frequency sweep covering the range between the data points during the UV illumination time ensured an identical spectral weight at the individual resonances. All error bars on the data points denote one s.e.m. (**c**) This signature can be explained using the strong spatially dependent state decomposition of this specific potential and the polarization-dependent two-photon Rabi frequencies $\widetilde{\Omega}_{\tilde{\alpha}}$ and $\widetilde{\Omega}_{\tilde{\beta}}$. Figure adapted from Ref. [411].

5.3 Distance-dependent electronic structure

After presenting a rigorous theoretical and experimental benchmark of photoassociation into different macrodimer states $|\Omega^{\pm}_{g/u}|$, it is now worth to have a more detailed look into the previously studied 0_g^+ potential blue-detuned from $35P_{1/2}$, see section 4.2. The spectroscopy presented in Fig. 4.4 was performed for linear UV polarization in the atomic plane. A zoom into the spectroscopic signal at higher vibrational quantum numbers ν is shown in Fig. 5.9 (**a**). In agreement with the Franck-Condon principle and also other studied macrodimer potentials, one generally finds larger excitation rates for even ν. Interestingly, performing the spectroscopy for a linear polarization pointing out of the atomic plane, one finds stronger excitation rates for odd ν, see Fig. 5.9 (**b**). This observation contradicts the approximated expression on the right side of Eq. 5.11 where the Franck-Condon integral contributes via an overall scaling factor because the electronic structure is assumed to be constant over the spatial extension of the vibrational wavepacket.

Studying the electronic structure of the pair potentials which originates from the particularly sharp avoided crossing between the potentials $|\tilde{\alpha}\rangle$ and $|\widetilde{\beta}\rangle$, one finds an abrupt change at the binding potential minimum. In Fig. 5.9 (**c**) one can see that the coefficient $c_{\tilde{\alpha}}$ dominates the potential at the left side while the coefficient $c_{\tilde{\beta}}$ dominates at the right side. Accounting for this spatial dependence of the specific 0_g^+ potential, the optical coupling

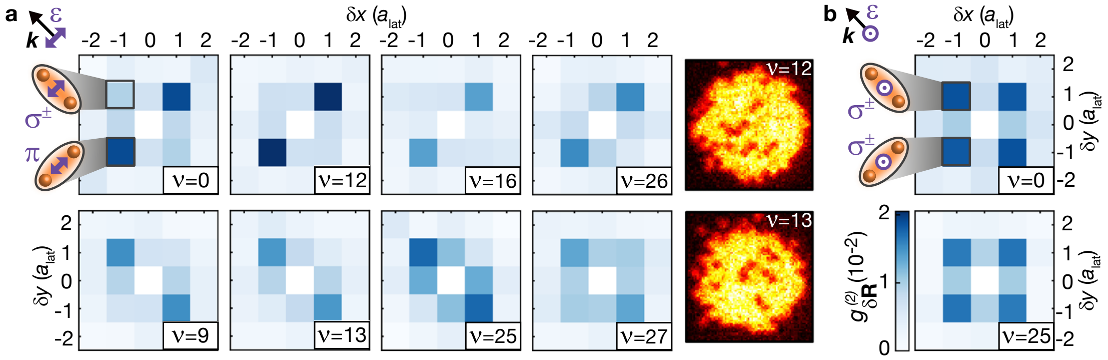

Figure 5.10: **Molecular alignment via vibrational state parity** (**a**) Evaluating $g^{(2)}_{\delta \boldsymbol{R}}$ after illuminating the atoms with UV light polarized in the atomic plane for various macrodimer lines ν confirms the understanding obtained from the spectroscopy. Whereas the excitation rate $\gamma_{\|}$ along the polarization of the excitation laser dominates for even vibrational states, odd states favor molecule excitation $\gamma_{\perp}$ perpendicular to the polarization. For both cases, an exemplary image from the quantum gas microscope is included. As before, the light is π polarized for $\boldsymbol{\varepsilon} \parallel \boldsymbol{R}$ and $\sigma^{\pm}$ polarized for $\boldsymbol{\varepsilon} \perp \boldsymbol{R}$. (**b**) For out-of-plane polarization, there is no longer a preferred direction and one observes equal correlations for both diagonal directions. Figure adapted from Ref. [411].

rate using the left side of Eq. 5.11 writes

$$\widetilde{\Omega}_{\nu} = f^{\nu}_{\widetilde{\alpha}}\widetilde{\Omega}_{\widetilde{\alpha}} + f^{\nu}_{\widetilde{\beta}}\widetilde{\Omega}_{\widetilde{\beta}}. \tag{5.22}$$

Here, $f^{\nu}_{\widetilde{\alpha}} = \int \Phi^{\star}_{\nu}(R) c^{\star}_{\widetilde{\alpha}}(R) \Phi_{\text{rel}}(R) R^2 \mathrm{d}R$ and $f^{\nu}_{\widetilde{\beta}} = \int \Phi^{\star}_{\nu}(R) c^{\star}_{\widetilde{\beta}}(R) \Phi_{\text{rel}}(R) R^2 \mathrm{d}R$ are the Franck-Condon factors of both pair potentials $|\widetilde{\alpha}\rangle$ and $|\widetilde{\beta}\rangle$. Because the motional ground state wave function $\Phi_{\text{rel}}(R)$ is much broader than the states $\Phi_{\nu}(R)$, it is intuitively clear that the relative sign between $f^{\nu}_{\widetilde{\alpha}}$ and $f^{\nu}_{\widetilde{\beta}}$ is the same for even ν and opposite for odd ν. Calculating the couplings rates into the pair potentials $\widetilde{\Omega}_{\widetilde{\alpha}}$ and $\widetilde{\Omega}_{\widetilde{\beta}}$, one finds a positive relative sign for $\boldsymbol{\varepsilon} \parallel \boldsymbol{R}$ (π polarization) and a negative relative sign for $\boldsymbol{\varepsilon} \perp \boldsymbol{R}$ ($\sigma^{\pm}$ polarization). This result can already be obtained by only accounting for the two asymptotic states $|e\uparrow e\downarrow; 0^{+}_{g}\rangle$ and $|e\uparrow e'\downarrow; 0^{+}_{g}\rangle$ that contribute the most to the two pair potentials $|\widetilde{\alpha}\rangle$ and $|\widetilde{\beta}\rangle$, see Eq. 4.4 and 4.5. In conclusion, one expects constructive interference in Eq. 5.22 for either even vibrational modes and $\boldsymbol{\varepsilon} \parallel \boldsymbol{R}$ or odd vibrational modes and $\boldsymbol{\varepsilon} \perp \boldsymbol{R}$.

In the spectroscopy where the polarization vector was laying in the atomic plane, both spatial configurations contribute to the total excitation rate which is given by $\gamma = \gamma_{\|} + \gamma_{\perp}$. While $\gamma_{\|}$ is larger for even ν, $\gamma_{\perp}$ is larger for odd ν. In total, the strong excitation rates $\gamma_{\|}$ at even modes dominate the signal in Fig. 5.9 (**a**). However, rotating the polarization out of the plane, only perpendicular configurations $\gamma_{\perp}$ remain. As a consequence, odd vibrational resonances dominate the spectroscopic signal in Fig. 5.9 (**b**).

In addition to the ensemble-averaged signal, this dependence on the parity of the vibrational state has also been tested by measuring the correlation signal $g^{(2)}_{\delta \boldsymbol{R}}$ at different vibrational resonances, see Fig. 5.10 (**a**). In agreement with the calculations, molecular excitation at even vibrational modes occurs predominantly parallel to the light polarization, while it occurs predominantly perpendicular at odd vibrational modes. Rotating the polarization out of the atomic plane, both orientations are equivalent and the correlation signal is symmetric.

Finally, the strong directional excitation of Rydberg pair states for $\boldsymbol{\varepsilon} \perp \boldsymbol{R}$ observed at the lower branch of the avoided crossing discussed at the end of chapter 4 in Fig. 4.6 (**b**) can be understood. The excited motional continuum modes are located in the spatial region close to the maximum of the potential well where the electronic states $|\widetilde{\alpha}\rangle$ and $|\widetilde{\beta}\rangle$ are mixed with similar amplitude. First, one might expect to observe a similar directionality in the excitation rate as for the narrow lowest vibrational mode $\nu = 0$ on the upper side of the avoided crossing. Here, the two terms in Eq. 5.22 interfere constructively for $\boldsymbol{\varepsilon} \parallel \boldsymbol{R}$. However, as for any avoided crossing, the relative sign between the coefficients $c_{\widetilde{\alpha}}$ and $c_{\widetilde{\beta}}$ is opposite on the upper and the lower side. As a consequence, constructive interference now occurs for $\boldsymbol{\varepsilon} \perp \boldsymbol{R}$.

Chapter 6

Vibronic structure

The Born-Oppenheimer approximation [433] is one of the cornerstones of molecular physics and was implicitly assumed to hold in the previous chapters. Here, the fast electron dynamics adiabatically follows the much slower motion of the nuclei [415]. When the interatomic distance varies during the vibration, the electronic structure adapts itself according to the spatially dependent electronic structure of the pair potential. As a consequence, the molecular states can be described by isolated electronic binding potentials and their vibrational eigenstates. This can be illustrated by the example discussed in section 5.3 where the electronic state will oscillate between the states $|\widetilde{\alpha}\rangle$ and $|\widetilde{\beta}\rangle$ during the vibration.

In many cases in molecular physics, the Born-Oppenheimer approximation does not hold. Such a breakdown of the Born-Oppenheimer approximation occurs if the motional states hosted by a single isolated electronic pair potential cannot be regarded as eigenstates because of non-adiabatic coupling terms to other nearby potentials. These cases are discussed in this chapter. As will be discussed below, the Born-Oppenheimer framework still provides intuition in the context of a more general Born-Oppenheimer expansion.

In the context of conventional molecules, these non-adiabatic terms are often necessary to describe transition rates in photochemistry [415]. With the advance of femtosecond spectroscopy, the study of time-resolved relaxation dynamics revealed the importance of non-adiabatic transitions to other crossing potential curves [434]. In many cases, the observed non-radiative relaxation occurs at timescales well below the radiative lifetime. Also in photodissociation experiments, such transitions are often important [435]. Here, molecules are first excited into a higher-lying state with large Franck-Condon overlap. Non-adiabatic coupling terms between the binding potentials and a repulsive potential branch can then induce the breakup of the molecule, a process called predissociation [436]. In the context of polyatomic molecules, the crossing between multidimensional potential surfaces leads to so-called conical intersections [437]. They are believed to play an important role in many photobiological processes such as photosynthesis [438, 439].

Using macrodimers, these phenomena can be studied in a regime where the crossing pair potentials, their electronic structure, and the contributing motional states are obtained from ab initio calculations. This makes them an ideal testbed to study these phenomena. Because of the small binding energies of macrodimers, the non-adiabatic coupling terms can be easily induced by applying external fields. The induced coupling strength depends on the molecular orientation relative to the applied fields and can be controlled in an experimental apparatus such as the one used here. This discussions follow the publications [411] and [413]. The theoretical description of the observations was developed in close discussion with Valentin Walther.

6.1 Non-adiabatic vibrational motion

As discussed in section 4.1.2, the adiabatic Born-Oppenheimer potentials $\bar{V}_j(R)$ are obtained from diagonalizing the electronic Hamiltonian $\hat{H}_e$ introduced in Eq. 2.19 via

$$\hat{H}_e|\bar{\Psi}^j_{\text{el}}(R)\rangle = \bar{V}_j(R)|\bar{\Psi}^j_{\text{el}}(R)\rangle. \tag{6.1}$$

The parametric dependence of the electronic eigenstates $|\bar{\Psi}^j_{\text{el}}(R)\rangle$ on the nuclear coordinate R was observed in section 5.3.

Adding the kinetic energy operator $\hat{T} = \frac{-\hbar^2}{2\mu_{\text{Rb}}}\frac{\partial^2}{\partial R^2}$ leads to motional eigenstates $\Phi_j(R)$, see Eq. 4.7. Dependent on the shape of the potentials $\bar{V}_j(R)$, the states $\Phi_j(R)$ can be bound vibrational states or motional continuum modes. Within the Born-Oppenheimer approximation, the motional modes $\Phi_j(R)$ are supported by a single electronic potential $\bar{V}_j(R)$. Here, the molecular states can be written as $|\Psi_{\text{Mol}}\rangle = \Phi_j(R)|\bar{\Psi}^j_{\text{el}}(R)\rangle$.

In a more general framework, the vibronic molecular wave function can be expressed in a Born-Oppenheimer expansion

$$|\Psi_{\text{Mol}}\rangle = \sum_j \bar{\Phi}_j(R)|\bar{\Psi}^j_{\text{el}}(R)\rangle. \tag{6.2}$$

Now, different Born-Oppenheimer potentials $|\bar{\Psi}^j_{\text{el}}(R)\rangle$ are admixed through spatially dependent amplitudes $\bar{\Phi}_j(R)$. As a consequence, the concept of an internuclear motional state supported by a well-defined electronic potential breaks down. Inserting Eq. 6.2 into the total Hamiltonian $\hat{H} = \hat{H}_e + \hat{T}$, multiplying $\langle\bar{\Psi}_j(R)|$ from the left and using $\langle\bar{\Psi}_j(R)|\bar{\Psi}_{j'}(R)\rangle = \delta_{jj'}$ yields

$$\left[\hat{T} + \bar{V}_j(R)\right]\bar{\Phi}_j(R) - \frac{\hbar^2}{2\mu_{\text{Rb}}}\sum_{j'}\left[2\bar{d}_{jj'}\frac{\partial}{\partial R} + \bar{D}_{jj'}\right]\bar{\Phi}_{j'}(R) = E\bar{\Phi}_j(R). \tag{6.3}$$

The kinetic energy operator $\hat{T}$ acts on $\Phi_j(R)$ as well as $|\bar{\Psi}^j_{\text{el}}(R)\rangle$. In addition to the terms present in Eq. 4.7, one now finds non-adiabatic coupling terms

$$\bar{d}_{jj'} = \langle\bar{\Psi}^j_{\text{el}}(R)|\frac{\partial}{\partial R}|\bar{\Psi}^{j'}_{\text{el}}(R)\rangle, \tag{6.4}$$

$$\bar{D}_{jj'} = \langle\bar{\Psi}^j_{\text{el}}(R)|\frac{\partial^2}{\partial R^2}|\bar{\Psi}^{j'}_{\text{el}}(R)\rangle \tag{6.5}$$

between different electronic states.

An elegant way to calculate the vibronic eigenstates utilizes the framework of gauge transformations [437]. Choosing a proper gauge, the non-adiabatic couplings between the different pair potentials can be canceled out. As a result, one obtains new diabatic potentials whose eigenstates can be calculated using the Born-Oppenheimer approximation [411]. As presented in the next section, the coupled vibronic eigenstates are then calculated by diagonalizing the pair potentials, which become off-diagonal after such a gauge transformation.

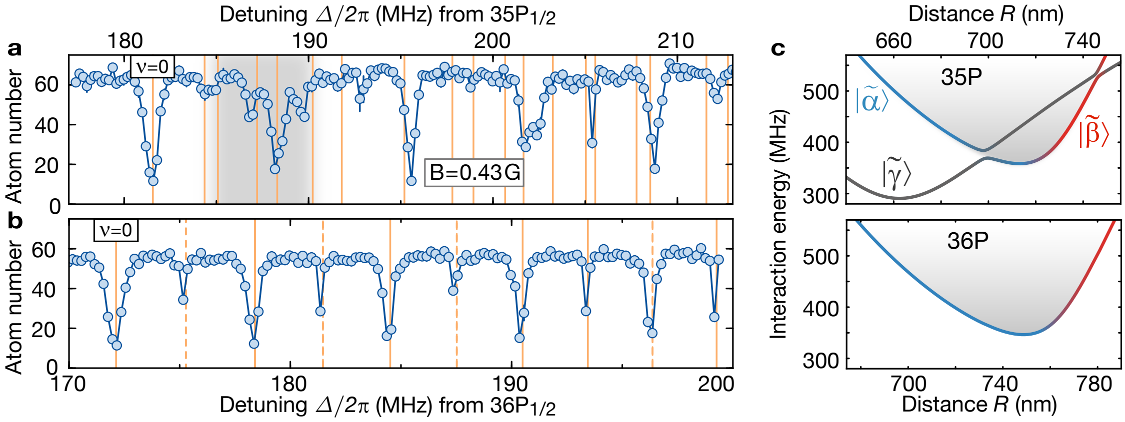

Figure 6.1: **Breakdown of the Born-Oppenheimer approximation** (**a**) A closer look at the vibrational spectrum of the 0_g^+ potential blue-detuned from $35P_{1/2}$ at low vibrational quantum numbers reveals a significant perturbation from the equidistant harmonic oscillator eigenenergies expected from the previous discussion. The gray area indicates the region where the perturbations are the strongest. Using the formalism discussed in the text, most of the observed reonances can be calculated (orange vertical lines). (**b**) For the corresponding 0_g^+ potential for $n = 36$, the perturbation is absent. Solid (dashed) lines indicate the calculated resonance positions of the even (odd) vibrational resonances. (**c**) The reason for the perturbed vibrational spectrum for $n = 35$ is a weakly coupled pair potential $|\widetilde{\gamma}\rangle$ crossing the binding potential formed by $|\widetilde{\alpha}\rangle$ and $|\widetilde{\beta}\rangle$ close to the potential minimum. For $n = 36$, such an additional crossing cannot be found. As expected from the discussion in section 4.1.2, the binding potential for $n = 35$ is slightly more off-resonant and shifted towards shorter distances. All error bars on the data points denote one standard error of the mean (s.e.m.). Figure adapted from Ref. [411].

6.2 Higher-order multipole interactions

In the previous chapters, the vibrational eigenenergies were calculated by diagonalizing the interatomic motion in the Born-Oppenheimer potentials using Eq. 4.7. The binding potentials were surprisingly harmonic, predicting a clean spectrum of equidistantly spaced resonances. However, a more careful look at the observed spectrum at lower vibrational resonances shown in Fig. 4.2 (**b**) and Fig. 4.6 (**a**) reveals a significant deviation from an equidistantly spaced harmonic oscillator energy spectrum. Also the broadening at the blue-detuned side of the lowest vibrational mode in Fig. 4.2 (**c**) and at the second vibrational mode shown in Fig. 5.6 (**a**) suggests perturbations for some of the vibrational resonances. An additional spectroscopy of the perturbed frequency region for the 0_g^+ potential blue detuned from $35P_{1/2}$ at a magnetic field $B = 0.43\,$G is shown in Fig. 6.1 (**a**). The magnetic field only acts as an initial quantization axis and is too small to affect the magnetically insensitive 0_g^+ potential. Again, the observed spectrum contradicts an adiabatic motion in the previously dicussed 0_g^+ binding potential. Increasing the principal quantum number to $n = 36$, such a perturbation cannot be observed, see Fig. 6.1 (**b**).

The binding potentials are typically formed by the strong dipole-dipole interaction term Eq. 2.25 which induces large-scale avoided crossings between coupled pair potentials. However, also crossings between pair potentials where admixed electronic pair states have vanishing single-atom dipole matrix elements occur frequently. In these cases, higher-order multipole interaction terms can still induce smaller gaps. In Fig. 4.2 (**a**), one can see that the previously studied 0_g^+ potential blue-detuned from $35P_{1/2}$ crosses another pair potential $|\widetilde{\gamma}\rangle$ asymptotically connected to $|32D_{3/2}37P_{3/2}\rangle$. Here, weak dipole-quadrupole interactions induce a coupling between two macrodimer potential wells which is comparable to the vibrational energy in the original binding potential. As a consequence, the vibrational motion close to the gap will neither follow the adiabatic nor the diabatic path. For $n = 36$, this additional crossing is absent and the Born-Oppenheimer approximation holds. If the couplings are mediated by even higher-order terms, the induced gaps will be even smaller. In these cases, the gap will not be recognized by the vibrational motion which crosses the gap diabatically.

A complete treatment for $n = 35$ requires to account for non-adiabatic couplings between the vibrational modes of both potential wells by the kinetic energy operator. Applying the unitary transformation

$$\hat{U} = \begin{pmatrix} \cos(\varphi(R)) & \sin(\varphi(R)) \\ -\sin(\varphi(R)) & \cos(\varphi(R)) \end{pmatrix} \tag{6.6}$$

in the basis $|\bar{\Psi}^1_{\text{el}}(R)\rangle$ and $|\bar{\Psi}^2_{\text{el}}(R)\rangle$ with the gauge $\varphi(R) = \int_{R_0}^{R} \bar{d}_{12}(R')dR'$, one can eliminate the coupling in Eq. 6.3 between the potentials $\bar{V}_1(R)$ and $\bar{V}_2(R)$ [411]. This leads to a two-component Schrödinger equation

$$\left(\frac{\hbar^2}{2\mu_{\text{Rb}}} \frac{\partial^2}{\partial R^2} \mathbb{1} + \hat{V}(R)\right) \boldsymbol{\Phi} = E\boldsymbol{\Phi}. \tag{6.7}$$

In contrast to Eq. 6.3, the non-adiabatic coupling terms are absent. Instead, the coupling now appears in the operator $\hat{V}(R) = \hat{U}(R)\hat{\bar{V}}(R)\hat{U}(R)$ that was diagonal before the transformation, yielding

$$\hat{V}(R) = \begin{pmatrix} \cos^2(\varphi)\bar{V}_1(R) + \sin^2(\varphi)\bar{V}_2(R) & \sin(\varphi)\cos(\varphi)\left[\bar{V}_1(R) - \bar{V}_2(R)\right] \\ \sin(\varphi)\cos(\varphi)\left[\bar{V}_1(R) - \bar{V}_2(R)\right] & \sin^2(\varphi)\bar{V}_1(R) + \cos^2(\varphi)\bar{V}_2(R) \end{pmatrix}. \tag{6.8}$$

The diagonal elements provide diabatic potentials $V_{11}(R) \equiv V_1(R)$ and $V_{22}(R) \equiv V_2(R)$ and electronic states $|\Psi^1_{\text{el}}(R)\rangle$ and $|\Psi^2_{\text{el}}(R)\rangle$, see Fig. 6.2 (**a**). Here, diabatic refers to the absence of the coupling by the kinetic energy operator which guarantees a diabatic vibrational motion at the crossing. The potential $V_1(R)$ is the potential formed by the crossing between $|\widetilde{\alpha}\rangle$ and $|\widetilde{\beta}\rangle$, see Fig. 5.10. Far away from the crossing, the observed vibrational resonances and the microscopic excitation rates are well described by the binding potential $V_1(R)$, see Fig. 5.9 and Fig. 5.10. The corresponding Born-Oppenheimer wave functions can be written as $|\Psi^1_{\text{Mol}}\rangle = \Phi^1_\nu(R)|\Psi^1_{\text{el}}(R)\rangle$. The second potential $V_2(R)$ supports another set of Born-Oppenheimer states $|\Psi^2_{\text{Mol}}\rangle = \Phi^2_\nu(R)|\Psi^2_{\text{el}}(R)\rangle$.

A convenient way to solve the coupled problem is to expand Eq. 6.7 into these diabatic eigenstates and then diagonalize the coupled Hamiltonian. This provides vibronic molecular states

$$|\Psi_{\text{Mol}}\rangle = \sum_{\nu, i \in \{1,2\}} C_i^\nu \Phi^i_\nu(R)|\Psi^i_{\text{el}}(R)\rangle. \tag{6.9}$$

The calculated energies of the vibronic states which experience the strongest optical excitation rates are shown as vertical orange lines in the upper spectroscopy presented in

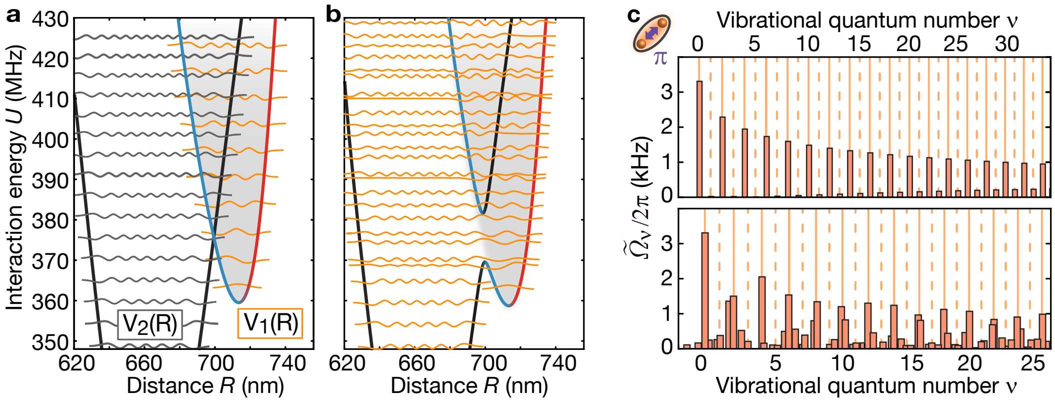

Figure 6.2: **Diabatic and adiabatic binding potentials.** (**a**) In the diabatic basis obtained by a gauge transformation, one finds two sets of vibrational modes $\{\Phi^1_\nu(R)\}$ and $\{\Phi^2_\nu(R)\}$. (**b**) A solution of the coupled problem provides vibronic states which are a superposition of both sets of bound states. (**c**) The calculated $\nu-$dependent Rabi frequencies for the eigenstates in the diabatic and the coupled potentials, for a linear light polarization $\boldsymbol{\varepsilon} \parallel \boldsymbol{R}$. The resonance position of the even (odd) vibrational modes in the diabatic potential are indicated as solid (dashed) vertical orange lines for both plots. While the coupling modifies the spectrum in the energetic vicinity of the gap, the overal structure is similar in both cases. Figure adapted from Ref. [411].

Fig. 6.1 (**b**). Now, most of the observed resonances in the vicinity of the gap can be predicted by the calculation. The coupled spatial modes which now extend over the spatial extension of both potentials are shown in Fig. 6.2 (**b**). The same formalism as the one presented in chapter 5 can be used to calculate the optical excitation rates of the vibronic states. The expected two-photon Rabi frequencies into the diabatic and vibronic molecular states are shown in Fig. 6.2 (**c**) for a typical UV intensity. The excitation laser was assumed to be π polarized where the polarization vector is aligned with the interatomic axis. The calculated spectrum in the diabatic potential $V_1(R)$ agrees with the observations far away from the crossing. Using the vibronic states, one finds additional resonances. Particularly in the vicinity of the gap, a coupling between the eigenmodes in the potentials $V_1(R)$ and $V_2(R)$ leads to a splitting of the modes that can be excited by the UV laser. As expected, the description in the diabatic potential $V_1(R)$ is a good approximation away from the gap. In this region, the vibrational states in the additional diabatic potential $V_2(R)$ are only weakly coupled to the modes in the potential $V_1(R)$ that are coupled by the light field.

6.2.1 Finite magnetic fields

The studied 0_g^+ binding potential showed no first order Zeeman coupling and the spectroscopy at low magnetic field agreed with calculations at zero field. However, at higher fields, higher-order contributions from the magnetic field are expected to contribute. Because the coupled vibronic eigenenergies critically depend on the gap position, the perturbed eigenmodes might change. A spectrocopy for $B = 28.8\,$G perpendicular to the atomic plane is shown in Fig. 6.3. The magnetic field was pointing out of the atomic plane. As a consequence, it was perpendicular to the distance vectors of all atom pairs that were excited into macrodimer states. In comparison with the low field result, one finds a modi-

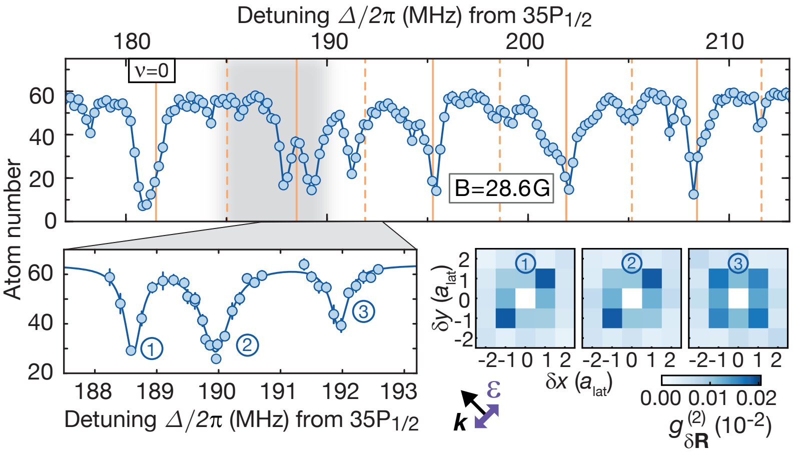

Figure 6.3: **Effects of a magnetic field on the vibronic eigenstates.** Applying a magnetic field $B = 28.8\,\mathrm{G}$ perpendicular to the atomic plane modifies the vibronic structure of the magnetically insensitive potential close to the gap. Because accurate calculations were not feasible in this regime, the locations of the vibrational energies calculated in the diabatic potential $V_1(R)$ at zero field are plotted instead. Again, the expected location of the gap is indicated in gray. Comparing the correlation signal at the three resonances close to the gap suggests that the two left resonances correspond to the same diabatic eigenstate, split by the non-adiabatic couplings. A small frequency offset between the resonance positions in the upper and the lower spectrocopy is related to an uncertainty in the calibrated $35P_{1/2}$ Rydberg resonance. All error bars on the data points denote one s.e.m. Figure adapted from Ref. [411].

fication of the perturbed spectrum as well as a broadening for most lines. Currently, the precision of the potential calculations at finite fields are not accurate enough to provide accurate predictions. However, the electronic structure of the split states can still be experimentally studied by measuring orientation-dependent excitation rates. For the three dominant resonances close to the gap, one finds similar signatures for the two left lines, while the right line is different. This might indicate that the two left resonances have strong admixtures of the same eigenstate in the diabatic potential $V_1(R)$.

6.3 Potential engineering & predissociation

In the previous discussion, the macrodimer binding potentials originated from the avoided crossings induced by the Rydberg interactions between crossing potential curves. This section discusses the possibility to engineer binding potentials by inducing avoided crossings with external magnetic fields. The discussion focuses on two pair potentials $V_{0_u^-(R)}$ and $V_{1_u}(R)$ that cross at an interaction shift $U \approx 3\,\mathrm{GHz}$ above the $|36P_{1/2}36P_{1/2}\rangle$ asymptote, see also Fig. 5.1 (**c**). At zero field, the 0_u^- binding potential cannot be coupled to the repulsive 1_u potential because the molecular quantum number Ω is protected by the symmetry of the interaction Hamiltonian, see section 4.1.1. The observed spectrum agrees well with the calcuated eigenmodes in the isolated 0_u^- binding potential up to high vibrational quantum numbers, see Fig. 6.4 (**a**). For an external field that is not aligned with the interatomic axis, the rotational symmetry of the molecule is broken. As a consequence, Ω cannot be regarded as a good quantum number and avoided crossings between the crossing pair potentials can occur. In the experiment, the magnetic field of variable strength was applied perpendicular to the atomic plane. In this configuration, this induces a gap between the two crossing potentials that is identical for all pairs in the plane, see Fig. 6.4 (**b**).

In the presence of a coupling between $V_{0_u^-(R)}$ and $V_{1_u}(R)$, the continuum modes supported by the repulsive 1_u potential are admixed to the bound vibrational states. Dependent on the strength of the coupling, this is expected to reduce the lifetime of the vibrational states and broaden the vibrational resonances. This phenomenon where molecules can dissociate due to non-adiabatic transitions to repulsive potential barriers is another example where the Born-Oppenheimer approximation breaks down and is called predissociation [436].

A calculation of the electronic decomposition of both crossing pair potentials $V_{0_u^-(R)}$ and $V_{1_u}(R)$ by diagonalizing the Rydberg interaction Hamiltonian is again only possible at high precision at zero field. For low fields, the interaction with the field can again be predicted using perturbation theory. The induced couplings between both potentials can be calculated using the Hamiltonian $\hat{H}_1 = \hat{H}_B^{(1)} \otimes \mathbb{1}^{(2)} + \mathbb{1}^{(1)} \otimes \hat{H}_B^{(2)}$ introduced in Eq. 5.14. For $\boldsymbol{B} \perp \boldsymbol{R}$, the single particle Hamiltonians can be expressed as

$$\hat{H}_B = \mu_B \left(g_S \hat{S}_x + g_L \hat{L}_x \right) B_x. \tag{6.10}$$

Again, $\boldsymbol{R}$ is assumed to be parallel to the $z-$axis. Without loss of generality, the magnetic field was chosen to point along the $x-$axis. The relevant electronic pair states are $|\Psi_{\mathrm{Mol}}; \pm 1_u\rangle$ and $|\Psi_{\mathrm{Mol}}; 0_u^-\rangle$. In the following discussion, it is convenient to define states

$$|\Psi_{\mathrm{Mol}}; S_u\rangle = \frac{1}{\sqrt{2}} \left(|\Psi_{\mathrm{Mol}}; +1_u\rangle + |\Psi_{\mathrm{Mol}}; -1_u\rangle \right) \tag{6.11}$$

$$|\Psi_{\mathrm{Mol}}; A_u\rangle = \frac{1}{\sqrt{2}} \left(|\Psi_{\mathrm{Mol}}; +1_u\rangle - |\Psi_{\mathrm{Mol}}; -1_u\rangle \right). \tag{6.12}$$

The magnetic field induces a coupling

$$\Delta_C(R) = \langle \Psi_{\mathrm{Mol}}; 0_u^- | \hat{H}_1 | \Psi_{\mathrm{Mol}}; S_u \rangle \tag{6.13}$$

which is proportional to the magnetic field and can again be calculated using the decomposition of the molecular state into asymptotic states $|r_i r_j\rangle$, see Eq. 4.2. Again, the molecular state decompositions depend on R.

Because $\langle \Psi_{\mathrm{Mol}}; +1_u | \hat{H}_1 | \Psi_{\mathrm{Mol}}; 0_u^- \rangle = \langle \Psi_{\mathrm{Mol}}; -1_u | \hat{H}_1 | \Psi_{\mathrm{Mol}}; 0_u^- \rangle$, the state $|\Psi_{\mathrm{Mol}}; A_u\rangle$ remains uncoupled, leaving one of the two crossing 1_u potential energy curves unchanged. The new combined potentials are obtained by diagonalizing the Hamiltonian

$$\hat{H} = \begin{pmatrix} V_{1_u}(R) & \Delta_C(R) \\ \Delta_C(R) & V_{0_u^-}(R) \end{pmatrix}. \tag{6.14}$$

At the crossing point R_c of both potentials, the gap size is $2\Delta_C(R_c)$.

The coupling of the bound states to the continuum states does not only depend on the electronic coupling $\Delta_C(R)$ but also on the spatial overlap between both sets of motional states. In our case, where one potential is a repulsive potential well, a Franck-Condon density (FCD) estimates the coupling strength between a vibrational state $\Phi_\nu(R)$ to nearby continuum modes. An estimation of the FCD by the overlap integral of the vibrational

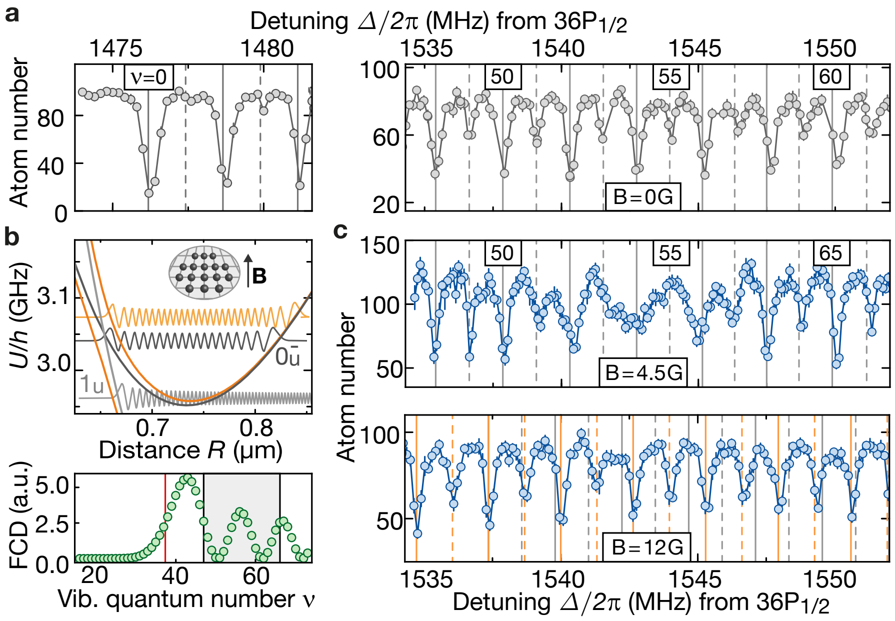

Figure 6.4: **Potential engineering & predissociation.** (**a**) The observed spectrum at zero field agrees with the calculated resonance positions. These are indicated as solid (dashed) vertical lines for even (odd) vibrational states ν. (**b**) At a magnetic field perpendicular to the molecular axis, the binding potential $V_{0_u^-}(R)$ (dark gray) can be coupled to a repulsive potential barrier $V_{1_u}(R)$ (light gray). As a consequence, the vibrational modes in the binding potential are coupled to the continuum modes supported by $V_{1_u}(R)$. For large gaps, one expects a new binding potential hosting stable eigenmodes (orange). Above the crossing point (vertical red line), the Franck-Condon density (FCD) between the bound states and the continuum modes oscillates with the vibrational quantum number. The gray area indicates the frequency region studied in the spectroscopies. (**c**) At a magnetic field of $B = 4.5\,\mathrm{G}$, the resonance positions still agree with the unperturbed vibrational energies. However, a broadening of some vibrational resonances confirms the coupling to the continuum. At an even higher field of $B = 12\,\mathrm{G}$, the perturbation in the spectrum is absent again. Now, the vibrational spacing exceeds the calculated value in the isolated potential (vertical gray lines) but agrees with a calculation in the combined potential (vertical orange lines). Because of an overall energy shift that appears at higher magnetic field values, both sets of calculated eigenenergies were manually overlapped with the first observed vibrational resonance $\nu = 48$. All error bars on the data points denote one s.e.m. Figure adapted from Ref. [413].

bound states with the continuum states at same energy is shown in Fig. 6.4 (**b**). We find that the FCD vanishes for vibrational states energetically below the crossing, while it oscillates with the vibrational quantum number ν above. This is consistent with previous studies on predissociation [440] and can be understood by comparing the continuum states with the vibrational states $\Phi_\nu(R)$, see the upper plot in Fig. 6.4 (**b**). The FCD reaches a maximum when the first lobes of the continuum states coincide with the first lobe of $\Phi_\nu(R)$. In contrast, it becomes small when it matches with the first zero crossing of $\Phi_\nu(R)$. It increases again when the first lobes of the continuum states match with the second lobe of $\Phi_\nu(R)$ and so on.

In the experiment, we find perturbations in the vibrational spectra for magnetic fields within the range between $B = 3.5\,\mathrm{G}$ and $B = 6.5\,\mathrm{G}$. Spectroscopic data starting from $|F = 2, m_F = 0\rangle$ for detunings above the crossing point and finite field values are presented in Fig. 6.4 (**c**). For $B = 4.5\,\mathrm{G}$, where the calculated gap size is $2\Delta_C \approx 17\,\mathrm{MHz}$, one finds a significant broadening of the vibrational resonances for vibrational quantum numbers $\nu \approx 54$. The resonance positions are still in agreement with the calculations of the eigenmodes in the isolated potential $V_{0_u^-}(R)$ calculated at zero field. For a larger field $B = 12\,\mathrm{G}$ where $2\Delta_C \approx 40\,\mathrm{MHz}$, the perturbations in the spectra disappear again. However, the resonance positions are now shifted from the vibrational energies at zero field. Furthermore, the observed vibrational spacing $\Delta_\nu^{\mathrm{exp}} \approx 2.66(1)\,\mathrm{MHz}$ is found to be significantly above the calculated value $\Delta_\nu^{0_u^-} \approx 2.45(1)\,\mathrm{MHz}$ within the binding potential $V_{0_u^-}(R)$ but agrees with the calculation $\Delta_\nu^{\mathrm{C}} \approx 2.66(2)\,\mathrm{MHz}$ in the combined potential. This observation indicates that the vibrational wave function at higher magnetic fields is confined in the combined potential $V_C(R)$ rather than the isolated 0_u^- potential.

For larger magnetic fields where the vibrational resonances were shifted by the magnetic field, a quantitative agreement between the calculated and the observed vibrational energies could not be achieved. A quantitative agreement in this regime would require to account for more than just the two potentials $V_{0_u^-}(R)$ and $V_{1_u}(R)$. However, the spacing between neighboring vibrational resonances is still a useful quantity to describe the binding potential. The experimental values for the vibrational spacings $\Delta_\nu^{\mathrm{exp}}$ were obtained by fitting a vibrational series with varying frequency spacing to the data. Uncertainties on the calculated values $\Delta\nu_{0_u^-}$ and Δ_ν^{C} account for the anharmonicity of both molecular potentials in the frequency range of the spectroscopies performed above the potential crossing.

Magnetically induced predissociation has also been observed for conventional deeply bound molecules [440, 441]. In such experiments, spectroscopic signals are averages over all molecular orientations in the samples. If gaps between crossing potentials are induced by external fields, this is critical because the gap depends on the orientation of the field relative to the molecular axis. For macrodimers, the wide tuning range covering both Born-Oppenheimer limits is possible because of the small binding energies. Even larger tunabilities can be expected from using electric instead of magnetic fields because of the large polarizability of the contributing Rydberg states. This once more shows that macrodimers can serve as an interesting playground to study generic features of molecules with maximum experimental control in a regime where ab-initio calculations provide reliable predictions.

Chapter 7

Two-color macrodimer excitation

The last chapters provided a detailed experimental and theoretical study of Rydberg macrodimers and their optical excitation. This chapter focuses on a new two-color excitation scheme where the molecular Rabi freuqencies are strongly enhanced. In combination with an optimized choice of the contributing electronic states and the light polarization, this enables an increase of the molecular Rabi frequencies by up to a factor of 50. The small intermediate state detunings of the new coupling scheme also induces a level shift of the macrodimer resonance that originates from the optical coupling into photodissociated motional continuum states. This chapter follows the publication [442]. The theoretical description of the observations was developed in close discussion with Andreas Kruckenhauser and Valentin Walther.

7.1 Optimizing the angular overlap coefficients

In order to realize maximum excitation rates, all contributing Clebsch-Gordan coefficients have to reach a maximum. As discussed in chapter 5, this is generally more difficult compared to the optical coupling between two internal states of an atom where the quantization axis, e.g. the magnetic field $\boldsymbol{B}$, and the polarization of the light field $\boldsymbol{\varepsilon}$ are the only two contributing vectors. Now, also the interatomic distance vector $\boldsymbol{R}$ contributes.

The angular momentum projection of the initial ground state atom pairs is only well-defined relative to $\boldsymbol{B}$, see also Fig. 5.2. As a first optimization step it therefore makes sense to optimize the Rabi rates into molecules with an orientation $\boldsymbol{R} \parallel \boldsymbol{B}$. Here, the description of the optical coupling does not require apply a rotation Eq. 5.1 on the contributing quantum states. This reduces the mixing of different angular momentum projections, allowing the full quantum state to contribute to the coupling. For the same reason, it makes sense to choose a stretched state $|F = 2, m_F = \pm 2\rangle = |m_J = \pm\frac{1}{2}\rangle_J \otimes |m_I \pm \frac{3}{2}\rangle_I$ with maximum $|m_F| = F$ as an initial state. Here, the nuclear spin projection m_I remains unentangled from the electronic angular momentum projection m_J and mixing between different m_J does not occur.

In the optical excitation, large Clebsch-Gordan coefficients can be found using pure σ transitions. Describing the excitation in the frame of the oriented molecule, this requires $\boldsymbol{R}$ to be parallel to the wave vector $\boldsymbol{k}$ of the light, see also section 3.7.3 and section 3.7.3. Comparing the possible initial states presented in Fig. 5.2 for the molecular states 0_g^+, 0_u^- and 1_u available in our system, one finds that only molecular states 1_u with $\Omega = \pm 1$ can be coupled by two σ polarized photons of the same kind.

In order to fulfill these conditions, the ground state atoms in this chapter were prepared in the hyperfine ground state $|5S_{1/2}, F = 2, m_F = -2\rangle$, see Fig. 7.1 (**a**). From the set of available 1_u potentials, we chose the vibrational spectrum energetically located blue-detuned from $|36P_{1/2}\rangle \equiv |e\rangle$, see Fig. 5.6. As in previous chapters the Rydberg P-state with $J = \frac{1}{2}$ is denoted as $|e\rangle$. The magnetic field $B = 0.5\,\mathrm{G}$ was pointing along the lattice

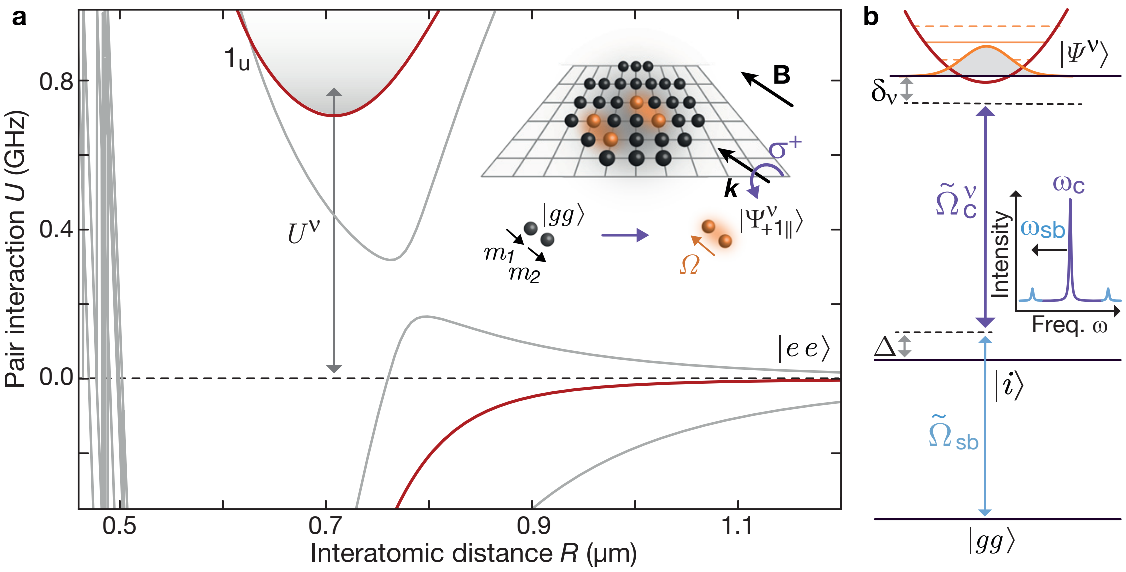

Figure 7.1: **Optimizing molecular Rabi frequencies.** (**a**) Throughout this chapter, only the 1_u potential blue-detuned from the $|36P_{1/2}\rangle \equiv |e\rangle$ resonance is optically excited. Coupling ground state atoms $|F = 2, m_F = -2\rangle$ to molecular states with $\Omega = +1$ with a orientation $\boldsymbol{R} \parallel \boldsymbol{B} \parallel \boldsymbol{k}$ using σ^+ polarized light realizes stong molecular Rabi couplings. (**b**) Modulating a weak sideband at a frequency ω_{sb} on the carrier frequency ω_C enables two-photon excitation with one sideband photon and one carrier photon. Now, the ground state $|gg\rangle$ is coupled to the intermediate state $|i\rangle = 1/\sqrt{2}\,(|eg\rangle + |ge\rangle)$ with a tunable Rabi frequency $\widetilde{\Omega}_{\text{sb}}$. The intermediate states are coupled by carrier Rabi frequencies $\widetilde{\Omega}^\nu_C$ to the macrodimer states. For modulation frequencies ω_{sb} similar to the interaction shifts U^ν of the macrodimer states $|\Psi^\nu_\Omega\rangle$, this allows to drastically reduce the large intermediate state detunings Δ observed in Fig. 5.6 for the same binding potential. The detuning Δ and the two-photon detunings δ_ν are typically on the order of a few megahertz and can be independently tuned with the modulation frequency. Figure adapted from Ref. [442].

diagonal direction which coincides with the propagation direction of the UV light $\boldsymbol{k} \parallel \boldsymbol{B}$. This configuration is identical to the one chosen for the study of the molecular excitation rate on the light polarization in Fig. 5.9 (**d**). The excitation light was purely σ^+ polarized.

The calculated bond length $R_\nu = 0.712(5)\,\mu\text{m}$ of the macrodimers is again close to the diagonal distance $\sqrt{2}a_{\text{lat}}$ in the optical lattice, with $a_{\text{lat}} = 532\,\text{nm}$. As a consequence, the excited molecules are either parallel or orthogonal to $\boldsymbol{B}$ and $\boldsymbol{k}$, with the possible orientations $\Omega = \pm 1$. The four possible states can then be labelled as $|\Psi^\nu_{\Omega_\parallel}\rangle$ and $|\Psi^\nu_{\Omega_\perp}\rangle$, with ν the vibrational quantum number. In the given configuration, the initial pair state $|gg\rangle = |-1_u\rangle_J \otimes |M_I = -3\rangle_I$ can be strongly excited into molecular states $|\Psi^\nu_{+1_\parallel}\rangle$ with $\Omega = +1$. Using the notation introduced in section 5.1, the subindex specifies the ungerade symmetry of the state $|-1_u\rangle_J = |-\frac{1}{2}\rangle_J \otimes |-\frac{1}{2}\rangle_J$.

In contrast, excitation rates into the two states $|\Psi^\nu_{\Omega_\perp}\rangle$ with orthogonal molecular orientation $\boldsymbol{R} \parallel \boldsymbol{B}$ are strongly suppressed because of two reasons. First, in this perpendicular molecular frame, the light is not σ^+ polarized anymore. Second, as one can see from Fig. 5.2 (**a**) for a rotation angle of 90°, the initial states expressed in the molecular frame now do not have a well-defined angular momentum projection m_J.

7.2 Two-color Rydberg macrodimer excitation

A second obstacle towards the realization of strong molecular Rabi couplings is the large intermediate state detuning in the two-photon excitation scheme. For the previously studied 1_u potential, the lowest vibrational state with vibrational quantum number $\nu = 0$ was observed at a detuning $\varDelta/2\pi = U^0/2 = 367.65(5)\,\mathrm{MHz}$, corresponding to an interaction shift $U^0 = 735.3(1)\,\mathrm{MHz}$, see Fig. 5.6. The large intermediate state detuning can be reduced by using two UV photons oscillating at two different frequencies, see Fig. 7.1 (**b**). If the first photon in the two-photon excitation scheme is closer to the singly-excited intermediate state, this will directly increase the molecular Rabi frequencies. Keeping the power in the near-resonant field low, also the scattering at the singly-excited intermediate states remains sufficiently low. Here, the second field is created by phase modulating the carrier field using an electro-optical modulator (EOM). The modulation frequency $\omega_{\mathrm{sb}}/(2\pi)$ is chosen to be sligthly lower than U^0.

For the given light polarization, the possible intermediate states are $|eg\rangle$ and $|ge\rangle$. For the same reason as discussed in section 2.5.1 one finds that for 1_u molecules with ungerade symmetry only the symmetric superposition $|i\rangle = 1/\sqrt{2}\,(|eg\rangle + |ge\rangle)$ contributes to the coupling. Because the coupling to the antisymmetric superposition vanishes, it will be neglected in the following description.

7.2.1 Two-color vibrational spectroscopy

The easiest way to perform the two-color spectroscopy is to vary the overall UV frequency while keeping ω_{sb} identical. The reason is that the EOM has an integrated resonant circuit matched to the modulation frequency. Whenever ω_{sb} is changed, also the resonant circuit has to be adjusted accordingly. The starting point for the spectroscopy is the single-photon Rydberg transition between a ground state atom $|g\rangle$ and a Rydberg state $|e\rangle$. After performing Rydberg spectroscopy with the carrier field, the corresponding resonance of the red sideband can be found by increasing the overall UV frequency by ω_{sb} from the observed carrier resonance. Throughout this chapter, this single-photon transition driven by the red sideband acts as the new reference for the detuning of the UV light, see Fig. 7.2. As previously observed in Fig. 4.2, the resonance is asymmetrically broadened towards red detunings due to attractively interacting van der Waals potentials.

For interaction shifts U^ν of the vibrational states sligthly larger than ω_{sb}, the vibrational states become two-photon resonant by one photon from the red sideband and one photon from the far detuned carrier field if the laser frequency is sligthly detuned from the new reference $\varDelta = 0$. The vibrational resonances are expected to appear at detunings

$$\frac{\varDelta}{2\pi} = \frac{1}{2}\left(U^\nu - \frac{\omega_{\mathrm{sb}}}{2\pi}\right). \tag{7.1}$$

The factor of two enters the description because the overall UV frequency was swept during the spectroscopy. Because this changes the frequency of the carrier and the sideband, the UV laser only has to be varied by half the subtracted value between U^ν and $\omega_{\mathrm{sb}}/(2\pi)$ to become two-photon resonant to the macrodimer states.

In contrast to previously observed vibrational spectra, the intermediate state detuning is now on the same order of magnitude as the vibrational frequencies ω_{vib}. As a consequence, higher vibrational states are not only suppressed because of the lower Franck-

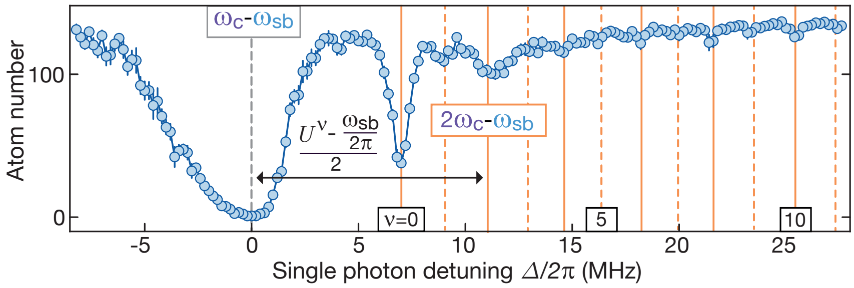

Figure 7.2: **Vibrational spectroscopy using two-color excitation.** The two-photon and two-color macrodimer resonances between ground states $|gg\rangle$ and macrodimer states $|\Psi^{\nu}\rangle$ can be observed at the single-photon detunings calculated by Eq. 7.1 (vertical orange lines) relative to the Rydberg transition $|g\rangle \to |e\rangle$ driven by the red sideband of the phase modulated UV laser. Here, the modulation frequency was $\omega_{\mathrm{sb}}/(2\pi) = 723\,\mathrm{MHz}$. Error bars denote one standard error of the mean (s.e.m.). Figure adapted from Ref. [442].

Condon factors discussed in section 4.2 but also experience significantly higher intermediate state detunings.

7.3 Photodissociation into the motional continuum

The spectroscopy data presented in Fig. 7.2 has been taken at low overall UV power. Using either higher powers or modulation frequencies closer to the vibrational energies where the intermediate state detunings are smaller, the vibrational resonances experience an additional energy shift V_{pd}^{ν} which modifies the resonance position obtained from Eq. 7.1. An exemplary dataset for the lowest vibrational state is shown in Fig. 7.3 (**a**). The shift

$$\frac{V_{\mathrm{pd}}^{\nu}}{2\pi} = a(\Delta_C)\left(\frac{\widetilde{\Omega}}{2\pi}\right)^2 \tag{7.2}$$

depends linearly on the UV intensity and quadratically on the calibrated carrier Rabi frequency $\widetilde{\Omega}$ that couples $|g\rangle$ to $|e\rangle$, see Fig. 7.3 (**b**). For all measurements presented here, the power in the sideband was low and did not contribute to V_{pd}^{ν}. This suggests that V_{pd}^{ν} is a second order AC Stark shift induced by the carrier field. In any three-level system, both paths in principle induce AC Stark shifts. However, the Rabi frequencies contributing to the excitation are not strong enough to explain the observed shift.

The origin of the unexpectedly large shift is carrier-induced photodissociation into motional states at kinetic energies similar to the one of the vibrational wave function $\Phi_0(R)$. Calculating the shift requires to explicitly account for the accessible motional states contributing to the intermediate state $|i\rangle$, see Fig. 7.3 (**c**). In the two-photon excitation, only motional states which have a finite Franck-Condon overlap with both the initial and the final motional wave functions can contribute. However, the carrier field can photodissociate an excited macrodimer state also into higher energetic motional states. The quantitative model describing this process will be discussed in the following paragraphs.

7.3.1 Overlap with continuum states

Separating the relative coordinate of both unbound atoms in an angular and a radial component leads to motional states $\Psi_\ell^k(\boldsymbol{R}) = j_\ell(kR)Y_\ell^m(\theta)$. Their energies are given by $E_k = \hbar^2k^2/(2\mu) = \hbar\omega_k$, with $\mu = m_{\mathrm{Rb}}/2$ the reduced mass of ^{87}Rb. The spherical Bessel functions $j_\ell(kR)$ account for motional excitations at wavenumber k and the rotational states $Y_\ell^m(\theta)$ account for the angular momentum ℓ of the atom pair and its projection m. In this and the next chapter, all lattices had a depth of $1000\,E_r$, with $E_r = h^2/(8m_{\mathrm{Rb}}a_{\mathrm{lat}}^2) = h \times 2.0\,\mathrm{kHz}$ the recoil energy of the lattice. As discussed in section 4.3.1, only spherical harmonics $Y_\ell^0(\theta)$ with $m = 0$ are expected to contribute for isotropic trapping conditions. Note that the assumption of motional states $\Psi_\ell^k(\boldsymbol{R})$ neglects the lattice potential for the intermediate states $|i\rangle$. Because the lattice potential is significantly lower than the kinetic energy stored in the vibrational wave function of the macrodimer state, the treatment still covers the essential physics. What is essential is that there is a complete basis of motional states where the molecular state can be coupled to.

The Franck-Condon integrals $f_{g\ell}^k$ between the ground state relative wave function $\Phi_{\mathrm{rel}}(R)$ and the motional states $\Psi_\ell^k(\boldsymbol{R})$ are given by

$$f_{g\ell}^k = f_\ell \int_0^\infty j_\ell(kR)\Phi_{\mathrm{rel}}(R)R^2dR. \tag{7.3}$$

The angular overlap coefficients f_ℓ are determined from independent angular integrals, see section 4.3. The calculated overlap $f_{g\ell}^k$ for $\ell = 0$ and different wavenumbers k is presented in the upper plot in Fig. 7.3 (d). The envelope of the distribution is essentially given by the Fourier transform of the Gaussian wave function and the period of the underlying oscillation is determined by the interatomic distance R_ν. Besides a suppression of the overlap at low $k-$values as well as a phase shift in the oscillations, the results for $\ell \neq 0$ look similar.

Similar as for the ground state, the overlap between the vibrational state $\Phi_\nu(R)$ and the Bessel functions is given by

$$f_{\nu\ell}^k = \int_0^\infty j_\ell(kR)\Phi_\nu(R)R^2dR. \tag{7.4}$$

A calculation for $\nu = 0$ provides the vibrational state $\Phi_0(R) = \left(2\pi R_0^4\sigma_0^2\right)^{-\frac{1}{4}} e^{-\left(\frac{R-R_\nu}{2\sigma_0}\right)^2}$, with $\sigma_0 \approx 5.5\,\mathrm{nm}$. The corresponding overlap $f_{\nu\ell}^k$ for $\ell = 0$ is shown in the lower plot in Fig. 7.3 (**d**). As expected, the motional wave function which is more narrow in real space has a broader distribution $\propto e^{-2k^2\sigma_0^2}$ in k-space.

7.3.2 Excitation model

In the optical coupling, the Rabi frequency between $|g\rangle$ and $|i_\ell^k\rangle$ can be parametrized as $\widetilde{\Omega}_{\mathrm{sb}} = \beta\sqrt{2}\widetilde{\Omega}$. Here, β is the ratio between the field amplitude in the sideband and the calibrated single-particle Rabi frequency of the carrier field $\widetilde{\Omega}$, see section 3.7.2. As for the Rydberg blockade, the factor of $\sqrt{2}$ enters from the symmetric electronic intermediate state $|i\rangle$, see section 2.5.1. The Rabi frequency between $|i_\ell^k\rangle$ and the molecular state can be parametrized as $\widetilde{\Omega}_C = \alpha\sqrt{2}\widetilde{\Omega}$. The scaling factor $\alpha = 1.04$ accounts for the electronic structure of the molecular state $|\Psi_{+1_\parallel}^\nu\rangle$, see section 5. Defining single-photon detunings

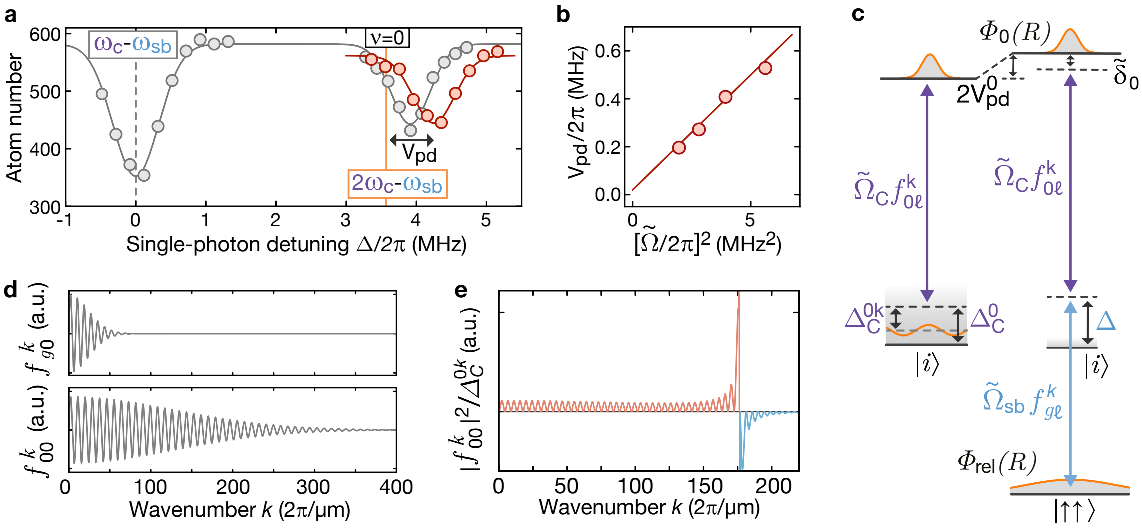

Figure 7.3: **Photodissociation into continuum states.** (**a**) A closer look reveals an additional shift V^0_{pd} which increases for higher UV intensities (gray to red). Here, the modulation frequency was $\omega_{\text{sb}}/(2\pi) = 728\,\text{MHz}$. (**b**) The observed shift V^0_{pd} depends quadratically on the calibrated single-atom Rabi frequency $\widetilde{\Omega}$. (**c**) The shift originates from the coupling of the molecular state to the motional continuum energetically located above the bare electronic intermediate state $|i\rangle$ by the strong carrier field $\widetilde{\Omega}_{\text{C}}$, shown here for $\nu = 0$. On-resonant coupling for k-modes where $\Delta^{0k}_{\text{C}} = 0$ furthermore induces photodissociation. In the excitation from the ground state $|gg\rangle$, only modes at low k with finite overlap with $\Phi_{\text{rel}}(R)$ as well as $\Phi_\nu(R)$ contribute. (**d**) A decomposition of $\Phi_{\text{rel}}(R)$ (upper plot) and the lowest vibrational wavepacket $\Phi_0(R)$ (lower plot) for $\ell = 0$ into photodissociated states at various wavenumbers k reveals the significantly higher kinetic energy stored in $\Phi_0(R)$. (**e**) The shift is described by the real part of Eq. 7.7. The contributions $|f^k_{\nu\ell}|^2/(\Delta^{\nu k}_C)$, shown here for $\nu = 0$, $\ell = 0$, and $\Delta_C/(2\pi) = -6.3\,\text{MHz}$, are distributed over the whole energy band of the coupled continuum states and switch sign at the divergence.

$\Delta_k = \Delta - \omega_k$ of the sideband field relative to the intermediate states $|i^k_\ell\rangle$ and two-photon detunings δ_ν relative to the vibrational states, the Hamiltonian is given by

$$\hat{H} = \frac{\widetilde{\Omega}_{\text{sb}}}{2}\sum_{\ell k}\left(f^k_{g\ell}|\Psi_{gg}\rangle\langle i^k_\ell| + h.c.\right) - \sum_{\ell k}\Delta_k|i^k_\ell\rangle\langle i^k_\ell| \qquad (7.5)$$
$$+ \frac{\widetilde{\Omega}_{\text{C}}}{2}\sum_{\nu\ell k}\left(f^k_{\nu\ell}|\Psi^{\nu\ell}_{+1_\parallel}\rangle\langle i^k_\ell| + h.c.\right) - \sum_{\nu\ell}\delta_\nu|\Psi^{\nu\ell}_{+1_\parallel}\rangle\langle\Psi^{\nu\ell}_{+1_\parallel}|.$$

While the illustration of the coupling in Fig. 7.3 (**c**) only accounts for the lowest vibrational state, the Hamiltonian covers also the higher-lying states $\nu \neq 0$. The electronic and motional ground state are combined into the state $|\Psi_{gg}\rangle$. The molecular states in rotational states $Y^0_\ell(\theta)$ are labelled as $|\Psi^{\nu\ell}_{+1_\parallel}\rangle$. The oriented molecular states are again obtained by the superposition $|\Psi^\nu_{+1_\parallel}\rangle = \sum f_\ell|\Psi^{\nu\ell}_{+1_\parallel}\rangle$. Using the vibrational frequency $\omega_{\text{vib}}/(2\pi) = 3.80\,\text{MHz}$ of the macrodimer potential, the two-photon detunings δ_ν can be expressed as $\delta_\nu = \delta_0 - \nu\omega_{\text{vib}}$.

7.3.3 Elimination of the continuum

In this paragraph, the dressing of the macrodimer states with the motional continuum is calculated. The total wave function of the system can be expressed as

$$|\Psi_{\text{tot}}(t)\rangle = c_{gg}(t)|\Psi_{gg}\rangle + \sum_{\ell k} c_{k\ell}(t)|i_\ell^k\rangle + \sum_{\nu\ell} c_{\nu\ell}(t)|\Psi_{+1_{\|}}^{\nu\ell}\rangle.$$

For an initially prepared macrodimer state with $c_{\nu\ell}(t=0)=1$ at a rotational quantum number ℓ, the coupling to the motional continuum is described by the time-dependent Schrödinger equation

$$\begin{aligned} i\frac{d}{dt}\,c_{k\ell}(t) &= \Delta_{\text{C}}^{\nu k}\,c_{k\ell}(t) + \frac{\widetilde{\Omega}_{\text{C}}}{2}c_{\nu\ell}(t)f_{\nu\ell}^k \\ i\frac{d}{dt}\,c_{\nu\ell}(t) &= \frac{\widetilde{\Omega}_{\text{C}}}{2}\sum_k c_{k\ell}(t)f_{\nu\ell}^k. \end{aligned} \tag{7.6}$$

Here, $\Delta_{\text{C}}^{\nu k} = \Delta_{\text{C}}^{\nu} + \omega_k$ is the single-photon detuning of the carrier field relative to the transition from the macrodimer states to the intermediate states $|i_\ell^k\rangle$. The single-photon detunings Δ and Δ_{C}^{ν} are related via $\delta_\nu = \Delta + \Delta_{\text{C}}^{\nu}$. While most motional states are off-resonantly coupled where $\Delta_{\text{C}}^{\nu k} \gg \widetilde{\Omega}_{\text{C}} f_{\nu\ell}^k$, there is also a small on-resonant part $\Delta_{\text{C}}^{\nu k}=0$ where the kinetic energy of the motional states compensates for the detuning Δ_{C}^{ν}.

In the stationary limit $\frac{d}{dt}\,c_{k\ell}(t)=0$, one obtains

$$i\frac{d}{dt}c_{\nu\ell} = \int_0^\infty dk\frac{\rho|\widetilde{\Omega}_{\text{C}} f_{\nu\ell}^k|^2}{4\Delta_{\text{C}}^{\nu k}}c_{\nu\ell} = 2\left(V_{\text{pd}}^{\nu\ell} + i\gamma_{\text{pd}}^{\nu\ell}\right)c_{\nu\ell}. \tag{7.7}$$

Assuming a large system size, the sum can be replaced by an integral $\sum_k \to \int \rho\, dk$, with ρ the density of states along the radial coordinate. The integral can be solved by using the Sokhotski-Plemelj theorem. [443, 444] The real part represents the summed AC Stark shift of the contributing $k-$modes which modifies the two-photon detuning $\widetilde{\delta}_\nu^\ell = \delta_\nu - 2V_{\text{pd}}^{\nu\ell}$. Generally, contributions can be found for all wavenumbers where $f_{\nu\ell}^k$ does not vanish, also close to the divergence. If the carrier detuning Δ_C is small such that the divergence appears at wavenumbers within the envelope of $f_{\nu\ell}^k$, the final AC Stark shift is a combination of blue-detuned and red-detuned contributions, see Fig. 7.3 (**e**).

The imarginary part of the integral $\gamma_{\text{pd}}^{\nu\ell}$ represents on-resonant deexcitation. For $\nu=0$, an analytical calculation of the imaginary part provides

$$2\gamma_{\text{pd}}^{0\ell} = \frac{\Omega_{\text{C}}^2\sigma_0}{2}\sqrt{\frac{4\pi\mu}{\hbar\Delta_{\text{C}}^0}}e^{-4\mu|\Delta_{\text{C}}^0|\sigma_0^2/\hbar}, \tag{7.8}$$

which is identical to the result obtained from Fermi's Golden rule. The dependence of $V_{\text{pd}}^{\nu\ell}$ and $\gamma_{\text{pd}}^{\nu\ell}$ on the rotational quantum number ℓ arises from the oscillatory behavior of $f_{\nu\ell}^k$ at wavenumbers close to the divergence in Eq. (7.7), see Fig. 7.3 (**c,d,e**). Dependent on the slope of coefficients $f_{\nu\ell}^k$ at the wavenumber where $\Delta_C^{\nu,k}=0$, the shift $V_{\text{pd}}^{\nu\ell}$ varies in its amplitude, in particular at smaller detunings Δ_C^{ν}.

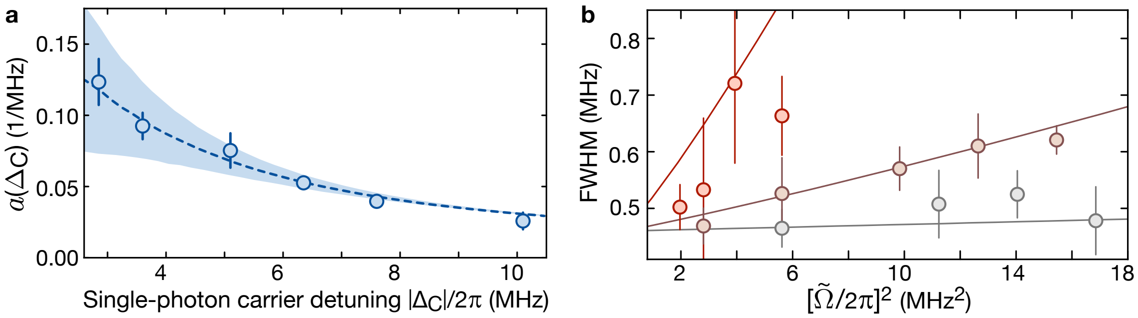

Figure 7.4: **Line shift and broadening induced by photodissociation.** (**a**) The experimental line shifts obtained from Eq. 7.2 agree with the theoretical expectations based on Eq. 7.7 and Eq. 7.9. The AC Stark shifts also depend on the different contributing rotational angular momenta ℓ. The closer the detunings, the more the corresponding energy shifts deviate. The blue shaded region denotes the corresponding minimum and maximum values. (**b**) Full width half maximum (FWHM) of the resonance profiles for $\varDelta_C/(2\pi) = -3.6\,\mathrm{MHz}$, $-6.35\,\mathrm{MHz}$, and $-10.1\,\mathrm{MHz}$ (gray to red) at different Rabi frequencies. The observation again agrees with the calculation (solid lines). Error bars on the data points mark the $1\sigma - 67\%$ confidence interval of the fitted resonance profiles. Figure adapted from Ref. [442].

7.3.4 Level shift and line profiles

For the calculation of the optical excitation signatures, the system is assumed to be initially in the ground state where $c_{gg}(t=0) = 1$. Accounting for the full Hilbert space, the time-dependent Schrödinger equation is given by

$$
\begin{aligned}
i\frac{d}{dt}\,c_{gg}(t) &= \frac{\widetilde{\varOmega}_{\mathrm{sb}}}{2}\sum_{\ell k} f^k_{g\ell}\,c_{k\ell}(t)\\
i\frac{d}{dt}\,c_{k\ell}(t) &= -\varDelta_k\,c_{k\ell}(t) + \frac{\widetilde{\varOmega}_{\mathrm{C}}}{2} f^k_{\nu\ell}\,c_{\nu\ell}(t) + \frac{\widetilde{\varOmega}_{\mathrm{sb}}}{2} f^k_{g\ell}\,c_{gg}(t)\\
i\frac{d}{dt}\,c_{\nu\ell}(t) &= \left(-\delta^\ell_\nu - i\gamma_{\mathrm{lp}}\right)\,c_{\nu\ell}(t) + \frac{\widetilde{\varOmega}_{\mathrm{C}}}{2}\sum_k f^k_{\nu\ell}\,c_{k\ell}(t).
\end{aligned}
$$

In order to also include the resonance profile to the description, the experimentally observed linewidth $2\gamma_{\mathrm{lp}} = 2\pi \times 920\,\mathrm{kHz}$ at low UV intensities was included as a non-Hermitian term to the differential equation. In order to calculate the resonance profile observed in two-photon spectroscopy, one can restrict the description to detunings close to the two-photon resonance. Here, the hierarchy of energy scales $|\varDelta| \gg \delta_\nu, f^k_{\nu\ell}|\widetilde{\varOmega}_{\mathrm{C}}|, f^k_{g\ell}|\widetilde{\varOmega}_{\mathrm{sb}}|$ allows to adiabatically eliminate the intermediate state. Calculating again the stationary solution via $i\frac{d}{dt}\,c_{k\ell}(t) = 0$ and inserting the obtained expression for the coefficients $c_{k\ell}(t)$ in the remaining equations, one again obtains the level shift $V^{\nu\ell}_{\mathrm{pd}}$ and the photodissociation rate $\gamma^{\nu\ell}_{\mathrm{pd}}$. After neglecting terms quadratic in $\widetilde{\varOmega}_{\mathrm{sb}}$ which represent a negligible energy shift in the ground state, one obtains

$$\begin{aligned} i\hbar \frac{d}{dt} c_{gg}(t) &= \sum_{\ell} \frac{\widetilde{\Omega}_{\nu}^{\ell}}{2} c_{\nu\ell}(t) \\ i\hbar \frac{d}{dt} c_{\nu\ell}(t) &= \left[-\widetilde{\delta}_{\nu}^{\ell} - i(\gamma_{\mathrm{lp}} + \gamma_{\mathrm{pd}}^{\nu\ell}) \right] c_{\nu\ell}(t) + \frac{\widetilde{\Omega}_{\nu}^{\ell}}{2} c_{gg}(t). \end{aligned}$$

Here, $\widetilde{\Omega}_{\nu}^{\ell}$ is the effective two-photon Rabi frequency coupling the ground state and the molecular states $|\Psi_{+1_{\|}}^{\nu}\rangle$. A detuning-dependent steady-state analysis of the total macrodimer population $\sum_{\ell} |c_{\nu\ell}|^2$ for $c_{gg}(t) \approx 1$ provides the resonance profile

$$\Gamma^{\nu}(\delta) \propto \sum_{\ell} \frac{|f_{\ell}|^2}{\left(\frac{\delta_{\nu}}{2} - V_{\mathrm{pd}}^{\nu\ell}\right)^2 + \frac{1}{4}\left(\gamma_{\mathrm{lp}} + \gamma_{\mathrm{pd}}^{\nu\ell}\right)^2}. \tag{7.9}$$

As expected from section 7.3.3, the two-photon resonances are shifted by $V_{\mathrm{pd}}^{\nu\ell}$. The shift agrees with the experimental results obtained from fitting Eq. 7.2 at different single-photon detunings Δ_C, see Fig. 7.4 (**a**). Experimentally, different values for Δ_C were realized by changing the modulation frequency ω_{sb} where two-photon resonance occurs at different intermediate state detunings. In the individual spectra, only the overall frequency of the UV laser was varied while ω_{sb} was kept the same.

The calculations furthermore show that $V_{\mathrm{pd}}^{\nu\ell}$ are effectively $\ell-$independent for larger single-photon detunings Δ_C but start to deviate at small detunings. As a consequence, the resonance profile at small detunings Δ_C is expected to broaden because different angular momentum state become resonant at slightly different laser frequencies. Furthermore, on-resonant photodissociation into motional states where $\Delta_C^{\nu} = -\omega_k$ directly increases the width of the individual resonances. Both effects are small at detunings Δ_C^{ν} larger than the energy band of the continuum states contributing to the vibrational wave function but become important at smaller detunings. Experimental values for the power-dependent linewidths at three different values of Δ_C^{ν} are presented in Fig. 7.4 (**b**). Again, the calculations agree with the observations.

Further comments

The experimental value for the linewidth observed at low powers which was included into the model was larger compared to measurements taken at different macrodimer resonances, see also section 4.2.2. One reason for this is that the measurements were performed at deep lattice depths where broadening due to the larger amount of rotational states related to the deeper lattice depth contributes, see also section 4.2.2. Furthermore, the resonances of the chosen 1_u binding potential at low vibrational quantum numbers were naturally sligthly broader, see also Fig. 5.6 (a). The broadening which is particularly present for the second even vibrational resonance originates from another crossing pair potential which affects the spectrum due to non-adiabatic motional couplings as discussed in chapter 6.

Direct photodissociation of a molecular state into a non-interacting electronic state [445, 446] is uncommon. In typical photodissociation experiments, "conventional" molecules are optically excited into energetically higher electronic pair potentials. Dissociation happens mostly because these pair potentials are repulsive or because of predissociation. Here, this direct coupling into pair potentials is realized because the interaction between both Rydberg atoms are much stronger compared to the negligible interactions between a ground state atom and a Rydberg atom.

7.4 Two-color Rabi frequencies

In the last section, adiabatic elimination provided two-color Rabi frequencies coupling the ground state into macrodimer states $|\Psi^{\nu\ell}_{+1_{\|}}\rangle$ at fixed rotational quantum number ℓ. Assuming large detunings Δ_C such that the splitting of the rotational states can be neglected, the oriented molecular state $|\Psi^{\nu}_{+1_{\|}}\rangle = \sum f_\ell |\Psi^{\nu\ell}_{+1_{\|}}\rangle$ will be coupled with a combined Rabi rate $\widetilde{\Omega}_\nu = \sum f_\ell \widetilde{\Omega}^\ell_\nu$ which is given by

$$\widetilde{\Omega}_\nu = \widetilde{\Omega}_{\mathrm{sb}} \widetilde{\Omega}_{\mathrm{C}} \sum_{\ell k} f_\ell \frac{f^k_{g\ell} f^k_{\nu\ell}}{2\Delta_k} \approx \frac{\widetilde{\Omega}_{\mathrm{sb}} \widetilde{\Omega}_{\mathrm{C}}}{2\Delta} f^\nu_g = \frac{\alpha\beta|\widetilde{\Omega}|^2}{\Delta} f^\nu_g. \tag{7.10}$$

In agreement with the previous discussion, the small kinetic energy in the ground state restricts contributions from $f^k_{g\ell}$ to small wavenumbers where $\Delta_k \approx \Delta$ is effectively independent of k and the above sums collapse to identities

$$\sum_k f^k_{\ell g} f^k_{\nu\ell} = f_\ell f^\nu_g = f_\ell \int_0^\infty \Phi_g(R)\Phi_\nu(R) R^2 dR. \tag{7.11}$$

The second sum over the variable ℓ vanishes because of the normalization condition $\sum_\ell |f_\ell|^2 = 1$. As a consequence, the calculated two-color Rabi frequencies match the intuitive initial guess without accounting for the continuum state. However, the frequency where the macrodimer resonance can be observed and the linewidth of the transition are still affected by Eq. 7.9.

Comparing the two-color excitation scheme with the single-color scheme, one finds that the intermediate state detuning can easily be decreased by more than two orders of magnitude. At the same time, one of both Rabi frequencies is decreased by the sideband amplitude β which was typically between 0.05 and 0.3. Because the power in the sideband is proportional to $\propto \beta^2$, the carrier still had by far the dominant power for the available modulation depths of the EOM. Combining both factors, the two-photon Rabi frequencies can be increased by one to two orders of magnitude, leading to Rabi frequencies up to $\widetilde{\Omega}_\nu/(2\pi) \approx 100\,\mathrm{kHz}$. These Rabi frequencies are in principle high enough to observe Rabi oscillations between ground state atom pairs and Rydberg macrodimers, see also section 9.2.

Chapter 8

Rydberg macrodimer dressing

This chapter discusses Rydberg dressing based on macrodimer states. Off-resonant admixing of the macrodimer states realizes strongly distance-selective interactions where the interaction potential of the dressed ground state atoms feature a sharp peak in the interatomic distance. The optical coupling scheme used in this chapter is based on the configurations presented in the previous chapter and most of the notation will be adopted. Because the Hamiltonian realized in this chapter can be mapped to a spin model, the previous ground state will be labelled as $|g\rangle \equiv |\uparrow\rangle$. The experiments are based on a Ramsey sequence where the dressed interactions faciliate the formation of two-spin and three-spin correlations. Despite of the large amount of contributing parameters, the observed dynamics can be predicted reasonably well. The chapter follows the publication [442]. The idea of using a two-color excitation scheme for Rydberg dressing was developed in close discussion with Jun Rui.

8.1 Engineering distance-selective interactions

The idea of Rydberg dressing is to engineer long-range interactions between ground state atoms by off-resonantly admixing Rydberg states, see also section 2.5.2. So far, experimental schemes were based off-resonant coupling to the asymptotic van der Waals potentials [155, 220–222]. A typical Rydberg-dressed potential using this conventional coupling scheme is shown in Fig. 8.1 (a) for the chosen principal quantum number $n = 36$. The typically soft-core shaped interactions J_{sc} decay algebraically at large distances and are non-vanishing over an extended distance range [218]. The depth of the soft-core potential can be approximated by $\widetilde{\Omega}^4/(8\Delta^3)$ and depends on the Rabi coupling $\widetilde{\Omega}$ and the detuning Δ. For a larger spin system, this scheme makes it hard to isolate interactions to a selected distance. As a consequence, the individual atoms always interact with several atoms in their environment, with an interaction strength given by the profile of the soft-core potential.

The first theoretical proposal to use spatial minima or maxima of the pair potentials for Rydberg dressing was published in [239]. Originally, the idea was to increase the ratio of coherent interactions and admixed atom loss. The loss coefficients were only considering single-atom loss and neglected experimentally observed density-dependent losses [154, 155]. Another signature of the new dressing scheme is the different distance dependence of the admixed interactions. Because the admixed interactions are finite only at distances close to the potential minimum or maximum, the potentials are strongly peaked in the interatomic distance. The width of the engineered interaction profile is typically limited by the spatial extension of the relative wave function in the ground state and not the narrow dressing potential. In this chapter, these distance-selective interactions are used to engineer a spin model in a two-dimensional spin lattice. Based on the results from the previous chapters, the description of the original proposal is extended by the contrib-

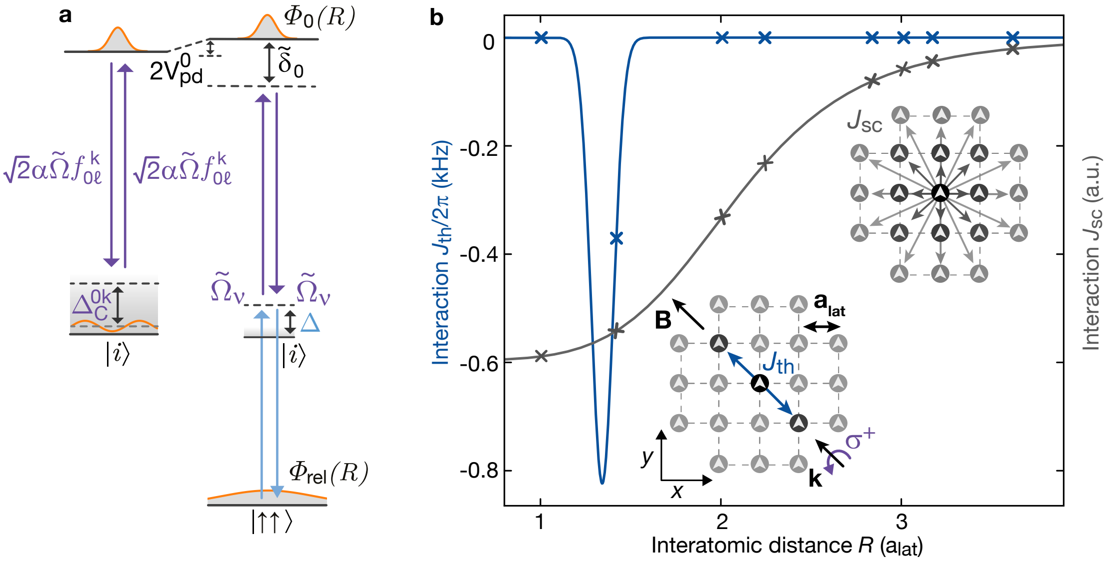

Figure 8.1: **Distance-selective dressing potentials.** (**a**) In an off-resonant coupling configuration, Rydberg-dressed interactions arise from a virtual four-photon coupling into the macrodimer state (here shown for the lowest vibrational state). The two two-photon processes can be combined into an effective Rabi frequency $\widetilde{\Omega}_\nu$. In the experiment, the coupling of the macrodimer state into photodissociated continuum states induces an energy shift V^0_{pd} which had to be taken into account. The notation was adopted from the previous chapter, where the coupling into the continuum states was discussed. (**b**) The calculated macrodimer-dressed interactions J_{th} are strongly peaked in distance (blue), in stark contrast to typical soft-core interactions J_{sc} cobtained by coupling to asymptotic interaction curves (gray). Crosses denote the distances present in the optical lattice. The atoms are arranged in a two-dimensional square array with a spacing a_{lat} and are illuminated by the σ^+ polarized UV laser with wave vector $\boldsymbol{k}$ oriented along the diagonal direction of the lattice and parallel to the magnetic field $\boldsymbol{B}$. Figure adapted from Ref. [442].

uting Franck-Condon factors and the electronic structure of the potentials [411, 413].

Previous chapters focused on the on-resonant excitation of macrodimers with molecular Rabi frequencies $\widetilde{\Omega}_\nu$ for vanishing two-photon detunings $\delta_\nu \approx 0$. In an off-resonant coupling configuration $\delta_\nu \neq 0$, the coupling gives rise to a dispersive energy shift $J_\nu = \frac{\widetilde{\Omega}^2_\nu}{4\delta_\nu}$ which can be understood as an AC Stark shift originating from the two-photon coupling to the macrodimer state. Because the AC Stark shift only contributes if both ground state atoms are placed at the distance where their relative motional state has a large overlap with the macrodimer states, this represents an interaction potential between the ground state atoms. The sign of the potential can be tuned by the detuning δ_ν.

8.1.1 Two-color macrodimer dressing

Using a single UV frequency, the macrodimer-dressed interaction potential is too weak for the available UV intensities. However, using the two-color excitation scheme as well as the optimized coupling configuration presented in chapter 7, the realized potentials are sufficiently strong. The EOM modulation frequency for the UV sideband was set to

$\omega_{\mathrm{sb}}/(2\pi) = 726\,\mathrm{MHz}$. At low powers, the two-photon resonance $\delta_0 = 0$ of the lowest vibrational state can be observed at intermediate state detunings $\varDelta/(2\pi) = -\varDelta_C/(2\pi) = 4.65(5)\,\mathrm{MHz}$, see Eq. 7.1 and Fig. 3.2 and Fig. 3.3 (**a**). Decreasing the intermediate state detuning to the value $\varDelta/(2\pi) = 3.58\,\mathrm{MHz}$ chosen for the dressing configuration provides a two-photon detuning $\delta_0/(2\pi) = 2\,(4.65(5) - 3.58)\ \mathrm{MHz} = -2.14(10)\,\mathrm{MHz}$. Increasing the carrier Rabi frequency between $|g\rangle \equiv |\uparrow\rangle$ and $|e\rangle$ to $\widetilde{\varOmega}/(2\pi) = 2.83(5)\,\mathrm{MHz}$ shifts the lowest macrodimer state $\nu = 0$ by V^0_{pd} because of the coupling into the motional continuum, see Fig. 3.4 (**a**). This leads to a modified two-photon detuning $\widetilde{\delta}_0 = \delta_0 - 2V^0_{\mathrm{pd}} = -2\pi\times 3.01\,\mathrm{MHz}$, where V^ν_{pd} can be calculated based on Eq. 7.2 using the extracted value for the scaling factor $a(\varDelta_C)$. The intermediate state detuning $\varDelta$ remains unaffected. Shifts V^ν_{pd} for higher-lying states $\nu \neq 0$ can be neglected because they are further detuned. The modification of the electronic structure of the molecular state due to the admixing of single-atom Rydberg states in the photodissociation channel was neglected.

A calculation of the overall interaction strength accounting for many vibrational levels provides

$$J_{\mathrm{th}} = \sum_\nu J^\nu_{\mathrm{th}} = \sum_\nu \frac{\widetilde{\varOmega}^2_\nu}{4\widetilde{\delta}_\nu} = \frac{\alpha^2\beta^2\widetilde{\varOmega}^4}{4\varDelta^2}\sum_\nu \frac{\left(f^\nu_g\right)^2}{\widetilde{\delta}_\nu} \approx 2\pi\times 370(40)\mathrm{Hz}. \tag{8.1}$$

The calculation depends on the electronic structure of the molecular state which enters with the parameter $\alpha = 1.04$ and the sideband amplitude $\beta = 0.062$ which was extracted from the manual of the EOM. Furthermore, $\widetilde{\delta}_\nu$ are the two-photon detunings and f^ν_g are the Franck-Condon integrals between the relative wave function in the ground state and the vibrational wave function. The estimated uncertainty of the calculated spin interaction $J \propto \widetilde{\varOmega}^4$ is dominated by the uncertainty in the calibrated Rabi frequenciy $\widetilde{\varOmega} = 2.83(5)\,\mathrm{MHz}$. The strong distance selectivity of the admixed interactions arise from to the Franck-Condon integrals f^ν_g, see also Fig. 8.1 (**b**). Because of the large Franck-Condon integral $f^0_g \approx 0.37$ of the lowest vibrational state at lattice diagonal distance and the smaller detunings, the contribution of $J^0_{\mathrm{th}} \approx 2/3 J_{\mathrm{th}}$ has the largest contribution to the total dressed interaction. For the same reasons as discussed in section 7.4 for the molecular Rabi frequencies $\widetilde{\varOmega}_\nu$, extending the calculation of J_{th} by the available motional states in the intermediate state has negligible consequences on the spin interaction. It only enters as a level shift because the molecular state shifts by V^ν_{pd}. The strong directionality originating from the coupling to the oriented molecular state can be included into the coefficient α. For the chosen configuration, the coupling into molecular states oriented perpendicular to the direction of $\boldsymbol{B}$ is suppressed. For a calculation at the orthogonal orientation, a spin coupling $J^\perp_{\mathrm{th}} \approx 0.06 J_{\mathrm{th}}$ remains.

8.2 A distance-selective Ising spin model

The presence of the dressed interactions can in principle be studied in several ways. Similar as for a Mott insulator where the competition of on-site interactions and hopping gives rise to a insulating phase, the formation of certain atomic configurations on the lattice would be an interesting direction [225, 447, 448]. However, such a study in the itinerant regime requires coherence times on motional timescales [222]. Decreasing the lattice depths lowers the Franck-Condon factors and furthermore has been found to increase collective loss rates which limit many Rydberg dressing experiments, see also appendix C. Also the

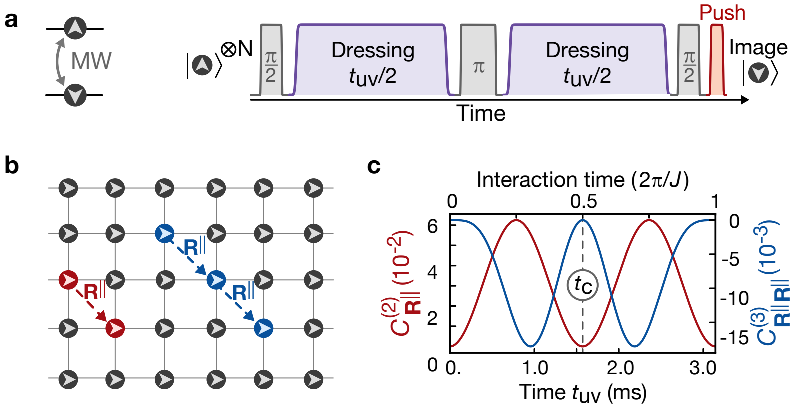

Figure 8.2: **Many-body interferometry.** (**a**) The two hyperfine ground states $|{\downarrow}\rangle$ and $|{\uparrow}\rangle$ representing the spin model are coupled using a microwave field (MW). The spin interactions are studied using a Ramsey sequence where two dressing pulses are inerrupted by a spin echo. Finally, the state of each spin is observed using the site-resolved detection. (**b**) The presence of the dressed potential gives rise to two-spin correlations $C^{(2)}_{\mathrm{R}^{\parallel}}$ as well as multi-spin correlations, here shown by the example of the three-spin correlator $C^{(3)}_{\mathrm{R}^{\parallel}\mathrm{R}^{\parallel}}$. (**c**) The calculated dynamics of $C^{(2)}_{\mathrm{R}^{\parallel}}(t_{\mathrm{uv}})$ and $C^{(3)}_{\mathrm{R}^{\parallel}\mathrm{R}^{\parallel}}(t_{\mathrm{uv}})$ in the absence of dissipation shows coherent oscillation cycles between entanglement and disentanglement. At a time $t = t_c$, the system realizes a highly-entangled cluster state. Figure adapted from Ref. [442].

gradient of the AC Stark shift admixed from the single-photon transitions contributing to the coupling is problematic [248]. As a consequence, the lattices were kept at a depth of $1000\,E_r$ where all motional dynamics is frozen. In this regime, macrodimer-dressed interactions can be used to realize a two-dimensional spin model where the spin interactions are finite only at a selected distance in the lattice.

In order to realize a spin model, a second spin state was encoded in the ground state $|{\downarrow}\rangle = |F = 1, m_F = -1\rangle$. The single-spin states $|{\downarrow}\rangle$ and $|{\uparrow}\rangle$ can be coherently coupled using microwave fields. While the state $|{\uparrow}\rangle$ is coupled to the Rydberg state, $|{\downarrow}\rangle$ remains off-resonant to Rydberg transitions. In this configuration, the energy of pair states $|{\uparrow\uparrow}\rangle$ shifts at the selected distance due to the admixed interaction while all other combinations experience no energy shift. For the chosen configuration of the coupling, this adds interaction terms $J_{\mathrm{th}}\,|{\uparrow\uparrow}\rangle\langle{\uparrow\uparrow}|$ for all spin pairs at distance vectors $\boldsymbol{R}^{\parallel} = (+1, -1)\,a_{\mathrm{lat}}$ to the Hamiltonian. Using the identification $|{\uparrow}\rangle\langle{\uparrow}| = \hat{S}^z + \frac{1}{2}\mathbb{1}$, the interaction term transfers into spin interactions $\hat{S}^z\hat{S}^z$ and terms proportional to single-spin operators $\hat{S}^z$.

8.2.1 Many-body Ramsey interferometry

Because the $\hat{S}^z\hat{S}^z$ interaction terms are restricted to the $z-$basis, dynamics can only be observed if the initial atoms are not prepared in an eigenstate of $\hat{S}^z$. Here, many-body Ramsey interferometry provides a suitable pathway [155]. Initially, the system is prepared in the state $|{\uparrow}\rangle^{\otimes N_0}$, with N_0 the total number of spins in the system. By performing a first $\pi/2-$rotation that is resonant with the microwave transition $|{\downarrow}\rangle \to |{\uparrow}\rangle$ in the absence of the UV light, the state leaves the $z-$basis and transfers into $|{\rightarrow}\rangle^{\otimes N}$, with $\frac{1}{\sqrt{2}}\left(|{\downarrow}\rangle - i\,|{\uparrow}\rangle\right)$, see Fig. 8.2 (**a**). Then, a first dressing pulse with an illumination time $t_{\mathrm{uv}}/2$ is applied. Here, all spin pairs at the correct distance $\boldsymbol{R}^{\|}$ are expected to accumulate a phase $|\uparrow\uparrow\rangle \rightarrow e^{i\varphi_J(t_{\mathrm{uv}})}\,|\uparrow\uparrow\rangle$ with $\varphi_J(t_{\mathrm{uv}}) = -J_{\mathrm{th}}\frac{t_{\mathrm{uv}}}{2}$. Furthermore, single-spin states $|\uparrow\rangle$ accumulate phases because the off-resonant coupling to the single-atom Rydberg state shifts their energy by the AC Stark shift $\varDelta_{\mathrm{AC}}$. Subsequently, a resonant $\pi-$pulse transforms the single-spin states according to $|\uparrow\rangle \rightarrow -i\,|\downarrow\rangle$ and $|\downarrow\rangle \rightarrow -i\,|\uparrow\rangle$. Then, a second dressing pulse whose illumination time $\frac{t_{\mathrm{uv}}}{2}$ is identical to the first one induces interactions between the terms which were previously in the non-interacing state $|\downarrow\downarrow\rangle$. The spin echo between both UV pulses is important because it cancels the contribution of single-spin terms such as the strong AC Stark shift $\varDelta_{\mathrm{AC}}$. In contrast, the two-spin operator $\hat{S}^z\hat{S}^z$ of the Ising interaction is symmetric under the $\pi-$pulse and does not cancel in the evolution. The Hamiltonian describing the dynamics can therefore be written as

$$\hat{H} = \hbar \sum_{\boldsymbol{i}\neq\boldsymbol{j}} \frac{J_{\boldsymbol{ij}}}{2}\hat{S}^z_{\boldsymbol{i}}\hat{S}^z_{\boldsymbol{j}}, \tag{8.2}$$

where interactions $J_{\boldsymbol{ij}} = J\delta_{\boldsymbol{i}-\boldsymbol{j},\boldsymbol{R}^{\|}}$ are restricted to the relevant distance vector $\boldsymbol{R}^{\|}$ and indices $\boldsymbol{i}(\boldsymbol{j})$ represent the position vectors in the lattice. Applying a push-out beam resonant with the cycling transition $|\uparrow\rangle \rightarrow |5P_{3/2}, F' = 3\rangle$ using a laser operating at the wavelength $\lambda_{D_2} = 780\,\mathrm{nm}$ removes all spins $|\uparrow\rangle$. Spins $|\downarrow\rangle$ remain are unaffected. Finally, the remaining spins in the state $|\downarrow\rangle$ are imaged with the microscope.

In principle, the near-resonant sideband as well as the far-detuned carrier also give rise to conventional Rydberg-dressed soft-core potentials, see section 2.5.2. However, because the sideband has only very low intensity and because the carrier field is more than seven hundred megahertz detuned from the $|\uparrow\rangle \rightarrow |e\rangle$ transition, the corresponding interaction strengths are below $5\,\mathrm{Hz}$ and therefore negligible. For the same reason, the two contributing single-atom AC Stark shifts $\varDelta_{\mathrm{AC}}$ are both only around two kilohertz, only a few times larger than J_{th}. In previous Rydberg dressing experiments, the ratio between $\varDelta_{\mathrm{AC}}$ and the admixed interactions was significantly larger, see also Ref. [155, 221]. In the chosen two-color coupling scheme where the detuning of the carrier field is almost one third of the fine-structure splitting to the higher-lying fine-structure state $|36P_{3/2}\rangle$, the contribution from the off-resonant carrier field is further decreased because both states $|e\rangle = |36P_{1/2}\rangle$ and $|36P_{3/2}\rangle$ contribute with a different sign. As a consequence, the scheme is less sensitive to a power imbalance between both UV pulses arising from imperfect intensity stabilization.

Calculated dynamics without dissipation

In order to provide further intuition, the expected dynamics is first discussed without the presence of decoherence. For a system of two isolated spins, an analytical calculation of the time-dependent pair state yields $|\varPsi(t_{\mathrm{uv}})\rangle = -\frac{1}{\sqrt{2}}\cos\left(\frac{\varphi_J}{4}\right)|\uparrow\uparrow\rangle + i\frac{1}{\sqrt{2}}\sin\left(\frac{\varphi_J}{4}\right)|\downarrow\downarrow\rangle$ after neglecting a global phase. For a vanishing interaction phase $\varphi_J = 0$, the spin orientation of the state $|\varPsi(0)\rangle = |\uparrow\uparrow\rangle$ is equal to the initial configuration because all three microwave pulses add up to a $2\pi-$pulse. In this case, no spins will be observed in the images after the resonant push-out. For times unequal to zero, the interaction triggers correlated spin flips into the state $|\downarrow\downarrow\rangle$. This gives rise to finite connected two-spin correlations $C^{(2)} = \langle\hat{S}^z_1\hat{S}^z_2\rangle - \langle\hat{S}^z_1\rangle\langle\hat{S}^z_2\rangle$ between both spin orientations. At the time $t_c = \pi/J$, the system evolves into the maximally entangled Bell state where the correlations reach a maximum $C^{(2)}_{\mathbf{R}} = \frac{1}{4}$. After evolving into the inverted initial state $i\,|\uparrow\uparrow\rangle$ and passing the Bell state a second time, the state evolves back into the initial spin state at $t = 4t_c$.

For a larger two-dimensional spin lattice, the dynamics looks qualitatively similar. Because only interactions at the distance $\boldsymbol{R}^{\|}$ are relevant on the accessible timescales, the system decouples into several one dimensional spin chains oriented along the diagonal direction of the lattice. Again, accumulated phases trigger correlated spin flips which give rise to correlation signals, see Fig 8.3 (**b**). Because any of the spins in the chain can flip their state during the sequence, the correlation signal

$$C^{(2)}_{\boldsymbol{R}} = (\langle \hat{S}^z_{\boldsymbol{R}'} \hat{S}^z_{\boldsymbol{R}'+\boldsymbol{R}} \rangle - \langle \hat{S}^z_{\boldsymbol{R}'} \rangle \langle \hat{S}^z_{\mathbf{R}'+\boldsymbol{R}} \rangle)_{\boldsymbol{R}'} \tag{8.3}$$

of spins at a distance $\boldsymbol{R}$ is now averaged over the positions $\boldsymbol{R}'$ in a central region of interest in the lattice, denoted by $(\,.\,)_{\boldsymbol{R}'}$. Here, also the maximum correlation strength is lower than for the case of two isolated spins. The two-spin correlation signal $C^{(2)}_{\boldsymbol{R}^{\|}}$ is restricted to distances $\boldsymbol{R} = \boldsymbol{R}^{\|}$.

Even if interactions occur only pairwise, also multi-spin correlations are expected to be present in the dynamics [449]. This can be intuitively explained by the example of three spins. Here, because a spin within the chain can either participate in a spin flip process with one of both neighboring spins, the state of all three spins becomes correlated. The coresponding connected three-spin correlator is defined by

$$C^{(3)}_{\mathbf{R}_1\mathbf{R}_2} = \left(\left\langle \left(\hat{S}^z_{\mathbf{R}'} - \langle \hat{S}^z_{\mathbf{R}'} \rangle\right) \left(\hat{S}^z_{\mathbf{R}'+\mathbf{R}_1} - \langle \hat{S}^z_{\mathbf{R}'+\mathbf{R}_1} \rangle\right) \left(\hat{S}^z_{\mathbf{R}'+\mathbf{R}_2} - \langle \hat{S}^z_{\mathbf{R}'+\mathbf{R}_2} \rangle\right) \right\rangle\right)_{\mathbf{R}'}, \tag{8.4}$$

where $(\,.\,)_{\boldsymbol{R}'}$ denotes averaging over three-spin subsystems with distances $\boldsymbol{R}_1$ and $\boldsymbol{R}_2$. In the realized system, three-spin correlations are expected to be present at distances $\boldsymbol{R}_1 = \boldsymbol{R}_2 = \boldsymbol{R}^{\|}$, see also Fig. 8.2 (**b**). It can be shown that in such a system without dissipation, the presence of multi-spin correlations can be directly linked to multi-spin entanglement [450]. The calculated correlation signals $C^{(2)}_{\boldsymbol{R}^{\|}}(t_{\mathrm{uv}})$ and $C^{(3)}_{\boldsymbol{R}^{\|}\boldsymbol{R}^{\|}}(t_{\mathrm{uv}})$ for the calculated spin coupling J_{th} is shown in Fig. 8.2 (**c**). The onset of three-spin correlations $C^{(3)}_{\boldsymbol{R}^{\|}\boldsymbol{R}^{\|}}$ occurs with a delay relative to $C^{(2)}_{\boldsymbol{R}^{\|}}$ because it can be regarded as a higher-order process.

At later times, even higher-order correlations form. At the time t_c, the system evolves into an highly-entangled cluster state, see Fig 8.3 (**c**). Here, lower-order correlators such as $C^{(2)}_{\boldsymbol{R}^{\|}}(t_c) = 0$ and $C^{(3)}_{\boldsymbol{R}^{\|}\boldsymbol{R}^{\|}}(t_c) = 0$ vanish but the system is still globally correlated [450]. Furthermore, the magnetization $\langle \hat{S}^z \rangle$ of the cluster state vanishes. After passing the cluster state, the system disentangles again and refocuses into the initial state $|\uparrow\rangle$ with mean magnetization $\langle \hat{S}^z \rangle = 0.5$ at a revival time $t_r = 2t_c$ where $\varphi_J = \pi$.

The realization of the paradigmatic nearest-neighbor Ising Hamiltonian using Rydberg macrodimer dressing is ideal for the realization of cluster states [451]. The presented Ramsey sequence naturally realizes the standard preparation scheme which consists of a Hadamard gate, an Ising interaction time to create entanglement, and a second Hadamard gate [452]. Cluster states are discussed as resource states for one-way quantum computing [453].

The reason why the revival time occurs at an interaction phase of $\varphi_J = \pi$ instead of 2π where all states of the overall system rephase in the Ramsey sequence is that the evaluation is restricted to a centered region of the system. For the spins at the edge of the system, a revival time takes twice as long [221], see also the discussion of two isolated spins in the first part of the paragraph.

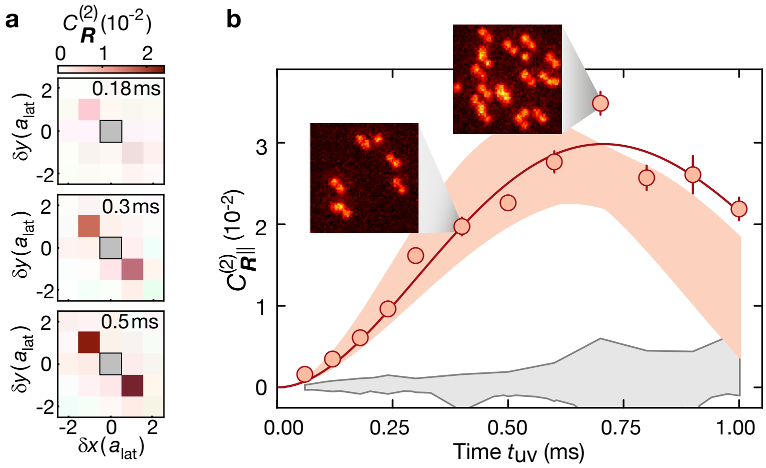

Figure 8.3: **Observed two-spin correlation signal.** (**a**) With increasing Ramsey interaction time $t_{\rm uv}$, correlations $C^{(2)}_{\boldsymbol{R}}(t_{\rm uv})$ can be observed at the distance $\boldsymbol{R} = (\delta x, \delta y) = \boldsymbol{R}^{\|}$, here shown for $t_{\rm uv} = 0.18\,\mathrm{ms}, 0.3\,\mathrm{ms}, 0.5\,\mathrm{ms}$. At distances $\boldsymbol{R} \neq \boldsymbol{R}^{\|}$, no correlations form. As in previous chapters, the signal for $\boldsymbol{R} = 0$ was excluded from the plot. (**b**) The correlation dynamics $C^{(2)}_{\boldsymbol{R}^{\|}}(t_{\rm uv})$ agrees with the calculations based on the expected interaction $J_{\rm th} = 2\pi \times 370(40)\,\mathrm{Hz}$ after accounting also for the observed atom loss (red shaded region). This is in agreement with the result $J = 2\pi \times 318(20)\,\mathrm{Hz}$ obtained from a fit (solid red line). Again, spins at distances $\boldsymbol{R} \neq \boldsymbol{R}^{\|}$ remain uncorrelated (gray shaded area). The insets show exemplary images from the quantum gas microscope. Error bars on the data points were calculated using a bootstrap algorithm (delete-1 jackknife). Figure adapted from Ref. [442].

8.3 Observed spin dynamics

Both previously discussed correlators are experimentally accessible from the reconstructed images from our microscope taken after the Ramsey sequences. The experimental datasets clearly show correlations $C^{(2)}_{\boldsymbol{R}}(t_{\rm uv})$ that are increasing with illumination time $t_{\rm uv}$. Furthermore, the correlations are restricted to $\boldsymbol{R}^{\|}$ and $-\boldsymbol{R}^{\|}$ where the distance machtes the molecular bond length and the direction matches the orientation of the strongly coupled molecular state, see Fig. 8.3 (a). Both signals $C^{(2)}_{\boldsymbol{R}^{\|}} = C^{(2)}_{-\boldsymbol{R}^{\|}}$ are identical after spatially averaging over all spin pairs in the system. The flipped spin pairs are also directly visible in the individual images, see Fig. 8.3 (b). Analysing the recorded time-dependent correlation signal $C^{(2)}_{\boldsymbol{R}^{\|}}(t_{\rm uv})$ shows qualitative agreement with the calculation using the calculated spin coupling $J_{\rm th}$ based on the experimentally calibrated single-atom Rabi frequency $\widetilde{\Omega}/(2\pi) = 2.83\,\mathrm{MHz}$ without dissipation. The main difference is the smaller correlation amplitude due to the presence of dissipation. Extending the model by atom-loss terms which can be motivated by off-resonant Rydberg excitation, the full dynamics can be described.

The calculations including dissipation are based on a master equation and solved using *QuTip* [454]. In addition to both spin states, the single-atom Hilbert space was extended by a third state $|0\rangle$ which represents an atom lost because of excitation. The simulation accounted for the fact that lost atoms in the state $|0\rangle$ are identified as an atom in the state $|\uparrow\rangle$ in our spin-dependent imaging technique. The loss rates were included as single-spin

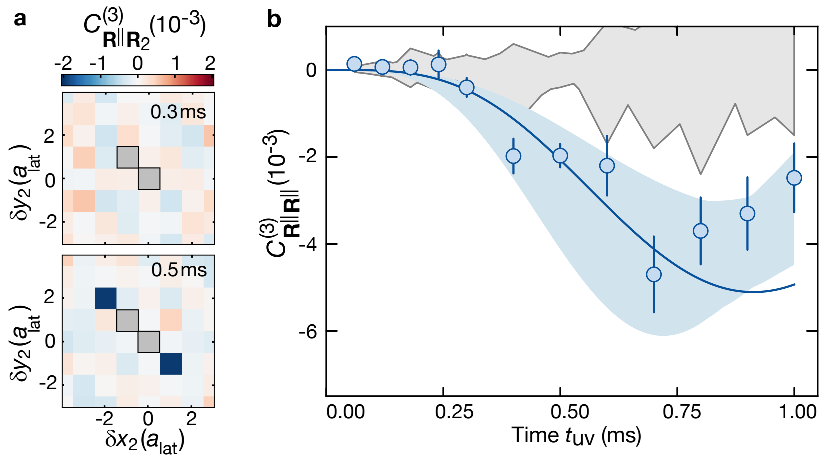

Figure 8.4: **Observed three-spin correlation signal.** (**a**) Two dimensional plots of correlations $C^{(3)}_{\boldsymbol{R}^{\parallel}\boldsymbol{R}_2}$ for various values of the distance vector $\boldsymbol{R}_2$. At later times, correlations $C^{(3)}_{\boldsymbol{R}^{\parallel}\boldsymbol{R}^{\parallel}}$ can be observed for $\boldsymbol{R}_2 = \boldsymbol{R}^{\parallel}$, here shown for $t_{\mathrm{uv}} = 0.3\,\mathrm{ms}, 0.5\,\mathrm{ms}$. As discussed in the text, the signal for $\boldsymbol{R}_2 = 0$ and $\boldsymbol{R}_2 = (-1, +1)\,a_{\mathrm{lat}}$ was excluded. (**b**) Again, the observed signal $C^{(3)}_{\boldsymbol{R}^{\parallel}\boldsymbol{R}^{\parallel}}(t_{\mathrm{uv}})$ is in agreement with the theoretical expectation (blue shaded region). The signal at other distances $\boldsymbol{R}_2 \neq \boldsymbol{R}^{\parallel}$ is shown in gray. The expectation based on the fit result for the two-spin signal (solid blue line) shows that both signals are consistent with respect to the model. Error bars in the correlation signal were calculated using a bootstrap algorithm (delete-1 jackknife). Figure adapted from Ref. [442].

Lindblad operators that project the spin states $|{\rightarrow}\rangle$ into $|0\rangle$ at a rate $\Gamma^{\mathrm{ex}}_{|\rightarrow\rangle} = 0.6(1)\,\mathrm{ms}^{-1}$. The experimentally calibrated loss rate $\Gamma^{\mathrm{ex}}_{|\rightarrow\rangle}$ was obtained from independent reference measurements, see section 8.3.1. In order to describe the dynamics, it was not necessary to include density-dependent correlated losses that might also be present in the system. It was also not required to include projections from $|{\uparrow}\rangle$ to $|{\downarrow}\rangle$ induced by the coupling to the Rydberg state [221], possibly because antitrapped Rydberg excitations leave the system too fast. The same model which was used to calculate the spin dynamics based on the expected parameters J_{th} and $\Gamma^{\mathrm{ex}}_{|\rightarrow\rangle}$ can also be used to determine J and $\Gamma^{\mathrm{fit}}_{|\rightarrow\rangle}$ from fitting. The obtained values $J = 2\pi \times 318(20)\mathrm{Hz}$ and $\Gamma^{\mathrm{fit}}_{|\rightarrow\rangle} = 0.46(5)\,\mathrm{ms}^{-1}$ are in agreement with the expectations.

In addition to $C^{(2)}_{\boldsymbol{R}}$, also the three-spin correlations $C^{(3)}_{\boldsymbol{R}_1\boldsymbol{R}_2}$ can be evaluated from the same experimental dataset. The correlation signal $C^{(3)}_{\boldsymbol{R}_1\boldsymbol{R}_2}$ depends on two distances $\boldsymbol{R}_1$ and $\boldsymbol{R}_2$. Fixing one distance $\boldsymbol{R}_1 = \boldsymbol{R}^{\parallel}$ enables to display $C^{(3)}_{\boldsymbol{R}^{\parallel}\boldsymbol{R}_2}(t_{\mathrm{uv}})$ for the positions $\boldsymbol{R}_2$ in a two dimensional plot similar as the ones presented for two-spin correlations, see Fig. 4.4 (**a**). Only the three-spin correlation signal where all three spins are located at different lattice sites are presented in the plot. As a consequence, the signal was excluded at distances $\boldsymbol{R}_2 = 0$ and $\boldsymbol{R}_2 = -\boldsymbol{R}^{\parallel}$, see also Fig. 8.2 (**b**).

At short times $t_{\mathrm{uv}} = 0.3\,\mathrm{ms}$ where two-spin correlations were already large, the three-spin correlation signal is still negligible. This observation is covered by the previously discussed delay of the three-spin correlation dynamics relative to the two-spin correlation dynamics. Later, a negative signal can be observed at distances $\boldsymbol{R}_2 = \boldsymbol{R}^{\parallel}$ and $\boldsymbol{R}_2 = -2\boldsymbol{R}^{\parallel}$. As one can infer from the illustration presented in Fig. 8.2 (**b**), the signal at both distances is identical after spatially averaging the correlation signal. Three-spin correlations at other distances remain within the background. Again, the observed time dependence of $C^{(3)}_{\boldsymbol{R}\|\boldsymbol{R}}(t_{\mathrm{uv}})$ follows the theoretical expectation. It also agrees with a calculation based on the parameters obtained from fiting the model to the two-spin correlation data.

Finally, also the magnetization $\langle \hat{S}^z \rangle = \frac{N_0/2 - \langle N_{\mathrm{at}} \rangle}{N_0}$ of the dataset can be analyzed, with N_0 the total number of intially prepared spins in the region of interest (ROI) of 11×11 lattice sites. The initial state at t_{uv} where all atoms N_0 are removed by the push-out pulse before taking the empty images with $\langle N_{\mathrm{at}} \rangle \approx 0$ corresponds to a magnetized system $\langle \hat{S}^z \rangle = \frac{1}{2}$, see Fig. 8.5 (**a**). As expected, the magnetization decreases in the presence of the dressed interactions because the flipped spin pairs are not removed by the push-out pulse, leading to $N_{\mathrm{at}} \neq 0$. Similar as for the correlation dynamics, the observed magnetization dynamics agrees with the theoretical expectation.

8.3.1 Limitations

At later times, where calculations without dissipation predict oscillations, the experimental spin dynamics was dominated by atom loss. Here, the atoms initialized in the state $|{\rightarrow}\rangle$ after the first $\pi/2-$pulse are either Rydberg-excited and then leaving system or projected into the state $|{\downarrow}\rangle$ which is not coupled to the Rydberg state. The dressing quality factor which is the ratio of coherent interaction and dissipation realized in the experiments was $J/\Gamma^{\mathrm{ex}}_{|\rightarrow\rangle} \approx 2\pi \times 0.5$. This is similar as the quality factors achieved in the same laboratory for two-dimensional systems [155] using conventional Rydberg dressing but below the achievements in one dimension where coherent revivals have been observed [221]. The atom loss was experimentally calibrated in independent measurements where atoms are either prepared in the state $|{\rightarrow}\rangle$ or in the state $|{\uparrow}\rangle$, see Fig. 8.5 (**b**). All other parameters were identical to those in the dressing sequence. The observed loss coefficients $\Gamma^{\mathrm{ex}}_{|\rightarrow\rangle} = 0.6(1)\mathrm{ms}^{-1}$ and $\Gamma^{\mathrm{ex}}_{|\uparrow\rangle} = 3.0(5)\,\mathrm{ms}^{-1}$ were significantly above the expectations $\Gamma^{\mathrm{th}}_{|\rightarrow\rangle} = 0.011\,\mathrm{ms}^{-1}$ assuming only off-resonant excitations of single-atom Rydberg states or macrodimers. The expected loss rates $\Gamma^{\mathrm{th}}_{|\rightarrow\rangle} \approx \frac{\gamma_{\mathrm{e}}}{2}\left(\frac{\beta\tilde{\Omega}}{2\Delta}\right)^2 + \frac{\gamma_\nu}{2}\sum_\nu \left(\frac{\tilde{\Omega}_\nu}{2\delta_\nu}\right)^2$ were calculated based on the admixture in the ground state and the decay rates of both kinds of excited states. Factors of $1/2$ account for the probability to be in the coupled state $|{\uparrow}\rangle$ and the fact that macrodimer excitation removes two atoms in a single event.

It has been experimentally verified that off-resonant excitation of macrodimers did not play a role during the dressing experiments. One the one hand, the datasets used for the calibration of the loss-rates shown in Fig. 8.5 (**b**) did not contain the pair correlation signal that is typical for macrodimer excitation, see chapter 5. On the other hand, the calculations of the spin dynamics showed that the presence of macrodimer excitations would have strong implications on the correlation signal observed during the Ramsey sequences. However, the observed dynamics can be described by using a model where all dissipative terms represent single-atom loss rates. Furthermore, the atom loss was only dependent on the power in the near-resonant sideband and not on the off-resonant carrier field which contributes to the macrodimer excitation.

Comparing the two experimental values $\Gamma^{\mathrm{ex}}_{|\rightarrow\rangle}$ and $\Gamma^{\mathrm{ex}}_{|\uparrow\rangle}$ one finds that the atom loss rate for both atoms prepared in the state $|{\uparrow}\rangle$ is more than two times the excitation rate observed for the atoms in $|{\rightarrow}\rangle$ where the probability to be in the optically coupled state is reduced by $1/2$. This indicates the presence of density-dependent losses such as the

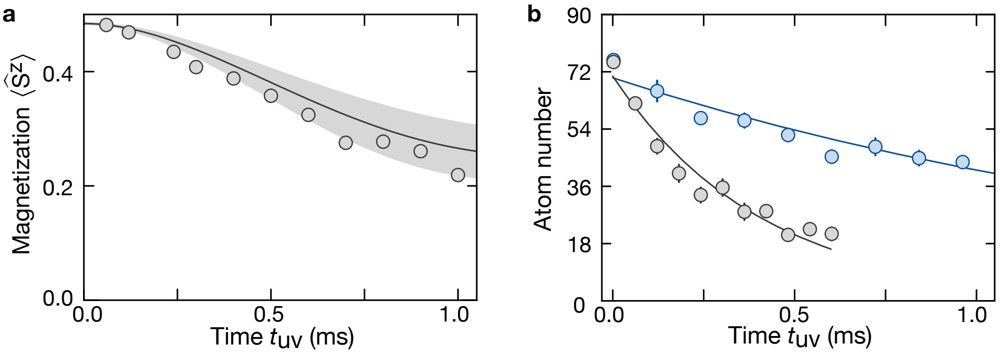

Figure 8.5: **Further details of the spin dynamics.** (**a**) The observed magnetization dynamics in the two-dimenional spin lattice agrees with the expectation (gray shaded region). The solid line again represents a calculation using the parameters obtained from the fit of the two-spin correlation dynamics $C_{\boldsymbol{R}}^{(2)}(t_{\mathrm{uv}})$. (**b**) Independent measurements of the lifetime of the two-dimensional unity filled lattice initially prepared in the states $|{\rightarrow}\rangle$ (gray) or $|{\uparrow}\rangle$ (blue) provided atom loss coefficients of $\mathit{\Gamma}^{\mathrm{ex}}_{|\uparrow\rangle} = 3.0\,(5)\mathrm{ms}^{-1}$ and $\mathit{\Gamma}^{\mathrm{ex}}_{|\rightarrow\rangle} = 0.6(1)\mathrm{ms}^{-1}$ for both cases. All error bars on the data points denote one standard error of the mean. Figure adapted from Ref. [442].

ones observed in earlier Rydberg dressing experiments because the density of atoms that populate the relevant state is twice as high when all atoms populate the state $|{\uparrow}\rangle$, see also appendix C.1. Also phase noise induced by the UV laser is expected to increase the off-resonant single-atom excitation rate, in particular for the small detuning $\mathit{\Delta}$ of the near-resonant sideband [130].

In addition to atom loss, also the coherence time of the Ramsey sequence represents an experimental limitation. Here, global phase fluctuations limit experimental timescales to $t_{\mathrm{uv}} \leq 1\,\mathrm{ms}$. In addition to magnetic field fluctuations that are independent of the coupling to the Rydberg state, UV intensity fluctuations contribute because they induce an imbalance of the two accumulated AC Stark shifts $\mathit{\Delta}_{\mathrm{AC}}$ during both dressing pulses with durations $t_{\mathrm{uv}}/2$. In order to efficiently cancel the AC Stark shift using the spin echo, the ratio between the spin interaction J and the AC Stark shift of the chosen coupling scheme is critical. In the Ramsey sequence, global phase fluctuations are expected to influence the magnetization of the spin system. The observation that the system demagnetizes sligthly faster than expected might indicate that global phase fluctuations have a small contribution to the spin dynamics, see Fig. 8.5 (**b**).

Finally, also the motional states that contribute to the molecular dressing scheme but were absent in conventional Rydberg dressing schemes add limitations. The contribution of Franck-Condon factors f_g^{ν} between the ground state wave function and the vibrational wave function decrease the achievable coupling strengths. For the two-color excitation scheme, also the coupling into the motional continuum observed in Fig. 7.3 introduces limitations. Here, the single-photon detuning $\mathit{\Delta}_C$ between the carrier field and the photodissociation transition from the molecular state into the intermediate state has to be larger than the kinetic energy band of continuum states contributing to the molecular wave function. During macrodimer dressing, the detuning $\mathit{\Delta}_C/(2\pi) = -6.3\,\mathrm{MHz}$ was chosen to be large enough such that the power-dependent broadening of the vibrational resonances was small, see also Fig. 7.4. However, as discussed previously, the level shift V^0_{pd} originating from the coupling into the motional continuum still had to be taken into account.

These limitations arising from the contributing motional states can be reduced by coupling to more shallow macrodimer potentials where the molecular wave function are similar as the initial relative wave function that can be achieved using optical traps. These are available at higher principal quantum numbers $n \approx 70$ where the macrodimer bond length increases and the confinement within the binding potentials is reduced. Pinning the initial atom pairs at the distance where the relative wave function has maximum overlap with the molecular wave function, Franck-Condon factors $f_g^\nu \approx 1$ close to unity are achievable. Note that for the potential chosen here, the binding potential minimum was sligthly displaced from the diagonal distance in the lattice, see Fig. 8.1 (**b**). Because an increase of f_g^ν directly increases $J \propto \left(f_g^\nu\right)^2$ but keeps the losses induced by the limiting near-resonant sideband identical, larger Franck-Condon factors will significantly increase the dressing quality factor. An additional advantage of the broader vibrational wave functions is that the kinetic energy band of the photodissociated continuum modes is more narrow. This allows to operate at smaller single-photon detunings where the observed broadening of the vibrational line due to photodissociation was already limiting for the vibrational wave functions chosen here.

Chapter 9

Summary and Outlook

9.1 Summary

This dissertation provides the first vibrationally and microscopically resolved study of Rydberg macrodimers. The narrow vibrational resonances resolved in two-photon spectroscopy demonstrate their importance for benchmarking the interaction potentials. Calculating the observed vibrational resonances required to include thousands of basis states and to account for higher-order multipole terms [73, 339]. The contribution of hyperfine interactions to the Rydberg pair potentials has been observed for the first time [50]. Furthermore, the response of macrodimer states to magnetic fields has been measured and confirmed by theoretical calculations.

The hierarchy of energy scales furthermore enabled photoassociation studies in a regime where the ground state atom pairs as well as the associated molecules were oriented in the laboratory frame. Here, because of the negligible rotational energies, the rotational states of the associated molecule were populated such that alignment remained conserved in the excitation process. This provided direct access to the molecular frame of reference and the electronic structure of the molecular state. Using the site-resolved detection method of the experiment, the selection rules contributing to the photoassociation into molecular quantum states was microscopically benchmarked in the molecular frame of reference. While similar observations could in principle be observed for any aligned diatomic molecule, it is the large size of Rydberg macrodimers which made such experiments possible here.

Using a new two-color excitation scheme furthermore enabled to engineer significantly increased Rabi frequencies into macrodimer states. In an off-resonant coupling configuration, the new scheme realizes distance-selective interaction potentials in the ground state that were strong enough to be observable in an experiment. The presence of the spin interactions was experimentally verfied by evaluating spin correlations after a Ramsey sequence. The observed two-spin and three-spin correlations match the theoretical expectations after accounting for an additional energy shift originating from the optical coupling into unbound motional states

9.2 Outlook

At present, this dissertation represents the most detailed experimental characterization of Rydberg interaction potentials. It is remarkable that the calculations match the observations after accounting for sufficiently many basis states in the diagonalization. Performing spectroscopies at even higher resolution might further characterize the pair potentials or even reveal other unexpected contributions, also for atomic species where the Rydberg states and their quantum defects are not known to such a high precision as for rubidium.

Studying the dependency of the molecular excitation rates on the molecular orientation reveals the significance of the interatomic axis for molecular quantum states. Furthermore, it provides the required formalism to optimize the coupling into macrodimer states such that they can be utilized for future applications in quantum science. At present, quantum simulations and quantum computations using Rydberg atoms are mainly using the asymptotic shape of the pair potentials at large distances. The realization of distance-selective interactions by off-resonant coupling to macrodimer binding potentials located in the non-perturbative distance regime represents a first application towards this direction.

Several directions how the research presented in this dissertation might be continued are presented in the following paragraphs.

Realization of cluster states

The realized distance-selective interactions presented in chapter 8 were restricted along one diagonal direction in order to optimize the Clebsch-Gordan coefficients contributing to the coupling. Changing the direction of the magnetic field and the light polarization, also symmetric Ising interactions in a two-dimensional spin system are available. For extended coherence times, this enables the realization of two-dimensional cluster states in a single entanglement operation. Such a study will require to use more shallow macrodimer potentials where Franck-Condon factors are higher as well as higher UV power. Both improvements combined, the coupling rates between the ground pair states and the macrodimer states might be strong enough.

Coherent macrodimer excitation and macrodimer blockade

There are also research directions using the two-color excitation scheme discussed in chapter 7. The molecular Rabi frequencies $\widetilde{\Omega}_{\nu} \approx 100\,\mathrm{kHz}$ available in the two-color excitation scheme exceed the calculated decay rates. For specific configurations, this might enable the observation of coherent Rabi oscillations between ground state atoms and the molecular states. Here, it will be crucial to keep the lattices deep enough to provide high Franck-Condon factors with the initial motional ground state in the lattice. This is not only important to maximize the molecular Rabi frequency but also because the coherent deexcitation of the macrodimer state back into the electronic ground state after the first $\pi-$pulse can otherwise populate many different motional states. In larger systems, an even larger molecular Rabi frequency might be available because of the presence of a collectively enhanced Rabi rate similar to the ones observed in Rydberg blockade measurements, see also section 2.5.1. First experimental signals already indicate that such a fast excitation pulse enables the observation of a spatial blockade between pairs of macrodimers. In the absence of dephasing on the relevant timescales, such a blockade mechanism can in principle be used to realize four-atom gates.

Hybridization of macrodimers and Rydberg atoms

In the discussion of the two-color excitation scheme it has been found that macrodimer resonances broaden at small intermediate-state detunings because of the photodissociation into the motional continuum, see Fig. 7.3 and Fig. 7.4. It would be interesting to study the excitation in the Autler-Towns regime where the phase modulated laser is at the same time single-photon resonant with the transitions $|g\rangle \rightarrow |36P_{1/2}\rangle$ as well as two-photon resonant with $|gg\rangle \rightarrow |\Psi^\nu\rangle$. In the limit where the upper carrier Rabi frequency is much higher than the lower sideband Rabi frequency, which acts as a probe, one might observe a Autler-Towns splitting where the intermediate states $|ge\rangle$ and $|\Psi^\nu\rangle$ hybridize. In order to avoid the observed broadening of the macrodimer resonance, this might require the Rabi coupling of the carrier field to be larger than the bandwidth of the motional states contributing to the vibrational wave function. In this limit, the intermediate state $|ge\rangle$ contributing to the hybridized states of the Autler Towns splitting is intuitively expected to inherit the motional state of the vibrational wave function.

Light-mediated spatial macrodimer exchange

Using the two-color excitation scheme introduced in Fig. 7.1, the two-photon transition from the ground state $|gg\rangle$ into molecular states $|\Psi^\nu\rangle$ in the optical lattice is not the only two-photon transition that is expected to contribute to the experiments. Assume an initially prepared state $|ggg\rangle$ of three ground state atoms aligned along a straight line and separated by one lattice diagonal distance. After exciting the left two atoms into a macrodimer state $|\Psi^\nu g\rangle$, another transition which is naturally on resonance is the two photon transition between $|\Psi^\nu g\rangle \rightarrow |g\Psi^\nu\rangle$ driven by the strong carrier field. This corresponds to an light-mediated spatial exchange process of the macrodimer state by one lattice diagonal distance. Both photons in this transition are absorbed from the strong carrier field. As a consequence, the expected transition rates between both spatially displaced macrodimers should be significantly larger than the two-color Rabi frequencies from the ground state where the weak sideband $\widetilde{\Omega}_{\mathrm{sb}}$ contributes. For large carrier Rabi frequencies $\widetilde{\Omega}_{\mathrm{C}}$ and low intermediate state detunings, first estimates provide Rabi rates that approach the megahertz regime.

The exchange should also be observable since after such an exchange all three atoms will leave the system. Because of the release of the kinetic energy stored in the original molecular wave function after the exchange, also the atom transfered from the molecular state back to the electronic ground state will carry enough kinetic energy to be removed from the system. First measurements indicate a statistically significant loss of three atoms aligned along the lattice diagonal direction if the two-color excitation is on resonant to the macrodimer resonance at strong carrier field. Also the correlation signal of four lost atoms aligned along the diagonal direction of the lattice is significant, indicating the presence of secondary processes. Longer chains cannot be observed, most likely due to motional dephasing such as the ones discussed in Fig. 4.5. As expected, the signal disappears after decreasing the power in the carrier field. Possible future studies might also include to observe signatures related to this exchange mechanism in the two-color and two-photon spectroscopies similar as the ones presented in Fig. 7.2 and Fig. 7.3 or to time-resolve the exchange.

Correlated and collective loss signatures

Furthermore, correlated loss signatures that were observed off-resonant to the Rydberg resonance can be studied in further detail, see also appendix C. Some rare individual shots from our miroscope reveal long chains of missing atoms oriented along the lattice diagonal direction. This observation seems consistent with the proposed light-mediated macrodimer exchange using the two-color excitation scheme proposed in the previous paragraph.

However, most images were taken using the single-color excitation scheme where the UV laser had a detuning of several hundreds of megahertz and the estimated optical exchange rates are too small. The observations also indicate that an additional trigger process is required to start the loss process, suggesting that the microscopic process is different.

Additionally, previously observed collective loss signatures that represent a strict limitation for many Rydberg dressing proposals might be studied in more detail.

Itinerant lattice models and macrodimers

The macrodimer-excitation mediated loss of atom pairs represents a dissipation mechanism which might allow for interesting quantum Zeno dynamics [455]. In the itinerant regime where atoms are allowed to tunnel in the lattice, the coherent tunneling might be prevented if the atom loss rate induced by macrodimer excitation with another nearby ground state atom is larger than the coherent tunneling rate [456]. An additional interesting direction might be to study the dressed interaction potentials directly in the itinerant regime [248]. Both projects require to keep the AC Stark shift induced by the off-resonantly coupled UV laser low such that coherent tunneling to neighboring sites is not inhibited due to the spatially varying UV intensity. Here, the two-color excitation scheme might again be beneficial because the AC Stark shift of the off-resonant carrier field can be further reduced.

Rydberg macrotrimers

Also the observation of Rydberg macrotrimers might be within reach [457, 458]. If accurate calculations of mactrotrimer potentials are available, the spectroscopic and microscopic schemes developed in this dissertation can directly be applied. A possible excitation scheme would be a three-photon transition from a ground state $|ggg\rangle$ via singly-excited and doubly-excited intermediate states into the mactrotrimer states. Again, the prefered spatial arrangment of the states $|ggg\rangle$ will be such that the Franck-Condon overlap reaches a maximum. In contrast to the two-photon excitation into macrodimer states where all intermediate states are non-interacting, the doubly-excited intermediate states will be interacting pair potentials. Because the coupling rates are expected to be lower than for macrodimers, large illumination times will be required. Here, studies will be restricted to the incoherent coupling regime where the excitation rates are proportional to the third power in the UV intensity.

By observing correlation signals for three holes after illuminating an initially prepared Mott insulator and again studying their dependence on the orientation the magnetic field and the light polarization, the resonances will be distinguished from macrodimers. Mactrotrimer spectroscopies will furthermore have a richer substructure because the contribution of an additional atom leads to more than one vibrational frequency.

Appendix A

Van der Waals potentials

This section approaches the van der Waals potentials introduced in section 2.3.2 using the language of molecular physics introduced in chapter 4 and compare the interactions for different Rydberg states. In section 2.3.2 it was mentioned that the presense of a strong external quantization axis allows one to define angularly dependent C_6-coefficients. For an external magnetic field, the arguments are similar as for the dipole-dipole interactions discussed in Fig. 2.3 where the single-atom states contributing to the asymptotic pair states have well-defined magnetic quantum numbers m. Here, one finds isotropic interactions for Rydberg S-states. Additionally, as for example discussed in [72, 155, 184], Rydberg P-states and states with even higher L can have strong angular dependencies. Again, the picture only holds as long as the interaction energies are lower than the energy scale related with the external quantization axis, such as the splitting by the magnetic field.

If there is no external quantization axis, the van der Waals potentials decouple into molecular potentials with different quantum numbers $\Omega^{\pm}_{g/u}$. For Rydberg S-states, 0_g^+, 0_u^- and 1_u potentials are possible. Consistently, the isotropic interactions observed in the presence of an external quantization axis translate into van der Waals interactions that are independent of the molecular quantum number, see Fig. A.1 (**a**) for $36S_{1/2}$. Here, because of the repulsive interaction with the lower-lying states $|36P_J, 35P_J\rangle$ and $|35P_J, 36P_J\rangle$, interactions are repulsive. For $36P_{1/2}$ Rydberg pair states, one finds the same set of molecular quantum numbers, see Fig. A.1 (**b**). However, now the different molecular symmetries decouple into different asymptotic van der Waals potentials. As described in Fig. 2.2 (**b**) by a simple two-channel model, two branches have attractive interactions because they get repelled from the energetically highly-lying states $|36S_{1/2}37S_{1/2}\rangle$ and $|37S_{1/2}36S_{1/2}\rangle$. On the blue-detuned side, one can furthermore find the macrodimer binding potential observed in Fig. 5.5. Van der Waals potentials for $36P_{3/2}$ pair states are shown in Fig. A.1 (**c**). The asymptotic pair state $|36P_{3/2}36P_{3/2}\rangle$ are almost Förster resonant to the pair states $|35P_{1/2}36P_{1/2}\rangle$ and $|36S_{1/2}35S_{1/2}\rangle$. As a consequence, the symmetries 0_u^-, 0_g^+ and 1_u that can be found for both sets of pair states feature large van der Waals coefficients. At closer distances, the pair potentials mix and interactions become non-perturbative. On the other hand, the remaining potentials 1_g, 2_g, 2_u and 3_u which cannot couple to the pair states $|35P_{1/2}36P_{1/2}\rangle$ have small van der Waals coefficients. Note that the energy separation of the asymptotic pair states $|36P_{1/2}36P_{1/2}\rangle$ and $|36P_{3/2}36P_{3/2}\rangle$ in Fig. A.1 (**b**) and Fig. A.1 (**c**) is only twice the single-atom fine-structure splitting.

A.1 Optical coupling to van der Waals potentials

For many experiments, the relevant question is how strongly the different pair potentials are optically coupled. Here, the formalism introduced in chapter 5 holds, which can be explained by an example. Assume an initial state $|g\rangle = |2, -2\rangle = |-\frac{1}{2}\rangle_J \otimes |-\frac{3}{2}\rangle_I$ optically coupled to $|36P_{3/2}\rangle$ using a single-photon transition. The initial pair state is

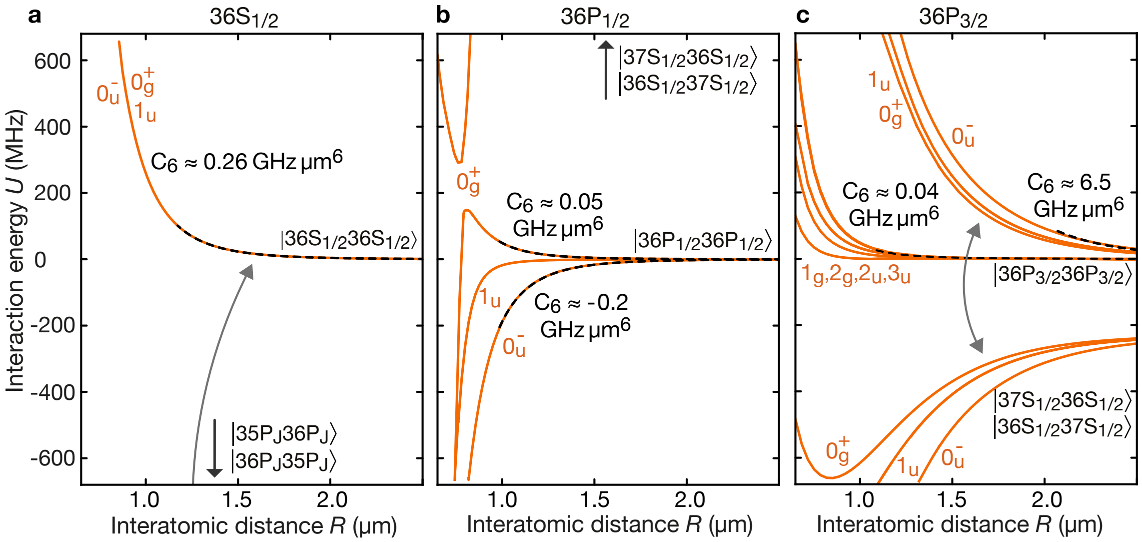

Figure A.1: **Van der Waals interactions between different Rydberg states at zero magnetic field.** (**a**) Repulsive van der Waals interactions for $36S_{1/2}$ are independent of the molecular symmetry. The part of the potential used for fitting the C_6 coefficient is indicated by the dashed black line. (**b**) For $36P_{1/2}$, the interaction strength and the sign of the potentials depend on the molecular symmetry. (**c**) For $36P_{3/2}$, all pair states which can couple to the almost Förster resonant pair states $|37S_{1/2}36S_{1/2}\rangle$ and $|36S_{1/2}37S_{1/2}\rangle$ feature strong van der Waals interactions. The C_6 coefficients of the remaining potentials 1_g, 2_u, 2_g and 3_u are smaller.

$|gg\rangle = |-1\rangle_J \otimes |-3\rangle_I$ and the relevant potentials can be found in Fig. A.1 (**c**). A small magnetic field $\boldsymbol{B}$ ensures an initial quantization axis. The induced Zeeman shifts are assumed to be below the Rabi frequency and the interaction shifts due to the pair potentials. The light is assumed to be σ^- polarized in this initial frame. From angular momentum conservation, the initial state $|-1\rangle_J$ for $\boldsymbol{R} \parallel \boldsymbol{B}$ can only couple to the 3_u pair potential. Because its van der Waals potential is small, the corresponding Rydberg blockade will be small. For an orthogonal configuration $\boldsymbol{R} \parallel \boldsymbol{B}$, the quantization axis of the pair potential is different from the quantization axis of the initial atoms. Here, the formalism presented in chapter 5 applies. After rotating the initial state and the light polarization into the frame perpendicular to $\boldsymbol{B}$, one finds that more than one pair potential contributes to the coupling. In particular, one finds a large contribution from the strongly interacting pair potentials 0_u^- and 1_u, whose Rydberg blockade is significantly larger than for 3_u. As a result, one expects to find a Rydberg blockade which significantly depends on the orientation of the atom pairs, as found in [72]. The picture presented here is consistent with Fig. 4 (c) and (d) in the supplementary information of Ref. [155] where Rydberg-dressed interactions are calculated based on the coupled pair states for the same configuration but slightly lower principal quantum number as discussed here.

Appendix B

Precision test of pair potentials

This section discusses the calculation of the macrodimer binding potentials using the *pair interaction* software [50] and the precision required in order to describe the observations. The discussion focuses on the 1_u potential blue-detuned from the $36P_{1/2}$ resonance which was first discussed in Fig. 5.6 and later used in chapter 7 and 8. The intuition obtained here can also be applied to the other binding potentials studied in this dissertation. The experimentally determined interaction shift of the lowest vibrational resonance $\nu = 0$ was $U^0 = 735.3(1)\,\mathrm{MHz}$. Using the single color coupling scheme at zero field, U^0 is twice the single-photon detuning where the vibrational state is on resonance, see section 4.2.

All single-atom states within an energy band $\Delta E = 550\,\mathrm{GHz}$ were included to the calculation. For the pair state basis, the same energy band was chosen as an additional selection criterion. The single-atom states were further restricted according to $\Delta n = 6$, $\Delta L = 4$, $\Delta J = 4$, $\Delta m_J = 4$, see also section 4.2.1. The calculations only accounted for ungerade states. Furthermore external fields were chosen to be zero and the sum of angular momentum projections along the interatomic axis was conserved.

B.1 Higher-order multipole terms

This section compares calculations of the 1_u binding potential accounting for different orders in the multipole expansion Eq 2.20. All other parameters were kept idential.

Using only the first non-vanishing term in the multipole expansion leads to the dipole-dipole interaction Hamiltonian $\hat{H}_3(R) \equiv \hat{H}_{\mathrm{dd}}(\boldsymbol{R})$ which scales as $\propto 1/R^3$, see Eq. 2.25. The calculated potential obtaind from exact diagonalization for the specified basis states is shown in Fig. B.1 (**a**). Most other Rydberg experiments that rely on asymptotic dipole-dipole interactions or van der Waals interactions can be quantitatively described using $\hat{H}_{\mathrm{dd}}(\boldsymbol{R})$. However, a calculation of the vibrational macrodimer resonances requires more precision [73, 176]. As one can see, the calculation underestimates the interaction energy by several tens of megahertz.

Additionally accounting for dipole-quadrupole terms which scale as $\propto 1/R^4$ leads to the Hamiltonian $\hat{H}_4(R)$ [200, 204]. The calculated pair potential using $\hat{H}_4(R)$ is shown in Fig. B.1 (**b**). Even if the lowest vibrational energy shifted closer towards the experimental value, the deviation is still substantial. Furthermore, another crossing pair potential which can couple to the binding potential via the dipole-quadrupole term opens a gap in the binding potential. The gap leads to a perturbation of the vibrational motion due to non-adiabatic motional coupling terms similar as the ones discussed in chapter 6. This is the reason why the vibrational state $\nu = 2$ in Fig. 5.6 (**a**) appears broader compared to the other vibrational states. The calculations of the vibrational energies presented in Fig. 5.6 (**a**) neglected this additional perturbation in the binding potential and assumed diabatic transitions at the avoided crossing.

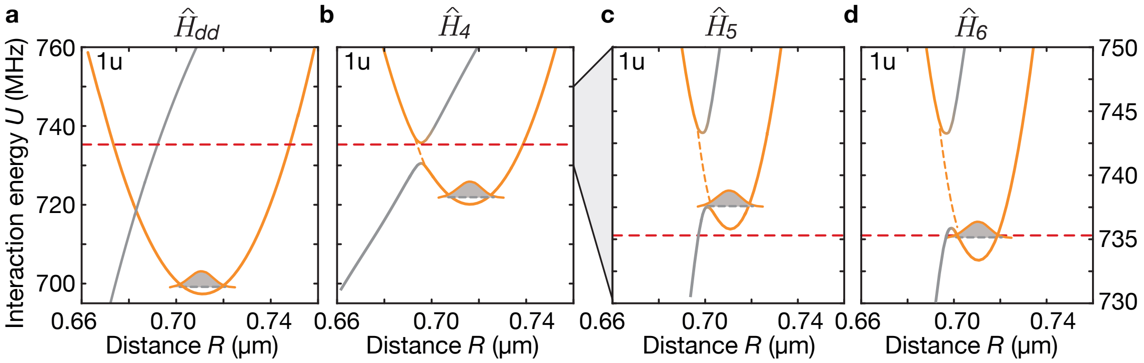

Figure B.1: **Convergence of the multipole expansion.** (**a**) A calculation of the 1_u binding potential using the dipole-dipole interaction Hamiltonian $\hat{H}_{dd}(R)$ underestimates the experimentally obtained location of the lowest vibrational resonance (dashed red line), see Fig. 5.6 (**a**). (**b**) Accounting also for dipole-quadrupole interactions using the Hamiltonian $\hat{H}_4(R)$ is not sufficient to predict the observed vibrational resonances. (**c**) Adding also multipole terms proportional to $\propto 1/R^5$ reduced the deviation between the measured and the calculated vibrational energy to about one megahertz. (**d**) A calculation based on $H_6(R)$ where also multipole terms which scale as $\propto 1/R^6$ were added finally led to an agreement.

Acounting also for dipole-octupole and quadrupole-quadrupole terms in the multipole expansion which scale as $\propto 1/R^5$ leads to $\hat{H}_5(R)$, see Fig. B.1 (**c**). The calculated lowest vibrational energy shifts even closer to the observed value but there is still a deviation larger than a megahertz. After also accounting for octupole-octupole interactions and other terms that scale as $\propto 1/R^6$, the observations and the calculations agree. For some of the studied potentials, also terms scaling as $\propto 1/R^7$ had to be taken into account. Sometimes, these further modified the energy of the binding potential by another few hundred kilohertz.

Appendix C

Correlated losses

Off-resonant coupling to Rydberg states can trigger correlated loss processes. This section first discusses collective losses which represent a strong limitation for many experiments. Second, the discussion focuses on rare observations of correlated losses where atoms aligned along a given direction in the lattice leave the system at once while the environment remains unaffected.

C.1 Collective loss

Many recent Rydberg dressing experiments at high densities suffered from atom loss rates that were much larger than expected [154, 155, 247]. Only at low densities, the loss rates were in agreement with the calculated single-atom loss rates [221]. The present understanding is that they are triggered by black-body transitions to neighboring Rydberg states, followed by an excitation avalanche at distances where the interaction shift of the created impurity compensates for the detuning [130]. Such a Rydberg *antiblockade* [426] where interactions shift an applied light field at a specific distance into resonance and therefore facilitate further excitations have been observed in other circumstances [70, 459–462]. This work focuses on Rydberg P-states $|nP_J\rangle$ with principal quantum numbers n between 30 and 40 and fine-structure states $J = \frac{1}{2}$ and $J = \frac{3}{2}$. Collective losses were observed detuned from both fine-structure states and broaden the observed Rydberg resonances. However, for $J = \frac{3}{2}$, they extend to much higher detunings.

Neglecting collective lossess, the higher-lying state $|nP_{3/2}\rangle$ would be the better choice in most cases. Dressing experiments benefit from higher Rabi frequencies compared to $|nP_{1/2}\rangle$. Furthermore, the shallow macrodimer potentials close to the $|nP_{3/2}nP_{3/2}\rangle$ asymptote give rise to higher Franck-Condon factors, see Fig. A.1 (**c**). Because these advantages cannot compensate for the higher collective loss rates, most of our Rydberg dressing experiments were performed close to the $nP_{1/2}$ resonance. Also the macrodimer studies presented here were restricted to potentials closer to the $|nP_{1/2}nP_{1/2}\rangle$ asymptote, see Fig. 5.1 (**c**). Interestingly, the observed collective atom loss detuned from the lower-lying state $|nP_{1/2}\rangle$ is reduced at detunings higher than a few tens of megahertz, such that the much higher macrodimer excitation rates on-resonant to the vibrational resonances located at detunings higher than hundred megahertz can be observed. In contrast, binding potentials closer to the $|nP_{3/2}nP_{3/2}\rangle$ asymptote were not accessible because the loss was higher than the macrodimer excitation rates, even several hundred megahertz detuned.

In order to experimentally study the loss rates, a unity-filled Mott insulator in the electronic ground state $|g\rangle = |F = 2, m_F = -2\rangle$ was illuminated by the ultraviolet (UV) laser red detuned from the $|g\rangle \to |36P_{3/2}\rangle$ transition. A small magnetic field of $B \approx 3\,\text{G}$ directing out of the atomic plane acted as a quantization axis. The UV laser was linearly polarized in the atomic plane perpendicular to $\boldsymbol{B}$. This configuration realizes σ^+ and σ^- polarization at equal weights, while it does not allow for π polarization. The Rabi frequen-

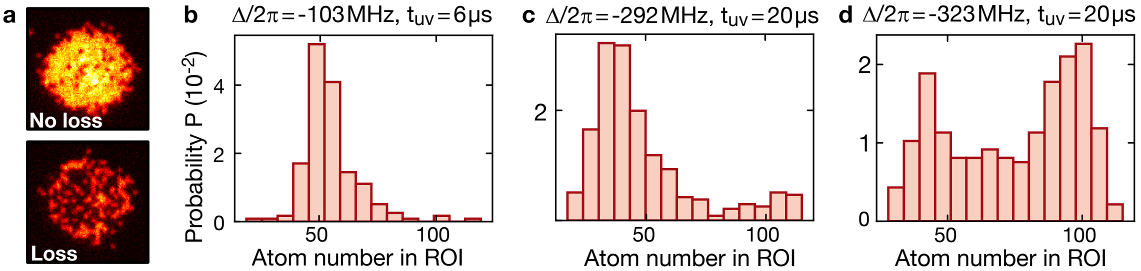

Figure C.1: **Collective loss signatures.** (**a**) Detuned from the Rydberg transition, one finds collective avalanche losses that represent limitations for many Rydberg experiments. If the collective loss process did not occur, the initially prepared Mott insulator is not affected by the UV pulse. After the avalanche process, only a dilute cloud of ground state atoms remains. (**b**,**c**,**d**) Atom number histograms for various detunings Δ from the $|36P_{3/2}\rangle$ resonance and illumination times t_{uv} show the presence of unexpectedly large collective loss rates.

cies coupling the ground state and the off-resonant states $|36P_{3/2}\rangle$ with $m_J = +1/2$ and $m_J = -3/2$ were $\widetilde{\Omega}_{-3/2}/(2\pi) \approx 3.2(3)\,\mathrm{MHz}$ and $\widetilde{\Omega}_{+1/2}/(2\pi) \approx 1.8(2)\,\mathrm{MHz}$.

During the illumination time t_{uv}, the collective loss process decreases the atom number in the chosen region of interest (ROI) from $N_{\mathrm{roi}} \approx 100$ to roughly $N_{\mathrm{roi}} \approx 50$, see Fig. C.1 (**a**). Histrograms of the final atom number after the illumination are presented in Fig. C.1 (**b**,**c**,**d**). For detunings $\Delta/(2\pi) = -103\,\mathrm{MHz}$, it takes illumination times $t_{\mathrm{uv}} \approx 6\,\mu\mathrm{s}$ until such an avalanche occured in almost all sequences. Even for $\Delta/(2\pi) = -292\,\mathrm{MHz}$ and $t_{\mathrm{uv}} \approx 20\,\mu\mathrm{s}$ one can see that the avalanche process was triggered in most cases. Further increasing the detuning to $\Delta/(2\pi) \approx -323\,\mathrm{MHz}$ finally leads to a slightly reduced loss rate. The observed bimodality in the histogram clearly shows the collective nature of the loss where a single event is responsible for the loss [155]. At even larger detunings $\Delta/(2\pi) < -323\,\mathrm{MHz}$ where the loss reduces further, macrodimer potentials can be studied.

These experiments at the given Rabi frequencies showed experimental collective loss rates $\Gamma^{\mathrm{ex}}_{\mathrm{col}} \geq 100\mathrm{ms}^{-1}$ over a large range of detunings. Assuming that the collective loss is triggered by a single black-body transition [155], the rate can be estimated via

$$\Gamma^{\mathrm{th}}_{\mathrm{col}} = N_0 \left(\beta_{-\frac{3}{2}}\right)^2 \Gamma_{\mathrm{bb}} + N_0 \left(\beta_{+\frac{1}{2}}\right)^2 \Gamma_{\mathrm{bb}}, \tag{C.1}$$

with $N_0 \approx 250$ the total initial atom number in the system, $\Gamma_{\mathrm{bb}} \approx 14.4\,\mathrm{ms}^{-1}$ the black-body decay rate into neighboring Rydberg states (see also table 2.2) and $\beta_i = \frac{\widetilde{\Omega}_i}{2\Delta_i}$ the Rydberg fractions of both states $m_J = -\frac{3}{2}, +\frac{1}{2}$ in the dressed ground state. For the parameters presented in Fig. C.1 (**b**,**c**,**d**), Eq. C.1 provides $\Gamma^{\mathrm{th}}_{\mathrm{col}} = 1.1\,\mathrm{ms}^{-1}$, $0.14\,\mathrm{ms}^{-1}$, $0.12\,\mathrm{ms}^{-1}$. Even if Eq. C.1 already assumes that a single black-body process can trigger a collective loss where all atoms leave the system, it underestimates the observed atom loss rate by three orders of magnitude.

One difference between the states $|36P_{1/2}\rangle$ and $|36P_{3/2}\rangle$ is that their interactions are significantly higher for the higher-lying $J = 3/2$ state because the pair state $|36P_{3/2}36P_{3/2}\rangle$ is close to a Förster resonance. However, these interactions do not contribute to the admixed single-atom black-body transitions estimated by Eq. C.1. After a black-body transition, the relevant quantity is the interaction between the created impurity atom and the optically coupled Rydberg state and not the interaction between P-state pairs. The black-body rates for the states $|36P_{1/2}\rangle$ and $|36P_{3/2}\rangle$ are basically identical. One difference are the final Rydberg D-states available for black-body transitions. Here, the state $|36P_{3/2}\rangle$ decays more prominently into $|nD_{5/2}\rangle$ while $|36P_{1/2}\rangle$ can only decay into $|nD_{3/2}\rangle$. While the C_3 coefficients after a black-body decay with the optically coupled state are slightly larger for $|36P_{3/2}\rangle$, further studies are required to verify whether this can explain the larger difference between both states.

Possible future directions

To further study the connection between black-body transitions and the observed collective losses rates, the impurity atoms could be deterministically prepared. This could be done by exciting a Rydberg S-state or a Rydberg D-state using the conventional two-photon excitation schemes from the ground state. The required lasers at wavelengths $780\,\mathrm{nm}$ and $480\,\mathrm{nm}$ are available in the laboratory [212]. Also a microwave transition between excited P-state atoms to nearby Rydberg states can be used. The initial state, the magnetic field direction or the polarization of the UV light are additional tuning knobs. It might also be interesting to study whether the nearby Förster resonance has some contribution to the loss rates.

The length scale of the collective loss and the typical distance between the removed atoms can be studied. In particular the dependence on the detuning Δ and the Rabi frequency $\widetilde{\Omega}$ is interesting. Because the presence of several Rydberg atoms spreads the Rydberg transition frequencies of the remaining atoms over a large energy band, one would intuitively expect to observe a fast saturation and a subsequent reduction of the excitation rates. Similarly as for a Rydberg blockade, a picture based on an excitation avalanche should in principle only allow for a limited amount of possible Rydberg excitations, and their distance should strongly depend on the laser detuning.

It might also be interesting to measure the dependence of the collective loss signatures on the lattice depth to further study the role of doubly occupied sites and the motional energies in the ground state. We observed that the loss coefficient is larger at low lattice depths where the atoms form a BEC. Measurements also indicate that even after the phase transition deep in the Mott insulating state the loss coefficients further decrease by increasing the lattice depth.

C.2 Oriented loss chains

Under some specific configurations also other correlated loss signatures were observed, see Fig. C.2 (**a**). Here, initially unity-filled Mott insulatores were illuminated with the UV beam which was again detuned from a Rydberg P-state transition. Some rare images show the presence of a correlated loss process where atoms aligned along the lattice diagonal parallel as well as perpendicular to the propagation direction of the UV laser are removed from the system. The loss rates were small and not limiting other Rydberg experiments. Nevertheless, it would be interesting to study the underlying microscopic process.

All images were taken on resonance to Rydberg pair potentials such as the vibrational resonance of macrodimers. Here, the UV laser was up to hundreds of megahertz detuned from the Rydberg resonance. Off-resonant to pair potentials, such events were not ob-

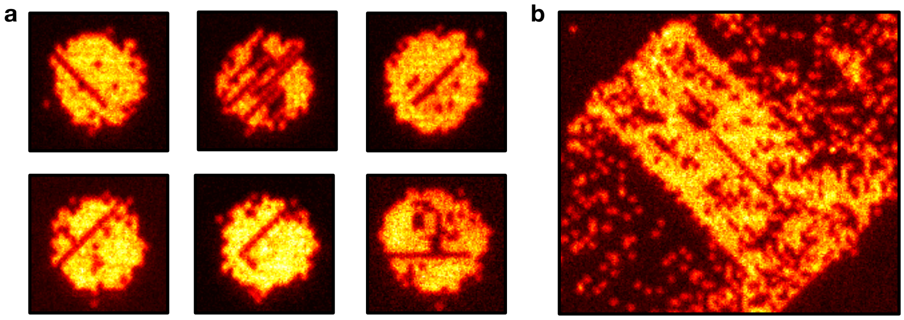

Figure C.2: **Diagonal loss signatures.** (**a**) Even far detuned from the Rydberg states where collective losses have not been observed, images taken from the microscope show the presence of rare loss channels along the lattice diagonal distance. For some parameters, also chains oriented along the direction of the lattice were observed. (**b**) Further studies will benefit from using larger Mott insulators as initial state where it is easier to get statistical significant rates for these rare events.

served. Many images contributed to the presented correlation signals presented in chapter 5. In these datasets, the excitation of macrodimers was the main correlated loss process in most of the images. Otherwise, the background in the correlation signals would have been larger. Most images contained only a few correlated pair losses. However, some images also contained longer chains of missing atoms. For most configurations, the macrodimer excitation rates were strongly directional. The direction of the diagonal loss was aligned with the favoured orientation of the coupled macrodimer state in almost all cases. Combining these observations it seems plausible that interacting Rydberg pair states such as macrodimers are required as an initial state before such a loss can be triggered.

It was noticeable that several, but not all, images were part of the datasets used for the evaluation of the correlation signals presented in Fig. 5.10. A few images taken at large detunings close the binding potential studied in Fig. 6.4 showed that the directed loss channel was aligned with the lattice, see the last image in Fig. 8.3 (**a**).

A possible trigger event might again be a black-body process for one of both Rydberg atoms which transfers the pair state into another Rydberg pair state. After such an event, in order to observe images as the ones presented, the process has to happen significantly faster than the macrodimer excitation that happens in parallel. Some of the images were taken at illumination times less than 20 microseconds, to give an absolute timescale.

After a black-body transition to a pair state with repulsive C_3 interactions, the atom pair will rapidly accelerate along the radial coordinate of the decayed macrodimer and then move through the system, see section 4.3.2. It might therefore be interesting to study whether motion contributes to the underlying microscopic process. Other atoms hit by the moving Rydberg atom might also become Rydberg-excited (e.g. due to antiblockade [426]) and subsequently leave the system. However, it seems likely that the interactions between the moving Rydberg atom and secondarily excited Rydberg atoms will affect the motion of the moving Rydberg atom and therefore stop the avalanche or change the direction. At least at deep lattice depths, the excited macrodimers will also lose their relative orientation before they decay, see Fig. 4.5. Furthermore, they will be repelled by the optical lattice. It might also be interesting whether dipolar interactions of the pair state created after such a black-body transition with the Rydberg-dressed background gas can be contributing to the process. Experimentally, the contribution of a black-body decay can be studied by coupling the excited macrodimers into unbound pair states using microwave fields. In order to increase the size of the datasets, future studies will strongly benefit from the larger Mott insulators that are accessible in the present experimental system [367], see Fig. C.2 (**b**).

Bibliography

[1] J. Rydberg, *XXXIV. On the structure of the line-spectra of the chemical elements*, The London, Edinburgh, and Dublin Philosophical Magazine and Journal of Science **29**, 331–337, (1890). (Cited on pp. 1 and 6.)

[2] N. Bohr, *The spectra of helium and hydrogen*, Nature **92**, 231–232, (1913). (Not cited.)

[3] A. Sommerfeld, *Atombau und Spektrallinien*, vol. 2, F. Vieweg & Sohn, (1921). (Not cited.)

[4] B. H. Bransden and C. J. Joachain, *Physics of Atoms and Molecules; 2nd ed.*, Prentice-Hall, Harlow, (2003). (Cited on pp. 27 and 52.)

[5] C. J. Foot, *Atomic physics*, vol. 7, OUP Oxford, (2004). (Cited on pp. 1, 9, 20, 46, and 73.)

[6] E. Schrödinger, *Quantisierung als Eigenwertproblem*, Annalen der Physik **385**, 437–490, (1926). (Cited on p. 1.)

[7] W. Heisenberg, *Über quantentheoretische Umdeutung kinematischer und mechanischer Beziehungen.*, Zeitschrift für Physik **33**, 879–893, (1925). (Not cited.)

[8] P. A. M. Dirac et al., *The principles of quantum mechanics*, no. 27, Oxford university press, (1981). (Not cited.)

[9] C. Cohen-Tannoudji, B. Diu, and F. Laloë, *Quantum mechanics; 1st ed.*, Wiley, New York, NY, (1977). (Cited on p. 65.)

[10] R. Shankar, *Principles of quantum mechanics*, Plenum, New York, NY, (1980). (Cited on p. 1.)

[11] W. E. Lamb and R. C. Retherford, *Fine Structure of the Hydrogen Atom by a Microwave Method*, Phys. Rev. **72**, 241–243, (1947). (Cited on p. 1.)

[12] R. P. Feynman, *Quantum Electrodynamics*, Addison-Wesley, Reading, MA, (1998). (Not cited.)

[13] R. Pohl, A. Antognini, F. Nez, F. D. Amaro, F. Biraben, J. M. R. Cardoso, D. S. Covita, A. Dax, S. Dhawan, L. M. P. Fernandes, A. Giesen, T. Graf, T. W. Hänsch, P. Indelicato, L. Julien, C.-Y. Kao, P. Knowles, E.-O. Le Bigot, Y.-W. Liu, J. A. M. Lopes, L. Ludhova, C. M. B. Monteiro, F. Mulhauser, T. Nebel, P. Rabinowitz, J. M. F. dos Santos, L. A. Schaller, K. Schuhmann, C. Schwob, D. Taqqu, J. F. C. A. Veloso, and F. Kottmann, *The size of the proton*, Nature **466**, 213–216, (2010). (Cited on p. 1.)

[14] W. Ubachs, J. C. J. Koelemeij, K. S. E. Eikema, and E. J. Salumbides, *Physics beyond the Standard Model from hydrogen spectroscopy*, Journal of Molecular Spectroscopy **320**, 1–12, (2016). (Cited on p. 1.)

[15] D. Hanneke, S. Fogwell, and G. Gabrielse, *New Measurement of the Electron Magnetic Moment and the Fine Structure Constant*, Phys. Rev. Lett. **100**, 120801, (2008). (Not cited.)

[16] V. Andreev, D. G. Ang, D. DeMille, J. M. Doyle, G. Gabrielse, J. Haefner, N. R. Hutzler, Z. Lasner, C. Meisenhelder, B. R. O'Leary, C. D. Panda, A. D. West, E. P. West, X. Wu, and ACME Collaboration, *Improved limit on the electric dipole moment of the electron*, Nature **562**, 355–360, (2018). (Cited on p. 1.)

[17] A. E. Siegman, *Lasers*, University Science Books, (1986). (Cited on p. 1.)

[18] W. Demtröder, *Laser spectroscopy: basic concepts and instrumentation*, Springer Science & Business Media, (2013). (Cited on p. 1.)

[19] H. J. Metcalf and P. Van der Straten, *Laser cooling and trapping of neutral atoms*, Wiley Online Library, (2007). (Cited on pp. 1, 9, and 34.)

[20] M. H. Anderson, J. R. Ensher, M. R. Matthews, C. E. Wieman, and E. A. Cornell, *Observation of Bose-Einstein Condensation in a Dilute Atomic Vapor*, Science **269**, 198–201, (1995). (Cited on pp. 1 and 34.)

[21] K. B. Davis, M. O. Mewes, M. R. Andrews, N. J. van Druten, D. M. Durfee, D. Stamper-Kurn, and W. Ketterle, *Bose-Einstein Condensation in a Gas of Sodium Atoms*, Phys. Rev. Lett. **75**, 3969–3973, (1995). (Cited on p. 34.)

[22] C. J. Pethick and H. Smith, *Bose–Einstein condensation in dilute gases*, Cambridge university press, (2008). (Cited on p. 1.)

[23] K. M. O'Hara, S. L. Hemmer, M. E. Gehm, S. R. Granade, and J. E. Thomas, *Observation of a Strongly Interacting Degenerate Fermi Gas of Atoms*, Science **298**, 2179–2182, (2002). (Cited on p. 1.)

[24] R. P. Feynman, *Simulating physics with computers*, International Journal of Theoretical Physics **21**, 133–153, (1982). (Cited on p. 1.)

[25] I. M. Georgescu, S. Ashhab, and F. Nori, *Quantum simulation*, Rev. Mod. Phys. 153, (2014). (Cited on p. 1.)

[26] I. Bloch, J. Dalibard, and W. Zwerger, *Many-body physics with ultracold gases*, Rev. Mod. Phys. **80**, 885–964, (2008). (Cited on pp. 1, 5, 31, 32, 36, and 63.)

[27] M. Lewenstein, A. Sanpera, and V. Ahufinger, *Ultracold Atoms in Optical Lattices: Simulating quantum many-body systems*, OUP Oxford, (2012). (Cited on p. 1.)

[28] C. Gross and I. Bloch, *Quantum simulations with ultracold atoms in optical lattices*, Science **357**, 995–1001, (2017). (Cited on p. 31.)

[29] F. Schäfer, T. Fukuhara, S. Sugawa, Y. Takasu, and Y. Takahashi, *Tools for quantum simulation with ultracold atoms in optical lattices*, Nature Reviews Physics **2**, 411–425, (2020). (Cited on pp. 1 and 31.)

[30] D. Jaksch, C. Bruder, J. I. Cirac, C. W. Gardiner, and P. Zoller, *Cold Bosonic Atoms in Optical Lattices*, Phys. Rev. Lett. **81**, 3108–3111, (1998). (Cited on pp. 1 and 32.)

[31] L. Tarruell and L. Sanchez-Palencia, *Quantum simulation of the Hubbard model with ultracold fermions in optical lattices*, Comptes Rendus Physique **19**, 365–393, (2018). (Cited on p. 1.)

[32] M. Greiner, O. Mandel, T. Esslinger, T. W. Hänsch, and I. Bloch, *Quantum phase transition from a superfluid to a Mott insulator in a gas of ultracold atoms*, Nature **415**, 39–44, (2002). (Cited on pp. 1 and 32.)

[33] S. Sachdev, *Quantum phase transitions*, Cambridge university press, (2011). (Cited on p. 1.)

[34] P. N. Jepsen, J. Amato-Grill, I. Dimitrova, W. W. Ho, E. Demler, and W. Ketterle, *Spin transport in a tunable Heisenberg model realized with ultracold atoms*, Nature **588**, 403–407, (2020). (Cited on pp. 1 and 33.)

[35] J. Koepsell, J. Vijayan, P. Sompet, F. Grusdt, T. A. Hilker, E. Demler, G. Salomon, I. Bloch, and C. Gross, *Imaging magnetic polarons in the doped Fermi–Hubbard model*, Nature **572**, 358–362, (2019). (Cited on pp. 1 and 32.)

[36] X. Zhou, W.-S. Lee, M. Imada, N. Trivedi, P. Phillips, H.-Y. Kee, P. Törmä, and M. Eremets, *High-temperature superconductivity*, Nature Reviews Physics **3**, 462–465, (2021). (Cited on pp. 1 and 32.)

[37] M. Qin, C.-M. Chung, H. Shi, E. Vitali, C. Hubig, U. Schollwöck, S. R. White, and S. Zhang, *Absence of Superconductivity in the Pure Two-Dimensional Hubbard Model*, Phys. Rev. X **10**, 031016, (2020). (Cited on p. 32.)

[38] A. Auerbach, *Interacting electrons and quantum magnetism*, Springer Science & Business Media, (2012). (Cited on p. 1.)

[39] C. Gross and W. S. Bakr, *Quantum gas microscopy for single atom and spin detection*, Nature Physics **17**, 1316–1323, (2021). (Cited on pp. 2 and 31.)

[40] W. S. Bakr, J. I. Gillen, A. Peng, S. Fölling, and M. Greiner, *A quantum gas microscope for detecting single atoms in a Hubbard-regime optical lattice*, Nature **462**, 74–77, (2009). (Cited on pp. 2 and 31.)

[41] J. F. Sherson, C. Weitenberg, M. Endres, M. Cheneau, I. Bloch, and S. Kuhr, *Single-atom-resolved fluorescence imaging of an atomic mott insulator*, Nature **467**, 68–72, (2010). (Cited on pp. 31 and 32.)

[42] C. Weitenberg, M. Endres, J. F. Sherson, M. Cheneau, P. Schauß, T. Fukuhara, I. Bloch, and S. Kuhr, *Single-spin addressing in an atomic Mott insulator*, Nature **471**, 319–324, (2011). (Cited on pp. 2 and 37.)

[43] M. Endres, M. Cheneau, T. Fukuhara, C. Weitenberg, P. Schauß, C. Gross, L. Mazza, M. C. Bañuls, L. Pollet, I. Bloch, and S. Kuhr, *Observation of Correlated Particle-Hole Pairs and String Order in Low-Dimensional Mott Insulators*, Science **334**, 200–203, (2011). (Cited on pp. 2 and 32.)

[44] A. Mazurenko, C. S. Chiu, G. Ji, M. F. Parsons, M. Kanász-Nagy, R. Schmidt, F. Grusdt, E. Demler, D. Greif, and M. Greiner, *A cold-atom Fermi–Hubbard antiferromagnet*, Nature **545**, 462–466, (2017). (Cited on pp. 2 and 32.)

[45] C. Chin, R. Grimm, P. Julienne, and E. Tiesinga, *Feshbach resonances in ultracold gases*, Rev. Mod. Phys. **82**, 1225–1286, (2010). (Cited on pp. 2, 27, 29, and 32.)

[46] H. Kadau, M. Schmitt, M. Wenzel, C. Wink, T. Maier, I. Ferrier-Barbut, and T. Pfau, *Observing the Rosensweig instability of a quantum ferrofluid*, Nature **530**, 194–197, (2016). (Cited on pp. 2 and 5.)

[47] L. D. Carr, D. DeMille, R. V. Krems, and J. Ye, *Cold and ultracold molecules: science, technology and applications*, New Journal of Physics **11**, 055049, (2009). (Cited on pp. 2 and 5.)

[48] T. F. Gallagher, *Rydberg Atoms*, Cambridge Monographs on Atomic, Molecular and Chemical Physics, Cambridge University Press, (1994). (Cited on pp. 2, 6, 7, 12, 19, and 20.)

[49] M. Saffman, T. G. Walker, and K. Mølmer, *Quantum information with Rydberg atoms*, Rev. Mod. Phys. **82**, 2313, (2010). (Cited on pp. 2, 5, 14, 17, 20, and 24.)

[50] S. Weber, C. Tresp, H. Menke, A. Urvoy, O. Firstenberg, H. P. Büchler, and S. Hofferberth, *Calculation of Rydberg interaction potentials*, J. Phys. B: At. Mol. Opt. Phys. **50**, 133001, (2017). (Cited on pp. 2, 5, 9, 14, 17, 19, 20, 51, 55, 60, 119, and 125.)

[51] D. Bluvstein, A. Omran, H. Levine, A. Keesling, G. Semeghini, S. Ebadi, T. T. Wang, A. A. Michailidis, N. Maskara, W. W. Ho, S. Choi, M. Serbyn, M. Greiner, V. Vuletić, and M. D. Lukin, *Controlling quantum many-body dynamics in driven Rydberg atom arrays*, Science **371**, 1355–1359, (2021). (Cited on p. 2.)

[52] A. Browaeys and T. Lahaye, *Many-body physics with individually controlled Rydberg atoms*, Nat. Phys. **16**, 132–142, (2020). (Cited on pp. 5, 14, and 20.)

[53] P. Scholl, M. Schuler, H. J. Williams, A. A. Eberharter, D. Barredo, K.-N. Schymik, V. Lienhard, L.-P. Henry, T. C. Lang, T. Lahaye, A. M. Läuchli, and A. Browaeys, *Quantum simulation of 2D antiferromagnets with hundreds of Rydberg atoms*, Nature **595**, 233–238, (2021). (Cited on p. 2.)

[54] D. Bluvstein, H. Levine, G. Semeghini, T. T. Wang, S. Ebadi, M. Kalinowski, A. Keesling, N. Maskara, H. Pichler, M. Greiner, V. Vuletic, and M. D. Lukin, *A quantum processor based on coherent transport of entangled atom arrays* (2021). (Cited on pp. 2, 20, and 25.)

[55] N. Šibalić, J. D. Pritchard, C. S. Adams, and K. J. Weatherill, *ARC: An open-source library for calculating properties of alkali Rydberg atoms*, Computer Physics Communications **220**, 319–331, (2017). (Cited on pp. 2, 9, 10, 11, 13, 14, 17, 19, 20, 47, and 53.)

[56] M. Endres, H. Bernien, A. Keesling, H. Levine, E. R. Anschuetz, A. Krajenbrink, C. Senko, V. Vuletic, M. Greiner, and M. D. Lukin, *Atom-by-Atom Assembly of Defect-Free One-Dimensional Cold Atom Arrays*, Science **354**, 1024–1027, (2016). (Cited on pp. 2, 5, and 33.)

[57] D. Barredo, S. d. Léséleuc, V. Lienhard, T. Lahaye, and A. Browaeys, *An atom-by-atom assembler of defect-free arbitrary two-dimensional atomic arrays*, Science **354**, 1021–1023, (2016). (Cited on pp. 2, 5, and 33.)

[58] K. M. Jones, E. Tiesinga, P. D. Lett, and P. S. Julienne, *Ultracold photoassociation spectroscopy: Long-range molecules and atomic scattering*, Rev. Mod. Phys. **78**, 483, (2006). (Cited on pp. 2, 27, and 29.)

[59] E. A. Donley, N. R. Claussen, S. T. Thompson, and C. E. Wieman, *Atom–molecule coherence in a Bose–Einstein condensate*, Nature **417**, 529–533, (2002). (Cited on p. 2.)

[60] W. B. Cairncross, J. T. Zhang, L. R. B. Picard, Y. Yu, K. Wang, and K.-K. Ni, *Assembly of a Rovibrational Ground State Molecule in an Optical Tweezer*, Phys. Rev. Lett. **126**, 123402, (2021). (Cited on p. 2.)

[61] P. K. Molony, P. D. Gregory, Z. Ji, B. Lu, M. P. Köppinger, C. R. Le Sueur, C. L. Blackley, J. M. Hutson, and S. L. Cornish, *Creation of Ultracold* $^{87}\mathrm{Rb}^{133}\mathrm{Cs}$ *Molecules in the Rovibrational Ground State*, Phys. Rev. Lett. **113**, 255301, (2014). (Cited on p. 2.)

[62] F. Seeßelberg, X.-Y. Luo, M. Li, R. Bause, S. Kotochigova, I. Bloch, and C. Gohle, *Extending rotational coherence of interacting polar molecules in a spin-decoupled magic trap*, Phys. Rev. Lett. **121**, 253401, (2018). (Cited on p. 2.)

[63] J. A. Blackmore, L. Caldwell, P. D. Gregory, E. M. Bridge, R. Sawant, J. Aldegunde, J. Mur-Petit, D. Jaksch, J. M. Hutson, B. E. Sauer, M. R. Tarbutt, and S. L. Cornish, *Ultracold molecules for quantum simulation: rotational coherences in CaF and RbCs*, Quantum Science and Technology **4**, 014010, (2018). (Cited on p. 2.)

[64] M.-G. Hu, Y. Liu, D. D. Grimes, Y.-W. Lin, A. H. Gheorghe, R. Vexiau, N. Bouloufa-Maafa, O. Dulieu, T. Rosenband, and K.-K. Ni, *Direct observation of bimolecular reactions of ultracold KRb molecules*, Science **366**, 1111–1115, (2019). (Cited on p. 2.)

[65] J. P. Shaffer, S. T. Rittenhouse, and H. R. Sadeghpour, *Ultracold Rydberg molecules*, Nature Communications **9**, 1965, (2018). (Cited on pp. 2, 5, 27, and 28.)

[66] V. Bendkowsky, B. Butscher, J. Nipper, J. P. Shaffer, R. Löw, and T. Pfau, *Observation of ultralong-range Rydberg molecules*, Nature **458**, 1005–1008, (2009). (Cited on pp. 2 and 28.)

[67] C. Boisseau, I. Simbotin, and R. Côté, *Macrodimers: Ultralong Range Rydberg Molecules*, Phys. Rev. Lett. **88**, 133004, (2002). (Cited on pp. 2, 27, 28, 51, 57, and 58.)

[68] S. M. Farooqi, D. Tong, S. Krishnan, J. Stanojevic, Y. P. Zhang, J. R. Ensher, A. S. Estrin, C. Boisseau, R. Côté, E. E. Eyler, and P. L. Gould, *Long-Range Molecular Resonances in a Cold Rydberg Gas*, Phys. Rev. Lett. **91**, 183002, (2003). (Cited on pp. 2 and 28.)

[69] K. R. Overstreet, A. Schwettmann, J. Tallant, D. Booth, and J. P. Shaffer, *Observation of Electric-Field-Induced Cs Rydberg Atom Macrodimers*, Nat. Phys. **5**, 581–585, (2009). (Cited on pp. 28 and 58.)

[70] H. Saßmannshausen and J. Deiglmayr, *Observation of Rydberg-Atom Macrodimers: Micrometer-Sized Diatomic Molecules*, Phys. Rev. Lett. **117**, 083401, (2016). (Cited on pp. 2, 28, 58, and 127.)

[71] C. Weitenberg, *Single-Atom Resolved Imaging and Manipulation in an Atomic Mott Insulator*, Ludwig-Maximilians-Universität München, PhD thesis, (2011). (Cited on pp. 2, 31, 34, 35, 37, and 48.)

[72] J. Zeiher, *Realization of Rydberg-dressed quantum magnets*, Ludwig-Maximilians-Universität München, PhD thesis, (2017). (Cited on pp. 2, 12, 17, 23, 31, 34, 35, 38, 40, 45, 47, 48, 61, 123, and 124.)

[73] J. Deiglmayr, *Long-range interactions between Rydberg atoms*, Phys. Scr. **91**, 104007, (2016). (Cited on pp. 5, 14, 60, 119, and 125.)

[74] C. S. Adams, J. D. Pritchard, and J. P. Shaffer, *Rydberg atom quantum technologies*, J. Phys. B: At. Mol. Opt. Phys. **53**, (2019). (Cited on pp. 5 and 24.)

[75] X. Wu, X. Liang, Y. Tian, F. Yang, C. Chen, Y.-C. Liu, M. K. Tey, and L. You, *A concise review of Rydberg atom based quantum computation and quantum simulation*, Chinese Physics B **30**, 020305, (2021). (Cited on p. 5.)

[76] H. Levine, A. Keesling, G. Semeghini, A. Omran, T. T. Wang, S. Ebadi, H. Bernien, M. Greiner, V. Vuletić, H. Pichler, and M. D. Lukin, *Parallel Implementation of High-Fidelity Multiqubit Gates with Neutral Atoms*, Phys. Rev. Lett. **123**, 170503, (2019). (Cited on pp. 5 and 25.)

[77] T. M. Graham, M. Kwon, B. Grinkemeyer, Z. Marra, X. Jiang, M. T. Lichtman, Y. Sun, M. Ebert, and M. Saffman, *Rydberg-Mediated Entanglement in a Two-Dimensional Neutral Atom Qubit Array*, Phys. Rev. Lett. **123**, 230501, (2019). (Not cited.)

[78] I. S. Madjarov, J. P. Covey, A. L. Shaw, J. Choi, A. Kale, A. Cooper, H. Pichler, V. Schkolnik, J. R. Williams, and M. Endres, *High-fidelity entanglement and detection of alkaline-earth Rydberg atoms*, Nature Physics **16**, 857–861, (2020). (Cited on pp. 5, 24, and 26.)

[79] T. Lahaye, J. Metz, B. Fröhlich, T. Koch, M. Meister, A. Griesmaier, T. Pfau, H. Saito, Y. Kawaguchi, and M. Ueda, *d-Wave Collapse and Explosion of a Dipolar Bose-Einstein Condensate*, Phys. Rev. Lett. **101**, (2008). (Cited on p. 5.)

[80] M. A. Norcia and F. Ferlaino, *Developments in atomic control using ultracold magnetic lanthanides*, Nature Physics **17**, 1349–1357, (2021). (Cited on p. 5.)

[81] M. Guo, F. Böttcher, J. Hertkorn, J.-N. Schmidt, M. Wenzel, H. P. Büchler, T. Langen, and T. Pfau, *The low-energy Goldstone mode in a trapped dipolar supersolid*, Nature **574**, (2019). (Cited on p. 5.)

[82] M. A. Norcia, C. Politi, L. Klaus, E. Poli, M. Sohmen, M. J. Mark, R. N. Bisset, L. Santos, and F. Ferlaino, *Two-dimensional supersolidity in a dipolar quantum gas*, Nature **596**, 357–361, (2021). (Not cited.)

[83] L. Chomaz, R. M. W. van Bijnen, D. Petter, G. Faraoni, S. Baier, J. H. Becher, M. J. Mark, F. Wächtler, L. Santos, and F. Ferlaino, *Observation of roton mode population in a dipolar quantum gas*, Nature Physics **14**, 442–446, (2018). (Cited on p. 5.)

[84] L. R. Liu, J. D. Hood, Y. Yu, J. T. Zhang, N. R. Hutzler, T. Rosenband, and K.-K. Ni, *Building one molecule from a reservoir of two atoms*, Science **360**, 900–903, (2018). (Cited on p. 5.)

[85] E. S. Shuman, J. F. Barry, and D. DeMille, *Laser cooling of a diatomic molecule*, Nature **467**, 820–823, (2010). (Cited on p. 5.)

[86] D. McCarron, *Laser cooling and trapping molecules*, J. Phys. B: At. Mol. Opt. Phys. **51**, 212001, (2018). (Cited on p. 5.)

[87] P. D. Gregory, M. D. Frye, J. A. Blackmore, E. M. Bridge, R. Sawant, J. M. Hutson, and S. L. Cornish, *Sticky collisions of ultracold RbCs molecules*, Nature **10**, 3104, (2019). (Cited on p. 5.)

[88] L. Anderegg, S. Burchesky, Y. Bao, S. S. Yu, T. Karman, E. Chae, K.-K. Ni, W. Ketterle, and J. M. Doyle, *Observation of microwave shielding of ultracold molecules*, Science **373**, 779–782, (2021). (Cited on p. 5.)

[89] B. Yan, S. A. Moses, B. Gadway, J. P. Covey, K. R. A. Hazzard, A. M. Rey, D. S. Jin, and J. Ye, *Observation of Dipolar Spin-Exchange Interactions with Lattice-Confined Polar Molecules*, Nature **501**, 521–525, (2013). (Cited on p. 5.)

[90] A. M. Kaufman and K.-K. Ni, *Quantum science with optical tweezer arrays of ultracold atoms and molecules*, Nature Physics **17**, 1324–1333, (2021). (Cited on p. 5.)

[91] W. B. Cairncross, J. T. Zhang, L. R. B. Picard, Y. Yu, K. Wang, and K.-K. Ni, *Assembly of a Rovibrational Ground State Molecule in an Optical Tweezer*, Phys. Rev. Lett. **126**, 123402, (2021). (Cited on p. 6.)

[92] S. de Léséleuc, V. Lienhard, P. Scholl, D. Barredo, S. Weber, N. Lang, H. P. Büchler, T. Lahaye, and A. Browaeys, *Observation of a symmetry-protected topological phase of interacting bosons with Rydberg atoms*, Science **365**, (2019). (Cited on pp. 6, 18, and 24.)

[93] H. Bernien, S. Schwartz, A. Keesling, H. Levine, A. Omran, H. Pichler, S. Choi, A. S. Zibrov, M. Endres, M. Greiner, V. Vuletić, and M. D. Lukin, *Probing many-body dynamics on a 51-atom quantum simulator*, Nature **551**, (2017). (Cited on p. 22.)

[94] M. Morgado and S. Whitlock, *Quantum simulation and computing with Rydberg-interacting qubits*, AVS Quantum Science **3**, 023501, (2021). (Cited on pp. 6 and 24.)

[95] B. M. Spar, E. Guardado-Sanchez, S. Chi, Z. Z. Yan, and W. S. Bakr, *A Fermi-Hubbard Optical Tweezer Array*, (2021). (Cited on p. 6.)

[96] N. Schine, A. W. Young, W. J. Eckner, M. J. Martin, and A. M. Kaufman, *Long-lived Bell states in an array of optical clock qubits*, (2021). (Cited on pp. 6 and 25.)

[97] G. Facchinetti, S. D. Jenkins, and J. Ruostekoski, *Storing Light with Subradiant Correlations in Arrays of Atoms*, Phys. Rev. Lett. **117**, 243601, (2016). (Cited on p. 6.)

[98] A. Asenjo-Garcia, M. Moreno-Cardoner, A. Albrecht, H. J. Kimble, and D. E. Chang, *Exponential Improvement in Photon Storage Fidelities Using Subradiance and "Selective Radiance" in Atomic Arrays*, Phys. Rev. X **7**, 031024, (2017). (Cited on pp. 6 and 33.)

[99] M. A. Norcia, J. R. K. Cline, J. A. Muniz, J. M. Robinson, R. B. Hutson, A. Goban, G. E. Marti, J. Ye, and J. K. Thompson, *Frequency Measurements of Superradiance from the Strontium Clock Transition*, Phys. Rev. X **8**, 021036, (2018). (Cited on p. 6.)

[100] M. O. Araújo, I. Krešić, R. Kaiser, and W. Guerin, *Superradiance in a Large and Dilute Cloud of Cold Atoms in the Linear-Optics Regime*, Phys. Rev. Lett. **117**, 073002, (2016). (Cited on pp. 6 and 33.)

[101] J. Rui, D. Wei, A. Rubio-Abadal, S. Hollerith, J. Zeiher, D. M. Stamper-Kurn, C. Gross, and I. Bloch, *A subradiant optical mirror formed by a single structured atomic layer*, Nature **583**, 369–374, (20201). (Cited on pp. 6 and 33.)

[102] K. Baumann, C. Guerlin, F. Brennecke, and T. Esslinger, *Dicke quantum phase transition with a superfluid gas in an optical cavity*, Nature **464**, 1301–1306, (2010). (Cited on p. 6.)

[103] V. D. Vaidya, Y. Guo, R. M. Kroeze, K. E. Ballantine, A. J. Kollár, J. Keeling, and B. L. Lev, *Tunable-Range, Photon-Mediated Atomic Interactions in Multimode Cavity QED*, Phys. Rev. X **8**, 011002, (2018). (Not cited.)

[104] M. A. Norcia, R. J. Lewis-Swan, J. R. K. Cline, B. Zhu, A. M. Rey, and J. K. Thompson, *Cavity-mediated collective spin-exchange interactions in a strontium superradiant laser*, Science **361**, 259–262, (2018). (Not cited.)

[105] J. Léonard, A. Morales, P. Zupancic, T. Esslinger, and T. Donner, *Supersolid formation in a quantum gas breaking a continuous translational symmetry*, Nature **543**, 87–90, (2017). (Not cited.)

[106] J. A. Muniz, D. Barberena, R. J. Lewis-Swan, D. J. Young, J. R. K. Cline, A. M. Rey, and J. K. Thompson, *Exploring dynamical phase transitions with cold atoms in an optical cavity*, Nature **580**, 602–607, (2020). (Cited on p. 6.)

[107] A. Periwal, E. S. Cooper, P. Kunkel, J. F. Wienand, E. J. Davis, and M. Schleier-Smith, *Programmable interactions and emergent geometry in an array of atom clouds*, Nature **600**, 630–635, (2021). (Cited on p. 6.)

[108] W. Paul, *Electromagnetic traps for charged and neutral particles*, Rev. Mod. Phys. **62**, 531–540, (1990). (Cited on p. 6.)

[109] C. Schneider, M. Enderlein, T. Huber, and T. Schaetz, *Optical trapping of an ion*, Nature Photonics **4**, 772–775, (2010). (Cited on p. 6.)

[110] A. Lambrecht, J. Schmidt, P. Weckesser, M. Debatin, L. Karpa, and T. Schaetz, *Long lifetimes and effective isolation of ions in optical and electrostatic traps*, Nature Photonics **11**, 704–707, (2017). (Cited on p. 6.)

[111] F. B. Dunning, J. J. Mestayer, C. O. Reinhold, S. Yoshida, and J. Burgdörfer, *Engineering atomic Rydberg states with pulsed electric fields*, J. Phys. B: At. Mol. Opt. Phys. **42**, 022001, (2009). (Cited on p. 6.)

[112] M. A. El'yashevich, N. Kembrovskaya, and L. Tomil'chik, *Rydberg and the development of atomic spectroscopy (Centennial of J. R. Rydberg's paper on the laws governing atomic spectra)*, Soviet Physics Uspekhi **33**, 1047–1060, (1990). (Cited on p. 6.)

[113] I. Martinson and L. J. Curtis, *Janne Rydberg – his life and work*, Nuclear Instruments and Methods in Physics Research Section B: Beam Interactions with Materials and Atoms **235**, 17–22, (2005). (Cited on p. 6.)

[114] A. Beyer, *The Rydberg constant and proton size from atomic hydrogen*, Ludwig-Maximilians-Universität München, PhD thesis, (2016). (Cited on p. 6.)

[115] NIST, *Handbook of Basic Atomic Spectroscopic Data.*, (2017). (Cited on p. 6.)

[116] C.-J. Lorenzen and K. Niemax, *Quantum Defects of the $n^2P_{1/2,3/2}$ Levels in $^{39}K\ I$ and $^{85}Rb\ I$*, Physica Scripta **27**, 300, (1983). (Cited on p. 6.)

[117] N. Sibalic, *Rydberg atom ensembles under dephasing and dissipation: from single- to many-body dynamics*, (2017). (Cited on pp. 6 and 8.)

[118] M. Mack, F. Karlewski, H. Hattermann, S. Höckh, F. Jessen, D. Cano, and J. Fortágh, *Measurement of Absolute Transition Frequencies of ^{87}Rb to nS and nD Rydberg States by Means of Electromagnetically Induced Transparency*, Phys. Rev. A **83**, 052515, (2011). (Cited on p. 7.)

[119] T. F. Gallagher, *Rydberg atoms*, Reports on Progress in Physics **51**, 143–188, (1988). (Cited on p. 7.)

[120] S. J. Berl, C. A. Sackett, T. F. Gallagher, and J. Nunkaew, *Core polarizability of rubidium using spectroscopy of the ng to nh, ni Rydberg transitions*, Phys. Rev. A **102**, 062818, (2020). (Cited on p. 7.)

[121] J. E. Mayer and M. G. Mayer, *The Polarizabilities of Ions from Spectra*, Phys. Rev. **43**, 605–611, (1933). (Cited on p. 7.)

[122] W. Li, I. Mourachko, M. W. Noel, and T. F. Gallagher, *Millimeter-Wave Spectroscopy of Cold* Rb *Rydberg Atoms in a Magneto-Optical Trap: Quantum Defects of the ns, np, and nd Series*, Phys. Rev. A **67**, 052502, (2003). (Cited on pp. 7, 19, and 79.)

[123] A. Trautmann, M. J. Mark, P. Ilzhöfer, H. Edri, A. E. Arrach, J. G. Maloberti, C. H. Greene, F. Robicheaux, and F. Ferlaino, *Spectroscopy of Rydberg states in erbium using electromagnetically induced transparency*, Phys. Rev. Research **3**, 033165, (2021). (Cited on p. 7.)

[124] P. Schauss, *Hochauflösende Detektion von Ordnung in Rydberg Vielteilchensystemen*, Ludwig-Maximilians-Universität München, PhD thesis, (2015). (Cited on pp. 8, 31, 34, 35, and 48.)

[125] C. E. Theodosiou, *Lifetimes of alkali-metal—atom Rydberg states*, Phys. Rev. A **30**, 2881–2909, (1984). (Not cited.)

[126] M. Marinescu, H. R. Sadeghpour, and A. Dalgarno, *Dispersion coefficients for alkali-metal dimers*, Phys. Rev. A **49**, 982–988, (1994). (Cited on pp. 8 and 9.)

[127] B. E. King, *Angular Momentum Coupling and Rabi Frequencies for Simple Atomic Transitions*, (2008). (Cited on p. 10.)

[128] A. Chopinaud and J. Pritchard, *Optimal State Choice for Rydberg-Atom Microwave Sensors*, Phys. Rev. Applied **16**, 024008, (2021). (Cited on p. 11.)

[129] R. Löw, H. Weimer, J. Nipper, J. B. Balewski, B. Butscher, H. P. Büchler, and T. Pfau, *An experimental and theoretical guide to strongly interacting Rydberg gases*, J. Phys. B: At. Mol. Opt. Phys. **45**, 113001, (2012). (Cited on pp. 11, 16, and 19.)

[130] L. Festa, N. Lorenz, L.-M. Steinert, Z. Chen, P. Osterholz, R. Eberhard, and C. Gross, *Blackbody-radiation-induced facilitated excitation of Rydberg atoms in optical tweezers*, Phys. Rev. A **105**, 013109, (2022). (Cited on pp. 11, 24, 116, and 127.)

[131] M. G. Littman, M. L. Zimmerman, and D. Kleppner, *Tunneling Rates for Excited States of Sodium in a Static Electric Field*, Phys. Rev. Lett. **37**, 486, (1976). (Cited on p. 12.)

[132] M. L. Zimmerman, M. G. Littman, M. M. Kash, and D. Kleppner, *Stark structure of the Rydberg states of alkali-metal atoms*, Phys. Rev. A **20**, 2251, (1979). (Not cited.)

[133] K. Gawlas and S. D. Hogan, *Rydberg-state ionization dynamics and tunnel ionization rates in strong electric fields*, Phys. Rev. A **99**, 013421, (2019). (Cited on p. 12.)

[134] R. P. Abel, C. Carr, U. Krohn, and C. S. Adams, *Electrometry near a dielectric surface using Rydberg electromagnetically induced transparency*, Phys. Rev. A **84**, 023408, (2011). (Cited on p. 12.)

[135] P. Nordlander and F. B. Dunning, *Interaction of Rydberg atoms with surfaces: Electron tunneling processes*, Nuclear Instruments and Methods in Physics Research Section B: Beam Interactions with Materials and Atoms **125**, 300–304, (1997). (Not cited.)

[136] M. W. Kohlhoff, *Interaction of Rydberg atoms with surfaces*, The European Physical Journal Special Topics **225**, 3061–3085, (2016). (Cited on p. 12.)

[137] H. J. Levine, *Quantum Information Processing and Quantum Simulation with Programmable Rydberg Atom Arrays*. (2021). (Cited on pp. 12 and 48.)

[138] A. K. Contreras, *Quantum Simulation and QuantumInformation Processing withProgrammable Rydberg Atom Arrays*. (2021). (Not cited.)

[139] S. Saskin, *Building quantum systems with Ytterbium Rydberg arrays*. (2021). (Cited on pp. 12 and 48.)

[140] M. G. Littman, M. M. Kash, and D. Kleppner, *Field-Ionization Processes in Excited Atoms*, Phys. Rev. Lett. **41**, 103, (1978). (Cited on p. 12.)

[141] A. J. McCulloch, R. W. Speirs, J. Grimmel, B. M. Sparkes, D. Comparat, and R. E. Scholten, *Field ionization of Rydberg atoms for high-brightness electron and ion beams*, Phys. Rev. A **95**, 063845, (2017). (Cited on p. 12.)

[142] C. S. van Ditzhuijzen, A. F. Koenderink, L. D. Noordam, and H. van Linden van den Heuvell, *Simultaneous position and state measurement of Rydberg atoms*, The European Physical Journal D - Atomic, Molecular, Optical and Plasma Physics **40**, 13–17, (2006). (Cited on p. 12.)

[143] M. Stecker, R. Nold, L.-M. Steinert, J. Grimmel, D. Petrosyan, J. Fortágh, and A. Günther, *Controlling the Dipole Blockade and Ionization Rate of Rydberg Atoms in Strong Electric Fields*, Phys. Rev. Lett. **125**, 103602, (2020). (Not cited.)

[144] M. Robert-de Saint-Vincent, C. S. Hofmann, H. Schempp, G. Günter, S. Whitlock, and M. Weidemüller, *Spontaneous Avalanche Ionization of a Strongly Blockaded Rydberg Gas*, Phys. Rev. Lett. **110**, 045004, (2013). (Not cited.)

[145] C. Veit, N. Zuber, O. A. Herrera-Sancho, V. S. V. Anasuri, T. Schmid, F. Meinert, R. Löw, and T. Pfau, *Pulsed Ion Microscope to Probe Quantum Gases*, Phys. Rev. X **11**, 011036, (2021). (Cited on p. 12.)

[146] S. D. Hogan, *Rydberg-Stark deceleration of atoms and molecules*, EPJ Techniques and Instrumentation **3**, 1–50, (2016). (Cited on p. 12.)

[147] J. E. Palmer and S. D. Hogan, *Matter-wave interferometry with atoms in high Rydberg states*, Molecular Physics **117**, 3108–3119, (2019). (Cited on p. 12.)

[148] D. H. Meyer, Z. A. Castillo, K. C. Cox, and P. D. Kunz, *Assessment of Rydberg atoms for wideband electric field sensing*, J. Phys. B: At. Mol. Opt. Phys. **53**, 034001, (2020). (Cited on p. 12.)

[149] C. T. Fancher, D. R. Scherer, M. C. S. John, and B. L. S. Marlow, *Rydberg Atom Electric Field Sensors for Communications and Sensing*, IEEE Transactions on Quantum Engineering **2**, 1–13, (2021). (Cited on p. 12.)

[150] T. Amthor, M. Reetz-Lamour, S. Westermann, J. Denskat, and M. Weidemüller, *Mechanical Effect of van der Waals Interactions Observed in Real Time in an Ultracold Rydberg Gas*, Phys. Rev. Lett. **98**, 023004, (2007). (Cited on p. 12.)

[151] T. F. Gallagher, S. A. Edelstein, and R. M. Hill, *Radiative lifetimes of the S and D Rydberg levels of Na*, Phys. Rev. A **11**, 1504–1506, (1975). (Cited on p. 12.)

[152] T. F. Gallagher and W. E. Cooke, *Interactions of Blackbody Radiation with Atoms*, Phys. Rev. Lett. **42**, 835–839, (1979). (Cited on p. 12.)

[153] W. P. Spencer, A. G. Vaidyanathan, D. Kleppner, and T. W. Ducas, *Temperature dependence of blackbody-radiation-induced transfer among highly excited states of sodium*, Phys. Rev. A **25**, 380–384, (1982). (Cited on p. 12.)

[154] E. A. Goldschmidt, T. Boulier, R. C. Brown, S. B. Koller, J. T. Young, A. V. Gorshkov, S. L. Rolston, and J. V. Porto, *Anomalous Broadening in Driven Dissipative Rydberg Systems*, Phys. Rev. Lett. **116**, 113001, (2016). (Cited on pp. 13, 24, 107, and 127.)

[155] J. Zeiher, R. van Bijnen, P. Schauß, S. Hild, J.-y. Choi, T. Pohl, I. Bloch, and C. Gross, *Many-Body Interferometry of a Rydberg-Dressed Spin Lattice*, Nat. Phys. **12**, 1095–1099, (2016). (Cited on pp. 13, 23, 24, 33, 45, 49, 107, 110, 111, 115, 123, 124, 127, and 128.)

[156] T. Cantat-Moltrecht, R. Cortiñas, B. Ravon, P. Méhaignerie, S. Haroche, J. M. Raimond, M. Favier, M. Brune, and C. Sayrin, *Long-lived circular Rydberg states of laser-cooled rubidium atoms in a cryostat*, Phys. Rev. Research **2**, 022032, (2020). (Cited on pp. 13 and 26.)

[157] M. Mack, J. Grimmel, F. Karlewski, L. m. H. Sárkány, H. Hattermann, and J. Fortágh, *All-optical measurement of Rydberg-state lifetimes*, Phys. Rev. A **92**, 012517, (2015). (Cited on p. 13.)

[158] K.-N. Schymik, S. Pancaldi, F. Nogrette, D. Barredo, J. Paris, A. Browaeys, and T. Lahaye, *Single Atoms with 6000-Second Trapping Lifetimes in Optical-Tweezer Arrays at Cryogenic Temperatures*, Phys. Rev. Applied **16**, 034013, (2021). (Cited on p. 13.)

[159] S. Haroche, *Nobel Lecture: Controlling photons in a box and exploring the quantum to classical boundary*, Rev. Mod. Phys. **85**, 1083, (2013). (Cited on p. 13.)

[160] S. Haroche, M. Brune, and J. M. Raimond, *From cavity to circuit quantum electrodynamics*, Nature Physics **16**, 243–246, (2020). (Cited on pp. 13 and 25.)

[161] F. Assemat, D. Grosso, A. Signoles, A. Facon, I. Dotsenko, S. Haroche, J. M. Raimond, M. Brune, and S. Gleyzes, *Quantum Rabi Oscillations in Coherent and in Mesoscopic Cat Field States*, Phys. Rev. Lett. **123**, 143605, (2019). (Cited on p. 13.)

[162] S. R. Cohen and J. D. Thompson, *Quantum Computing with Circular Rydberg Atoms*, PRX Quantum **2**, 030322, (2021). (Cited on p. 13.)

[163] R. G. Hulet and D. Kleppner, *Rydberg Atoms in "Circular" States*, Phys. Rev. Lett. **51**, 1430–1433, (1983). (Cited on p. 13.)

[164] M. O. Scully and M. S. Zubairy, *Quantum Optics*, Cambridge University Press, (1997). (Cited on p. 13.)

[165] V. A. Nascimento, L. L. Caliri, A. L. de Oliveira, V. S. Bagnato, and L. G. Marcassa, *Measurement of the lifetimes of S and D states below* $n = 31$ *using cold Rydberg gas*, Phys. Rev. A **74**, 054501, (2006). (Cited on p. 13.)

[166] A. L. d. Oliveira, M. W. Mancini, V. S. Bagnato, and L. G. Marcassa, *Measurement of Rydberg-state lifetimes using cold trapped atoms*, Phys. Rev. A **65**, 031401, (2002). (Not cited.)

[167] J. Du, T. Gong, Z. Ji, C. Wang, Y. Zhao, L. Xiao, and S. Jia, *Radiative lifetime measurement of ultracold cesium Rydberg states by asimplified optical pumping method*, Appl. Opt. **60**, 276–280, (2021). (Cited on p. 13.)

[168] I. I. Beterov, I. I. Ryabtsev, D. B. Tretyakov, and V. M. Entin, *Quasiclassical calculations of blackbody-radiation-induced depopulation rates and effective lifetimes of Rydberg* nS, nP, *and* nD *alkali-metal atoms with* $n \leq 80$, Phys. Rev. A **79**, 052504, (2009). (Cited on p. 13.)

[169] V. D. Ovsiannikov, I. L. Glukhov, and E. A. Nekipelov, *Rates of blackbody radiation-induced transitions from rydberg states of alkali atoms*, Journal of Physics B: Atomic, Molecular and Optical Physics **44**, 195010, (2011). (Cited on p. 13.)

[170] M. Archimi, M. Ceccanti, M. Distefano, L. D. Virgilio, R. Franco, A. Greco, C. Simonelli, E. Arimondo, D. Ciampini, and O. Morsch, *Measurements of blackbody radiation-induced transition rates between high-lying S, P and D Rydberg levels*, (2021). (Cited on p. 14.)

[171] R. C. Stoneman, M. D. Adams, and T. F. Gallagher, *Resonant-collision spectroscopy of Rydberg atoms*, Phys. Rev. Lett. **58**, 1324, (1987). (Cited on p. 14.)

[172] W. R. Anderson, J. R. Veale, and T. F. Gallagher, *Resonant Dipole-Dipole Energy Transfer in a Nearly Frozen Rydberg Gas*, Phys. Rev. Lett. **80**, 249–252, (1998). (Not cited.)

[173] I. Mourachko, D. Comparat, F. de Tomasi, A. Fioretti, P. Nosbaum, V. M. Akulin, and P. Pillet, *Many-Body Effects in a Frozen Rydberg Gas*, Phys. Rev. Lett. **80**, 253–256, (1998). (Not cited.)

[174] I. Mourachko, W. Li, and T. F. Gallagher, *Controlled many-body interactions in a frozen Rydberg gas*, Phys. Rev. A **70**, 031401, (2004). (Cited on p. 14.)

[175] R. J. Le Roy, *Long-Range Potential Coefficients From RKR Turning Points: C_6 and C_8 for B($3\Pi^+_{Ou}$)-State Cl_2, Br_2, and I_2*, Canadian Journal of Physics **52**, 246–256, (1974). (Cited on p. 14.)

[176] N. Samboy, *Long-range interactions between rubidium and potassium Rydberg atoms*, Phys. Rev. A **95**, 032702, (2017). (Cited on pp. 14, 16, and 125.)

[177] K. Singer, J. Stanojevic, M. Weidemüller, and R. Côté, *Long-range interactions between alkali Rydberg atom pairs correlated to the ns-ns, np–np and nd–nd asymptotes*, J. Phys. B: At. Mol. Opt. Phys. **38**, S295, (2005). (Cited on pp. 14 and 51.)

[178] M. R. Flannery, D. Vrinceanu, and V. N. Ostrovsky, *Long-range interaction between polar Rydberg atoms*, J. Phys. B: At. Mol. Opt. Phys. **38**, S279, (2005). (Cited on p. 14.)

[179] A. Paris-Mandoki, C. Braun, and S. Hofferberth, *Correlations between interacting Rydberg atoms*, AIP Conference Proceedings **1950**, 020001, (2018). (Cited on p. 16.)

[180] A. A. Kamenski, N. L. Manakov, S. N. Mokhnenko, and V. D. Ovsiannikov, *Energy of van der Waals and dipole-dipole interactions between atoms in Rydberg states*, Phys. Rev. A **96**, 032716, (2017). (Cited on p. 16.)

[181] A. Reinhard, T. C. Liebisch, B. Knuffman, and G. Raithel, *Level shifts of rubidium Rydberg states due to binary interactions*, Phys. Rev. A **75**, 032712, (2007). (Cited on p. 16.)

[182] L. Béguin, A. Vernier, R. Chicireanu, T. Lahaye, and A. Browaeys, *Direct Measurement of the van der Waals Interaction between Two Rydberg Atoms*, Phys. Rev. Lett. **110**, 263201, (2013). (Cited on p. 16.)

[183] D. Barredo, S. Ravets, H. Labuhn, L. Béguin, A. Vernier, F. Nogrette, T. Lahaye, and A. Browaeys, *Demonstration of a Strong Rydberg Blockade in Three-Atom Systems with Anisotropic Interactions*, Phys. Rev. Lett. **112**, 183002, (2014). (Cited on p. 16.)

[184] T. G. Walker and M. Saffman, *Consequences of Zeeman degeneracy for the van der Waals blockade between Rydberg atoms*, Phys. Rev. A **77**, 032723, (2008). (Cited on pp. 16 and 123.)

[185] A. Reinhard, T. C. Liebisch, B. Knuffman, and G. Raithel, *Level shifts of rubidium Rydberg states due to binary interactions*, Phys. Rev. A **75**, (2007). (Cited on p. 17.)

[186] B. Vermersch, *Anisotropy and state mixing in the interactions between Rydberg states*, The European Physical Journal Special Topics **225**, 2977–2991, (2016). (Cited on p. 17.)

[187] D. Tiarks, S. Baur, K. Schneider, S. Dürr, and G. Rempe, *Single-Photon Transistor Using a Förster Resonance*, Phys. Rev. Lett. **113**, 053602, (2014). (Cited on pp. 17 and 25.)

[188] K. A. Safinya, J. F. Delpech, F. Gounand, W. Sandner, and T. F. Gallagher, *Resonant Rydberg-Atom-Rydberg-Atom Collisions*, Phys. Rev. Lett. **47**, 405–408, (1981). (Cited on p. 17.)

[189] T. Vogt, M. Viteau, J. Zhao, A. Chotia, D. Comparat, and P. Pillet, *Dipole Blockade at Förster Resonances in High Resolution Laser Excitation of Rydberg States of Cesium Atoms*, Phys. Rev. Lett. **97**, 083003, (2006). (Cited on p. 17.)

[190] S. Ravets, H. Labuhn, D. Barredo, L. Béguin, T. Lahaye, and A. Browaeys, *Coherent dipole–dipole coupling between two single Rydberg atoms at an electrically-tuned Förster resonance*, Nature Physics **10**, 914–917, (2014). (Cited on pp. 17 and 18.)

[191] S. Ravets, H. Labuhn, D. Barredo, T. Lahaye, and A. Browaeys, *Measurement of the angular dependence of the dipole-dipole interaction between two individual Rydberg atoms at a Förster resonance*, Phys. Rev. A **92**, 020701, (2015). (Cited on p. 17.)

[192] R. Faoro, B. Pelle, A. Zuliani, P. Cheinet, E. Arimondo, and P. Pillet, *Borromean three-body FRET in frozen Rydberg gases*, Nature Communications **6**, 8173, (2015). (Cited on p. 17.)

[193] D. B. Tretyakov, I. I. Beterov, E. A. Yakshina, V. M. Entin, I. I. Ryabtsev, P. Cheinet, and P. Pillet, *Observation of the Borromean Three-Body Förster Resonances for Three Interacting Rb Rydberg Atoms*, Phys. Rev. Lett. **119**, 173402, (2017). (Not cited.)

[194] I. I. Ryabtsev, I. I. Beterov, D. B. Tretyakov, E. A. Yakshina, V. M. Entin, P. Cheinet, and P. Pillet, *Coherence of three-body Förster resonances in Rydberg atoms*, Phys. Rev. A **98**, 052703, (2018). (Cited on p. 17.)

[195] J. H. Gurian, P. Cheinet, P. Huillery, A. Fioretti, J. Zhao, P. L. Gould, D. Comparat, and P. Pillet, *Observation of a Resonant Four-Body Interaction in Cold Cesium Rydberg Atoms*, Phys. Rev. Lett. **108**, 023005, (2012). (Cited on p. 17.)

[196] D. Barredo, H. Labuhn, S. Ravets, T. Lahaye, A. Browaeys, and C. S. Adams, *Coherent Excitation Transfer in a Spin Chain of Three Rydberg Atoms*, Phys. Rev. Lett. **114**, 113002, (2015). (Cited on pp. 18 and 24.)

[197] S. de Léséleuc, D. Barredo, V. Lienhard, A. Browaeys, and T. Lahaye, *Optical Control of the Resonant Dipole-Dipole Interaction between Rydberg Atoms*, Phys. Rev. Lett. **119**, 053202, (2017). (Cited on p. 18.)

[198] A. Schwettmann, J. Crawford, K. R. Overstreet, and J. P. Shaffer, *Cold Cs Rydberg-gas interactions*, Phys. Rev. A **74**, 020701, (2006). (Cited on p. 19.)

[199] J. Stanojevic, R. Côté, D. Tong, E. E. Eyler, and P. L. Gould, *Long-range potentials and* $(n-1)d + ns$ *molecular resonances in an ultracold Rydberg gas*, Phys. Rev. A **78**, 052709, (2008). (Cited on p. 19.)

[200] J. Deiglmayr, H. Saßmannshausen, P. Pillet, and F. Merkt, *Observation of Dipole-Quadrupole Interaction in an Ultracold Gas of Rydberg Atoms*, Phys. Rev. Lett. **113**, 193001, (2014). (Cited on pp. 19, 60, and 125.)

[201] S. Wüster and J.-M. Rost, *Rydberg aggregates*, J. Phys. B: At. Mol. Opt. Phys. **51**, 032001, (2018). (Cited on p. 19.)

[202] H. Schempp, G. Günter, M. Robert-de Saint-Vincent, C. S. Hofmann, D. Breyel, A. Komnik, D. W. Schönleber, M. Gärttner, J. Evers, S. Whitlock, and M. Weidemüller, *Full Counting Statistics of Laser Excited Rydberg Aggregates in a One-Dimensional Geometry*, Phys. Rev. Lett. **112**, 013002, (2014). (Not cited.)

[203] M. Gärttner, K. P. Heeg, T. Gasenzer, and J. Evers, *Dynamic formation of Rydberg aggregates at off-resonant excitation*, Phys. Rev. A **88**, 043410, (2013). (Cited on p. 19.)

[204] A. Urvoy, F. Ripka, I. Lesanovsky, D. Booth, J. P. Shaffer, T. Pfau, and R. Löw, *Strongly Correlated Growth of Rydberg Aggregates in a Vapor Cell*, Phys. Rev. Lett. **114**, 203002, (2015). (Cited on pp. 19, 60, and 125.)

[205] D. Jaksch, J. I. Cirac, P. Zoller, S. L. Rolston, R. Côté, and M. D. Lukin, *Fast Quantum Gates for Neutral Atoms*, Phys. Rev. Lett. **85**, 2208, (2000). (Cited on pp. 20 and 24.)

[206] M. D. Lukin, M. Fleischhauer, R. Cote, L. M. Duan, D. Jaksch, J. I. Cirac, and P. Zoller, *Dipole Blockade and Quantum Information Processing in Mesoscopic Atomic Ensembles*, Phys. Rev. Lett. **87**, 037901, (2001). (Cited on pp. 20 and 24.)

[207] A. Gaëtan, Y. Miroshnychenko, T. Wilk, A. Chotia, M. Viteau, D. Comparat, P. Pillet, A. Browaeys, and P. Grangier, *Observation of collective excitation of two individual atoms in the Rydberg blockade regime*, Nature Physics **5**, 115–118, (2009). (Cited on p. 22.)

[208] E. Urban, T. A. Johnson, T. Henage, L. Isenhower, D. D. Yavuz, T. G. Walker, and M. Saffman, *Observation of Rydberg blockade between two atoms*, Nature Physics **5**, 110–114, (2009). (Cited on p. 22.)

[209] P. Schauß, M. Cheneau, M. Endres, T. Fukuhara, S. Hild, A. Omran, T. Pohl, C. Gross, S. Kuhr, and I. Bloch, *Observation of spatially ordered structures in a two-dimensional Rydberg gas*, Nature **491**, 87–91, (2012). (Cited on pp. 22 and 33.)

[210] H. Labuhn, D. Barredo, S. Ravets, S. de Léséleuc, T. Macrì, T. Lahaye, and A. Browaeys, *Tunable two-dimensional arrays of single Rydberg atoms for realizing quantum Ising models*, Nature **534**, 667–670, (2016). (Cited on pp. 22 and 24.)

[211] J. Zeiher, P. Schauß, S. Hild, T. Macrì, I. Bloch, and C. Gross, *Microscopic Characterization of Scalable Coherent Rydberg Superatoms*, Phys. Rev. X **5**, 031015, (2015). (Cited on pp. 22 and 24.)

[212] P. Schauß, J. Zeiher, T. Fukuhara, S. Hild, M. Cheneau, T. Macrì, T. Pohl, I. Bloch, and C. Gross, *Crystallization in Ising quantum magnets*, Science **347**, 1455–1458, (2015). (Cited on pp. 22, 33, and 129.)

[213] E. Guardado-Sanchez, P. T. Brown, D. Mitra, T. Devakul, D. A. Huse, P. Schauß, and W. S. Bakr, *Probing the Quench Dynamics of Antiferromagnetic Correlations in a 2D Quantum Ising Spin System*, Phys. Rev. X **8**, 021069, (2018). (Cited on p. 33.)

[214] V. Lienhard, S. de Léséleuc, D. Barredo, T. Lahaye, A. Browaeys, M. Schuler, L.-P. Henry, and A. M. Läuchli, *Observing the Space- and Time-Dependent Growth of Correlations in Dynamically Tuned Synthetic Ising Models with Antiferromagnetic Interactions*, Phys. Rev. X **8**, 021070, (2018). (Cited on p. 22.)

[215] S. Ebadi, T. T. Wang, H. Levine, A. Keesling, G. Semeghini, A. Omran, D. Bluvstein, R. Samajdar, H. Pichler, W. W. Ho, S. Choi, S. Sachdev, M. Greiner, V. Vuletić, and M. D. Lukin, *Quantum phases of matter on a 256-atom programmable quantum simulator*, Nature **595**, 227–232, (2021). (Cited on p. 22.)

[216] G. Semeghini, H. Levine, A. Keesling, S. Ebadi, T. T. Wang, D. Bluvstein, R. Verresen, H. Pichler, M. Kalinowski, R. Samajdar, A. Omran, S. Sachdev, A. Vishwanath, M. Greiner, V. Vuletić, and M. D. Lukin, *Probing topological spin liquids on a programmable quantum simulator*, Science **374**, 1242–1247, (2021). (Cited on p. 22.)

[217] D. Bluvstein, A. Omran, H. Levine, A. Keesling, G. Semeghini, S. Ebadi, T. T. Wang, A. A. Michailidis, N. Maskara, W. W. Ho, S. Choi, M. Serbyn, M. Greiner, V. Vuletić, and M. D. Lukin, *Controlling quantum many-body dynamics in driven Rydberg atom arrays*, Science **371**, 1355–1359, (2021). (Cited on p. 22.)

[218] J. E. Johnson and S. L. Rolston, *Interactions between Rydberg-dressed atoms*, Phys. Rev. A **82**, 033412, (2010). (Cited on pp. 23 and 107.)

[219] S. Helmrich, A. Arias, N. Pehoviak, and S. Whitlock, *Two-body interactions and decay of three-level Rydberg-dressed atoms*, J. Phys. B: At. Mol. Opt. Phys. **49**, 03LT02, (2016). (Cited on p. 23.)

[220] Y.-Y. Jau, A. M. Hankin, T. Keating, I. H. Deutsch, and G. W. Biedermann, *Entangling atomic spins with a Rydberg-dressed spin-flip blockade*, Nat. Phys. **12**, 71–74, (2016). (Cited on pp. 23, 25, 53, and 107.)

[221] J. Zeiher, J.-y. Choi, A. Rubio-Abadal, T. Pohl, R. van Bijnen, I. Bloch, and C. Gross, *Coherent Many-Body Spin Dynamics in a Long-Range Interacting Ising Chain*, Phys. Rev. X **7**, 041063, (2017). (Cited on pp. 23, 33, 111, 112, 114, 115, and 127.)

[222] E. Guardado-Sanchez, B. M. Spar, P. Schauss, R. Belyansky, J. T. Young, P. Bienias, A. V. Gorshkov, T. Iadecola, and W. S. Bakr, *Quench Dynamics of a Fermi Gas with Strong Nonlocal Interactions*, Phys. Rev. X **11**, 021036, (2021). (Cited on pp. 23, 24, 45, 107, and 109.)

[223] I. Mourachko, D. Comparat, F. de Tomasi, A. Fioretti, P. Nosbaum, V. M. Akulin, and P. Pillet, *Many-Body Effects in a Frozen Rydberg Gas*, Phys. Rev. Lett. **80**, 253, (1998). (Cited on p. 23.)

[224] W. R. Anderson, J. R. Veale, and T. F. Gallagher, *Resonant Dipole-Dipole Energy Transfer in a Nearly Frozen Rydberg Gas*, Phys. Rev. Lett. **80**, 249, (1998). (Cited on p. 23.)

[225] N. Henkel, R. Nath, and T. Pohl, *Three-Dimensional Roton Excitations and Supersolid Formation in Rydberg-Excited Bose-Einstein Condensates*, Phys. Rev. Lett. **104**, 195302, (2010). (Cited on pp. 23 and 109.)

[226] G. Pupillo, A. Micheli, M. Boninsegni, I. Lesanovsky, and P. Zoller, *Strongly Correlated Gases of Rydberg-Dressed Atoms: Quantum and Classical Dynamics*, Phys. Rev. Lett. **104**, 223002, (2010). (Not cited.)

[227] F. Cinti, P. Jain, M. Boninsegni, A. Micheli, P. Zoller, and G. Pupillo, *Supersolid Droplet Crystal in a Dipole-Blockaded Gas*, Phys. Rev. Lett. **105**, 135301, (2010). (Not cited.)

[228] N. Henkel, F. Cinti, P. Jain, G. Pupillo, and T. Pohl, *Supersolid Vortex Crystals in Rydberg-Dressed Bose-Einstein Condensates*, Phys. Rev. Lett. **108**, 265301, (2012). (Not cited.)

[229] M. Mattioli, M. Dalmonte, W. Lechner, and G. Pupillo, *Cluster Luttinger Liquids of Rydberg-Dressed Atoms in Optical Lattices*, Phys. Rev. Lett. **111**, 165302, (2013). (Not cited.)

[230] D. Rossini and R. Fazio, *Phase diagram of the extended Bose–Hubbard model*, New J. Phys. **14**, 065012, (2012). (Not cited.)

[231] A. Geißler, I. Vasić, and W. Hofstetter, *Condensation versus long-range interaction: Competing quantum phases in bosonic optical lattice systems at near-resonant Rydberg dressing*, Phys. Rev. A **95**, 063608, (2017). (Cited on p. 23.)

[232] O. Dutta, M. Gajda, P. Hauke, M. Lewenstein, D.-S. Lühmann, B. A. Malomed, T. Sowiński, and J. Zakrzewski, *Non-standard Hubbard models in optical lattices: a review*, Rep. Prog. Phys. **78**, 066001, (2015). (Cited on p. 23.)

[233] M. Boninsegni, *Supersolid Phases of Cold Atom Assemblies*, J. Low Temp. Phys. **168**, 137–149, (2012). (Not cited.)

[234] G. Mazzarella, S. M. Giampaolo, and F. Illuminati, *Extended Bose Hubbard model of interacting bosonic atoms in optical lattices: From superfluidity to density waves*, Phys. Rev. A **73**, 013625, (2006). (Cited on p. 23.)

[235] J. B. Balewski, A. T. Krupp, A. Gaj, S. Hofferberth, R. Löw, and T. Pfau, *Rydberg dressing: understanding of collective many-body effects and implications for experiments*, New J. Phys. **16**, 063012, (2014). (Cited on p. 23.)

[236] J. Honer, H. Weimer, T. Pfau, and H. P. Büchler, *Collective Many-Body Interaction in Rydberg Dressed Atoms*, Phys. Rev. Lett. **105**, 160404, (2010). (Cited on p. 23.)

[237] A. Glaetzle, M. Dalmonte, R. Nath, I. Rousochatzakis, R. Moessner, and P. Zoller, *Quantum Spin-Ice and Dimer Models with Rydberg Atoms*, Phys. Rev. X **4**, 041037, (2014). (Cited on p. 23.)

[238] A. W. Glaetzle, M. Dalmonte, R. Nath, C. Gross, I. Bloch, and P. Zoller, *Designing Frustrated Quantum Magnets with Laser-Dressed Rydberg Atoms*, Phys. Rev. Lett. **114**, 173002, (2015). (Cited on p. 23.)

[239] R. M. W. van Bijnen and T. Pohl, *Quantum Magnetism and Topological Ordering via Rydberg Dressing near Förster Resonances*, Phys. Rev. Lett. **114**, 243002, (2015). (Cited on pp. 23, 26, and 107.)

[240] I.-D. Potirniche, A. C. Potter, M. Schleier-Smith, A. Vishwanath, and N. Y. Yao, *Floquet Symmetry-Protected Topological Phases in Cold-Atom Systems*, Phys. Rev. Lett. **119**, 123601, (2017). (Cited on p. 23.)

[241] L. Gil, R. Mukherjee, E. Bridge, M. Jones, and T. Pohl, *Spin Squeezing in a Rydberg Lattice Clock*, Phys. Rev. Lett. **112**, 103601, (2014). (Cited on p. 24.)

[242] W. Lechner, P. Hauke, and P. Zoller, *A Quantum Annealing Architecture with All-to-All Connectivity from Local Interactions*, Science Advances **1**, e1500838, (2015). (Cited on p. 24.)

[243] A. W. Glaetzle, R. M. W. van Bijnen, P. Zoller, and W. Lechner, *A Coherent Quantum Annealer with Rydberg Atoms*, Nature Communications **8**, 1–6, (2017). (Cited on p. 24.)

[244] A. W. Glaetzle, K. Ender, D. S. Wild, S. Choi, H. Pichler, M. D. Lukin, and P. Zoller, *Quantum Spin Lenses in Atomic Arrays*, Phys. Rev. X **7**, 031049, (2017). (Cited on p. 24.)

[245] S. Sevinçli and T. Pohl, *Microwave control of Rydberg atom interactions*, New Journal of Physics **16**, 123036, (2014). (Cited on p. 24.)

[246] D. Petrosyan and K. Mølmer, *Binding Potentials and Interaction Gates between Microwave-Dressed Rydberg Atoms*, Phys. Rev. Lett. **113**, 123003, (2014). (Cited on p. 24.)

[247] T. Boulier, E. Magnan, C. Bracamontes, J. Maslek, E. A. Goldschmidt, J. T. Young, A. V. Gorshkov, S. L. Rolston, and J. V. Porto, *Spontaneous avalanche dephasing in large Rydberg ensembles*, Phys. Rev. A **96**, 053409, (2017). (Cited on pp. 24 and 127.)

[248] M. Barbier, S. Hollerith, and W. Hofstetter, *Extended Bose-Hubbard models with Rydberg macrodimer dressing*, Phys. Rev. A **104**, 053304, (2021). (Cited on pp. 24, 26, 55, 110, and 122.)

[249] A. Browaeys, D. Barredo, and T. Lahaye, *Experimental investigations of dipole–dipole interactions between a few Rydberg atoms*, J. Phys. B: At. Mol. Opt. Phys. **49**, 113001, (2016). (Cited on pp. 24 and 51.)

[250] A. P. n. Orioli, A. Signoles, H. Wildhagen, G. Günter, J. Berges, S. Whitlock, and M. Weidemüller, *Relaxation of an Isolated Dipolar-Interacting Rydberg Quantum Spin System*, Phys. Rev. Lett. **120**, 063601, (2018). (Cited on p. 24.)

[251] V. Lienhard, P. Scholl, S. Weber, D. Barredo, S. de Léséleuc, R. Bai, N. Lang, M. Fleischhauer, H. P. Büchler, T. Lahaye, and A. Browaeys, *Realization of a Density-Dependent Peierls Phase in a Synthetic, Spin-Orbit Coupled Rydberg System*, Phys. Rev. X **10**, 021031, (2020). (Cited on p. 24.)

[252] A. Signoles, T. Franz, R. Ferracini Alves, M. Gärttner, S. Whitlock, G. Zürn, and M. Weidemüller, *Glassy Dynamics in a Disordered Heisenberg Quantum Spin System*, Phys. Rev. X **11**, 011011, (2021). (Cited on p. 24.)

[253] P. Scholl, H. J. Williams, G. Bornet, F. Wallner, D. Barredo, T. Lahaye, A. Browaeys, L. Henriet, A. Signoles, C. Hainaut, T. Franz, S. Geier, A. Tebben, A. Salzinger, G. Zürn, and M. Weidemüller, *Microwave-engineering of programmable XXZ Hamiltonians in arrays of Rydberg atoms*, (2021). (Not cited.)

[254] T. L. Nguyen, J. M. Raimond, C. Sayrin, R. Cortiñas, T. Cantat-Moltrecht, F. Assemat, I. Dotsenko, S. Gleyzes, S. Haroche, G. Roux, T. Jolicoeur, and M. Brune, *Towards Quantum Simulation with Circular Rydberg Atoms*, Phys. Rev. X **8**, 011032, (2018). (Not cited.)

[255] S. Geier, N. Thaicharoen, C. Hainaut, T. Franz, A. Salzinger, A. Tebben, D. Grimshandl, G. Zürn, and M. Weidemüller, *Floquet Hamiltonian engineering of an isolated many-body spin system*, Science **374**, 1149–1152, (2021). (Cited on p. 24.)

[256] A. Omran, H. Levine, A. Keesling, G. Semeghini, T. T. Wang, S. Ebadi, H. Bernien, A. S. Zibrov, H. Pichler, S. Choi, J. Cui, M. Rossignolo, P. Rembold, S. Montangero, T. Calarco, M. Endres, M. Greiner, V. Vuletić, and M. D. Lukin, *Generation and manipulation of Schrödinger cat states in Rydberg atom arrays*, Science **365**, 570–574, (2019). (Cited on p. 24.)

[257] C. J. Picken, R. Legaie, K. McDonnell, and J. D. Pritchard, *Entanglement of neutral-atom qubits with long ground-Rydberg coherence times*, Quantum Science and Technology **4**, 015011, (2018). (Cited on p. 24.)

[258] T. M. Graham, M. Kwon, B. Grinkemeyer, Z. Marra, X. Jiang, M. T. Lichtman, Y. Sun, M. Ebert, and M. Saffman, *Rydberg-mediated entanglement in a two-dimensional neutral atom qubit array*, Phys. Rev. Lett. **123**, (2019). (Cited on p. 25.)

[259] Y. Zeng, P. Xu, X. He, Y. Liu, M. Liu, J. Wang, D. J. Papoular, G. V. Shlyapnikov, and M. Zhan, *Entangling two individual atoms of different isotopes via rydberg blockade*, Phys. Rev. Lett. **119**, 160502, (2017). (Cited on p. 25.)

[260] S. Ma, A. P. Burgers, G. Liu, J. Wilson, B. Zhang, and J. D. Thompson, *Universal gate operations on nuclear spin qubits in an optical tweezer array of ^{171}Yb atoms*, (2021). (Cited on p. 25.)

[261] C. Zhang, F. Pokorny, W. Li, G. Higgins, A. Pöschl, I. Lesanovsky, and M. Hennrich, *Submicrosecond entangling gate between trapped ions via Rydberg interaction*, Nature **580**, 345–349, (2020). (Cited on p. 25.)

[262] J. M. Raimond, M. Brune, and S. Haroche, *Manipulating quantum entanglement with atoms and photons in a cavity*, Rev. Mod. Phys. **73**, 565–582, (2001). (Cited on p. 25.)

[263] S. Haroche, *Nobel Lecture: Controlling photons in a box and exploring the quantum to classical boundary*, Rev. Mod. Phys. **85**, 1083–1102, (2013). (Cited on p. 25.)

[264] G. Nogues, A. Rauschenbeutel, S. Osnaghi, M. Brune, J. M. Raimond, and S. Haroche, *Seeing a single photon without destroying it*, Nature **400**, 239–242, (1999). (Cited on p. 25.)

[265] M. Brune, S. Haroche, V. Lefevre, J. M. Raimond, and N. Zagury, *Quantum nondemolition measurement of small photon numbers by Rydberg-atom phase-sensitive detection*, Phys. Rev. Lett. **65**, (1990). (Cited on p. 25.)

[266] S. Gleyzes, S. Kuhr, C. Guerlin, J. Bernu, S. Deléglise, U. Busk Hoff, M. Brune, J.-M. Raimond, and S. Haroche, *Quantum jumps of light recording the birth and death of a photon in a cavity*, Nature **446**, 297–300, (2007). (Cited on p. 25.)

[267] C. Guerlin, J. Bernu, S. Deléglise, C. Sayrin, S. Gleyzes, S. Kuhr, M. Brune, J.-M. Raimond, and S. Haroche, *Progressive field-state collapse and quantum non-demolition photon counting*, Nature **448**, 889–893, (2007). (Cited on p. 25.)

[268] C. Sayrin, I. Dotsenko, X. Zhou, B. Peaudecerf, T. Rybarczyk, S. Gleyzes, P. Rouchon, M. Mirrahimi, H. Amini, M. Brune, J.-M. Raimond, and S. Haroche, *Real-time quantum feedback prepares and stabilizes photon number states*, Nature **477**, 73–77, (2011). (Cited on p. 25.)

[269] S. Deléglise, I. Dotsenko, C. Sayrin, J. Bernu, M. Brune, J.-M. Raimond, and S. Haroche, *Reconstruction of non-classical cavity field states with snapshots of their decoherence*, Nature **455**, 510–514, (2008). (Cited on p. 25.)

[270] Y. O. Dudin and A. Kuzmich, *Strongly Interacting Rydberg Excitations of a Cold Atomic Gas*, Science **336**, 887–889, (2012). (Cited on p. 25.)

[271] T. Peyronel, O. Firstenberg, Q.-Y. Liang, S. Hofferberth, A. V. Gorshkov, T. Pohl, M. D. Lukin, and V. Vuletić, *Quantum nonlinear optics with single photons enabled by strongly interacting atoms*, Nature **488**, 57–60, (2012). (Not cited.)

[272] D. E. Chang, V. Vuletić, and M. D. Lukin, *Quantum nonlinear optics — photon by photon*, Nature Photonics **8**, 685–694, (2014). (Cited on p. 25.)

[273] O. Firstenberg, C. S. Adams, and S. Hofferberth, *Nonlinear quantum optics mediated by Rydberg interactions*, J. Phys. B: At. Mol. Opt. Phys. **49**, 152003, (2016). (Cited on p. 25.)

[274] D. Petrosyan, J. Otterbach, and M. Fleischhauer, *Electromagnetically Induced Transparency with Rydberg Atoms*, Phys. Rev. Lett. **107**, (2011). (Not cited.)

[275] J. D. Pritchard, D. Maxwell, A. Gauguet, K. J. Weatherill, M. P. A. Jones, and C. S. Adams, *Cooperative Atom-Light Interaction in a Blockaded Rydberg Ensemble*, Phys. Rev. Lett. **105**, (2010). (Cited on p. 25.)

[276] M. Fleischhauer, A. Imamoglu, and J. P. Marangos, *Electromagnetically induced transparency: Optics in coherent media*, Rev. Mod. Phys. **77**, 633, (2005). (Cited on p. 25.)

[277] D. Maxwell, D. J. Szwer, D. Paredes-Barato, H. Busche, J. D. Pritchard, A. Gauguet, K. J. Weatherill, M. P. A. Jones, and C. S. Adams, *Storage and Control of Optical Photons Using Rydberg Polaritons*, Phys. Rev. Lett. **110**, 103001, (2013). (Cited on p. 25.)

[278] J. D. Thompson, T. L. Nicholson, Q.-Y. Liang, S. H. Cantu, A. V. Venkatramani, S. Choi, I. A. Fedorov, D. Viscor, T. Pohl, M. D. Lukin, and V. Vuletić, *Symmetry-protected collisions between strongly interacting photons*, Nature **542**, 206–209, (2017). (Not cited.)

[279] L. W. Clark, N. Schine, C. Baum, N. Jia, and J. Simon, *Observation of Laughlin states made of light*, Nature **582**, 41–45, (2020). (Cited on p. 25.)

[280] H. Gorniaczyk, C. Tresp, J. Schmidt, H. Fedder, and S. Hofferberth, *Single-Photon Transistor Mediated by Interstate Rydberg Interactions*, Phys. Rev. Lett. **113**, 053601, (2014). (Cited on p. 25.)

[281] D. Tiarks, S. Schmidt-Eberle, T. Stolz, G. Rempe, and S. Dürr, *A photon–photon quantum gate based on Rydberg interactions*, Nature Physics **15**, 124–126, (2019). (Cited on p. 25.)

[282] F. Ripka, H. Kübler, R. Löw, and T. Pfau, *A room-temperature single-photon source based on strongly interacting Rydberg atoms*, Science **362**, 446–449, (2018). (Cited on p. 25.)

[283] D. P. Ornelas-Huerta, A. N. Craddock, E. A. Goldschmidt, A. J. Hachtel, Y. Wang, P. Bienias, A. V. Gorshkov, S. L. Rolston, and J. V. Porto, *On-demand indistinguishable single photons from an efficient and pure source based on a Rydberg ensemble*, Optica **7**, 813–819, (2020). (Cited on p. 25.)

[284] N. Stiesdal, H. Busche, J. Kumlin, K. Kleinbeck, H. P. Büchler, and S. Hofferberth, *Observation of collective decay dynamics of a single Rydberg superatom*, Phys. Rev. Research **2**, 043339, (2020). (Cited on p. 25.)

[285] N. Stiesdal, J. Kumlin, K. Kleinbeck, P. Lunt, C. Braun, A. Paris-Mandoki, C. Tresp, H. P. Büchler, and S. Hofferberth, *Observation of Three-Body Correlations for Photons Coupled to a Rydberg Superatom*, Phys. Rev. Lett. **121**, 103601, (2018). (Cited on p. 25.)

[286] G. Günter, H. Schempp, M. R. de Saint-Vincent, V. Gavryusev, S. Helmrich, C. S. Hofmann, S. Whitlock, and M. Weidemüller, *Observing the Dynamics of Dipole-Mediated Energy Transport by Interaction-Enhanced Imaging*, Science **342**, 954–956, (2013). (Cited on p. 25.)

[287] M. Ferreira-Cao, V. Gavryusev, T. Franz, R. F. Alves, A. Signoles, G. Zürn, and M. Weidemüller, *Depletion imaging of Rydberg atoms in cold atomic gases*, J. Phys. B: At. Mol. Opt. Phys. **53**, 084004, (2020). (Not cited.)

[288] G. Günter, M. Robert-de Saint-Vincent, H. Schempp, C. S. Hofmann, S. Whitlock, and M. Weidemüller, *Interaction Enhanced Imaging of Individual Rydberg Atoms in Dense Gases*, Phys. Rev. Lett. **108**, 013002, (2012). (Not cited.)

[289] V. Gavryusev, M. Ferreira-Cao, A. Kekić, G. Zürn, and A. Signoles, *Interaction Enhanced Imaging of Rydberg P states*, The European Physical Journal Special Topics **225**, 2863–2889, (2016). (Cited on p. 25.)

[290] A. Paris-Mandoki, C. Braun, J. Kumlin, C. Tresp, I. Mirgorodskiy, F. Christaller, H. P. Büchler, and S. Hofferberth, *Free-Space Quantum Electrodynamics with a Single Rydberg Superatom*, Phys. Rev. X **7**, 041010, (2017). (Cited on p. 25.)

[291] A. Cooper, J. P. Covey, I. S. Madjarov, S. G. Porsev, M. S. Safronova, and M. Endres, *Alkaline-Earth Atoms in Optical Tweezers*, Phys. Rev. X **8**, 041055, (2018). (Cited on p. 26.)

[292] A. Jenkins, J. W. Lis, A. Senoo, W. F. McGrew, and A. M. Kaufman, *Ytterbium nuclear-spin qubits in an optical tweezer array*, (2021). (Cited on p. 26.)

[293] J. Wilson, S. Saskin, Y. Meng, S. Ma, R. Dilip, A. Burgers, and J. Thompson, *Trapped arrays of alkaline earth rydberg atoms in optical tweezers*, (2019). (Cited on p. 26.)

[294] J. P. Covey, I. S. Madjarov, A. Cooper, and M. Endres, *2000-Times Repeated Imaging of Strontium Atoms in Clock-Magic Tweezer Arrays*, Phys. Rev. Lett. **122**, 173201, (2019). (Cited on p. 26.)

[295] D. Barredo, V. Lienhard, P. Scholl, S. de Léséleuc, T. Boulier, A. Browaeys, and T. Lahaye, *Three-dimensional trapping of individual rydberg atoms in ponderomotive bottle beam traps*, Phys. Rev. Lett. **124**, 023201, (2020). (Cited on p. 26.)

[296] J. T. Wilson, S. Saskin, Y. Meng, S. Ma, R. Dilip, A. P. Burgers, and J. D. Thompson, *Trapping Alkaline Earth Rydberg Atoms Optical Tweezer Arrays*, Phys. Rev. Lett. **128**, 033201, (2022). (Cited on pp. 26 and 49.)

[297] S. R. Cohen and J. D. Thompson, *Quantum Computing with Circular Rydberg Atoms*, PRX Quantum **2**, 030322, (2021). (Cited on p. 26.)

[298] T. L. Nguyen, J. M. Raimond, C. Sayrin, R. Cortiñas, T. Cantat-Moltrecht, F. Assemat, I. Dotsenko, S. Gleyzes, S. Haroche, G. Roux, T. Jolicoeur, and M. Brune, *Towards Quantum Simulation with Circular Rydberg Atoms*, Phys. Rev. X **8**, 011032, (2018). (Cited on p. 26.)

[299] M. Mack, J. Grimmel, F. Karlewski, L. m. H. Sárkány, H. Hattermann, and J. Fortágh, *All-optical measurement of Rydberg-state lifetimes*, Phys. Rev. A **92**, (2015). (Cited on p. 26.)

[300] N. Takei, C. Sommer, C. Genes, G. Pupillo, H. Goto, K. Koyasu, H. Chiba, M. Weidemüller, and K. Ohmori, *Direct observation of ultrafast many-body electron dynamics in an ultracold Rydberg gas*, Nature Communications **7**, 1–12, (2016). (Cited on p. 26.)

[301] M. Mizoguchi, Y. Zhang, M. Kunimi, A. Tanaka, S. Takeda, N. Takei, V. Bharti, K. Koyasu, T. Kishimoto, D. Jaksch, A. Glaetzle, M. Kiffner, G. Masella, G. Pupillo, M. Weidemüller, and K. Ohmori, *Ultrafast Creation of Overlapping Rydberg Electrons in an Atomic BEC and Mott-Insulator Lattice*, Phys. Rev. Lett. **124**, 253201, (2020). (Not cited.)

[302] Y. Chew, T. Tomita, T. P. Mahesh, S. Sugawa, S. de Léséleuc, and K. Ohmori, *Ultrafast energy exchange between two single Rydberg atoms on the nanosecond timescale*, (2021). (Cited on p. 26.)

[303] T. Kazimierczuk, D. Fröhlich, S. Scheel, H. Stolz, and M. Bayer, *Giant Rydberg excitons in the copper oxide Cu2O*, Nature **514**, 343–347, (2014). (Cited on p. 26.)

[304] J. Heckötter, V. Walther, S. Scheel, M. Bayer, T. Pohl, and M. Aßmann, *Asymmetric Rydberg blockade of giant excitons in Cuprous Oxide*, Nature Communications **12**, 1–6, (2021). (Cited on p. 26.)

[305] V. Walther, R. Johne, and T. Pohl, *Giant optical nonlinearities from Rydberg excitons in semiconductor microcavities*, Nature Communications **9**, 1–6, (2018). (Cited on p. 26.)

[306] N. Sándor, R. González-Férez, P. S. Julienne, and G. Pupillo, *Rydberg optical Feshbach resonances in cold gases*, Phys. Rev. A **96**, 032719, (2017). (Cited on p. 26.)

[307] O. Thomas, C. Lippe, T. Eichert, and H. Ott, *Experimental realization of a Rydberg optical Feshbach resonance in a quantum many-body system*, Nature Communications **9**, 2238, (2018). (Cited on p. 26.)

[308] M. Nic, L. Hovorka, J. Jirát, B. Košata, and J. Znamenacek, *IUPAC compendium of chemical terminology-the gold book*, International Union of Pure and Applied Chemistry, (2005). (Cited on p. 26.)

[309] F. Merkt, *Molecules in high Rydberg states*, Annual Review of Physical Chemistry **48**, 675–709, (1997). (Cited on p. 27.)

[310] F. Merkt, S. R. Mackenzie, and T. P. Softley, *Rotational autoionization dynamics in high Rydberg states of nitrogen*, The Journal of Chemical Physics **103**, 4509–4518, (1995). (Not cited.)

[311] S. T. Pratt, J. L. Dehmer, P. M. Dehmer, and W. A. Chupka, *Reactions of Rydberg states of molecular hydrogen*, The Journal of Chemical Physics **101**, 882–890, (1994). (Not cited.)

[312] W. G. Scherzer, H. L. Selzle, E. W. Schlag, and R. D. Levine, *Long time stability of very high Rydberg states of vibrationally excited molecules*, Phys. Rev. Lett. **72**, 1435–1438, (1994). (Cited on p. 27.)

[313] C. H. Greene, A. S. Dickinson, and H. R. Sadeghpour, *Creation of Polar and Nonpolar Ultra-Long-Range Rydberg Molecules*, Phys. Rev. Lett. **85**, 2458–2461, (2000). (Cited on p. 27.)

[314] N. Zuber, V. S. V. Anasuri, M. Berngruber, Y. Q. Zou, F. Meinert, R. Löw, and T. Pfau, *Spatial imaging of a novel type of molecular ions*, (2021). (Cited on p. 27.)

[315] A. Duspayev, X. Han, M. A. Viray, L. Ma, J. Zhao, and G. Raithel, *Long-range Rydberg-atom–ion molecules of Rb and Cs*, Phys. Rev. Research **3**, 023114, (2021). (Cited on p. 27.)

[316] F. Engel, T. Dieterle, T. Schmid, C. Tomschitz, C. Veit, N. Zuber, R. Löw, T. Pfau, and F. Meinert, *Observation of Rydberg Blockade Induced by a Single Ion*, Phys. Rev. Lett. **121**, 193401, (2018). (Not cited.)

[317] N. V. Ewald, T. Feldker, H. Hirzler, H. A. Fürst, and R. Gerritsma, *Observation of Interactions between Trapped Ions and Ultracold Rydberg Atoms*, Phys. Rev. Lett. **122**, 253401, (2019). (Cited on p. 27.)

[318] W. C. Stwalley, Y.-H. Uang, and G. Pichler, *Pure Long-Range Molecules*, Phys. Rev. Lett. **41**, 1164, (1978). (Cited on pp. 27 and 29.)

[319] K. T. Tang and J. P. Toennies, *The van der Waals potentials between all the rare gas atoms from He to Rn*, The Journal of Chemical Physics **118**, 4976–4983, (2003). (Cited on pp. 27 and 29.)

[320] D. E. Freeman, K. Yoshino, and Y. Tanaka, *Vacuum ultraviolet absorption spectrum of the van der Waals molecule Xe_2. I. Ground state vibrational structure, potential well depth, and shape*, The Journal of Chemical Physics **61**, 4880–4889, (1974). (Not cited.)

[321] Y. Tanaka and K. Yoshino, *Absorption Spectra of Ne_2 and HeNe Molecules in the Vacuum-uv Region*, The Journal of Chemical Physics **57**, 2964–2976, (1972). (Cited on p. 27.)

[322] C. Fey, F. Hummel, and P. Schmelcher, *Ultralong-range Rydberg molecules*, Molecular Physics **118**, e1679401, (2020). (Cited on p. 28.)

[323] E. Amaldi and E. Segre, *Effetto della Pressione Sui Termini Elevati Degli Alcalini*, Il Nuovo Cimento (1924-1942) **11**, 145–156, (1934). (Cited on p. 28.)

[324] E. Fermi, *Sopra lo Spostamento per Pressione delle Righe Elevate delle Serie Spettrali*, Il Nuovo Cimento (1924-1942) **11**, 157–166, (1934). (Cited on p. 28.)

[325] C. Bahrim, U. Thumm, and I. I. Fabrikant, *$^3S^e$ and $^1S^e$ scattering lengths for e^- + Rb, Cs and Fr collisions*, J. Phys. B: At. Mol. Opt. Phys. **34**, L195–L201, (2001). (Cited on p. 28.)

[326] I. I. Fabrikant, *Interaction of Rydberg atoms and thermal electrons with K, Rb and Cs atoms*, J. Phys. B: At. Mol. Opt. Phys. **19**, 1527–1540, (1986). (Not cited.)

[327] H. Saßmannshausen, F. Merkt, and J. Deiglmayr, *Experimental Characterization of Singlet Scattering Channels in Long-Range Rydberg Molecules*, Phys. Rev. Lett. **114**, 133201, (2015). (Cited on p. 28.)

[328] T. Niederprüm, O. Thomas, T. Eichert, C. Lippe, J. Pérez-Ríos, C. H. Greene, and H. Ott, *Observation of pendular butterfly Rydberg molecules*, Nature Communications **7**, 12820, (2016). (Cited on p. 28.)

[329] M. A. Bellos, R. Carollo, J. Banerjee, E. E. Eyler, P. L. Gould, and W. C. Stwalley, *Excitation of Weakly Bound Molecules to Trilobitelike Rydberg States*, Phys. Rev. Lett. **111**, 053001, (2013). (Cited on p. 28.)

[330] W. Li, T. Pohl, J. M. Rost, S. T. Rittenhouse, H. R. Sadeghpour, J. Nipper, B. Butscher, J. B. Balewski, V. Bendkowsky, R. Löw, and T. Pfau, *A Homonuclear Molecule with a Permanent Electric Dipole Moment*, Science **334**, 1110–1114, (2011). (Cited on p. 28.)

[331] D. Booth, S. T. Rittenhouse, J. Yang, H. R. Sadeghpour, and J. P. Shaffer, *Production of trilobite Rydberg molecule dimers with kilo-Debye permanent electric dipole moments*, Science **348**, 99–102, (2015). (Cited on p. 28.)

[332] V. Bendkowsky, B. Butscher, J. Nipper, J. B. Balewski, J. P. Shaffer, R. Löw, T. Pfau, W. Li, J. Stanojevic, T. Pohl, and J. M. Rost, *Rydberg Trimers and Excited Dimers Bound by Internal Quantum Reflection*, Phys. Rev. Lett. **105**, 163201, (2010). (Cited on p. 28.)

[333] A. Gaj, A. T. Krupp, J. B. Balewski, R. Löw, S. Hofferberth, and T. Pfau, *From molecular spectra to a density shift in dense Rydberg gases*, Nature Communications **5**, 4546, (2014). (Cited on p. 28.)

[334] F. Camargo, R. Schmidt, J. D. Whalen, R. Ding, G. Woehl, S. Yoshida, J. Burgdörfer, F. B. Dunning, H. R. Sadeghpour, E. Demler, and T. C. Killian, *Creation of Rydberg Polarons in a Bose Gas*, Phys. Rev. Lett. **120**, 083401, (2018). (Cited on p. 28.)

[335] J. D. Whalen, S. K. Kanungo, R. Ding, M. Wagner, R. Schmidt, H. R. Sadeghpour, S. Yoshida, J. Burgdörfer, F. B. Dunning, and T. C. Killian, *Probing nonlocal spatial correlations in quantum gases with ultra-long-range Rydberg molecules*, Phys. Rev. A **100**, 011402, (2019). (Cited on p. 28.)

[336] J. Stanojevic, R. Cǒté, D. Tong, S. M. Farooqi, E. E. Eyler, and P. L. Gould, *Long-range Rydberg-Rydberg interactions and molecular resonances*, Eur. Phys. J. D **40**, 3–12, (2006). (Cited on p. 28.)

[337] A. Schwettmann, K. R. Overstreet, J. Tallant, and J. P. Shaffer, *Analysis of long-range Cs Rydberg potential wells*, Journal of Modern Optics **54**, 2551–2562, (2007). (Cited on pp. 28, 57, and 58.)

[338] H. Saßmannshausen, J. Deiglmayr, and F. Merkt, *Long-range rydberg molecules, rydberg macrodimers and rydberg aggregates in an ultracold cs gas*, The European Physical Journal Special Topics **225**, 2891–2918, (2016). (Cited on p. 28.)

[339] H. Saßmannshausen, F. Merkt, and J. Deiglmayr, *Pulsed excitation of Rydberg-atom-pair states in an ultracold Cs gas*, Phys. Rev. A **92**, 032505, (2015). (Cited on pp. 28, 60, and 119.)

[340] M. Movre and G. Pichler, *Resonance interaction and self-broadening of alkali resonance lines. I. Adiabatic potential curves*, J. Phys. B: At. Mol. Opt. Phys. **10**, 2631, (1977). (Cited on p. 29.)

[341] K. Enomoto, M. Kitagawa, S. Tojo, and Y. Takahashi, *Hyperfine-Structure-Induced Purely Long-Range Molecules*, Phys. Rev. Lett. **100**, 123001, (2008). (Cited on p. 29.)

[342] J. D. Miller, R. A. Cline, and D. J. Heinzen, *Photoassociation spectrum of ultracold Rb atoms*, Phys. Rev. Lett. **71**, 2204, (1993). (Not cited.)

[343] P. D. Lett, K. Helmerson, W. D. Phillips, L. P. Ratliff, S. L. Rolston, and M. E. Wagshul, *Spectroscopy of* Na_2 *by photoassociation of laser-cooled Na*, Phys. Rev. Lett. **71**, 2200, (1993). (Not cited.)

[344] J. Léonard, M. Walhout, A. P. Mosk, T. Müller, M. Leduc, and C. Cohen-Tannoudji, *Giant Helium Dimers Produced by Photoassociation of Ultracold Metastable Atoms*, Phys. Rev. Lett. **91**, 073203, (2003). (Cited on p. 29.)

[345] H. Li, G. Quéméner, J.-F. m. c. Wyart, O. Dulieu, and M. Lepers, *Purely long-range polar molecules composed of identical lanthanide atoms*, Phys. Rev. A **100**, 042711, (2019). (Cited on p. 29.)

[346] E. A. Kolganova, A. K. Motovilov, and W. Sandhas, *Scattering length of the helium-atom–helium-dimer collision*, Phys. Rev. A **70**, 052711, (2004). (Cited on p. 29.)

[347] R. E. Grisenti, W. Schöllkopf, J. P. Toennies, G. C. Hegerfeldt, T. Köhler, and M. Stoll, *Determination of the Bond Length and Binding Energy of the Helium Dimer by Diffraction from a Transmission Grating*, Phys. Rev. Lett. **85**, 2284–2287, (2000). (Not cited.)

[348] B. L. Blaney and G. E. Ewing, *Van Der Waals Molecules*, Annual Review of Physical Chemistry **27**, 553–584, (1976). (Not cited.)

[349] J. M. Hutson, *Intermolecular Forces from the Spectroscopy of Van Der Waals Molecules*, Annual Review of Physical Chemistry **41**, 123–154, (1990). (Cited on p. 29.)

[350] U. Kleinekathöfer, K. T. Tang, J. P. Toennies, and C. L. Yiu, *Van der Waals potentials of* He_2*,* Ne_2*, and* Ar_2 *with the exchange energy calculated by the surface integral method*, The Journal of Chemical Physics **107**, 9502–9513, (1997). (Cited on p. 29.)

[351] M. Endres, *Probing correlated quantum many-body systems at the single-particle level*, Ludwig-Maximilians-Universität München, PhD thesis, (2013). (Cited on pp. 31, 32, 34, 35, and 36.)

[352] S. Hild, *Microscopy of quantum many-body systems out of equilibrium*, Ludwig-Maximilians-Universität München, PhD thesis, (2016). (Not cited.)

[353] A. Rubio-Abadal, *Probing quantum thermalization and localization in Bose-Hubbard systems*, Ludwig-Maximilians-Universität München, PhD thesis, (2020). (Cited on pp. 31 and 34.)

[354] I. Bloch, J. Dalibard, and S. Nascimbène, *Quantum simulations with ultracold quantum gases*, Nat. Phys. **8**, 267–276, (2012). (Cited on p. 31.)

[355] S. Kuhr, *Quantum-gas microscopes: a new tool for cold-atom quantum simulators*, National Science Review **3**, 170–172, (2016). (Cited on p. 31.)

[356] A. Marte, T. Volz, J. Schuster, S. Dürr, G. Rempe, E. G. M. van Kempen, and B. J. Verhaar, *Feshbach Resonances in Rubidium 87: Precision Measurement and Analysis*, Phys. Rev. Lett. **89**, 283202, (2002). (Cited on p. 32.)

[357] T. Volz, S. Dürr, S. Ernst, A. Marte, and G. Rempe, *Characterization of elastic scattering near a Feshbach resonance in* $^{87}\mathrm{Rb}$, Phys. Rev. A **68**, 010702, (2003). (Not cited.)

[358] T. Volz, N. Syassen, D. M. Bauer, E. Hansis, S. Dürr, and G. Rempe, *Preparation of a quantum state with one molecule at each site of an optical lattice*, Nature Physics **2**, 692–695, (2006). (Cited on p. 32.)

[359] L. P. L. P. Pitaevskiĭ and S. Stringari, *Bose-Einstein condensation and superfluidity*, International series of monographs on physics ; 164, Oxford University Press, (2016). (Cited on p. 32.)

[360] J. F. Annett, *Superconductivity, superfluids and condensates*, vol. Oxford master series in condensed matter physics, Oxford University Press, (2004). (Cited on p. 32.)

[361] C. Pethick and H. Smith, *Bose-Einstein condensation in dilute gases*, Cambridge University Press, (2002). (Cited on p. 32.)

[362] M. Greiner, *Ultracold quantum gases in three-dimensional optical lattice potentials*, Ludwig-Maximilians-Universität München, PhD thesis, (2003). (Cited on p. 32.)

[363] L. W. Cheuk, M. A. Nichols, K. R. Lawrence, M. Okan, H. Zhang, and M. W. Zwierlein, *Observation of 2D Fermionic Mott Insulators of* ^{40}K *with Single-Site Resolution*, Phys. Rev. Lett. **116**, 235301, (2016). (Cited on p. 32.)

[364] L.-M. Duan, E. Demler, and M. D. Lukin, *Controlling Spin Exchange Interactions of Ultracold Atoms in Optical Lattices*, Phys. Rev. Lett. **91**, 090402, (2003). (Cited on p. 32.)

[365] T. Fukuhara, A. Kantian, M. Endres, M. Cheneau, P. Schauß, S. Hild, D. Bellem, U. Schollwöck, T. Giamarchi, C. Gross, I. Bloch, and S. Kuhr, *Quantum dynamics of a mobile spin impurity*, Nat. Phys. **9**, 235–241, (2013). (Cited on p. 32.)

[366] S. Hild, T. Fukuhara, P. Schauß, J. Zeiher, M. Knap, E. Demler, I. Bloch, and C. Gross, *Far-from-Equilibrium Spin Transport in Heisenberg Quantum Magnets*, Phys. Rev. Lett. **113**, 147205, (2014). (Not cited.)

[367] D. Wei, A. Rubio-Abadal, B. Ye, F. Machado, J. Kemp, K. Srakaew, S. Hollerith, J. Rui, S. Gopalakrishnan, N. Y. Yao, I. Bloch, and J. Zeiher, *Quantum gas microscopy of Kardar-Parisi-Zhang superdiffusion*, (2021). (Cited on pp. 32 and 131.)

[368] M. Boll, T. A. Hilker, G. Salomon, A. Omran, J. Nespolo, L. Pollet, I. Bloch, and C. Gross, *Spin- and density-resolved microscopy of antiferromagnetic correlations in Fermi-Hubbard chains*, Science **353**, 1257–1260, (2016). (Cited on p. 32.)

[369] T. A. Hilker, G. Salomon, F. Grusdt, A. Omran, M. Boll, E. Demler, I. Bloch, and C. Gross, *Revealing hidden antiferromagnetic correlations in doped Hubbard chains via string correlators*, Science **357**, 484–487, (2017). (Cited on p. 32.)

[370] J. Vijayan, P. Sompet, G. Salomon, J. Koepsell, S. Hirthe, A. Bohrdt, F. Grusdt, I. Bloch, and C. Gross, *Time-resolved observation of spin-charge deconfinement in fermionic Hubbard chains*, Science **367**, 186–189, (2020). (Not cited.)

[371] G. Salomon, J. Koepsell, J. Vijayan, T. A. Hilker, J. Nespolo, L. Pollet, I. Bloch, and C. Gross, *Direct observation of incommensurate magnetism in Hubbard chains*, Nature **565**, 56–60, (2019). (Not cited.)

[372] C. S. Chiu, G. Ji, A. Bohrdt, M. Xu, M. Knap, E. Demler, F. Grusdt, M. Greiner, and D. Greif, *String patterns in the doped Hubbard model*, Science **365**, 251–256, (2019). (Cited on p. 32.)

[373] A. Wietek, Y.-Y. He, S. R. White, A. Georges, and E. M. Stoudenmire, *Stripes, Antiferromagnetism, and the Pseudogap in the Doped Hubbard Model at Finite Temperature*, Phys. Rev. X **11**, 031007, (2021). (Cited on p. 32.)

[374] H.-C. Jiang and T. P. Devereaux, *Superconductivity in the doped Hubbard model and its interplay with next-nearest hopping t′*, Science **365**, 1424–1428, (2019). (Cited on p. 32.)

[375] B. Keimer, S. A. Kivelson, M. R. Norman, S. Uchida, and J. Zaanen, *From quantum matter to high-temperature superconductivity in copper oxides*, Nature **518**, 179–186, (2015). (Cited on p. 32.)

[376] B. Keimer and J. E. Moore, *The physics of quantum materials*, Nature Physics **13**, 1045–1055, (2017). (Cited on p. 32.)

[377] P. N. Jepsen, W. W. Ho, J. Amato-Grill, I. Dimitrova, E. Demler, and W. Ketterle, *Transverse Spin Dynamics in the Anisotropic Heisenberg Model Realized with Ultracold Atoms*, Phys. Rev. X **11**, 041054, (2021). (Cited on p. 33.)

[378] J.-y. Choi, S. Hild, J. Zeiher, P. Schauß, A. Rubio-Abadal, T. Yefsah, V. Khemani, D. A. Huse, I. Bloch, and C. Gross, *Exploring the many-body localization transition in two dimensions*, Science **352**, 1547–1552, (2016). (Cited on pp. 33 and 37.)

[379] A. Lukin, M. Rispoli, R. Schittko, M. E. Tai, A. M. Kaufman, S. Choi, V. Khemani, J. Léonard, and M. Greiner, *Probing entanglement in a many-body–localized system*, Science **364**, 256–260, (2019). (Not cited.)

[380] M. Rispoli, A. Lukin, R. Schittko, S. Kim, M. E. Tai, J. Léonard, and M. Greiner, *Quantum critical behaviour at the many-body localization transition*, Nature **573**, 385–389, (2019). (Not cited.)

[381] J. Léonard, M. Rispoli, A. Lukin, R. Schittko, S. Kim, J. Kwan, D. Sels, E. Demler, and M. Greiner, *Signatures of bath-induced quantum avalanches in a many-body–localized system*, (2020). (Cited on p. 33.)

[382] A. Rubio-Abadal, M. Ippoliti, S. Hollerith, D. Wei, J. Rui, S. L. Sondhi, V. Khemani, C. Gross, and I. Bloch, *Floquet Prethermalization in a Bose-Hubbard System*, Phys. Rev. X **10**, 021044, (2020). (Cited on p. 33.)

[383] M. E. Tai, A. Lukin, M. Rispoli, R. Schittko, T. Menke, Dan Borgnia, P. M. Preiss, F. Grusdt, A. M. Kaufman, and M. Greiner, *Microscopy of the interacting Harper–Hofstadter model in the two-body limit*, Nature **546**, 519–523, (2017). (Cited on p. 33.)

[384] M. Aidelsburger, M. Atala, M. Lohse, J. T. Barreiro, B. Paredes, and I. Bloch, *Realization of the Hofstadter Hamiltonian with Ultracold Atoms in Optical Lattices*, Phys. Rev. Lett. **111**, 185301, (2013). (Cited on p. 33.)

[385] H. Miyake, G. A. Siviloglou, C. J. Kennedy, W. C. Burton, and W. Ketterle, *Realizing the Harper Hamiltonian with Laser-Assisted Tunneling in Optical Lattices*, Phys. Rev. Lett. **111**, 185302, (2013). (Not cited.)

[386] M. Aidelsburger, M. Lohse, C. Schweizer, M. Atala, J. Barreiro, S. Nascimbène, N. Cooper, I. Bloch, and N. Goldman, *Measuring the Chern number of Hofstadter bands with ultracold bosonic atoms*, Nature Physics **11**, 162–166, (2015). (Not cited.)

[387] G. Jotzu, M. Messer, R. Desbuquois, M. Lebrat, T. Uehlinger, D. Greif, and T. Esslinger, *Experimental realization of the topological Haldane model with ultracold fermions*, Nature **515**, 237–240, (2014). (Cited on p. 33.)

[388] D. E. Chang, J. S. Douglas, A. González-Tudela, C.-L. Hung, and H. J. Kimble, *Colloquium: Quantum matter built from nanoscopic lattices of atoms and photons*, Rev. Mod. Phys. **90**, 031002, (2018). (Cited on p. 33.)

[389] S. Snigirev, A. J. Park, A. Heinz, I. Bloch, and S. Blatt, *Fast and dense magneto-optical traps for strontium*, Phys. Rev. A **99**, 063421, (2019). (Cited on p. 34.)

[390] P. D. Lett, R. N. Watts, C. I. Westbrook, W. D. Phillips, P. L. Gould, and H. J. Metcalf, *Observation of Atoms Laser Cooled below the Doppler Limit*, Phys. Rev. Lett. **61**, 169, (1988). (Cited on p. 34.)

[391] J. Dalibard and C. Cohen-Tannoudji, *Laser cooling below the Doppler limit by polarization gradients: simple theoretical models*, J. Opt. Soc. Am. B **6**, 2023–2045, (1989). (Cited on p. 34.)

[392] C. Monroe, D. M. Meekhof, B. E. King, S. R. Jefferts, W. M. Itano, D. J. Wineland, and P. Gould, *Resolved-Sideband Raman Cooling of a Bound Atom to the 3D Zero-Point Energy*, Phys. Rev. Lett. **75**, 4149, (1995). (Cited on p. 34.)

[393] S. E. Hamann, D. L. Haycock, G. Klose, P. H. Pax, I. H. Deutsch, and P. S. Jessen, *Resolved-Sideband Raman Cooling to the Ground State of an Optical Lattice*, Phys. Rev. Lett. **80**, 4149, (1998). (Cited on p. 34.)

[394] B. Capogrosso-Sansone, i. m. c. G. m. c. Söyler, N. Prokof'ev, and B. Svistunov, *Monte Carlo study of the two-dimensional Bose-Hubbard model*, Phys. Rev. A **77**, 015602, (2008). (Cited on p. 36.)

[395] A. Rubio-Abadal, J.-y. Choi, J. Zeiher, S. Hollerith, J. Rui, I. Bloch, and C. Gross, *Many-Body Delocalization in the Presence of a Quantum Bath*, Phys. Rev. X **9**, 041014, (2019). (Cited on pp. 37 and 66.)

[396] D. D. Yavuz, P. B. Kulatunga, E. Urban, T. A. Johnson, N. Proite, T. Henage, T. G. Walker, and M. Saffman, *Fast Ground State Manipulation of Neutral Atoms in Microscopic Optical Traps*, Phys. Rev. Lett. **96**, 063001, (2006). (Cited on p. 37.)

[397] R. W. P. Drever, J. L. Hall, F. V. Kowalski, J. Hough, G. M. Ford, A. J. Munley, and H. Ward, *Laser phase and frequency stabilization using an optical resonator*, Applied Physics B **31**, 97–105, (1983). (Cited on p. 38.)

[398] A. Taguchi, A. Miyamoto, Y. Mori, S. Haramura, T. Inoue, K. Nishijima, Y. Kagebayashi, H. Sakai, Y. K. Yap, and T. Sasaki, *Effects of the moisture on CLBO*, in Advanced Solid State Lasers, (1997). (Cited on p. 38.)

[399] F. Pan, X. Wang, G. Shen, and D. Shen, *Cracking mechanism in CLBO crystals at room temperature*, Journal of Crystal Growth **241**, 129–134, (2002). (Cited on p. 38.)

[400] N. Lorenz, *A Rydberg tweezer platform with potassium atoms*, Ludwig-Maximilians-Universität München, PhD thesis, (2021). (Cited on pp. 40, 41, 42, and 48.)

[401] G. D. Boyd and D. A. Kleinman, *Parametric Interaction of Focused Gaussian Light Beams*, Journal of Applied Physics **39**, 3597–3639, (1968). (Cited on p. 40.)

[402] T. C. Briles, D. C. Yost, A. Cingöz, J. Ye, and T. R. Schibli, *Simple piezoelectric-actuated mirror with 180 kHz servo bandwidth*, Opt. Express **18**, 9739–9746, (2010). (Cited on p. 41.)

[403] E. Hecht, *Optics*, Addison-Wesley, 4th ed., (1998). (Cited on p. 43.)

[404] T. R. O'Brian, J.-B. Kim, G. Lan, T. J. McIlrath, and T. B. Lucatorto, *Verification of the ponderomotive approximation for the ac Stark shift in Xe Rydberg levels*, Phys. Rev. A **49**, R649, (1994). (Cited on p. 48.)

[405] T. M. Weber, T. Niederprüm, T. Manthey, P. Langer, V. Guarrera, G. Barontini, and H. Ott, *Continuous coupling of ultracold atoms to an ionic plasma via Rydberg excitation*, Phys. Rev. A **86**, 020702, (2012). (Cited on p. 48.)

[406] F. Markert, P. Würtz, A. Koglbauer, T. Gericke, A. Vogler, and H. Ott, *ac-Stark shift and photoionization of Rydberg atoms in an optical dipole trap*, New Journal of Physics **12**, 113003, (2010). (Cited on pp. 48 and 49.)

[407] S. K. Dutta, J. R. Guest, D. Feldbaum, A. Walz-Flannigan, and G. Raithel, *Ponderomotive Optical Lattice for Rydberg Atoms*, Phys. Rev. Lett. **85**, 5551, (2000). (Cited on p. 49.)

[408] S. E. Anderson, K. C. Younge, and G. Raithel, *Spectroscopy of Rydberg Atoms in a Ponderomotive Optical Lattice*, in CLEO:2011 - Laser Applications to Photonic Applications, Optica Publishing Group, (2011). (Cited on p. 49.)

[409] K. C. Younge, B. Knuffman, S. E. Anderson, and G. Raithel, *State-Dependent Energy Shifts of Rydberg Atoms in a Ponderomotive Optical Lattice*, Phys. Rev. Lett. **104**, 173001, (2010). (Cited on p. 49.)

[410] M. Saffman and T. G. Walker, *Analysis of a quantum logic device based on dipole-dipole interactions of optically trapped rydberg atoms*, Phys. Rev. A **72**, (2005). (Cited on p. 49.)

[411] S. Hollerith, J. Zeiher, J. Rui, A. Rubio-Abadal, V. Walther, T. Pohl, D. M. Stamper-Kurn, I. Bloch, and C. Gross, *Quantum gas microscopy of Rydberg macrodimers*, Science **364**, 664–667, (2019). (Cited on pp. 51, 54, 57, 59, 65, 66, 67, 68, 83, 84, 87, 88, 89, 90, 91, 92, and 108.)

[412] N. Samboy and R. Côté, *Rubidium Rydberg Macrodimers*, J. Phys. B: At. Mol. Opt. Phys. **44**, 184006, (2011). (Cited on pp. 51, 55, and 68.)

[413] S. Hollerith, J. Rui, A. Rubio-Abadal, K. Srakaew, D. Wei, J. Zeiher, C. Gross, and I. Bloch, *Microscopic electronic structure tomography of Rydberg macrodimers*, Phys. Rev. Research **3**, 013252, (2021). (Cited on pp. 51, 67, 68, 70, 73, 75, 76, 78, 80, 82, 87, 94, and 108.)

[414] G. Herzberg, *Molecular spectra and molecular structure, Spectra of diatomic molecules*, vol. 1, Van Nostrand, (1950). (Cited on p. 52.)

[415] *Molecular symmetry and group theory*, in Molecular Physics, John Wiley & Sons, Ltd, (2005). (Cited on pp. 52 and 87.)

[416] B. V. Noumerov, *A Method of Extrapolation of Perturbations*, Monthly Notices of the Royal Astronomical Society **84**, 592–602, (1924). (Cited on p. 56.)

[417] B. Numerov, *Note on the numerical integration of* $d^2x/dt^2 = f(x, t)$, Astronomische Nachrichten **230**, 359–364, (1927). (Cited on p. 56.)

[418] W. Demtröder, *Molecular Physics*, John Wiley & Sons, Ltd, (2007). (Cited on p. 56.)

[419] Y. Hahn, *Density Dependence of Molecular Autoionization in a Cold Gas*, J. Phys. B: At. Mol. Opt. Phys. **33**, L655, (2000). (Cited on p. 58.)

[420] W. Li, P. J. Tanner, and T. F. Gallagher, *Dipole-Dipole Excitation and Ionization in an Ultracold Gas of Rydberg Atoms*, Phys. Rev. Lett. **94**, 173001, (2005). (Cited on p. 65.)

[421] P. J. Tanner, J. Han, E. S. Shuman, and T. F. Gallagher, *Many-Body Ionization in a Frozen Rydberg Gas*, Phys. Rev. Lett. **100**, 043002, (2008). (Not cited.)

[422] M. Kiffner, D. Ceresoli, W. Li, and D. Jaksch, *Quantum mechanical calculation of Rydberg–Rydberg autoionization rates*, J. Phys. B: At. Mol. Opt. Phys. **49**, 204004, (2016). (Not cited.)

[423] M. Mizoguchi, Y. Zhang, M. Kunimi, A. Tanaka, S. Takeda, N. Takei, V. Bharti, K. Koyasu, T. Kishimoto, D. Jaksch, A. Glaetzle, M. Kiffner, G. Masella, G. Pupillo, M. Weidemüller, and K. Ohmori, *Ultrafast Creation of Overlapping Rydberg Electrons in an Atomic BEC and Mott-Insulator Lattice*, Phys. Rev. Lett. **124**, 253201, (2020). (Cited on p. 58.)

[424] P. E. Siska, *Molecular-beam studies of Penning ionization*, Rev. Mod. Phys. **65**, 337, (1993). (Cited on p. 58.)

[425] D. K. Efimov, K. Miculis, N. N. Bezuglov, and A. Ekers, *Strong enhancement of Penning ionization for asymmetric atom pairs in cold Rydberg gases: the Tom and Jerry effect*, J. Phys. B: At. Mol. Opt. Phys. **49**, 125302, (2016). (Cited on p. 58.)

[426] J. T. Young, T. Boulier, E. Magnan, E. A. Goldschmidt, R. M. Wilson, S. L. Rolston, J. V. Porto, and A. V. Gorshkov, *Dissipation-induced dipole blockade and antiblockade in driven Rydberg systems*, Phys. Rev. A **97**, 023424, (2018). (Cited on pp. 58, 127, and 130.)

[427] W. Demtröder, *Widths and Profiles of Spectral Lines*, in Laser Spectroscopy: Basic Concepts and Instrumentation, Springer Berlin Heidelberg, (2003), 59–95. (Cited on p. 61.)

[428] N. Samboy, J. Stanojevic, and R. Côté, *Formation and properties of Rydberg macrodimers*, Phys. Rev. A **83**, 050501, (2011). (Cited on p. 67.)

[429] D. A. Steck, *Rubidium 87 D Line Data (revision 2.2.1)*, http://steck.us/alkalidata (2019). (Cited on p. 67.)

[430] N. Samboy, J. Stanojevic, and R. Côté, *Formation and Properties of Rydberg Macrodimers*, Phys. Rev. A **83**, 050501, (2011). (Cited on p. 68.)

[431] E. Arimondo, M. Inguscio, and P. Violino, *Experimental Determinations of the Hyperfine Structure in the Alkali Atoms*, Rev. Mod. Phys. **49**, 31, (1977). (Cited on p. 79.)

[432] A. Tauschinsky, R. Newell, H. B. van Linden van den Heuvell, and R. J. C. Spreeuw, *Measurement of ^{87}Rb Rydberg-state hyperfine splitting in a room-temperature vapor cell*, Phys. Rev. A **87**, 042522, (2013). (Cited on p. 79.)

[433] M. Born and R. Oppenheimer, *Zur Quantentheorie der Molekeln*, Annalen der Physik **389**, 457–484, (1927). (Cited on p. 87.)

[434] V. Blanchet, M. Z. Zgierski, T. Seideman, and A. Stolow, *Discerning vibronic molecular dynamics using time-resolved photoelectron spectroscopy*, Nature **401**, 52–54, (1999). (Cited on p. 87.)

[435] H. Lefebvre-Brion and R. W. Field, *The Spectra and Dynamics of Diatomic Molecules*, Academic Press, (2004). (Cited on p. 87.)

[436] H. Kato and M. Baba, *Dynamics of Excited Molecules: Predissociation*, Chem. Rev. **95**, 2311–2349, (1995). (Cited on pp. 87 and 93.)

[437] W. Domcke and D. R. Yarkony, *Role of Conical Intersections in Molecular Spectroscopy and Photoinduced Chemical Dynamics*, Annual Review of Physical Chemistry **63**, 325–352, (2012). (Cited on pp. 87 and 88.)

[438] G. Olaso-González, M. Merchán, and L. Serrano-Andrés, *Ultrafast Electron Transfer in Photosynthesis: Reduced Pheophytin and Quinone Interaction Mediated by Conical Intersections* **963**, 706–709, (2007). (Cited on p. 87.)

[439] E. Fernández, L. Blancafort, M. Olivucci, and M. A. Robb, *Intramolecular Electron Transfer: Independent (Ground State) Adiabatic (Chemical) and Nonadiabatic Reaction Pathways in Bis(hydrazine) Radical Cations*, J. Am. Chem. Soc. **122**, 7528–7533, (2000). (Cited on p. 87.)

[440] Vigué, J., Broyer, M., and Lehmann, J.C., *Natural Hyperfine and Magnetic Predissociation of the* I_2B *State II. - Experiments on Natural and Hyperfine Predissociation*, J. Phys. France **42**, 949–959, (1981). (Cited on pp. 94 and 95.)

[441] J. Vigué, M. Broyer, and J. Lehmann, *Natural Hyperfine and Magnetic Predissociation of the* I_2B *State II. - Experiments on Magnetic Predissociation*, Journal de Physique **42**, 961–978, (1981). (Cited on p. 95.)

[442] S. Hollerith, K. Srakaew, D. Wei, A. Rubio-Abadal, D. Adler, P. Weckesser, A. Kruckenhauser, V. Walther, R. van Bijnen, J. Rui, C. Gross, I. Bloch, and J. Zeiher, *Realizing Distance-Selective Interactions in a Rydberg-Dressed Atom Array*, Phys. Rev. Lett. **128**, 113602, (2022). (Cited on pp. 97, 98, 100, 104, 107, 108, 110, 113, 114, and 116.)

[443] S. Weinberg, *The Quantum Theory of Fields, Volume 1: Foundations*, Cambridge University Press, (2005). (Cited on p. 103.)

[444] Y. W. Sokhotskii, *On definite integrals and functions used in series expansions*, St. Petersburg (1873). (Cited on p. 103.)

[445] M. McDonald, B. H. McGuyer, F. Apfelbeck, C. H. Lee, I. Majewska, R. Moszynski, and T. Zelevinsky, *Photodissociation of ultracold diatomic strontium molecules with quantum state control*, Nature **535**, 122–126, (2016). (Cited on p. 105.)

[446] M. Peper and J. Deiglmayr, *Photodissociation of long-range rydberg molecules*, Phys. Rev. A **102**, 062819, (2020). (Cited on p. 105.)

[447] G. Pupillo, A. Micheli, M. Boninsegni, I. Lesanovsky, and P. Zoller, *Strongly Correlated Gases of Rydberg-Dressed Atoms: Quantum and Classical Dynamics*, Phys. Rev. Lett. **104**, 223002, (2010). (Cited on p. 109.)

[448] A. Geißler, U. Bissbort, and W. Hofstetter, *Quasiparticle spectra of supersolid lattice gases at near-resonant rydberg dressing*, Phys. Rev. A **98**, 063635, (2018). (Cited on p. 109.)

[449] P. Richerme, Z.-X. Gong, A. Lee, C. Senko, J. Smith, M. Foss-Feig, S. Michalakis, A. V. Gorshkov, and C. Monroe, *Non-local propagation of correlations in quantum systems with long-range interactions*, Nature **511**, 198–201, (2014). (Cited on p. 112.)

[450] M. C. Tran, J. R. Garrison, Z.-X. Gong, and A. V. Gorshkov, *Lieb-Robinson bounds on* n*-partite connected correlation functions*, Phys. Rev. A **96**, 052334, (2017). (Cited on p. 112.)

[451] M. Mamaev, R. Blatt, J. Ye, and A. M. Rey, *Cluster State Generation with Spin-Orbit Coupled Fermionic Atoms in Optical Lattices*, Phys. Rev. Lett. **122**, 160402, (2019). (Cited on p. 112.)

[452] O. Mandel, M. Greiner, A. Widera, T. Rom, T. W. Hänsch, and I. Bloch, *Controlled collisions for multi-particle entanglement of optically trapped atoms*, Nature **425**, 937–940, (2003). (Cited on p. 112.)

[453] R. Raussendorf and H. J. Briegel, *A One-Way Quantum Computer*, Phys. Rev. Lett. **86**, 5188–5191, (2001). (Cited on p. 112.)

[454] J. R. Johansson, P. D. Nation, and F. Nori, *QuTiP: An open-source python framework for the dynamics of open quantum systems*, Computer Physics Communications **183**, 1760–1772, (2012). (Cited on p. 113.)

[455] N. Syassen, D. M. Bauer, M. Lettner, T. Volz, D. Dietze, J. J. García-Ripoll, J. I. Cirac, G. Rempe, and S. Dürr, *Strong dissipation inhibits losses and induces correlations in cold molecular gases*, Science **320**, 1329–1331, (2008). (Cited on p. 122.)

[456] C. Ates, B. Olmos, W. Li, and I. Lesanovsky, *Dissipative Binding of Lattice Bosons through Distance-Selective Pair Loss*, Phys. Rev. Lett. **109**, 233003, (2012). (Cited on p. 122.)

[457] M. Kiffner, W. Li, and D. Jaksch, *Three-Body Bound States in Dipole-Dipole Interacting Rydberg Atoms*, Phys. Rev. Lett. **111**, 233003, (2013). (Cited on p. 122.)

[458] N. Samboy and R. Côté, *Rubidium Rydberg linear macrotrimers*, Phys. Rev. A **87**, 032512, (2013). (Cited on p. 122.)

[459] R. Gutiérrez, C. Simonelli, M. Archimi, F. Castellucci, E. Arimondo, D. Ciampini, M. Marcuzzi, I. Lesanovsky, and O. Morsch, *Experimental signatures of an absorbing-state phase transition in an open driven many-body quantum system*, Phys. Rev. A **96**, 041602, (2017). (Cited on p. 127.)

[460] C. Simonelli, M. M. Valado, G. Masella, L. Asteria, E. Arimondo, D. Ciampini, and O. Morsch, *Seeded excitation avalanches in off-resonantly driven Rydberg gases*, J. Phys. B: At. Mol. Opt. Phys. **49**, 154002, (2016). (Not cited.)

[461] T. M. Wintermantel, M. Buchhold, S. Shevate, M. Morgado, Y. Wang, G. Lochead, S. Diehl, and S. Whitlock, *Epidemic growth and Griffiths effects on an emergent network of excited atoms*, Nature **12**, 103, (2021). (Not cited.)

[462] S. Helmrich, A. Arias, G. Lochead, T. M. Wintermantel, M. Buchhold, S. Diehl, and S. Whitlock, *Signatures of self-organized criticality in an ultracold atomic gas*, Nature **577**, 481–486, (2020). (Cited on p. 127.)

Acknowledgements

Generally, projects like the one presented here require well-functioning teams and an efficient overall group structure, on a professional as well as a personal level. This environment was important for me, in several ways. I would like to thank

- Immanuel Bloch, for giving great lectures, offering me a position in this well-working experiment, and supporting all of us by well-organized regular group meetings and sending us to conferences. It is amazing that after more than ten succesfull scientific years, the quantum gas microscope where I got the opportunity to do my PhD is still able to do state-of-the art research and there are still many interesting directions.

- All team members. I start with Christian Groß for supervising me during my master's project as well as the first part of my PhD and Johannes Zeiher for introducing me to the experiment and answering tons of questions related to Rydberg atoms. I also remember running in Hamburg or enjoying the sunrise from the top of a mountain in France at five in the morning. I also thank Antonio Rubio-Abadal for being my lab partner. We had many stimulating discussions and nice hours in the lab together (such as during the Raman project), played music together at Christmas parties, and spend nice evenings at different locations, also together with Sarah Hirthe. I thank Jun Rui, he was an extremely motivated and focused postdoc and played a key role in my PhD, in particular because of his help in the description of macrodimer photoassociation. I thank David Wei for many stimulating discussions about physics, for preparing talks together, and playing music with Toni and me. I thank Kritsana Srakaew for discussing Rydberg physics, building and integrating the new UV system together, and also for cooking great Thai food. Both are not only good physicists and technically very skilled but also really good team players. I also want to thank our new members, our new postdoc Pascal Weckesser, for our motivating conversations at the frog pond and for sharing our different scientific backgrounds, and our new PhD student Daniel Adler. Both of them fit perfectly into the team and I am really looking forward to their upcoming projects.

- Other group members, in particular Simon Evered (discussions about macrodimers and frequency doubling), Jae-Yoon Choi (discussing Landau levels and the FQHE), Joannis Koeppsel (our Quantum Optics tutorial), Thomas Chalopin (discussions about topology and occasional evening conversations), Nikolaus Lorenz, Lorenzo Festa, Lea Steinert, and Philip Osterholz (discussions about Rydberg physics and UV lasers), Sebastian Hild (help during my master's thesis), Tarik Yefsah (discussions about physics and life in general), Martin Link (a very smart and nice person who helped installing a new monitoring system), and Sejal Aggarwal (discussions about modulation transfer spectroscopy).

- Dan Stamper-Kurn for many stimulating discussions during his time in Munich and also for inviting us to his place and discuss with his students. I am also very thankful for the opportunity to visit international conferences during my PhD and present our results! I remember great discussions with Thomas Pohl, Thomas Gallagher and Johannes Deiglmayr at a summer school about Rydberg atoms at Weizmann institute. I also remember DAMOP 2019 in Milwaukee and the week I spet in the group of Markus Greiner, and the discussions with Julian Léonard and Guillaume

Salomon during that week. I also thank Tilman Pfau for his enthusiasm which is definitely important for the German Rydberg community.

- Valentin Walther, Andreas Kruckenhauser, Rick van Bijnen, as well as Mathieu Barbier for their help in developing theoretical models. I always enjoyed the extended Sunday afternoon skype sessions.
- Katharina Kleinlein for giving a great tutorial in quantum mechanics, which in the end motivated me to contact the groups at MPQ. Christoph Gohle for many stimulating discussions and for giving me the opportunity to help the teams by soldering circuits, as well as Olivia Mödel for introducing me into the required skills.
- Anton Mayer for his help regarding mechanical designs, in particular for our new doubling cavities. Furthermore, I thank Karsten Förster for help regarding electronic issues. I also thank Kristina Schuldt and Doreen Seidl for their administrative work and also for always holding the group together and introducing new members. Having this broad specialised support is unique and a key to make the work done at MPQ possible.
- Everyone in the sustainability group at MPQ and also everyone in our group who contributed reading the latest IPCC report, in particular Raphaël Saint-Jalm and Benjamin Schiffer. Environmental issues affect human life in many aspects. After reading about some of the scientific background behind climate change I am convinced that it will be crucial to act and possibly also restructure societies in some aspects. I think many people still underestimate the problem (maybe because our behavior now affects the future in a few decades) and also how hard it will be to find solutions.
- All friends I found at MPQ. I thank Marcel Duda for attending lectures and solving problem sets together, and for having many nice evenings together with Denise and Franzi. I thank André Heinz for evening activities, as well as for sharing our musical taste. I thank both of them as well as Jan Dziewior for playing music together, inside and outside of the institute. I thank Roman Bause who I know now for ten years for many very stimulating discussions, about physics but also many other topics. I definitely thank Annie Jihyun Park for our running and discussion sessions. She is a really motivated physicist and extremely hard-working. Studying together helped me to contribute more to scientific discussions and also improved my English. She also helped me to get through a few tough times.
- Many people I played music with during now so many years. It was always a great experience and helped me to express myself in many ways and generally to connect to people.
- Alex for our extended hiking trips, ranging from Skandinavia to Kyrgyzstan, and our trips to Berlin.
- Finally, Franziska Kratzl, for living with me now for more than ten years. We have a similar background and know each other since both of us contributed to the local philosophy club, long before we decided to do science. We always supported each other and had an uncountable amount of great evenings, weekend activities, and holidays. Both of us would not be who we are without the other person. Our time was amazing and I am looking forward to what follows.